

X-ray Tomography for Evaluation of Damage in Concrete Bond

Tyler S. Sprague

A thesis submitted in partial fulfillment
of the requirements for the degree of

Master of Science in Civil Engineering

The University of Washington

2006

Program Authorized to Offer Degree:

Department of Civil and Environmental Engineering

University of Washington
Graduate School

This is to certify that I have examined this copy of a master's thesis by

Tyler S. Sprague

and have found that it is complete and satisfactory in all respects,
and that any and all revisions required by the final
examining committee have been made.

Committee Members:

George M. Turkiyyah

Laura N. Lowes

John F. Stanton

Date: _____

In presenting this thesis in partial fulfillment of the requirements for a master's degree at the University of Washington, I agree that the Library shall make its copies freely available for inspection. I further agree that extensive copying of this thesis is allowable only for scholarly purposes, consistent with "fair use" as prescribed in the U.S. Copyright Law. Any other reproduction for any purposes or by any means shall not be allowed without my written permission.

Signature _____

Date _____

University of Washington

Abstract

X-ray Tomography for Evaluation of Damage in Concrete Bond

Tyler S. Sprague

Chair of the Supervisory Committee:
Associate Professor George Turkiyyah
Department of Civil and Environmental Engineering

The bond between concrete and steel is vital to the performance of reinforced concrete buildings. A non-destructive, local bond evaluation is carried out through a series of reinforced concrete bond experiments inside a high-resolution X ray CT facility to capture and evaluate progressive bond failure. The results of these scans are full 3D images of our local bond sample at each loading increment.

In this project three different information extraction techniques are used to extract bond failure information: visual inspection, single-image processing and multi-image processing. Visual inspection provided general crack orientation and aggregate splitting information. Single image processing provided crack volumes and surface area for fracture energy calculations. Multi-image processing, using image registration techniques provided displacement fields as a step towards producing strain fields. Elastic registration and an XFEM extension were used to model both continuous and discontinuous displacements.

TABLE OF CONTENTS

List of Figures.....	iv
List of Tables.....	viii
Chapter 1: Introduction.....	1
1.0 Introduction	1
1.1 Background on X-ray CT applied to Civil Engineering	2
1.1.1 Image Processing Algorithms.....	4
1.1.2 Image Processing for Civil Engineering Applications.....	4
1.2 Experimental Testing in Investigate Bond	5
1.3 Thesis Organization	8
Chapter 2: X-Ray Computed Tomography.....	9
2.0 Introduction	9
2.1 X-ray Computed Tomography.....	9
2.2 The Imaging Process.....	9
2.2.1 The Source and Configuration.....	10
2.2.2 The Specimen to be Imaged	12
2.2.3 Detector	12
2.3 Project Facility Details.....	13
2.4 Variables Effecting X-ray CT Images.....	14
2.4.1 Calibration	14
2.4.2 Slice Thickness	15
2.4.3 Number of Views.....	17
2.4.4 Integration Time.....	18
2.4.5 Filtering.....	20
2.5 2D Image Reconstruction.....	21
2.6 3D Image Assembly.....	22
2.7 Effectiveness of Imaging.....	23
2.8 Conclusions	24
Chapter 3: Tools for Extracting Information from Images.....	25
3.0 Introduction	25
3.1 Visual Inspection	25
3.1.1 Examples	25
3.2 Single Image Processing	27
3.2.1 Previous Research.....	28
3.2.2 Threshold Segmentation for Feature Identification	28
3.2.3 Feature Characterization.....	30
3.2.4 Threshold Value Determination.....	31
3.3 Multiple-Image Processing - Image Registration	34
3.3.1 Image Registration Overview	35
3.3.2 Image Registration – Motion Estimation	38
3.3.3 Image Registration – Elastic Registration.....	39
3.3.4 Image Registration - XFEM Extension.....	46
3.4 Conclusions	58

Chapter 4: Extracted Bond Information	59
4.0 Introduction	59
4.1 Process One: Visual Inspection	59
4.1.1 Method	59
4.1.2 Results	60
4.1.3 Conclusions	63
4.2 Process Two: Image Thresholding and Crack Extraction	63
4.2.1 Method	63
4.2.2 Results	65
4.2.3 Conclusions	67
4.3 Process Three: Fracture Analysis	67
4.3.1 Method	67
4.3.2 Results	72
4.3.3 Conclusions	74
4.4 Process Four: Bond Displacements from Motion Estimation	74
4.4.1 Method	75
4.4.2 Results	79
4.4.3 Conclusions	80
4.5 Process 5: Bond Displacements from Elastic Registration	80
4.5.1 Method	80
4.5.2 Results	86
4.5.3 Conclusions	88
4.6 Process 6: Modified Elastic Registration	89
4.6.1 Method	89
4.6.2 Results	90
4.6.3 Conclusions	91
4.7 Process 7: Displacements as Elastic + Inelastic Deformations	91
4.7.1 Method	92
4.7.2 Results	94
4.7.3 Conclusions	95
Chapter 5: Conclusions.....	96
5.0 Summary	96
5.1 Conclusions	96
5.1.1 Visual Inspection	96
5.1.2 Image Threshold and Crack Extraction.....	97
5.1.3 Fracture Analysis	97
5.1.4 Overall Structural Deformations.....	97
5.1.5 Displacements as Elastic Deformations	97
5.1.6 Modified Elastic Registration	97
5.1.7 Displacements as Elastic + Inelastic Deformations	98
5.2 Recommendations for Future Research	98
Bibliography	99
Appendix A: Sample 3D Reconstructions.....	102
Appendix B: Crack Volume Reconstructions.....	124
Appendix C: Fracture Energy Calculations for Each Sample.....	136

Appendix D: Motion Estimation.....	145
Appendix E: Elastic Registration.....	156
Appendix F: Code Implementation.....	188

LIST OF FIGURES

Figure 1.1 - Concrete & Steel Image from Morgan et. al. (1980)	2
Figure 1.2 - Concrete & Steel Attenuation Study from Martz et al. 1993	3
Figure 1.3 - Mortar Compression Sample from Landis et al. 2003	4
Figure 1.4 - Progressive Cracking Extracted from Images from Zhang (2004)	5
Figure 1.5 – Bond Specimen Schematic.....	6
Figure 1.6 – Load Displacement Curve for Specimen P1	7
Figure 2.1 - X ray CT Set Up.....	10
Figure 2.2 – Energy Spectrum and Intensities for 420 keV source (Ketcham, 2001)	11
Figure 2.3 - Fan Beam Configuration	12
Figure 2.4 – X ray CT Facility at University of Texas, Austin	13
Figure 2.5 - Cement Wedge Calibration.....	15
Figure 2.6 - Air Wedge Calibration	15
Figure 2.7 - 1mm Slice Spacing.....	16
Figure 2.8 - 0.5mm Slice Spacing.....	16
Figure 2.9 - 1000 views	17
Figure 2.10 - 2000 views	18
Figure 2.11 - 32ms Integration Time.....	19
Figure 2.12 - 64ms Integration Time.....	19
Figure 2.13 - No Filtering.....	20
Figure 2.14 - Numerical Beam Hardening Filter	21
Figure 2.15 - 3D Reconstruction of Data Set.....	23
Figure 3.1 – P3W2-3, Visual Inspection	26
Figure 3.2 – P3F-3, Visual Inspection.....	27
Figure 3.3 - Images as Discrete Functions	28
Figure 3.4 – Sample Image from Specimen P1-3	29

Figure 3.5 – Histogram of Sample Image.....	30
Figure 3.6 - Crack Surface with Discontinuities.....	31
Figure 3.7 – Histogram of Image P1-3	32
Figure 3.8 - P1-3, Slice 20	32
Figure 3.9 - Threshold, $t = 13000$, P1-3, Slice 20.....	33
Figure 3.10 – P1-1 -> P1-4 Void Changes due to Threshold Value	33
Figure 3.11 – Template (T) and Reference Image (R).....	42
Figure 3.12 – Objective Criterion vs. Number of Iterations.....	43
Figure 3.13 – Deformed Template (T_u).....	43
Figure 3.14 – x and y Displacement Fields (on pixel scale).....	43
Figure 3.15 - Template (T) and Reference Image (R).....	44
Figure 3.16 - Known x and y Displacement Fields.....	44
Figure 3.17 – Objective Criterion vs. Number of Iterations.....	45
Figure 3.18 – Deformed Template	45
Figure 3.19 – x and y Displacement Fields Generated.....	45
Figure 3.20 – Elastic Mesh with Embedded Crack.....	48
Figure 3.21 – Deformed Template Image with Crack Opening	49
Figure 3.22 – x and y Elastic Displacement Fields.....	49
Figure 3.23 – x and y Discontinuous Displacement Fields	50
Figure 3.24 – Template Image	50
Figure 3.25 – Known x and y Displacement Fields	51
Figure 3.26 – New Reference Image.....	51
Figure 3.27 – Deformed Template (T_u).....	51
Figure 3.28 – Objective Criteria during XFEM Registration.....	52
Figure 3.29 – x and y XFEM Classical Displacements.....	52
Figure 3.30 – x and y Enriched Displacements	53
Figure 3.31 – Reference and Template Images	54

Figure 3.32 – Deformed Template Image	54
Figure 3.33 – Elastic Registration x and y Displacement Fields	54
Figure 3.34 – Principal Tensile Strains	55
Figure 3.35 – Principal Tensile Strains Contour.....	56
Figure 3.36 – Principal Strain Local Maxima.....	56
Figure 3.37 – Shortest-Distance Crack Connection.....	57
Figure 4.1 – Sample Image from Specimen P3W1B-4	60
Figure 4.2 – P1-3 Segmented Specimen.....	64
Figure 4.3 – P3F-3 -> P3F-4 Segmented Crack Growth.....	64
Figure 4.4 – P1-3 Radial Crack Measurement Locations.....	70
Figure 4.5 – Enlarged Crack Measurement Location	71
Figure 4.6 – P1-3, Crack Width vs. Height	71
Figure 4.7 – Assumed Crack, Diminishing With Height	72
Figure 4.8 - Cracking Image Sequence	75
Figure 4.9 – x Displacement Field (xy plane queried @ 0.5” from base).....	76
Figure 4.10 - y Displacement Field (xy plane queried @ 0.5” from base)	77
Figure 4.11 - z Displacement Field (xy plane queried @ 0.5” from base).....	77
Figure 4.12 – Cracked Specimen, with Sample points.....	78
Figure 4.13 – Specimen P3W1A, Image 1 -> Image 2	81
Figure 4.14 – x and y Displacement Fields for P3W1B-1->P3W1B-2.....	82
Figure 4.15 – Radial and Tangential Displacement Fields for P3W1B-1->P3W1B-2	82
Figure 4.16 – Maximum Principal Strain Field	83
Figure 4.17– P1-2 -> P1-3 Image Sequence.....	84
Figure 4.18 – x and y Displacement Fields for P1-2 -> P1-3	85
Figure 4.19 – Contour x and y Displacement Fields for P1-2 -> P1-3	85
Figure 4.20 – Maximum Principal Strains from x and y Displacement Fields	86
Figure 4.21 – Max. Principal Strain Field Contours (P3W1B-1->2, P3W1B-2->3)	87

Figure 4.22 – Max. Principal Strain Contours (P3W1B) at 1mm Height Intervals.....	88
Figure 4.23 – Elastic Registration Displacement Fields for P1-2->P1-3	90
Figure 4.24 – Modified Elastic Registration Displacement Fields for P1-2->P1-3.....	91
Figure 4.25 – Identify Crack Locations.....	92
Figure 4.26 – x and y Displacements from XFEM with Linear Crack	93
Figure 4.27 – x and y Displacement Field Contours.....	94

LIST OF TABLES

Table 1 – Imaged Specimens	6
Table 2 - Visual Inspection Results, Specimen P3W1B-4	60
Table 3 - Fracture Energy Calculation for Specimen P1-2 -> P1-3	73
Table 4 - Motion Estimation Sample Points	79

ACKNOWLEDGMENTS

The author would like to thank the National Science Foundation and the University of Washington, for without whom none of this would have been possible. This thesis would have never been completed without the love and encouragement of my fiancé Rachel, my parents and all my family and friends.

CHAPTER 1 : INTRODUCTION

1.0 Introduction

The bond between concrete and steel is vital to the performance of reinforced concrete structures. Yet the characteristics of local bond-zone behavior are still largely unknown due to the difficulty in observing and measuring such behavior. A non-destructive evaluation method is needed to enable investigation of bond behavior. In this project, a series of reinforced concrete bond experiments were conducted inside a high-resolution X-ray computed tomography (X ray CT) facility to observe progressive bond failure.

The test specimens for the investigation consisted of single 6-inch by 12-inch concrete cylinders. In each one, a single, 1-inch diameter steel reinforcing bar was embedded in over a length that varied from 1 -3 inches among specimens. The reinforcing bar was subjected to tensile “pull-out” loading to failure. Additional specimens were tested to investigate the impact of bonded length on response. Martin (2006) provided a complete discussion of the test program.

A subset of the test specimens, representing the range of design parameters and observed behavior modes was tested inside a high-resolution X ray CT facility at the University of Texas, Austin, UTCT Lab. For these specimens, X ray images and 3D reconstructions were generated at several times during the load histories, in particular prior to and immediately following failure.

These images provide improved understanding of the local mechanisms that determine the response. Coupled with powerful image processing software, this data has the potential to shed light on true bond behavior. Simple visual inspection of the images can provide information about the material failure, while multiple-image processing and finite element modeling can provide strain fields providing insight into the mechanics of progressive bond failure.

1.1 Background on X-ray CT applied to Civil Engineering

X ray CT technology was developed primarily for medical applications. The first X ray CT scanner was developed in England by G. N. Hounsfield in 1972 for the use of scanning human brains, with a maximum resolution of 80x80 pixels. The technology was brought to the United States in 1973, and was further developed at Georgetown University to image the whole body. X-ray CT has been improved by higher energy levels and faster computers to enable imaging of non-living specimens.

One of the first uses of CT for evaluation of concrete was in 1980 by a group of scientists and engineers at the University of Texas, Austin ([Morgan et. al., 1980](#)). They used 662-keV gamma rays to create 2D images, as seen in Figure 1.1, but did not attempt a 3D reconstruction. This process was an early evaluation of computerized tomography, and was limited to only visual inspection of the images.

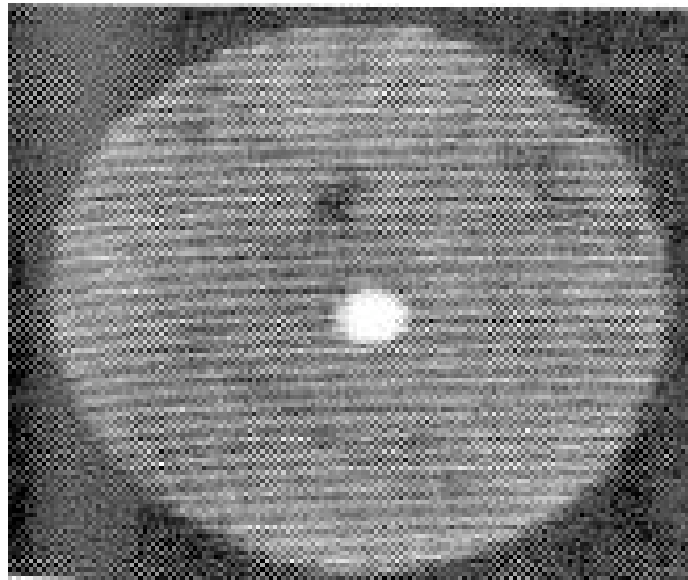


Figure 1.1 - Concrete & Steel Image from Morgan et. al. (1980)

In 1993, a similar experiment was carried out at the Lawrence Livermore National Lab ([Martz et al. 1993](#)). This time, concrete with reinforcing steel was imaged with particular

attention to the attenuation factors (the proportion of X rays absorbed) of each material. These attenuation factors, roughly proportional to material density, are currently used to create the 2D images. Both of these projects were limited by low energy sources, creating blurry images that were unusable in practice (Figure 1.2).

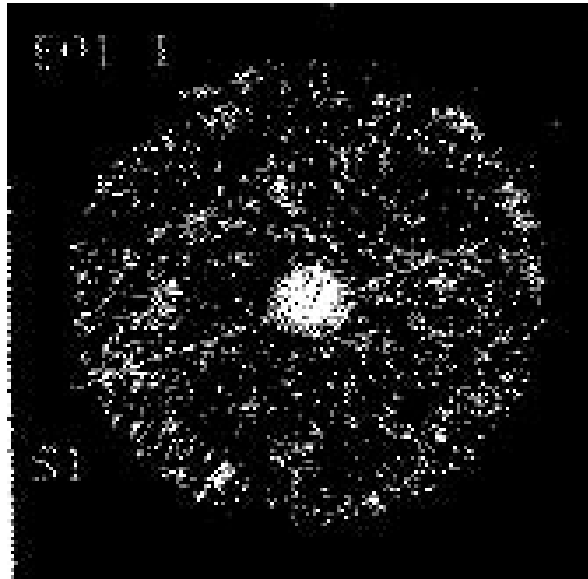


Figure 1.2 - Concrete & Steel Attenuation Study from Martz et al. 1993

Advances in CT technology brought higher energy radiation sources, improved imaging techniques, and improved CT algorithms. These improvements enabled the 2003 study by Landis et. al. in which micro X-ray CT was used to investigate crack propagation in mortar samples. Figure 1.3 shows a sample image. The images generated as part of his study were sufficiently high resolution (1024 pixel x 1024 pixel with 1 pixel = 6_μm) that Landis et al. were able to perform fracture analysis calculations and observe incremental cracking as the mortar was compressed. The mortar samples were 4mm diameter cylinder, and thus permitted use of a micro CT facility and extremely high resolution images.

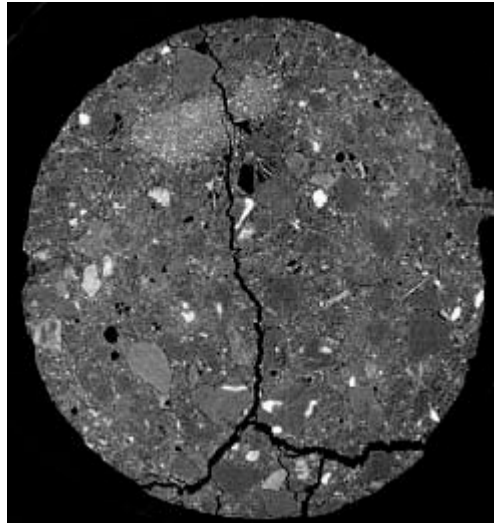


Figure 1.3 - Mortar Compression Sample from Landis et al. 2003

1.1.1 Image Processing Algorithms

Image processing is an extremely large field, generalized as any form of information processing that involves images. As imaging methods improve and computers get faster, images are used more and more to visualize phenomena and to extract information. Digital images, as merely arrays of scalar values, can be seen as functions – and can be processed in many ways.

Common uses of image processing include geometric transformations to enlarge, reduce or rotate an image; filtering to highlight certain areas of an image; and edge detection to enhance crack boundaries. Segmentation is a common method to separate an image into different portions. Image registration (or image alignment) is used to combine images or track changes between two images.

1.1.2 Image Processing for Civil Engineering Applications

A major contribution to the field of image processing for civil engineering applications was completed by Zhang (2004). This thesis focused on extracting crack patterns from small compression samples under load. (Figure 1.4) By using a type of

image registration, structural changes are tracked and then converted to crack surfaces and volumes. This routine was optimized for the concrete mortar specimens from Landis et al (2003), but was used for extraction of displacement fields in bond specimens with reasonable accuracy.



Figure 1.4 - Progressive Cracking Extracted from Images from Zhang (2004)

1.2 Experimental Testing in Investigate Bond

For this project five bond specimens were tested. These specimens were designed to isolate steel-concrete bond behavior. A schematic of the test specimens and loading is shown in Figure 1.5. Through a hydraulic ram reacting on against the top of the specimen, the center bar was loaded in tension. Each specimen was tested in an X-ray computed tomography facility, and imaged at different points on the load-displacement history.

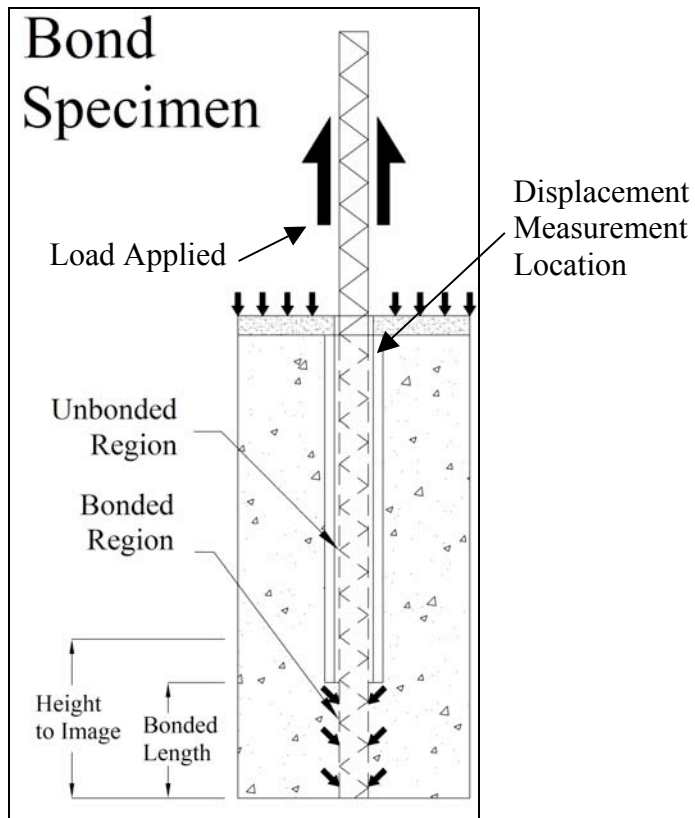


Figure 1.5 – Bond Specimen Schematic

Table 1 provides design details for each specimen as well as a specimen “name” which will be used through out this thesis to identify individual specimens. Individual images of a specific specimen will be referenced by a number at the end of the specimen name (eg. P1-2 indicated the second image of specimen P1.)

Table 1 – Imaged Specimens

Name	Diameter	Height	Bonded Length	Imaged Distance	Maximum Load	Confinement	No. Scans
P1	6"	12"	1"	2"	15.6 kips	Fiber Wrap	4
P3F	6"	12"	3"	4"	32.2 kips	Polyester Fibers	4
P3W1A	6"	12"	3"	4"	30.7 kips	0.054" wire	4
P3W1B	6"	12"	3"	4"	30.9 kips	0.074" wire	4
P3W2	6"	12"	3"	4"	33.9 kips	double 0.054" wire	5

Note: All samples tested had a 1” diameter bar (#8).

For each specimen, bar load and displacement data were recorded. Load data defined the tensile load applied to the protruding bar (Figure 1.5). Displacement data define the movement of the bar relative to the concrete, at the top face of the cylinder. Thus, the displacement includes the elongation of the bar over the un-bonded length.

Figure 1.6 shows a typical load-displacement curve for the bond specimens; dark circles represent the points at which X-ray scans were taken. The initial part of the curve defines the response of the un-cracked specimen and is nearly linear. After the peak load is reached, the specimen unloads too rapidly for the data acquisition system to capture data. Thereafter the resistance is provided by friction as the bar slides past the surrounding concrete.

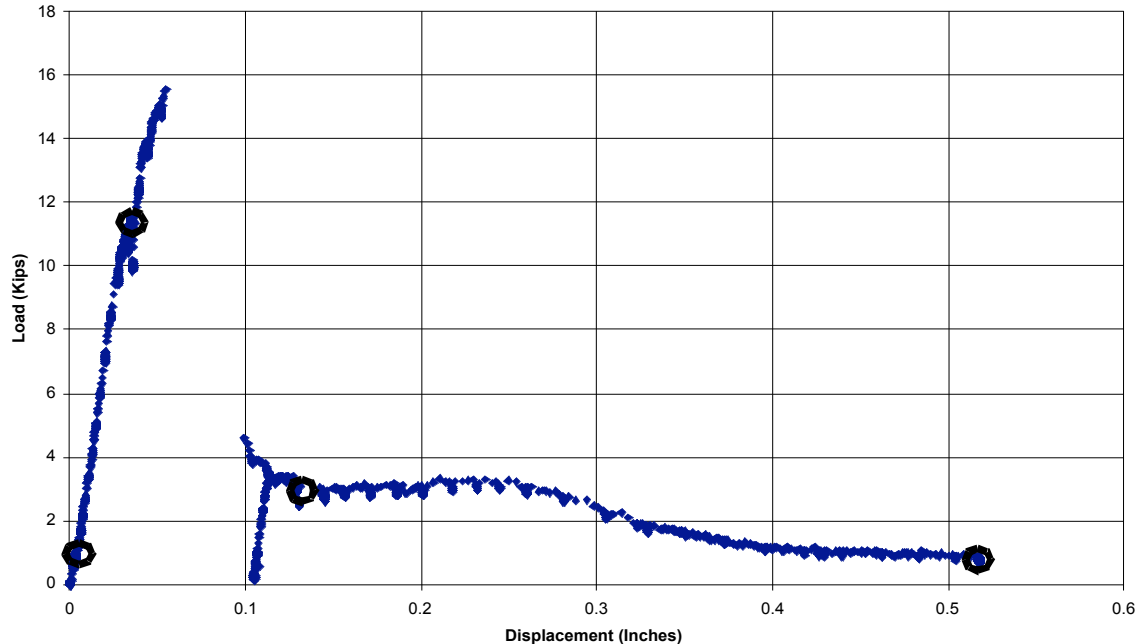


Figure 1.6 – Load Displacement Curve for Specimen P1

These test specimens, with varying bonded length and confinement, allow observation of changes with varying parameters. The use of X ray CT provides an in-depth view of local failure mechanisms.

1.3 Thesis Organization

The format of this thesis is as follows. Chapter 1 describes previous use of X-ray CT for civil engineering applications, introduces image processing and provides details about the specimens imaged for this project. Chapter 2 provides an overview of X-ray CT as an imaging technique, and specifics on the imaging process. This chapter will also discuss acquisition of X-ray CT data, and the variables that effect the quality of images received. Chapter 3 outlines several different tools used for extracting information from X-ray CT images in three broad categories: visual inspection, single image processing, and multiple image processing. Chapter 4 explains how using the tools outlined in the previous chapter were used to extract meaningful bond information from the specimens tested. Chapter 5 present conclusions about X-ray tomography, the effectiveness of the tools used for extracting information, and extracted bond information.

CHAPTER 2 : X-RAY COMPUTED TOMOGRAPHY

2.0 Introduction

This chapter provides an overview of X-ray computed tomography (X-ray CT). Specifics of the imaging process, including the acquisition of X-ray data and the variables that affect the quality of XY images are presented. This chapter concludes with a discussion of image reconstruction, including the presentation of a sample 3D reconstruction of a concrete specimen and an evaluation of the effectiveness of X-ray CT imaging of reinforced concrete.

2.1 X Ray Computed Tomography

Tomography derives from the Greek word “tomo” which means, “cut” or “section”. As a technique, tomography is a method of digitally cutting open a physical object to reveal its interior details, and can be used to reconstruct full three-dimensional images by collecting two-dimensional slices. X-rays are aimed at a specific location on the specimen and those that penetrate through the specimen are collected using a high-resolution detector panel. The amount of X-ray energy penetrating the specimen is converted to scalar, grey-scale values (roughly proportional to the material density) that are assigned to each spatial location within the specimen. Two-dimensional images are taken at many levels up the height of the specimen, and assembled to create a 3D image. Many different source and detector configurations exist, and the specific imaging process varies with each.

2.2 The Imaging Process

Collecting images with X-ray CT requires three main components: an X-ray source and configuration, a specimen to be imaged, and a detector. (Figure 2.1) With most facilities, 3D images are generated by assembling a series of 2D image reconstructions.

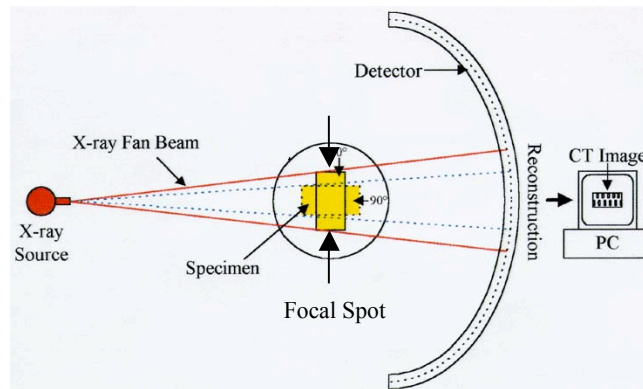


Figure 2.1 - X ray CT Set Up

2.2.1 The Source and Configuration

The important variables that determine the effectiveness of an X-ray source for a particular specimen are the size of the focal spot, the spectrum of X-ray energies created, and the maximum X-ray intensity. The focal-spot size, or width of the X-ray beam as it passes the imaged specimen, partially defines the spatial resolution of an image by determining the number of possible source-detector paths that can be collected from a given point in the imaged specimen. The more such source-detector paths there are, the more blurring of features there will be, making edges and cracks more difficult to define. As no source emits only single energy photons, the energy spectrum (Figure 2.2) defines the penetrative ability of the X-rays, as well as their expected relative attenuation as they pass through materials of different density. Higher-energy X-rays (e.g. 420 keV) penetrate more effectively than lower-energy ones (e.g. 60 keV), but are less sensitive to changes in material density (e.g. cement to aggregate) and composition. The X-ray intensity, or number of photons emitted at each energy level, directly affects the signal-to-noise ratio and thus image clarity. The higher numbers of photons improve the spatial accuracy of the final image.

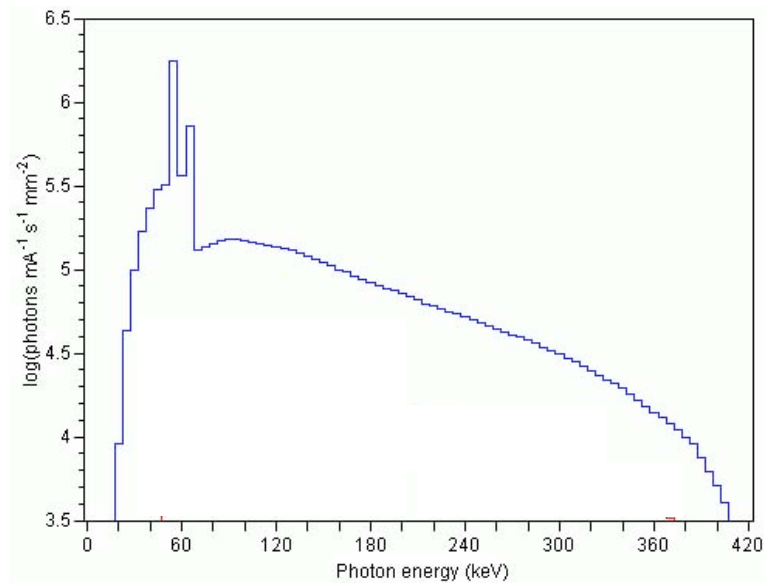


Figure 2.2 – Energy Spectrum and Intensities for 420 keV source (Ketcham, 2001)

There are many possible configurations of X-ray sources, but the most common are single-plane “pencil beam” sources, single-plane “fan beam” sources, and multiple plane “cone beam” sources. Pencil beam sources are commonly called “1st generation” sources. These sources emit X-rays essentially along a line in a single plane, and thus capture only a small amount of material per orientation. Fan beam sources emit X-rays over a fan-shaped area in a plane and thus are able to collect entire 2D planes at each orientation (Figure 2.3). Cone beam sources can capture 3D volumes at each orientation. For 3D imaging, fan beams are most commonly used (with a 2D to 3D reconstruction) for both efficiency and image quality, and were the only beams used for this project. Cone beam sources can be used for quick acquisition of 3D data, but usually suffer from poor image quality. This is due to the added complexity in recreating a 3D image without initial 2D slices.

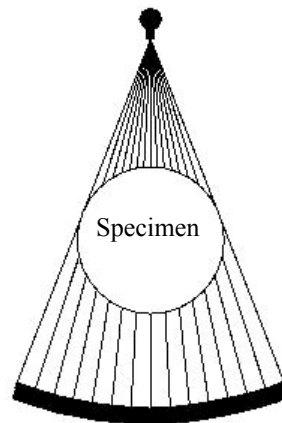


Figure 2.3 - Fan Beam Configuration

2.2.2 The Specimen to be Imaged

The only requirement for the specimen is that it fit within the field of view of the source. X-ray CT requires rotation of either the specimen or the source-detector in order to collect data. As such, the most efficient shape such that all material is exposed to the same number of X-rays is a stack of circles or a cylinder. X-rays are emitted from the source for a finite amount of time (called integration time) at each rotational alignment. For modern sources, integration times range from 32-64ms. Then the rotational alignment is changed incrementally by rotating either the specimen or source and detector, and x-rays are emitted again. This is known as one “view”, and is repeated for the total number of views until a complete 360-degree view has been imaged. The typical number of views ranges from 1000-2000.

2.2.3 Detector

Detectors for CT scanners are positioned on the opposite side of the imaged specimen from the source, and detect the amount of X-rays that penetrate the specimen. These detectors make use of scintillating materials that convert X-ray energies to electrical signals. Each detector is made up of many small scintillators, made of

cadmium tungstate or cesium iodide, and influence image quality through their size and efficiency in detecting the energy spectrum generated by the source. The size of an individual detector determines the proportion of the imaged specimen that is contained in a single intensity reading, while the number of detectors determines how much data can be gathered simultaneously, and thus the dimensions of the image.

2.3 Project Facility Details

The high-resolution X-ray CT facility at the University of Texas, Austin (Figure 2.4) was the primary facility used for this study. Specification for this facility and the test specimens include:

Source: 420-kV tungsten, fan beam

Specimen: Concrete-density $\approx 150 \text{ lb/ft}^3$

Steel-density $\approx 490 \text{ lb/ft}^3$

Composite-density $\approx 155 \text{ lb/ft}^3$

Detector 1: 512-channel linear array (high sensitivity, slices 5mm-0.25mm)

Vertical Motion Limit: 750mm (= 29.5in), can scan up to 1500mm (= 59in)

Information available at <http://www.ctlab.geo.utexas.edu>.



Figure 2.4 – X ray CT Facility at University of Texas, Austin

2.4 Variables Effecting X ray CT Images

A number of variables may affect image quality during the X-ray CT process. Imaging variables determine the quality and the overall effectiveness of the imaging before reconstruction begins. These variables can be adjusted to reduce imaging artifacts and improve image quality. The following sections discuss the most critical variables: calibration, slice thickness, number of views, integration time, and filtering.

2.4.1 Calibration

Before the scanning takes place, a calibration is always necessary to prepare the detector for the range of intensities coming from the source. This is typically done by scanning a “wedge” – a piece of material with the same diameter and roughly the same average attenuation as the specimen to be imaged. This allows the detector to reduce both the range of intensities it collects, and the number of physical scintillators activated, defining the 2D space of the image. Calibration improves image contrast when a wedge of material is not available, an “air wedge” is used. Figures 2.5 and 2.6 show that an image collected with a cement wedge is less blurry than an image collected with an air wedge.

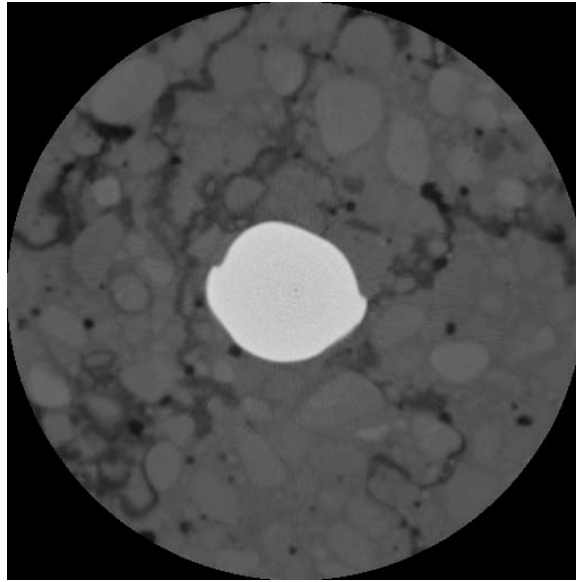


Figure 2.5 - Cement Wedge Calibration

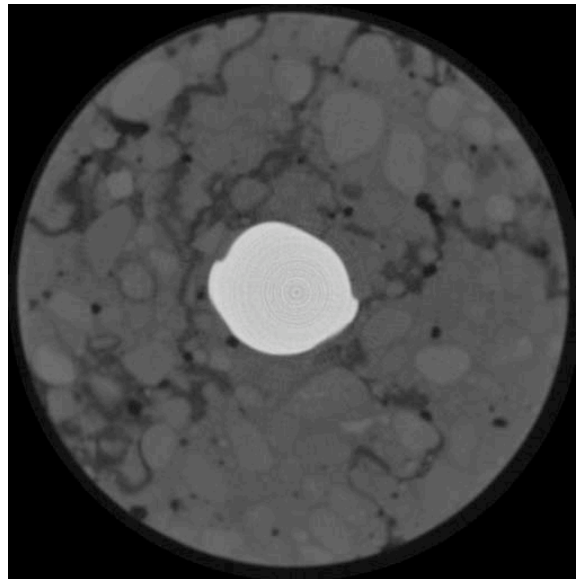


Figure 2.6 - Air Wedge Calibration

2.4.2 Slice Thickness

The UT Austin facility has a vertical rotational axis and the ability to collect 2D images. The thickness of the slice of material used to generate each individual 2D image

can be varied to improve the resolution of 3D images. Changing the size of the vertical aperture of the detector changes the thickness of the slice. Thinner slices lead to higher resolution in the 3D reconstruction, and detectors at the UT facility can accommodate a minimum slice thickness of 0.5mm. Figure 2.7 shows a vertical slice through a specimen imaged with 1mm slices, while Figure 2.8 shows a different specimen imaged using 0.5mm slices. Bar lugs and aggregate boundaries are most distinct in Figure 2.8 than Figure 2.7.

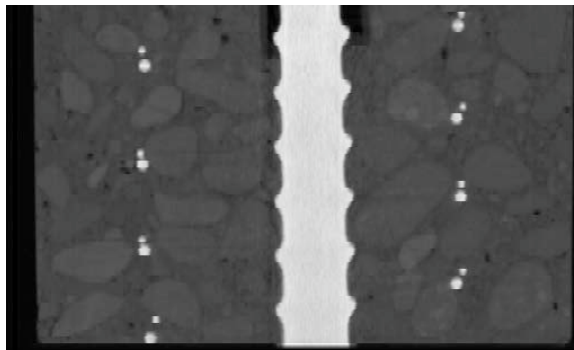


Figure 2.7 - 1mm Slice Spacing

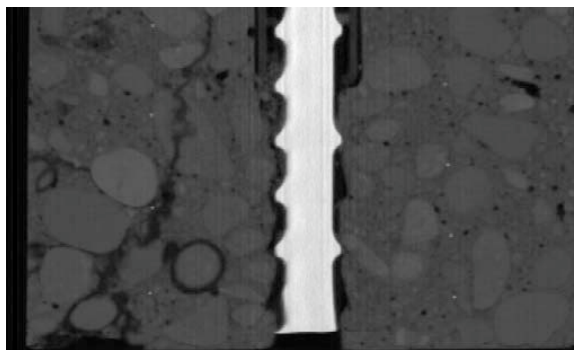


Figure 2.8 - 0.5mm Slice Spacing

2.4.3 *Number of Views*

Data from multiple views of the specimen are required to generate a 2D reconstruction. As the specimen rotates the source must, at discrete intervals, emit X-rays that then pass through the specimen and are collected by the detector. The X-rays collected at each interval, or “views”, are collected and numerically processed to reconstruct the 2D slice. If more views are used to generate the 2D reconstruction, a better image will be produced. A typical number of views is 1000 to 2000. Low numbers of views can result in streaking and poor spatial resolution, e.g. blurry boundaries. Figure 2.9 and Figure 2.10 show the same specimen imaged with 1000 and 2000 views. Figure 2.9 shows more radial “streaks” and aggregate boundaries are blurry.

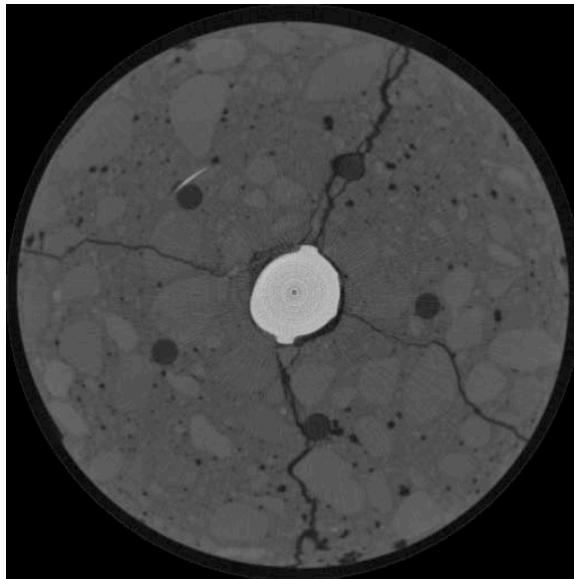


Figure 2.9 - 1000 views

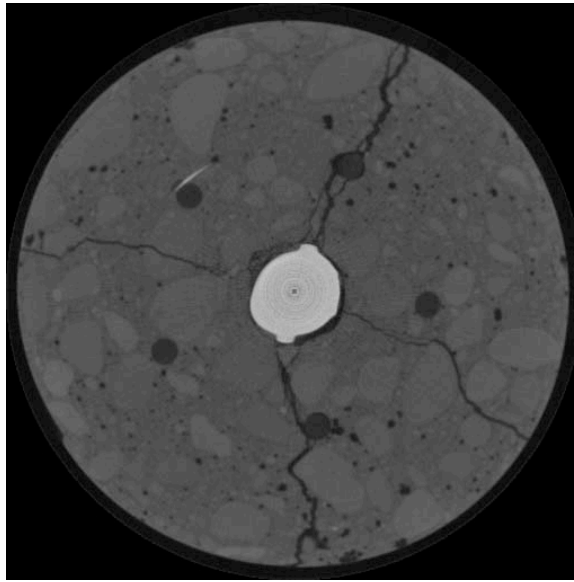


Figure 2.10 - 2000 views

2.4.4 Integration Time

At each view, the source emits X-rays for a discrete period of time; this time is referred to as the integration time. This variable defines the length of time for which the system is allowed to collect information during each view. The longer the integration time, the more information collected at each view. Additional collection time increases the accuracy of the collected X-ray intensities and creates a better image quality. An image collected with 32ms integration time (Figure 2.11) has much more streaking than an image collected with 64ms (Figure 2.12).

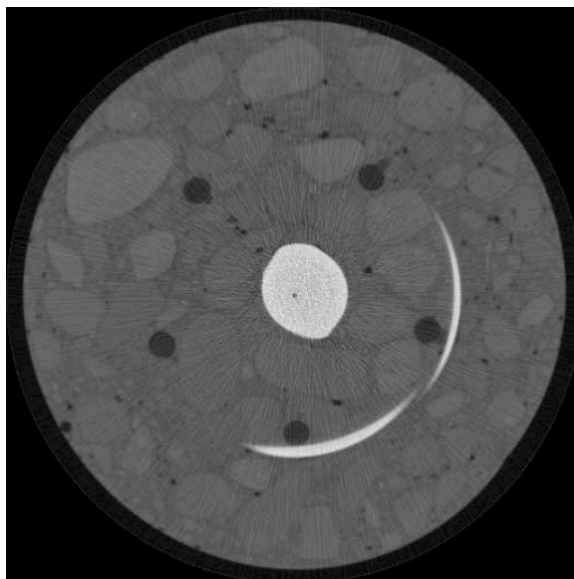


Figure 2.11 - 32ms Integration Time

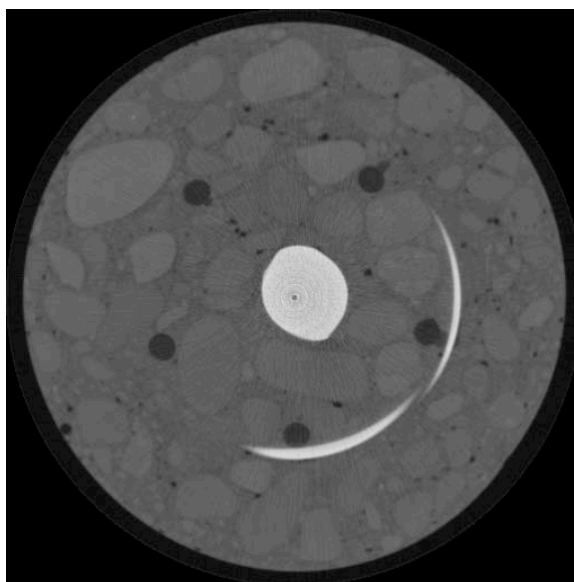


Figure 2.12 - 64ms Integration Time

2.4.5 Filtering

The X-ray source is idealized as a single-intensity energy source, and the detector is configured to detect X-rays of that intensity. However, the source actually produces a spectrum of energies, so adjustments must be made to account for this. This discrepancy manifests itself as “beam hardening”, where the center of the image appears darker than the edges. This can cause problems for many image-processing techniques. One solution to this problem is to use a physical brass filter to remove the lower energies before they pass through the specimen. Another solution is to use a numerical filter, after the images are collected, to counteract the phenomenon. Figure 2.13 and 2.14 show, respectively, images with and without filtering.

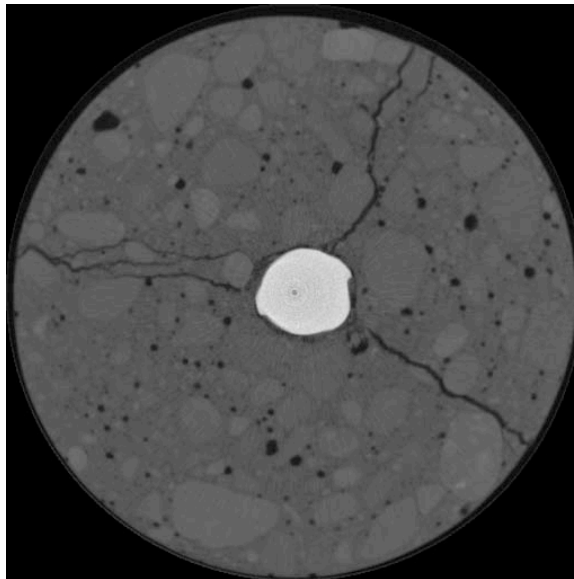


Figure 2.13 - No Filtering

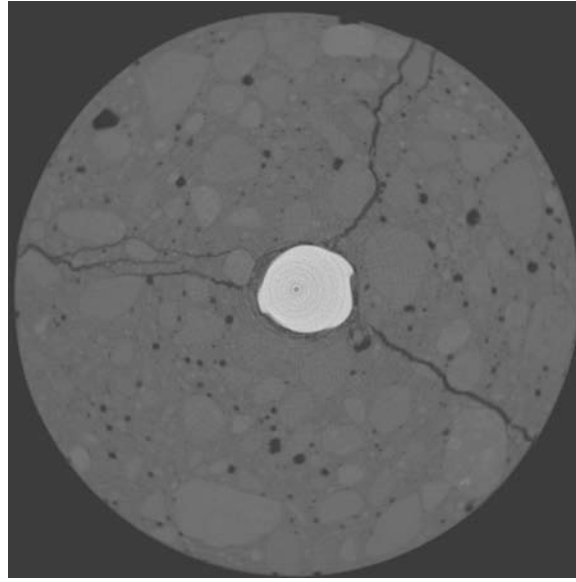


Figure 2.14 - Numerical Beam Hardening Filter

2.5 2D Image Reconstruction

As the X-rays pass through the specimen being imaged, the signal is attenuated by both scattering and absorption. Attenuation of a single energy beam through a homogeneous material (including both absorption and scatter) is given by Beer's Law in Equation 2.1.

$$I = I_o \exp[-\mu x] \quad ($$

where I_o is the initial X-ray intensity, μ is the linear attenuation coefficient for the material being scanned (units: 1/length), and x is the length of the X-ray path through the material. If the scan object is composed of a number of different materials, as is concrete, the equation becomes:

$$I = I_o \exp \left[\sum_i (-\mu_i x_i) \right] \quad (2.2)$$

where each increment i reflects a single material with attenuation coefficient μ_i over a path length x_i . Each pixel represents the integral of all the μ_i and x_i values along that

path. The reconstruction problem is to determine, using data from all of the different views, the individual μ_i and x_i values at each location in the image.

To accomplish the reconstruction, detector data are passed to photocathode, projected onto a screen, and converted to digital image data. In this reconstruction, each view is successively superimposed over a square grid, at an angle corresponding to its acquisition angle. Each location on the grid is then assigned a 8- or 16-bit value from an optimization problem based on the projected information from each scan. This is a numerically expensive process, with more views drastically increasing the complexity of the problem. Reconstruction of typical 2D images (1000 views, 64ms integration time) takes approximately 1 minute.

2.6 3D Image Assembly

2D reconstructed images can be “stacked” to form a 3D image. The resolution in the Z (vertical) direction is defined by the slice thickness. Then slices along any plane may be visualized by cutting through the 3D object. Figure 2.15 shows a 3D rendering of a stacked 3D volume and 3 “slices” of varying orientation: (XY plane (original 2D image), XZ plane, and YZ plane).

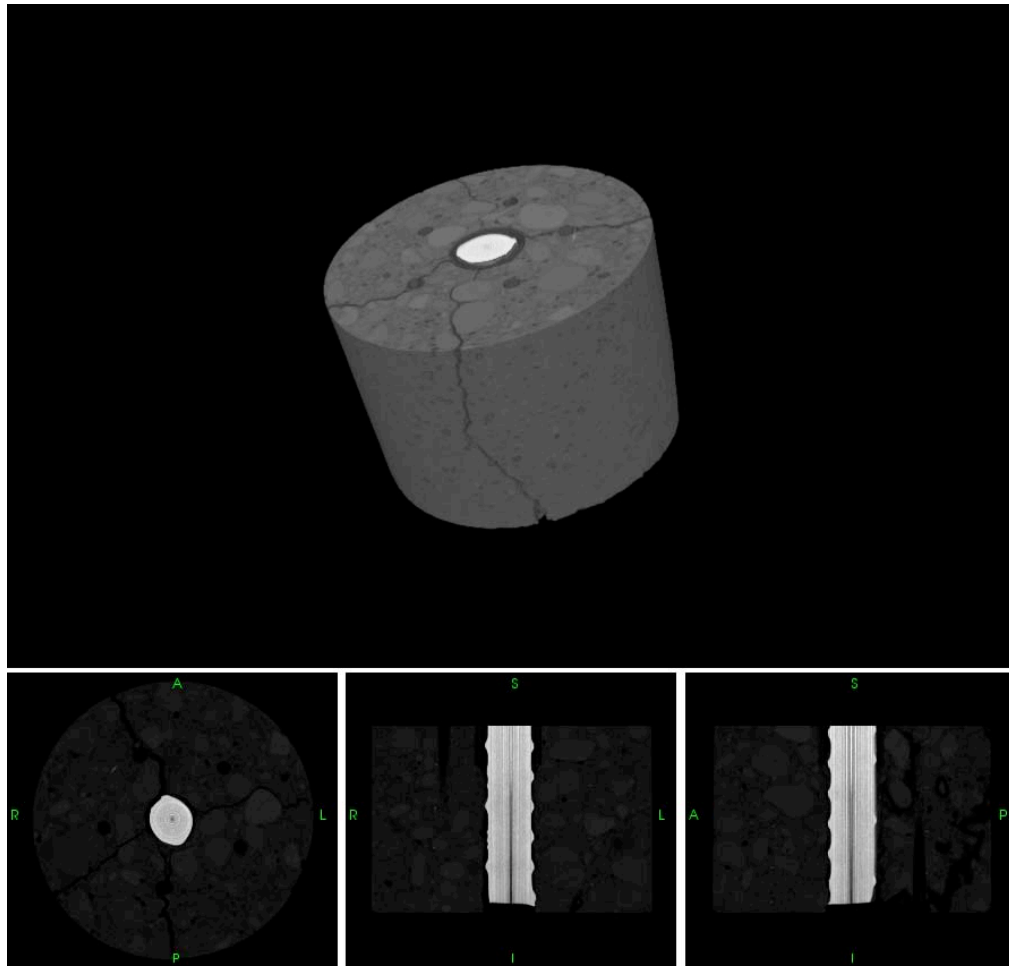


Figure 2.15 - 3D Reconstruction of Data Set

2.7 Effectiveness of Imaging

This section will discuss the effectiveness of X ray CT on imaging reinforced concrete. X ray CT is proving effective for high density, engineering materials that require higher energy X ray sources. A previous state-of-the-art review by Pla-Rucki et al. (1995) and research by Landis et al. (2003) and Martz et al. (1992) indicate concrete imaging by X-ray CT would be quite effective. Imaging artifacts, like streaking, beam hardening, and poor contrast, can hinder the imaging capabilities, but can also be adjusted and managed. Preliminary studies, based on visual inspection, confirm this imaging

effectiveness, but the true assessment lies in the ability to run image processing routines to extract information.

The high density reinforced concrete (155 lb/ft^3) requires a high-energy source (420 keV – 1 MeV). An imaging attempt of a 10-inch cylinder, with a 450 keV source did not provide sufficient photon collection for image reconstruction. Given the artifacts observed during this project, it is concluded that the maximum effective penetration of a 420-kV source is approximately 6 inches of reinforced concrete. Any thicker, and the detector would have difficulty in collecting photons, and thus reconstructing images. For this project, visually acceptable images were received and with the help of image processing, important bond information can be extracted. As with any imaging device, the longer the integration time and the better the resolution (smaller pixel size), the better the information to be retrieved.

2.8 Conclusions

Given the previous research, and the preliminary images received for this project, X-ray CT appears to be effective in the imaging of reinforced concrete. Quality images are received, and adequate for image processing. The main drawbacks of this process are the size requirement (both sample and loading rig must fit inside the lead containment chamber) and the time required to collect large images (approximately 2 hours for 4 inches of cylinder). These drawbacks are currently manageable and, as technology advances, will become less of a hindrance. The true evaluation of X ray CT depends on the information extracted from the images, which will be discussed in the next chapter.

CHAPTER 3 : TOOLS FOR EXTRACTING INFORMATION FROM IMAGES

3.0 Introduction

This chapter outlines three broad categories of tools used in this project for extracting information from X-ray CT images: visual inspection, single-image processing, and multiple-image processing. Visual inspection includes phenomena visible by the human eye, while single image processing refers to simple computer routines run on a single image. The multiple image processing section discusses a process called image registration, which is used to extract displacement fields from two sequential images of the same specimen. Three image registration routines are outlined: motion estimation, elastic image registration and elastic registration with XFEM extension.

3.1 Visual Inspection

This section will discuss how visual inspection of the images can be an effective method of information extraction. Simple visual inspection of each slice and the full 3D image provides insight into bond zone behavior and mechanisms of bond response. Specifically, visual inspection provides information like crack orientation, effect of grain boundaries on crack path, extent of crushing around bar-concrete interface, influence of individual lugs, etc. This inspection is qualitative and not quantitative, in nature. Also, visual inspection has the advantage that noise and imaging artifacts which may inhibit automated image processing routines are easily ignored by the human eye. Visual inspection is typically necessary before application of more sophisticated evaluation methods.

3.1.1 Examples

In Figure 3.1, visual inspection reveals bond failure by four dominant cracks and significant de-bonding around the surface of the bar. It is also interesting to note that the

cracks primarily follow grain boundaries and that the two widest cracks connect the bar to the wooden dowels used to support spiral reinforcement.

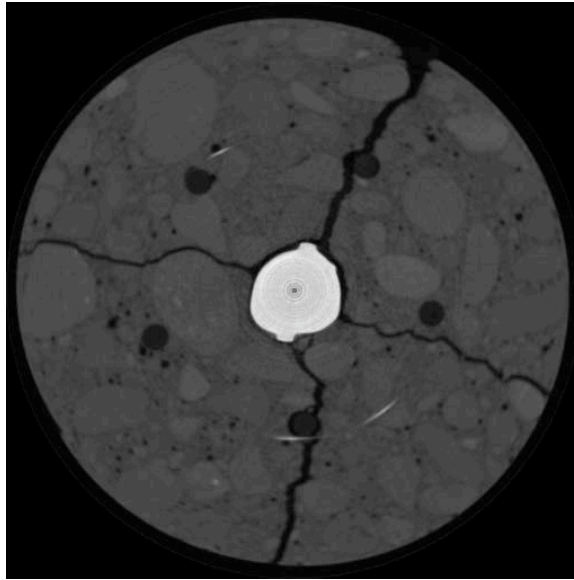


Figure 3.1 – P3W2-3, Visual Inspection

In Figure 3.2, visual inspection returns only three dominant cracks, but again significant de-bonding around the surface of the bar. This image also shows a split piece of aggregate, but in general cracks follow aggregate boundaries.

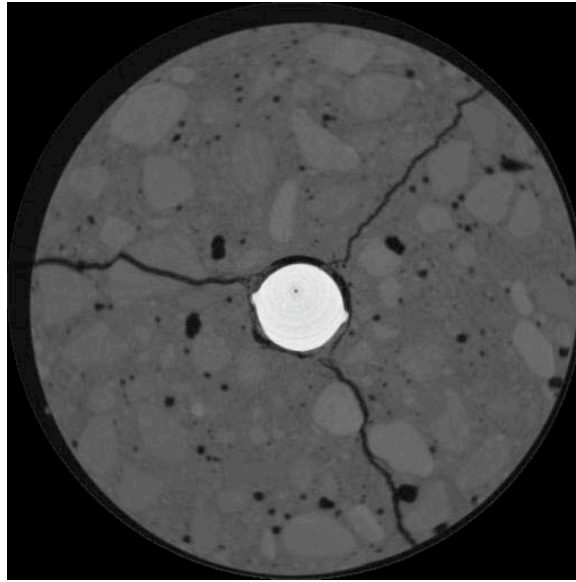


Figure 3.2 – P3F-3, Visual Inspection

3.2 Single Image Processing

This section will discuss single image processing for information extraction and then presents threshold segmentation in detail. The 3D digital image is a discrete representation of the specimen with each voxel of discrete size, having an 8 or 16-bit value that represents the density of the material in that location (a voxel is the 3D equivalent of a pixel). Each image can also be considered a discrete function with numerical properties that can be used to extract information as shown in Figure 3.3. Integrals, gradients and Hessians are all tools that can be used to evaluate the function and extract information about the specimen. Conversely, any function that is compactly supported (i.e. defined everywhere in the range), and has a finite integral over its domain can be considered an image. Single image processing utilizes these characteristics to extract information.

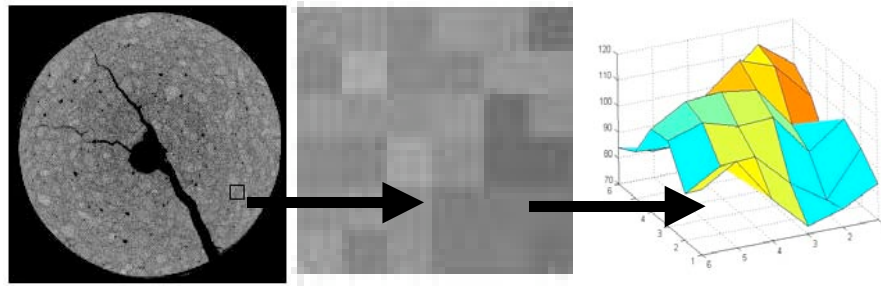


Figure 3.3 - Images as Discrete Functions

3.2.1 Previous Research

With images represented as 3D arrays, modern computers can be quite efficient in performing basic image processing routines, and many routines can provide useful data. Geometric transformations can be used to enlarge certain image areas, say, directly around the bar. Filters can be used to remove aggregate pieces of a chosen density. Edge detection routines can sharpen crack boundaries, and attempt to fit linear curves. Noise reduction can be used to diminish the effect of imaging artifacts, or to smooth boundaries. By utilizing fast, linear algebra routines, all of these routines can be run without being too computationally expensive. This project focused on one single-image processing routine: threshold segmentation.

3.2.2 Threshold Segmentation for Feature Identification

Because detection of cracks was the main focus of the project, the first step was to separate solid from void in the image – a process called segmentation. This can be done a variety of ways – with the simplest routine being threshold segmentation. This process separates each voxel based on its scalar value (approximate density). A threshold value is chosen, and all voxels above that value are assigned as solid, and all below as void.

This process is heavily dependent on the threshold value, but it enables the user to systematically extract information about the cracks and void space in each image, and

how they change at each load step (Landis 2003). This is due to the imprecise separation of solid and void in the scalar range of image values. Figure 3.5 shows a histogram of a sample image (Figure 3.4), where the range of 16-bit values defining void range from 0 to approximately 18000.

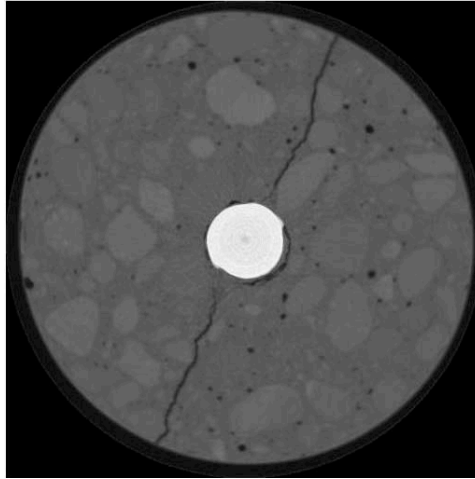


Figure 3.4 – Sample Image from Specimen P1-3

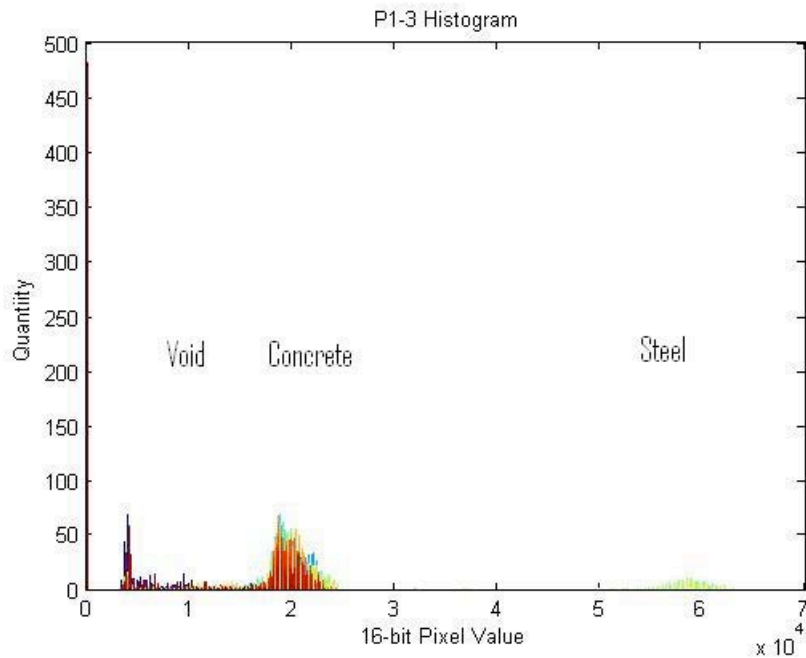


Figure 3.5 – Histogram of Sample Image

For this project a rational method for determining the threshold value was derived based on maximizing structural changes and is discussed in section 3.2.4.

3.2.3 Feature Characterization

Having identified the voids, a program called Blob3D was then used to inspect them. Written by researchers at the University of Texas, Blob3D (<ftp://ctlab.geo.utexas.edu/Blob3D>) first determines the connectivity of the voids or “blobs,” then generates isosurfaces, and calculates surface area and volume of each blob. Figure 3.6 shows a typical output from Blob3D, with four cracks emanating from the steel bar. Three of the four pass through one of the wood dowels that were used to support the spiral steel. The crack can be seen to pass around the dowel in each case. With additional post-processing, void ratio and approximate crack widths were extracted.

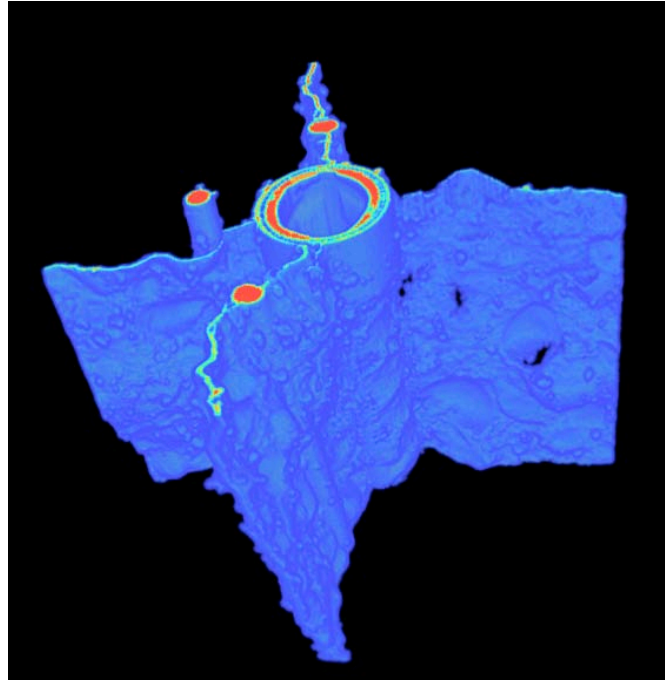


Figure 3.6 - Crack Surface with Discontinuities

3.2.4 Threshold Value Determination

The selection of the threshold value is vital to any segmentation routine. For this project, the threshold value was selected to maximize the change in void (i.e. crack) volume detected in the sequence of images. To accomplish this, the histograms of several images (Figure 3.7) were examined to identify the range of threshold values separating solid concrete from void. In images where wooden dowels were present, wood density fell within this range between solid and void. An image of concrete specimen in Figure 3.8 becomes the binary crack image in Figure 3.9.

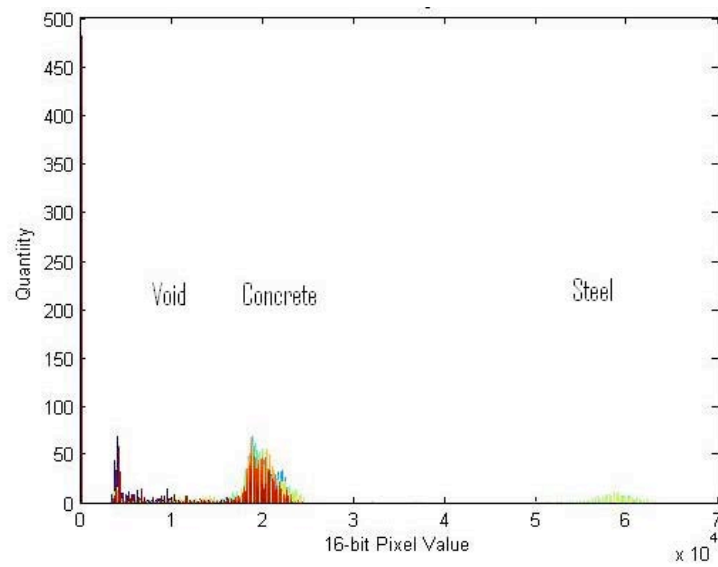


Figure 3.7 – Histogram of Image P1-3

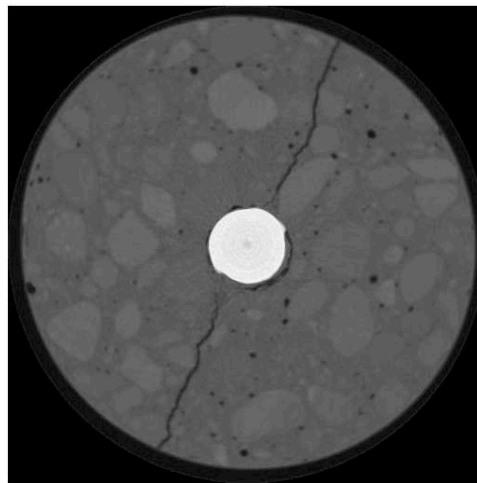


Figure 3.8 - P1-3, Slice 20

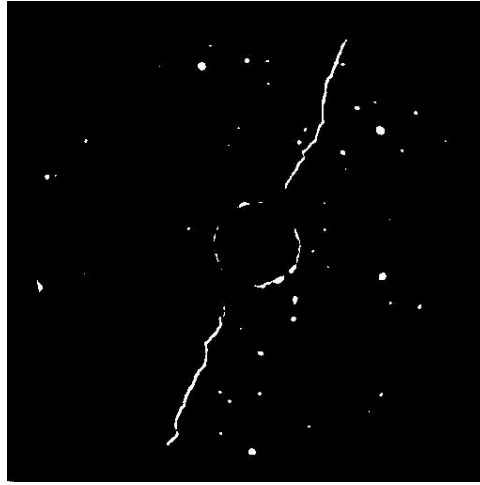


Figure 3.9 - Threshold, $t = 13000$, P1-3, Slice 20

Then, the initial un-cracked and the final cracked image in each sequence were processed (e.g. P1-1 and P1-4) using multiple threshold values within this range. For each segmented image Blob3D was used to extract the surface area of the void space, and calculating the percent increase. As the threshold value varied, a definite peak in void volume increase was found between two images of the specimen. This threshold value corresponding to the peak, enabled detection of the most structural changes (Figure 3.10).

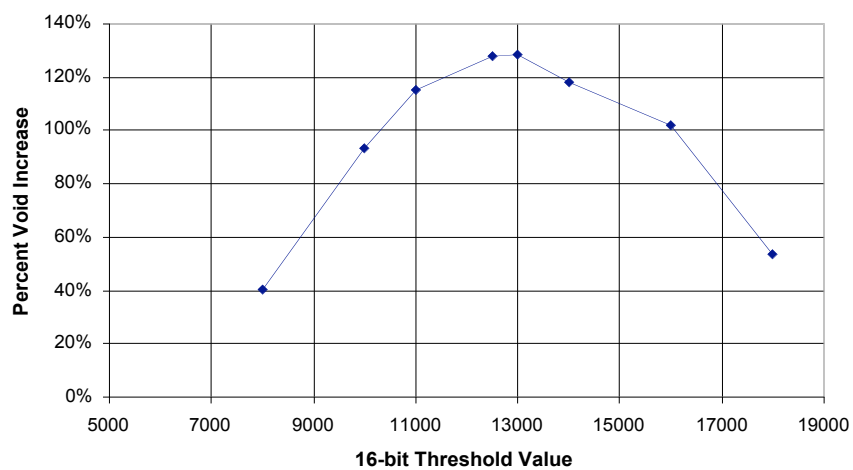


Figure 3.10 – P1-1 -> P1-4 Void Changes due to Threshold Value

There are many ways to segment solid from void in an image, and that method can drastically affect what is returned. Selection of the threshold value to maximize detection of cracks and voids is a non-subjective method of doing so, and produces logical, usable results.

3.3 Multiple-Image Processing - Image Registration

This section discusses how using multiple images in sequence can provide new bond information, specifically through image registration. This section will provide an overview of image registration, and provide detailed discussion of the three image registration routines used in this project. For this study, multiple images of each specimen were generated at multiple points on the load-displacement history to capture the progressive bond failure. Using multiple images together additional information about the structural changes and the mechanics of bond can be extracted. As a load increment is applied, cracks are formed and displacement is observed. Sequential images represent the state of the specimen before and after application of the load increment. Image registration methods compute the displacement field from two images.

The need for image registration is present in many different fields, including medicine ([Maintz & Viergever, 1998](#)), computer vision ([Zhang, 1994](#)) and astrophysics ([Alard, 2000](#)). Images acquired from different sources or perspectives must be aligned in order to correctly compare attributes or changes, including both rigid body motions (rotation, translation) and displacement of a deformable body. Image registration can be as simple as overlaying two images and using the human eye for visual alignment, or as complex as applying a diffusion-based model to capture image flow. Image registration is the process of matching two images.

3.3.1 *Image Registration Overview*

The task of image registration is to find an optimal geometric transformation (i.e. displacement field) between two images that minimizes a given functional criterion; essentially, change one image (the template image) to match another image (the reference image). Mathematically, image registration is an optimization problem. Previous research has resulted in a number of different image registration methods. As with any optimization method, these image registration methods are defined 1) by the functional form of the criterion used to define the optimum, 2) the form of the transformation field, and 3) the numerical method used to solve the problem. These components of the problem and previous research to develop image registration methods are presented in the following sections. The following standard nomenclature is used in this discussion.

R = Reference Image

T = Template Image

T_u = Deformed Template (Template deformed by Transformation)

u = Transformation (i.e. displacement field)

3.3.1.1 Criterion

In completing the image registration process, the template image, T is transformed, via the transformation, u , to create deformed template image, T_u , and compared with the reference image, R . A mathematical function quantifying the effectiveness of the registration is defined to both drive the image registration process and monitor its effectiveness. This function must compare the intensity of a specific location of the reference image to the intensity at the same location in the deformed template. Thus, the image registration problem may be defined as:

$$\begin{aligned} &\text{Find } u \text{ such that} \\ &D[R, T; u] = \min \end{aligned} \tag{3.1}$$

where $D[\]$ is a function that determines the difference between the two images. The most common criterion used for this application is the Sum of Squared Differences. For other, multi-modal (many imaging sources) applications, Mutual Information ([Viola, 1995](#)) or Gradient Intensity ([Modersitzki, 2004 \[1\]](#)) criterion can be used.

Sum of Squared Differences Criterion

The mean square error is the sum of the squared difference between the intensity of the reference image and the deformed template at the same position. (Equation 3.2)

$$D^{SSD}[R, T; u] = \frac{1}{2} \|T_u - R\|^2 \quad (3.2)$$

This criterion implies that the images must have similar histograms, and is only appropriate for images acquired by the same imaging device. The benefits of this criterion are that it is very fast to compute, and directly applicable to images acquired through X-ray CT.

However, research suggests ([Modersitzki, 2004](#)) that this problem is often ill posed. As a result, a regularizing term $S[u]$ is added such that the image registration problem is defined

$$\begin{aligned} &\text{Find } u \text{ such that} \\ &J[u] = D[R, T; u] + S[u] = \min \end{aligned} \quad (3.3)$$

These regularizing terms act like penalty functions. If the transformation, u , fits the pattern pre-defined by $S[u]$ poorly, the value of $S[u]$ becomes large and the optimization routine then seeks a better transformation.

Regularizing Terms

It is these regularizing terms that define the type of image registration, effectively forcing the deformations to follow a specific model. Fluid registration ([Freeborough 1998](#)) restricts the velocity ($\underline{v} = du/dt$) or change in displacement field in time, analogous to fluid flow as shown in Equation 3.4:

$$S[u] = \mu \Delta v + (\lambda + \mu) \nabla \text{div} v \quad (3.4)$$

where λ and μ are Navier-Lame material constants.

Motion segmentation (Zhang, 2004) uses optical flow constraints to restrict the movement of each pixel possible solutions (Equation 3.5).

$$S[u] = \frac{\partial T_u(x, y)}{\partial x} * \frac{\partial u_x}{\partial t} + \frac{\partial T_u(x, y)}{\partial y} * \frac{\partial u_y}{\partial t} \quad (3.5)$$

Elastic registration, (Broit, 1981) the method used in this project, restricts the deformations to those of an elastic field, using the potential linear strain energy of the system as a regularizing term (Equation 3.6). This is the same restriction at the heart of many finite element models.

$$S[u] = \iint_V D \cdot \varepsilon \, d\varepsilon \, dV \quad (3.6)$$

The influence of this regularizing term can be modified before or during the image registration by increasing or decreasing the value of E and ν (Young's modulus and Poisson's Ratio) within the constitutive matrix D .

3.3.1.2 Transformation

Image registration techniques are often classified by the transformations they support because the transformation determines the size and complexity of the optimization problem. Therefore each registration method will provide a transformation subject to certain constraints.

3.3.1.2.1 Parametric Transformations

A common way of simplifying the registration process is to constrain the transformation such that it can be defined by a few parameters. The registration process is then simplified as a search for these optimal parameters. Rigid body registration supports only translation and rotation. Landmark registration (Bookstein, 1989) relies on the identification of landmark points, and then a transformation based on the fitting of

splines to these points. Principal axis-based registration (Maurer & Fitzpatrick, 1993) treats each image as a density or mass function, derives the principal axes, and through registration, aligns the axes of the two images. Other parametric techniques exist, such as optimal linear registration (Modersitzki, 2004 [2]), but all rely on an over-simplification of the material behavior of concrete and were found not to be useful.

3.3.1.2.2 *Non-Parametric Transformations*

Most accurate registration schemes solve for independent transformations at each point in the image frame. These displacements are calculated over a continuous field, and then re-sampled at pixel locations. A continuous transformation, or in this case, a displacement field, is needed to derive useful information.

3.3.1.3 *Solver*

To solve this system of equations, a basic Newton's solver was used because of its ease of implementation. It would also be possible to utilize an iterative or Fourier transform solver.

3.3.2 *Image Registration – Motion Estimation*

This routine was written by Zhang, (2004) Displacement at each location (non-parametric transformation) is estimated by a cross correlation criterion (Equation 3.7).

$$D^{cc}[R, T, u] = \sum_x \frac{\text{cov}(R(x), Tu(x))}{\sigma_x \sigma_y} \quad (3.7)$$

Where σ_x and σ_y denote standard deviations, and cov denotes to the covariance of image $R(x)$ to $T_u(x)$. Features and voxel intensities in the template image are matched to the template image, restrained by regularizing terms of optical flow. The system is solved using both direct (Newton's) and indirect (iterative) algorithms.

This routine was written to optimize performance on concrete mortar specimens, and therefore has some difficulty with the presence of the steel bar. This routine also

operates on the pixel level, meaning the smallest displacement measurable is one voxel which can be a disadvantage with large voxel size. However, this routine is optimized to process large data sets, so full 3D displacement fields were obtained.

3.3.3 Image Registration – Elastic Registration

The routine begins by defining a sum of squared differences criterion, and using a regularizing term minimizing linear potential energy (Equation 3.8).

$$D^{SSD}[R, T; u] = \frac{1}{2} \|T_u - R\|_{L_2(\Omega)} \quad (3.8)$$

$$S[u] = \iint_V D \cdot \varepsilon \, d\varepsilon \, dV .$$

Then with a non-parametric transformation and a Newton's solver (Moderzitski, 2004), implementation of elastic registration begins to directly follow the finite element method. An image is already “meshed” with the pixilation, with each voxel acting as a node, and material properties (E, ν) assigned to “elements” in between.

Next, a displacement field is defined and “stiffness matrix” based on the second-derivates of the energy equation is initialized. For an image of size $m \times n$, the standard finite element displacement field is defined

$$u(x) = \sum_{i=1}^N \varphi_i(x) u_i , \quad (3.9)$$

where N is the number of nodes, equal to $(m * n)$, φ_i is the nodal shape function, and u_i is the displacement of each node or voxel. The stiffness matrix for each element is calculated, and assembled

$$k_{ij} = \int_{\Omega} (B_i)^T D B_j \, d\Omega , \quad (3.10)$$

$$B_i = \begin{bmatrix} \varphi_{i,x} & 0 \\ 0 & \varphi_{i,y} \\ \varphi_{i,y} & \varphi_{i,x} \end{bmatrix}$$

Boundary conditions must also be specified to solve the problem. The most commonly used boundary condition for image registration is a fixed (zero-displacement in all directions) boundary around the perimeter of the image. This keeps the image within the initial domain, but requires that sufficient black space be provided to reduce the effect on the registration. Boundary conditions have a great effect on the capability of image registration to converge, and should be considered in future research.

Then, in order to solve for displacements, forces must be applied that are related to the difference between the two images and would lead to convergence. To optimize the similarity criteria, its derivative must be used.

$$\begin{aligned} f(x, u(x)) &= d[D^{SSD}] = d\left[\frac{1}{2}\|T_u - R\|_{L^2(\Omega)}\right] \\ f(x, u(x)) &= (R(x) - T_u(x))\nabla T_u(x) \end{aligned} \quad (3.11)$$

This force calculation requires a gradient of the deformed template at each pixel location. With an image of finite pixels, a strategy must be employed to both provide accurate results and not be too computationally expensive. Many different techniques were tried from a simple central difference calculation with one pixel on either side of the location, to curve fitting three pixels on either side. In the end, a linear fit was used over five pixels, two on either side of the selected location. This provided decent accuracy while maintaining computational efficiency.

These forces are applied to the mesh, the system is solved, and the displacements then reduce the similarity criteria. The method used for solving this

problem has been a basic Newton's solver that solves a set of linear equations at every iteration.

$$U = K \setminus F \quad (3.12)$$

This was used mainly because of its similarity to a finite element problem.

Implemented in MATLAB:

Pseudo Code:

Define reference and template images	R, T
Select E, ν (regularizing terms)	E, ν
Assemble stiffness matrix	K
Apply boundary conditions to generate	Kff
Initialize displacement field	U
Apply displacement field to template	$T_u = T(u(x))=T$
Loop	
Initialize force vector	$f=0$
Calculate & Assemble force vector	$f(x,u(x))$
Apply boundary conditions	ff
Solve for displacements	$dU = Kff \setminus ff$
Update displacement field	$U = U+dU$
Apply displacement field to template	T_u
End if converged	
Observe displacement field	

To begin the routine, arbitrary values for E and ν are selected that define the elastic behavior of the FEM mesh, and minimize the similarity criteria. A higher stiffness requires a smoother displacement field, while a low stiffness allows more local differences. Best results have been found by starting with a high stiffness value for the

first iterations, then decreasing E for better refinement. The value of ν was kept at 0.25. These values are strictly for the purpose of image registration and have no real, physical meaning.

3.3.3.1 Example Application for Elastic Registration

Synthetic images were used to validate the elastic registration routine and implementation. Figure 3.11 shows the reference and template images of size 100x100x1 voxels. Both are simple images, yet require a relatively large-scale displacement fields to align correctly.

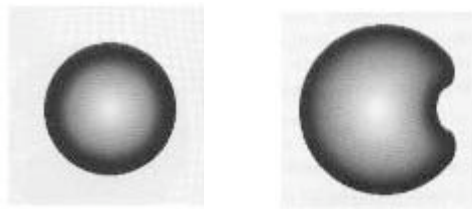


Figure 3.11 – Template (T) and Reference Image (R)

Application of the elastic registration routine to the images resulted in a converged solution after 20 iterations. Figure 3.12 shows the objective criterion, and Figure 3.13 shows the deformed template, T_u . The resulting x and y (horizontal and vertical) displacement fields are shown in Figure 3.14.

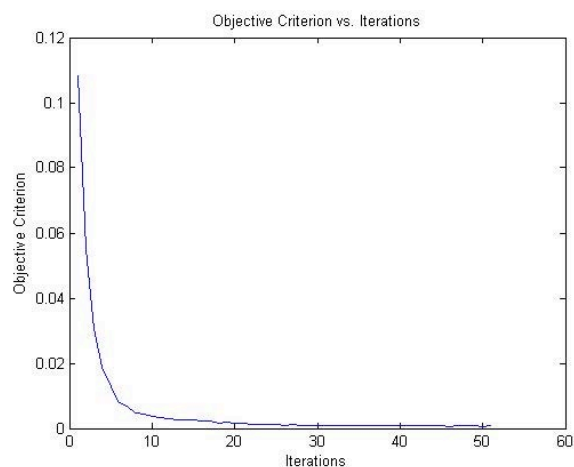


Figure 3.12 – Objective Criterion vs. Number of Iterations

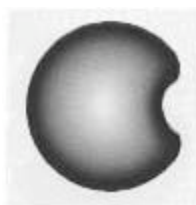


Figure 3.13 – Deformed Template (T_u)

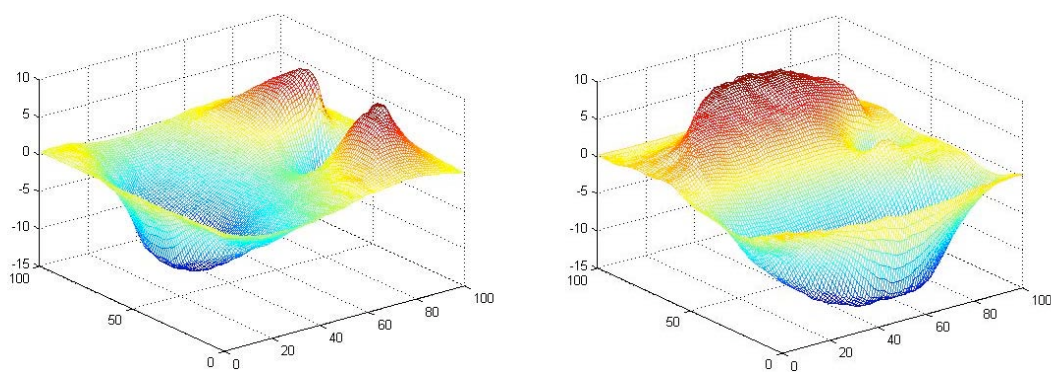


Figure 3.14 – x and y Displacement Fields (on pixel scale)

From this example it becomes apparent that the image registration routine does work well on elastic bodies which require continuous displacement fields, and (with the appropriately selected E and ν values) generates a smooth displacement field.

While elastic registration works well modeling continuous displacements, it does not do well modeling discontinuities. For example these two images in Figure 3.15 require a known, discontinuous displacement field, found in Figure 3.16, for a correct image registration.

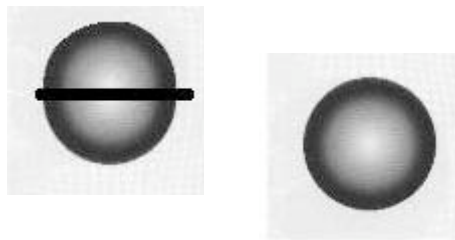


Figure 3.15 - Template (T) and Reference Image (R)

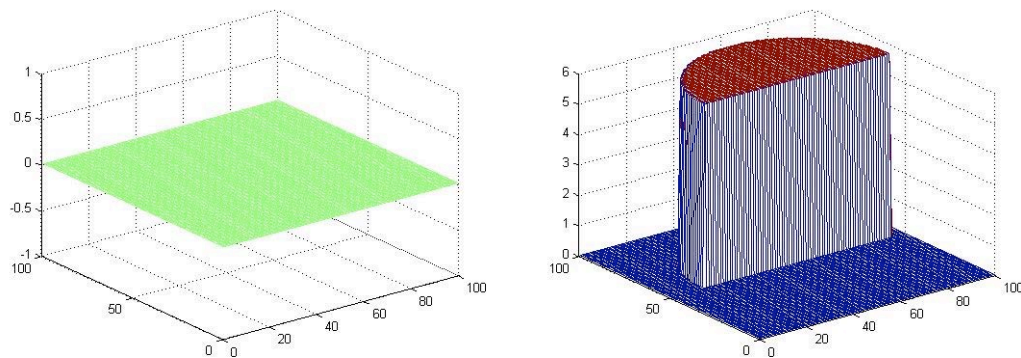


Figure 3.16 - Known x and y Displacement Fields

Not surprisingly, elastic registration provides a poor objective criterion convergence, as shown in Figure 3.17, and the deformed template, as shown in Figure 3.18, does not visually match the reference image. The displacement fields, as seen in Figure 3.19, reflect the inaccuracy.

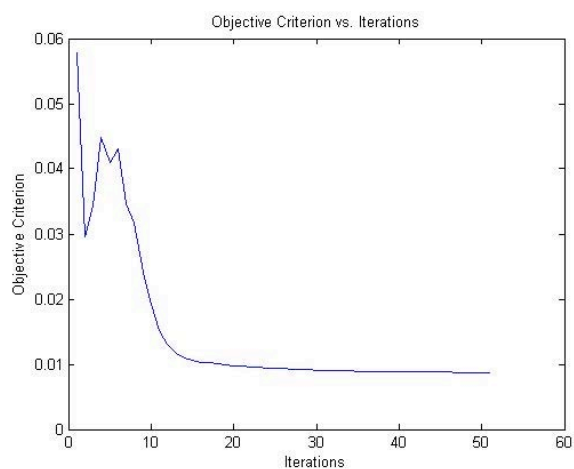


Figure 3.17 – Objective Criterion vs. Number of Iterations

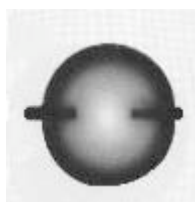


Figure 3.18 – Deformed Template

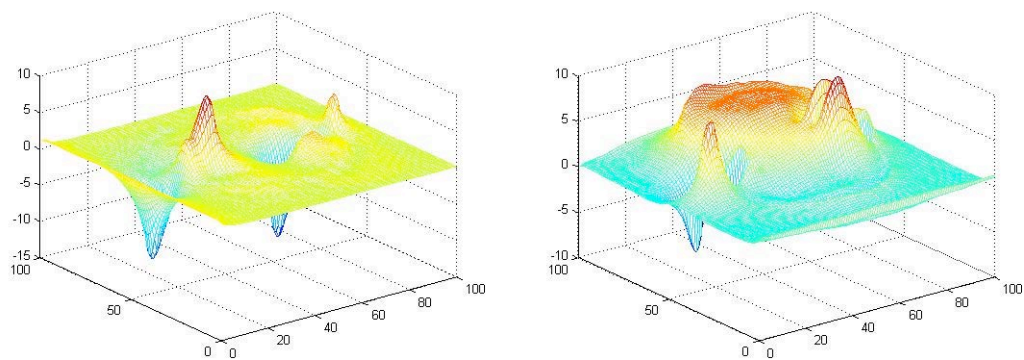


Figure 3.19 – x and y Displacement Fields Generated

To improve on this, this study extends the concept of elastic registration for the case of a displacement field with discontinuities, by employing a transformation with embedded discontinuities as is done in XFEM (Vigneron, et. al, 2004).

3.3.4 Image Registration - XFEM Extension

Elastic registration imposes a smooth displacement field, but concrete exhibits discrete cracking under loading. A recent and effective modification is called the Extended Finite Element Method or XFEM.

In XFEM the displacement field is “enriched” to include discontinuities defined using “Heaviside” functions to model crack opening, and crack-tip equations for each tip. Additional degrees of freedom are added at nodes whose support is fully cut by a crack, or partially cut. This effectively allows the solution of the XFEM equations to be discontinuous within mesh elements, a defined by crack geometry.

Thus the assumed form of the displacement field is:

$$u(x) = \sum_{i \in I} \varphi_i(x) u_i + \sum_{j \in J} \varphi_j(x) H(x) a_j + \sum_{k \in K} \varphi_k(x) \left(\sum_{l=1}^4 \phi_l(x) c_k^l \right). \quad (3.13)$$

The first term is the displacement field employed in classical finite element and elastic registration. The second term “enriches” the displacement field for elements with a crack that full intersects the element; a_j are the “enriched” nodal displacement and $H(x)$ is the Heaviside function defined in Equation 3.14.

$$\begin{aligned} H(x) &= 1 & \text{for } (x - x^*) \cdot e_n > 0 \\ H(x) &= -1 & \text{for } (x - x^*) \cdot e_n < 0 \end{aligned} \quad (3.14)$$

where x is a point of the solid, x^* the point on the crack closest to x , and e_n the unit outward normal to the crack at x^* . The third term enriches the displacement field for elements that are only partially cut by a crack. These enriched displacement functions incorporate the radial and angular behavior of the asymptotic crack-tip displacement field, with

$$\{\phi_1(r, \theta)\} = \left\{ \sqrt{r} \sin\left(\frac{\theta}{2}\right), \sqrt{r} \cos\left(\frac{\theta}{2}\right), \sqrt{r} \sin\left(\frac{\theta}{2}\right) \sin(\theta), \sqrt{r} \cos\left(\frac{\theta}{2}\right) \sin(\theta) \right\} \quad (3.15)$$

where r and θ are the local polar coordinates.

For XFEM image registration, the same objective criterion is used, but the regularizing term is locally modified by the XFEM extension. XFEM still requires potential energy minimization everywhere except across crack boundaries. XFEM image registration redefines the displacement field as above, and the stiffness matrix is calculated and assembled

$$k_{ij}^e = \begin{bmatrix} k_{ij}^{uu} & k_{ij}^{ua} & k_{ij}^{ub} \\ k_{ij}^{au} & k_{ij}^{aa} & k_{ij}^{ab} \\ k_{ij}^{ub} & k_{ij}^{ab} & k_{ij}^{bb} \end{bmatrix}, \quad (3.16)$$

$$k_{ij}^{rs} = \int_{\Omega} (B_i^r)^T D B_j^s d\Omega,$$

$$B_i^u = \begin{bmatrix} \varphi_{i,x} & 0 \\ 0 & \varphi_{i,y} \\ \varphi_{i,y} & \varphi_{i,x} \end{bmatrix}$$

$$B_i^a = \begin{bmatrix} (H\varphi_i)_x & 0 \\ 0 & (H\varphi_i)_y \\ (H\varphi_i)_y & (H\varphi_i)_x \end{bmatrix}$$

$$B_i^{bl} = \begin{bmatrix} (\phi_l \varphi_i)_x & 0 \\ 0 & (\phi_l \varphi_i)_y \\ (\phi_l \varphi_i)_y & (\phi_l \varphi_i)_x \end{bmatrix}$$

The forces are calculated and applied in the same manner as the classical FEM elastic registration. However, neither the Heaviside or crack-tip degrees of freedom had forces applied to them, although that possibility has not been explored.

Then solving the system using the same Newton's solver

$$U = K \setminus F \quad (3.17)$$

produces a discontinuous displacement field. Even with the introduced cracks, the objective is still the minimization of the similarity criterion, so the effectiveness of the XFEM routine was monitored in the same manner as before.

XFEM requires each crack to be discretely defined prior to running the image registration. With an arbitrary set of images the location of these cracks is often not known a priori, so criteria must be set for determining their location. In other finite element applications, cracks are identified in areas of high principal stresses after an elastic analysis has been performed. This study will attempt a similar strategy to identify crack locations for image registration. Crack identification is the greatest challenge in implementing a XFEM image registration routine.

3.3.4.1 XFEM Example

The first step in validating the XFEM registration routine implementation was to use the XFEM framework to solve a basic FEM problem. Here, the reference image was used to represent an elastic mesh. A crack was embedded in the mesh, and loads applied to open the crack, as shown in Figure 3.20. Then the XFEM form was used to compute the displacement field.

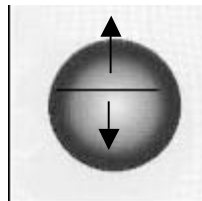


Figure 3.20 – Elastic Mesh with Embedded Crack

Elastic modulus and Poisson's ratio, as well as the force magnitudes were selected to generate visible deformations within the domain. The deformed template image (T_u) shows the opening of the crack in Figure 3.21. The displacement fields of the classical degrees of freedom are shown in Figure 3.22 and match expected results. The displacement fields of the enriched degrees of freedom are defined only around the crack, and demonstrate a wider opening at the center of the crack than the edges. (Figure 3.23)

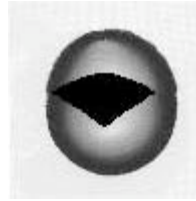


Figure 3.21 – Deformed Template Image with Crack Opening

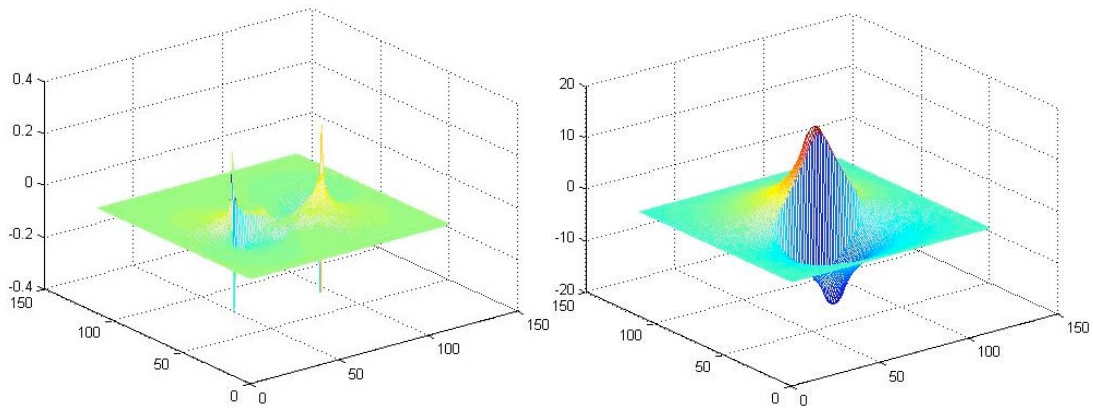


Figure 3.22 – x and y Elastic Displacement Fields

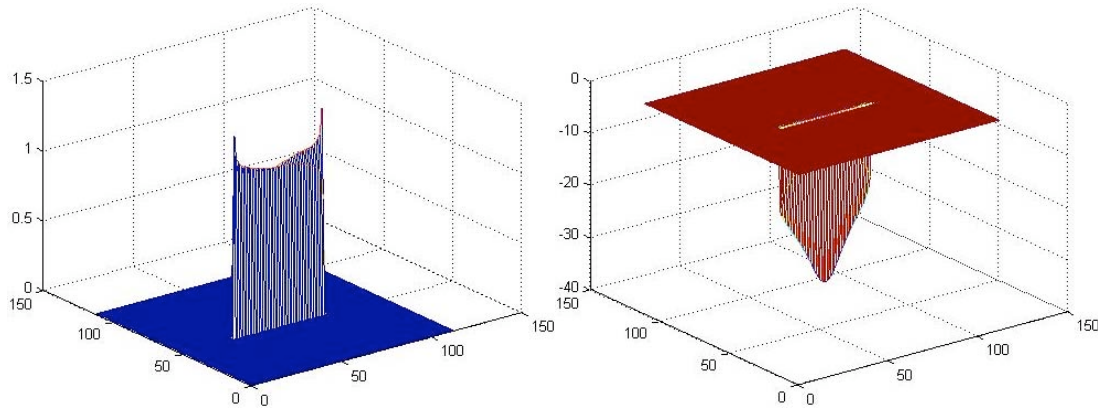


Figure 3.23 – x and y Discontinuous Displacement Fields

All displacements are scaled to a pixel dimension. From this example, it becomes apparent that XFEM can effectively model discontinuities. The next verification required is to determine whether XFEM can be used with image registration.

3.3.4.2 XFEM Image Registration with Pre-Defined Crack

The second step in the validation process was to apply the XFEM method to synthetic reference and template image (Figure 3.24) to retrieve a known displacement field with discontinuities (Figures 3.25).

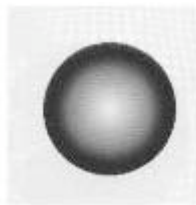


Figure 3.24 – Template Image

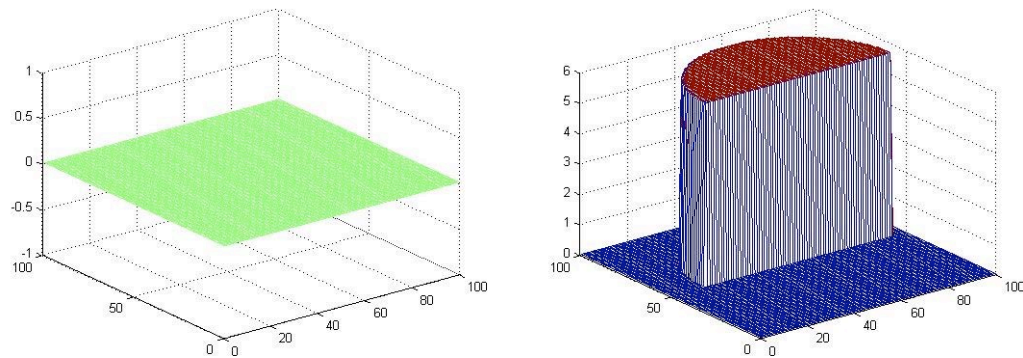


Figure 3.25 – Known x and y Displacement Fields

Applying this displacement field creates a new reference image. (Figure 3.26) Then the XFEM image registration routine is run, with, as a first step, a pre-defined crack location. By selecting appropriate E and ν values, the deformed template looks similar to the new reference image. (Figure 3.27) The objective criteria also demonstrates convergence (Figure 3.28).

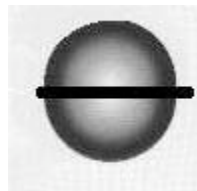


Figure 3.26 – New Reference Image

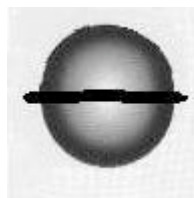


Figure 3.27 – Deformed Template (T_u)

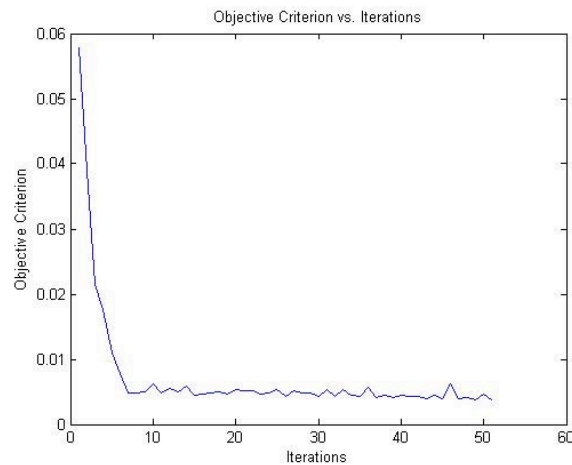


Figure 3.28 – Objective Criteria during XFEM Registration

The resulting classical displacement fields (Figure 3.29) show the dominant y displacement and the resulting x displacement from Poisson's effect and the fixed boundary. The displacement field does not match exactly due to the fixed boundary applied around the image. More empty space around the exterior of the image would improve the displacement field. The enriched displacement fields display the crack length behavior. (Figure 3.30)

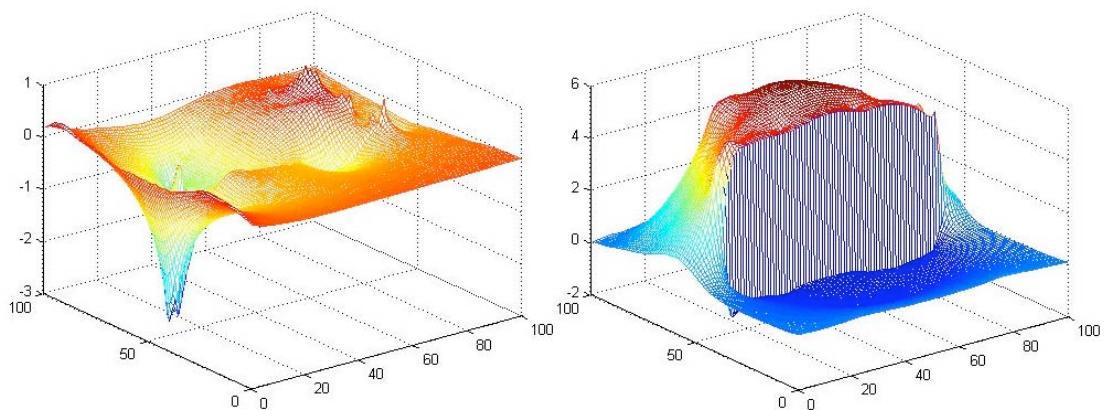


Figure 3.29 – x and y XFEM Classical Displacements

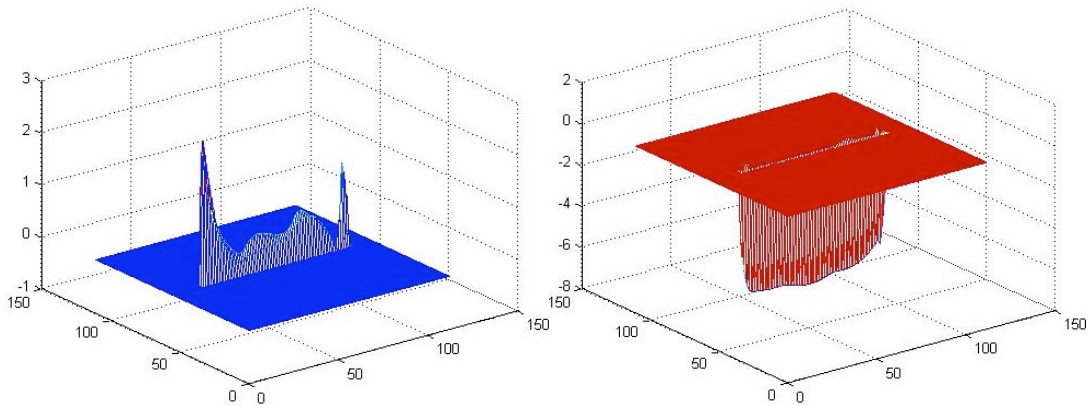


Figure 3.30 – x and y Enriched Displacements

This routine captures the main deformation trends with predefined discontinuities.

3.3.4.3 Advanced Technique Attempt: XFEM Image Registration with Automated Crack Definition

In order to truly take advantage of the image registration with the XFEM extension, the routine must be able to detect where discontinuities are “needed.” This section will describe one unsuccessful attempt to solve this issue, and the difficulties that prevented success.

By first registering two images elastically, the areas experiencing the most “strain” are the ones where discontinuities are likely to be. So the process consists of two registration routines: first, an elastic registration, used only to identify areas of maximum principal strains, then an inelastic XFEM registration using the identified crack locations.

Using the same known displacement field as used above, the same reference and template images are used without any previous crack definition (Figure 3.31). Running the elastic registration for 20 iterations returns a deformed template image in Figure 3.32, with x and y displacement fields shown in Figure 3.33.



Figure 3.31 – Reference and Template Images

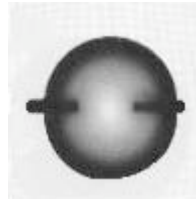


Figure 3.32 – Deformed Template Image

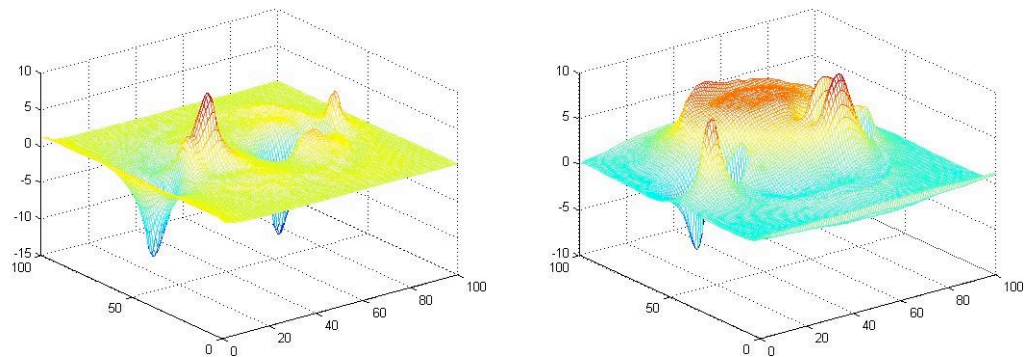


Figure 3.33 – Elastic Registration x and y Displacement Fields

This displacement field was used to calculate strains, then maximum principal strains at each location through Equation 3.18. With the displacement fields defined at nodal or “voxel” locations, this unit finite difference differentiation defines the strain within each element, continuing with basic finite element theory of cracked and uncracked elements. The principal strain calculations typically give us a positive and negative value – corresponding with either tension (positive) or compression (negative).

For these applications, only positive principal strain was evaluated, under the assertion that high tensile strains lead to crack opening. (Figure 3.34, 3.35)

$$\begin{aligned}
 \varepsilon_{xx} &= u_x(x+1, y) - u_x(x, y) \\
 \varepsilon_{yy} &= u_y(x, y+1) - u_y(x, y) \\
 \varepsilon_{xy} &= u_x(x, y+1) - u_x(x, y) \\
 \varepsilon_{yx} &= u_y(x+1, y) - u_y(x, y)
 \end{aligned}
 \tag{3.18}$$

$$\varepsilon_{p1,2} = \frac{\varepsilon_{xx} + \varepsilon_{yy}}{2} \pm \sqrt{\left(\frac{\varepsilon_{xx} - \varepsilon_{yy}}{2}\right)^2 + \varepsilon_{xy}^2}$$

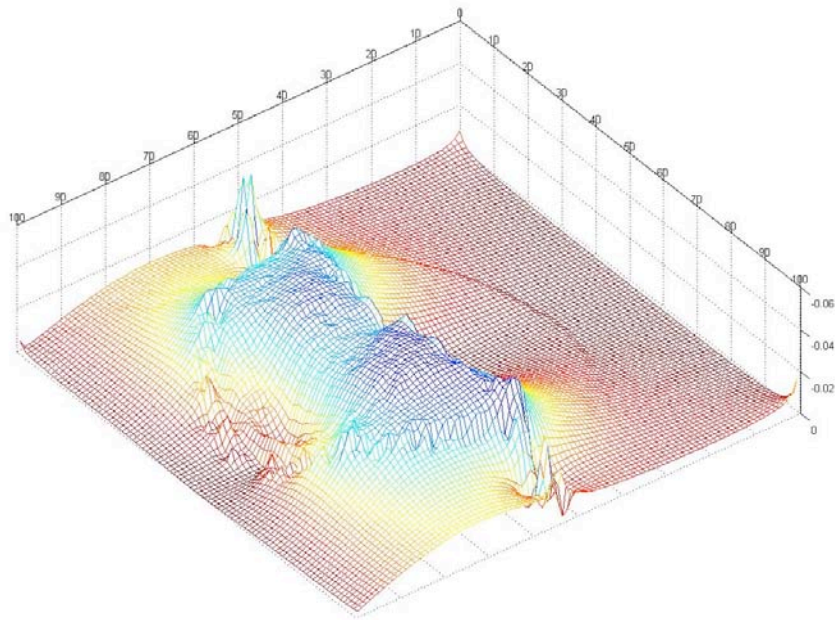


Figure 3.34 – Principal Tensile Strains

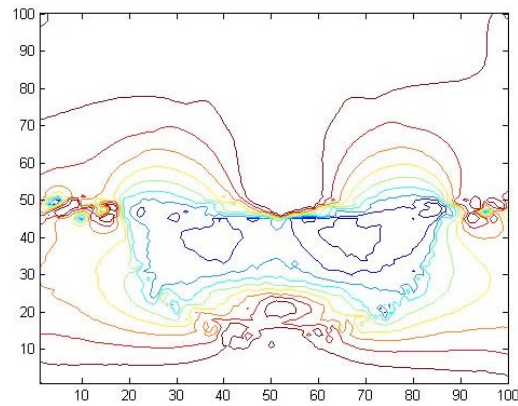


Figure 3.35 – Principal Tensile Strains Contour

The next step is to take these principal strains, and identify crack locations. Due to the nature of the XFEM method where each crack must be uniquely defined in each element, locations of local maxima were first identified (Figure 3.36), then these locations were connected with a “shortest-distance” criterion (Figure 3.37). Within both the maxima finding routine and the connectivity criterion there are variables such as sensitivity and starting point that are manually adjusted for the best results.

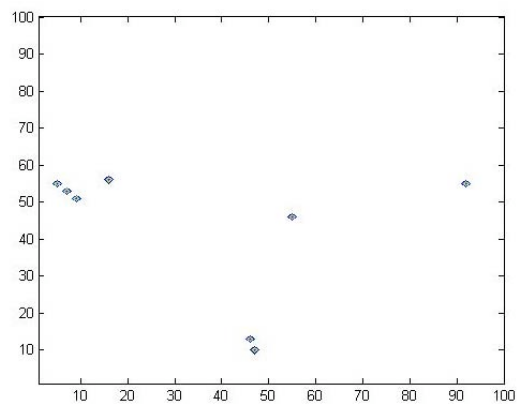


Figure 3.36 – Principal Strain Local Maxima

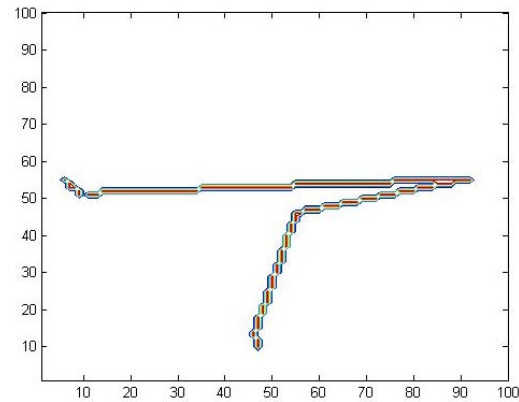


Figure 3.37 – Shortest-Distance Crack Connection

3.3.4.3.1 Restrictive Difficulties

At this point, this information is then passed to the XFEM image registration routine and major difficulties arise. Specifically, the crack “corners” present major singularities as a solution is attempted. At these corners, where single elements have two crack planes trying to “open up”, there are severe convergence issues, and displacement singularities occur.

Also, this routine does not differentiate between independent cracks, processing all areas of high principal strain as a single crack. This gives rise to the need for a routine that can identify not only cracks, but separate cracks that open independent of others. XFEM, unlike other discontinuous FEM routines, requires a linearly defined crack in each element, and that it is connected to other cracked elements to open.

Given the nature of elastic registration with a fixed boundary, this routine is unable to differentiate between cracking strains, and strains due to boundary conditions. This again reinforces the need for additional research with varying boundary conditions within elastic registration.

3.4 Conclusions

These tools are a set of possible methods for extracting usable information from X-ray CT images of bond specimens. Visual inspection is the most direct method; returning relative crack widths, crack orientations and other information by simply viewing the 2D images. Single image processing applies another level of sophistication, employing the use of computer algorithms. Given the interest in solids and voids, threshold segmentation is a relevant routine for extracting crack surfaces and volumes. Multiple image processing utilizes the sequential information collected. Continuous displacement fields can offer information about the mechanics of bond, but the effectiveness of these image registration techniques remains to be seen. XFEM appears to be a valid method for modeling discontinuities, but further research is required to locate cracks.

CHAPTER 4 : EXTRACTED BOND INFORMATION

4.0 Introduction

This chapter will explain how the tools outlined in the previous chapter were used to extract meaningful bond information from the specimens tested. The image processing routines presented in the previous chapter provide a means of extracting information from 3D images to provide improved understanding of bond. The processes discussed will be visual inspection, image thresholding and crack extraction, fracture analysis, displacements as elastic deformations, and displacements as elastic and inelastic deformations. Each process will discuss method, results, and conclusions.

These processes will be applied to the images received from the test series imaged at the University of Texas. They will be identified by name (e.g P3F-2), which can be referenced in the specimen overview in Chapter 1.

4.1 Process One: Visual Inspection

While all five specimens failed by radial splitting, there were variations in each. None of the specimens exhibited any visible changes between scans 1 and 2, and therefore all visual inspection was performed on the cracked, post-peak images.

4.1.1 Method

Visual inspection was performed by examining the 2D image (XY plane) at every height of the specimen that was imaged, like Figure 4.1. Several phenomena were recorded for each 3D image: number and orientation of dominant cracks, number of aggregates split, visual crack width, significant crack branching, connectivity of spiral reinforcing support dowels, and presence of lug crushing. Visual inspection information was assembled in tables like Table 2. All visual inspection results can be found in Appendix A.

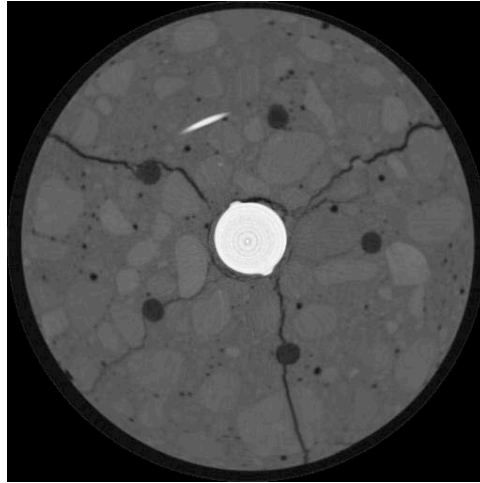


Figure 4.1 – Sample Image from Specimen P3W1B-4

Table 2 - Visual Inspection Results, Specimen P3W1B-4

P3W1B-4						
Dominant Cracks	Orientation of Dominant Cracks (deg)	Number of Aggregates Split	Visual Crack Width	Significant Crack Branching	Connect through Dowel ?	Significant Lug Crushing Around Bar
1	0	1	Wide	No	Yes	Some
2	100	1	Wide	Yes	No	
3	200	1	Wide	No	Yes	
4	260	0	Fine	No	Yes	

4.1.2 Results

Each specimen revealed slightly different failure characteristics, yet all are categorized as bond failure. A summary of the findings for each specimen will be discussed, and then general results about bond failure will be discussed.

4.1.2.1 Specimen Findings

P1-3,4 : Two dominant cracks split the cylinder, but there was a significant amount of crushing around the bar lugs. As no aggregates were split, it appears that most energy was dissipated through crushing which correlates to a small bonded length.

P3F-3,4 : Three very dominant cracks (no crack branching) split the cylinder approximately in thirds, often splitting aggregates. This correlates to the sudden failure observed, and the rapid drop in load post-peak. The fibers are not visible, and appeared to have no post-cracking resistance.

P3W1A-3,4 : Three fine cracks were opened only slightly as the bar pulled through, reflective of reinforcing spiral restraint. There was also significant branching of the cracks (not single surfaces created), suggesting stress may be still carried across fine crack widths.

P3W1B-3,4 : Three medium cracks were opened, all of which split aggregates, then a fourth at the final load. Three of the four cracks pass through wooden support dowels.

P3W2-3,4,5 : Two cracks on opposite sides can be seen first, then two other cracks open up. The double spiral prevents any wide cracks, and again, three of the four cracks connect wooden support dowels.

4.1.2.2 General Bond Results

The various levels of confinement and bonded length create slightly different failure mechanisms, and through visual inspection we can attempt to establish trends for better understanding of bond behavior.

1. Stress vs. Crack Width: Recent publications suggest that even after cracks form, significant stress can still be carried across small crack widths. This assumption is supported by the observed crack widths and the corresponding loss of load in bond failure. Specimens with the widest initial cracks (P1, P3F) experienced the most drastic loss in load despite fiber wrap (P1) and distributed fibers (P3F). The other specimens had spiral reinforcing, which undoubtedly provide some confinement, but also had very fine cracks, which could conceivably be continuing to carry stress.

2. Crack Branching: With the spiral reinforcement specimens (P3W1A, P3W1B, P3W2), there are several instances where multiple cracks have formed instead of one dominant crack. This demonstrates the distribution of stress along the spiral reinforcement and the stress transfer to the local concrete through bond. On an energy level, multiple cracks mean more crack surfaces, dissipating more energy at larger displacements and enabling the specimen to carry larger loads than specimens without spiral. This energy dissipation, in addition to the elastic confinement of the spiral, creates a less catastrophic failure. This mechanism is not apparent in either fiber specimen (P1, P3F).
3. Grain Boundaries vs. Aggregate Splitting: As the cracks propagate through the cylinder, they most often follow grain boundaries. However, with specimen (P3F) where the most dramatic failure was observed several aggregates were split. Presumably the cracks initiated around the bar at local weaknesses, but due to the ineffectiveness of the fibers, could only dissipate energy by rapidly forming crack surfaces. These cracks propagated radially from their initiation point so forcefully, any material in the way was split. This phenomenon correlates the highest energy release (in specimen P3F failure) to the most split aggregate, and is of importance because it effects aggregate interlock, another mechanism for post-crack stress transfer across crack width.
4. Crack Orientation Relative to Wood Dowels: To construct the spirally reinforced specimens, wooden dowels were used to space the spiral. Yet these dowels themselves seem to have an impact on the fracture patterns during bond failure; specifically, at least two cracks in each spirally-reinforced specimen directly connect to a wooden dowel. Under the presumption that cracks form first around the bar and (rapidly) propagate outward, there must be some local weakness “detected” by the crack tip that both initiates and propagates cracking.

4.1.3 Conclusions

The visual inspection results are most valuable in providing an explanation for many of the physical phenomena seen during testing. In general the amount and type of confinement can have a drastic effect on not only peak load but also the type of cracking and failure observed. The results from internal X-ray CT images give rise to many more interesting questions about bond failure and the fracture of concrete in general: How wide must a crack be to dissipate energy and affect failure response? Is there a direct relationship between energy released and split aggregate?

4.2 Process Two: Image Thresholding and Crack Extraction

Through threshold segmentation and feature characterization, crack surface areas and volumes can be extracted for both visualization and calculation purposes. Like the visual inspection, the only meaningful crack surfaces are found in the post-peak cracked images. All specimens were processed in this way.

4.2.1 Method

The method, previously described in Chapter 3, involves the selection of the threshold segmentation value to optimize the amount of crack change in a sequence of images. By examining the histogram of each image, the region of values that separate solid from void can be identified, a peak in structural changes is found and images can be segmented (Figure 4.2).

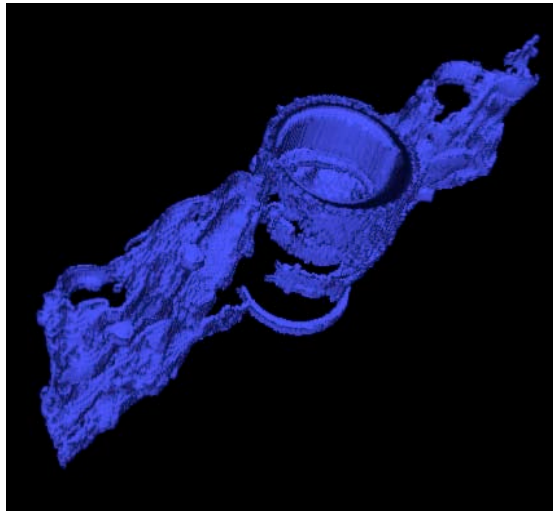


Figure 4.2 – P1-3 Segmented Specimen

After segmentation, the cracks and void spaces are processed via Blob3D to extract surface areas and volumes. With this information, simply dividing the volume by the surface area created approximated crack widths. This allowed monitoring of crack width growth during failure. By processing several images in sequence, changes in crack geometry, surface area and volume can be observed, as in Figure 4.3.

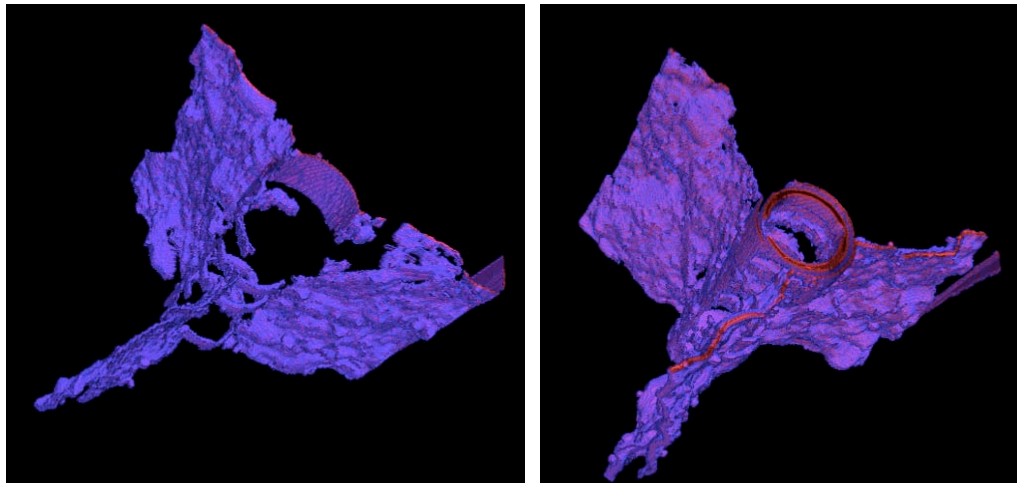


Figure 4.3 – P3F-3 -> P3F-4 Segmented Crack Growth

4.2.2 *Results*

Threshold segmentation provides a method for isolating the cracks created during bond failure. Feature characterization allows quantification of these cracks, and non-subjective extraction of meaningful failure data like crack width, surface area and volume. This section will include a discussion of the extracted crack surfaces for each specimen and then discuss general bond behavior.

4.2.2.1 *Specimen Findings*

P1-3,4: This specimen had a lot of crushing around the lugs of the bar, leading to a difficulty in separating solid from void. Threshold segmentation processed this “rubble” as void, and as a result, bar void is over twice the volume of each radial crack. This is logical given the short bonded length and lack of confinement. Crack widths grew from 0.026” to 0.034”.

P3F-3,4: This specimen exhibited the most dramatic failure, and as a result has the largest surface area created. Also this specimen had the “flatest” crack volumes, referring to how many aggregates were split during this failure and therefore the crack surface does not curve and twist along grain boundaries like others do. With this specimen, crack widths started large (0.054”) and grew (0.064”).

P3W1A-3,4: The presence of spiral reinforcement drastically changes the crack volume. There are still two dominant cracks, and those cracks radially connect through the support dowels. But the third crack shows more distributed cracking over an area, rather than a single surface. This shows the distribution of load from the spiral to the concrete. Cracks, in general grew from 0.036” to 0.048”.

P3W1B-3,4: With the slightly thicker spiral, a similar crack pattern develops. Three dominant cracks develop, with two of the three passing through the wooden dowel space. This crack volume appears much more “bumpy”, reflecting the crack path around aggregate boundaries. The cracks grew approximately from 0.036” to 0.043”.

P3W2-3,4,5: Double spiral confinement provided the smallest cracks. While detectable with visual inspection, threshold segmentation has a difficult time in detecting cracks this fine. The change in crack volume was still calculated, but visualization of the crack surfaces was very difficult with this routine. Estimated cracks grew from 0.012” to 0.017”

4.2.2.2 General Bond Results

Threshold segmentation, with feature characterization is a simple way of defining crack volumes. Issues observed with visual inspection can be explored in a different manner with some image processing

1. Stress vs. Crack width: The results from all the specimens showed discontinuous crack surfaces, meaning there were some portions of the crack that were not detected, presumably where the cracks are the narrowest. Further research could look at locations not included in crack surfaces and determine if those were locations where stress was still being transferred across crack widths.
2. Crack Branching: Crack volumes showed the observed crack branching, but also showed the cracks are still interconnected, not isolated.
3. Grain Boundaries vs. Aggregate Splitting: This phenomenon is observed in the “flatness” of the surfaces created. Given the basic crack geometry, a curve fitting routine could be run to model the crack as a continuous function. With a function in place, characteristics like tortuosity (bumpiness) could be extracted.
4. Crack Orientation Relative to Wood Dowels: By isolating the crack surfaces, we can see that in all three specimens with dowels (P3W1A, P3W1B, P3W2) have at least two dominant cracks passing through dowel void space. This

reinforces the thought that the local weakness due to the dowels affects both cracks initiation and crack growth.

Complete 3D renderings of the cracks and their corresponding values for surface area and volume can be found in Appendix B.

4.2.3 Conclusions

There are many ways to segment solid from void in an image, and that method can drastically affect what is returned. Selection of the threshold value to maximize detection of cracks and voids is a non-subjective method to do so, and produces logical, useable results. Further research should investigate other, more sophisticated segmentation routines, as well as surface-fitting routines to map actual crack paths. Segmentation is an important step in any crack extraction routine.

4.3 Process Three: Fracture Analysis

This section will discuss the release of energy during bond failure. The goal was to compare the energy released during bond fracture to the energy put into the system by the load. Using crack surface areas and elastic strain assumptions, simple fracture energy calculation can be performed between two images where cracking occurs. This fracture energy analysis was performed for all intervals for which cracking was observed (image 2 -> image 5), for all specimens.

4.3.1 Method

The total area of crack surface extracted from image data (previous section) can be combined with concrete fracture energy to determine energy dissipated in concrete cracking. Here, this computed energy was compared with total energy input into the system. If no energy is lost, these two energy values should be the same. A similar analysis was performed by Landis et al. 2003.

Equating input energy with energy dissipated through failure results in:

$$\Delta W = \Delta U_{STRAIN} + U_{FAILURE}$$

$$\Delta W = \Delta U_{STRAIN} + G_f * \Delta A + \Delta U_{NOISE}$$

where ΔU_{STRAIN} is the internal strain energy of both the steel and concrete, ΔW is the work done by the external load over the distance of bar slip, G_f is the concrete fracture energy density equal to the amount of energy required to create a unit area of crack, and ΔA is the change in crack surface area. Martin (2006) performed fracture tests of the concrete mix used to construct the specimens and provided an approximate value of G_f for use. This permits a calculation of how much energy is dissipated through other mechanisms, ΔU_{NOISE} . The different components of fracture energy were then computed:

- ΔW : Integrate under load displacement curve
- ΔU_{STRAIN} : Calculate the change in strain energy of steel and concrete
- ΔA : Extract and extrapolate surface area
- Calculate ΔU_{NOISE}

ΔW : Integrate Under Load Displacement Curve

Using the load-displacement curve, as referenced in Chapter 1, work done during fracture was obtained by integrating between the two imaged points where fracture occurred. Given the nature of bond failure and assuming most of the fracture occurs post-peak, integrating between scans 2 and 3, returns ΔW , the work done by the external load.

ΔU_{STRAIN} : Calculate the Change in Strain Energy in the Concrete and Steel

Calculating strain energy required the assumptions that both concrete and steel are linear elastic materials, and that the stress is uniform within each material. The energy in the steel is relatively easy to calculate, with the given quantities, but the concrete is less straight forward. With those assumptions, the energy calculations become:

$$\begin{aligned}
 U_c &= \frac{1}{2} \left(\frac{E_c A_c}{L_c} \right) \Delta_c^2 \\
 U_s &= \frac{1}{2} \left(\frac{E_s A_s}{L_s} \right) \Delta_s^2
 \end{aligned}
 \tag{4.1}$$

Substituting the equilibrium condition of,

$$P = \frac{E_c A_c \Delta_c}{L_c} = \frac{E_s A_s \Delta_s}{L_s}, \tag{4.2}$$

and assuming

$$L_s = L_c \tag{4.3}$$

the ratio of U_c to U_s becomes,

$$\frac{U_c}{U_s} = n\rho. \tag{4.4}$$

where

$$\begin{aligned}
 n &= \frac{E_s}{E_c} \\
 \rho &= \frac{A_s}{A_c}
 \end{aligned}$$

The values for the specimens in the project are:

$$\begin{aligned}
 n &= \frac{29000}{3625} = 8 \\
 p &= \frac{.5^2 * \pi}{3^2 * \pi} = \frac{1}{36} \\
 \frac{U_c}{U_s} &= \frac{2}{9} \\
 U_{STRAIN} &= U_c + U_s = \frac{11}{9} U_s = \frac{11}{9} \left(\frac{1}{2} \left(\frac{E_s A_s}{L_s} \right) \Delta_s^2 \right)
 \end{aligned}
 \tag{4.5}$$

By calculating this strain energy at two points on the load-displacement curve, the change in strain energy stored in the system can be computed, ΔU_{STRAIN} .

ΔA : Extract and Extrapolate Surface Area

To minimize imaging time and thus cost, the entire height of the specimen was not imaged. Only the part of the specimen in which the bar was bonded to the concrete was imaged. Thus the entire area of crack surface generated in the specimen is not known. To estimate this area, the cracks area assumed to be wedge shaped – wider at the base and narrowing to zero width at some point up the height of the specimen. This assumption is supported by visual inspection.

Visual crack measurements (aided by computer enlargements, normal to crack) were taken at three radial intervals (one and two bar-diameters from the center, and surface) up the cylinder, (Figure 4.4, Figure 4.5) and the rate at which the cracks were closing, assumed to be linear with distance up the cylinder was estimated.

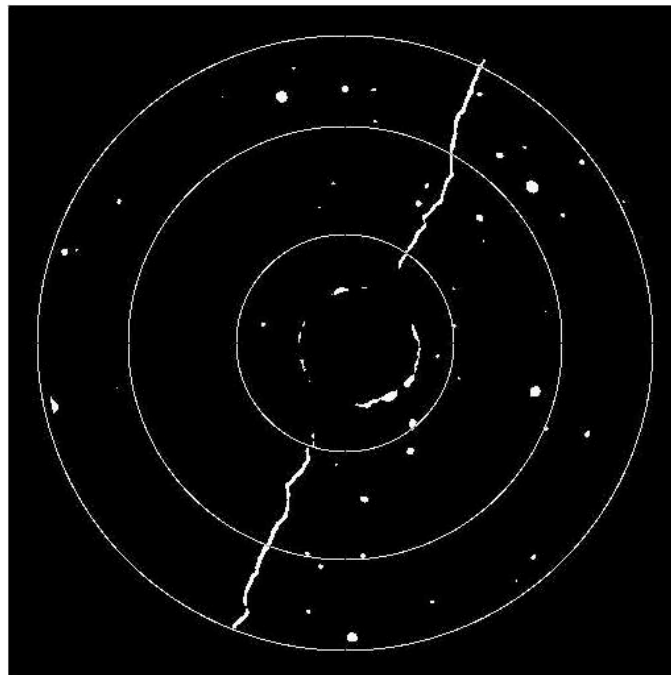


Figure 4.4 – P1-3 Radial Crack Measurement Locations

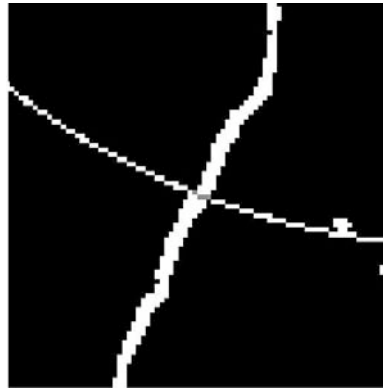


Figure 4.5 – Enlarged Crack Measurement Location

With that information, the height at which the cracks arrest was determined, and as a result, how large the crack surface area is (Figure 4.6).

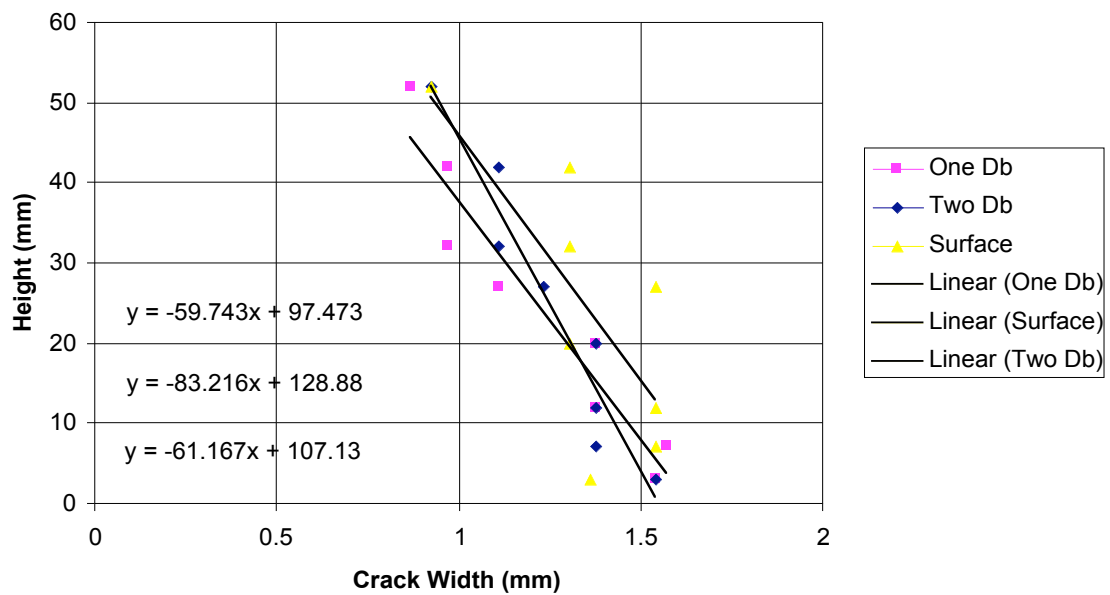


Figure 4.6 – P1-3, Crack Width vs. Height

This extrapolation operates on the assumption that each crack width diminishes linearly with height, and enables the Blob3D-measured value to be used for the imaged

crack surface area. Conversion of the returned surface area (whole 3D surface) to a surface usable in an energy calculation required a few simple calculations (Figure 4.7).

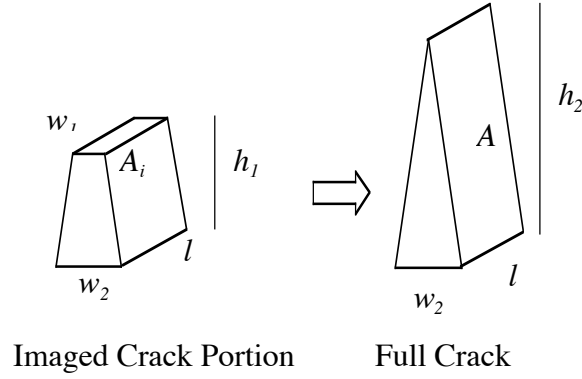


Figure 4.7 – Assumed Crack, Diminishing With Height

$$\begin{aligned}
 A_i &= l * \sqrt{h_1^2 + \left(\frac{w_2 - w_1}{2}\right)^2} \\
 A_i &= l * \sqrt{h^2 + \left(\frac{w_2}{2}\right)^2} \\
 A_i &= A_i * \frac{\sqrt{h_2^2 + \left(\frac{w_2}{2}\right)^2}}{\sqrt{h_1^2 + \left(\frac{w_2 - w_1}{2}\right)^2}}
 \end{aligned} \tag{4.6}$$

For each image then, extrapolation of A_i is possible, and then the difference between the two becomes ΔA .

4.3.2 Results

These data are calculated for specimen P1 and presented in Table 3.

Table 3 - Fracture Energy Calculation for Specimen P1-2 -> P1-3

P1	Energy Calculations	
	Image 2	Image 3
U in Bar (lb-in)	53.33	2.02
load (k)	15.6	3.03
stress (ksi)	19.84	3.86
Strain	0.00068	0.00013
displacement (in)	0.0068	0.0013
U in Concrete (lb-in)	13.33	0.50
U (Bar+Conc) (lb-in)	66.66	2.52
ΔU (lb-in)	-64.14	
ΔF (lb-in)	449.50	
ΔA (in²)	28.80	
Gf (lb/in)	0.65	
Gf * ΔA (lb-in)	18.72	
U_NOISE (lb-in)	494.92	

4.3.2.1 Specimen Findings

These calculations, and the ones from every other specimen, show a huge amount of energy during bond failure is lost due to “noise” – other unquantifiable, sources like audible noise, kinetic movement of the specimen, and creation of dust and debris. This experiment was not designed to capture those other energy loss mechanisms.

Assuming a heat capacity value of 1000 J/kg, this “Noise” term would convert to a temperature rise of roughly 400-degrees, which is obviously incorrect. Assuming kinetic movement of the bar passing through the specimen, this “Noise” term would require a bar speed of 22 feet/second, and a movement time of 0.00019 seconds, also

unlikely. Most likely, multiple mechanisms are occurring at once, including crushing around the bar lugs, and at this point, further calculations are not possible. Fracture energy calculations for all the specimens can be found in Appendix C.

However, we can still utilize some of the data calculated to help categorize bond failure. By examining the stress vs. crack opening curve, we see that all fracture energy has been dissipated by the time the cracks are approximately 0.006” wide. This crack width is far smaller than the observed crack width at the second image. Most likely, the cracks form and open, requiring fracture energy, then the rest of the bar displacement is due to strain release from the concrete and steel, and work done by the bar. Past the fracture surfaces created though, the other sources of energy loss cannot be quantified.

4.3.2.2 General Bond Results

In general, bond is a rapid failure where energy is dissipated through multiple mechanisms. The drastic difference in energy input and energy release through fracture is surprising. Additional factors like stiffness of the load rig, elastic rebound of the steel, and acoustic emissions must have a larger than expected energy dissipation.

4.3.3 Conclusions

To do a true energy loss calculation, more sophisticated energy techniques are needed. This process is an effective way to approximate the energy released during fracture in bond, the energy remaining in the concrete as elastic strain and the unaccountable energy loss due to “noise” but does not offer new insight into bond failure.

4.4 Process Four: Bond Displacements from Motion Estimation

This section will discuss the extraction of 3D displacement fields by motion estimation. 3D displacement fields are found, but given the noise and heavy dependence on image resolution, displacement fields are only generated for specimen P1.

4.4.1 Method

For each load interval, one can track the displacement of various regions of the bond specimen during failure (Figure 4.8) using these steps:

- Use motion estimation to extract displacement field
- Query displacement field in defined regions
- Extract vectors and their relative orientation

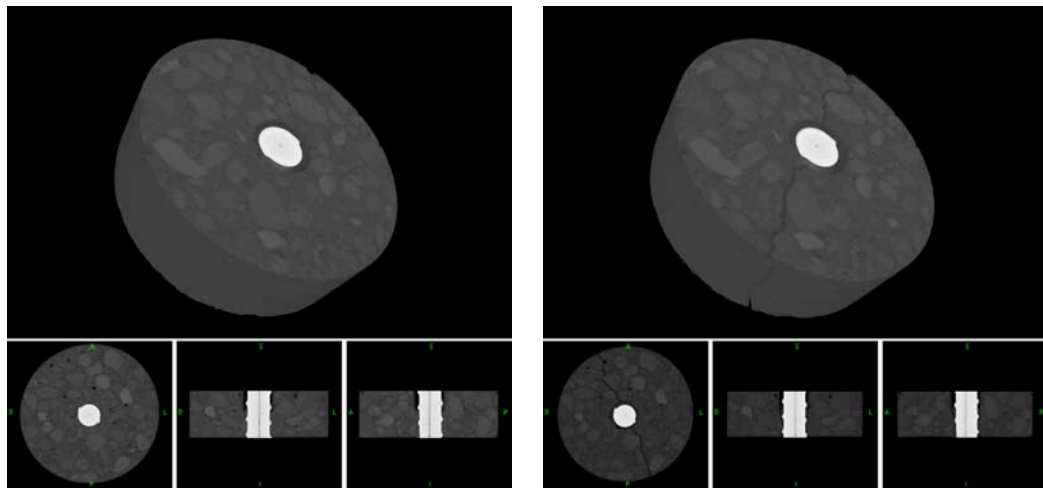


Figure 4.8 - Cracking Image Sequence

Use Motion Estimation to Extract Displacement Field

Using the motion estimation routine (Zhang, 2005), the 3D displacement field in the specimen can be extracted. This routine was run using the Unix emulator, Cygwin. In order to use this routine, the 3D image must be stored as an 8-bit file. By loading 2D images separately into MATLAB, the 3D array can be written to file with the `multibandwrite` command, and the 'bsq' ordering. Code implementation details can be found in Appendix F.

Query Displacement Field in Defined Regions

Using MATLAB, the code output was extracted in to separate x, y, and z vectors (Figure 4.9, 4.10, 4.11). Each of same dimension as the image, it becomes possible to visualize each component separately, calculate magnitudes, and establish trends.

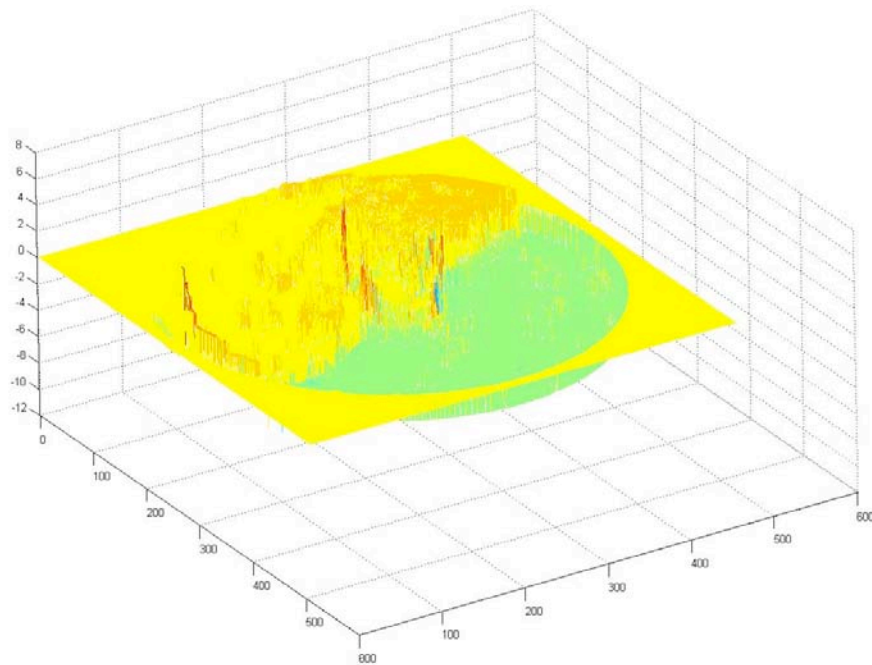


Figure 4.9 – x Displacement Field (xy plane queried @ 0.5” from base)

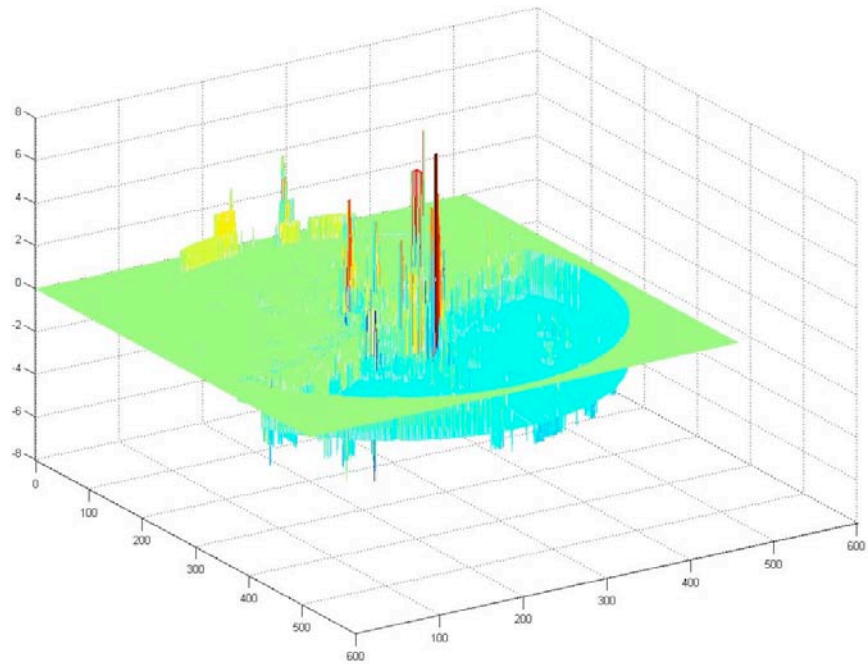


Figure 4.10 - y Displacement Field (xy plane queried @ 0.5" from base)

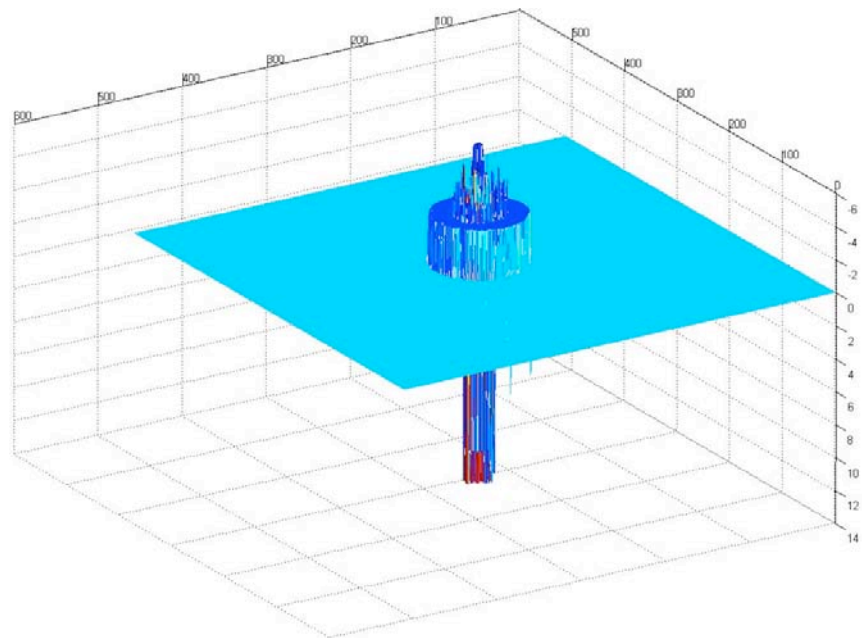


Figure 4.11 - z Displacement Field (xy plane queried @ 0.5" from base)

The x and y displacement fields show the displacement of the concrete. Two concrete pieces and the bar can be identified, but there is a large amount of noise. In the z direction, no displacement of the concrete is detected, but substantial displacements are detected around the steel bar. These displacements around the bar are orders of magnitude larger than the bar displacements collected during the test. This is due to the presence of imaging artifacts in the steel.

Extract Vectors and Their Orientation

Given the shape and loading of the test specimens, it makes sense to extract displacement vectors at specific heights up the cylinder. This is reinforced by the results which show zero displacement in the z direction (upward). By sampling in this manner a smaller set of displacements is obtained, to help quantify observed behavior. For example, Table 4 presents x and y displacements (on voxel scale), at sampled locations (Figure 4.12) in the displacement fields, that helps extract bond information.

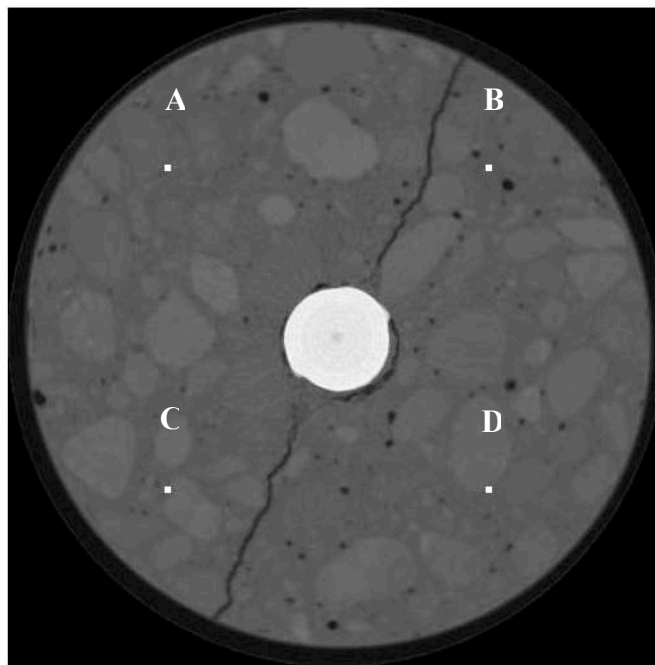


Figure 4.12 – Cracked Specimen, with Sample points

Table 4 - Motion Estimation Sample Points

	X,Y Displacements				
	Location	A	B	C	D
Height (Slice)		125,125	125,375	375,125	375,375
5		0,0	-2,-2	0,0	-1,-1
10		0,0	-2,-2	1,0	-1,-2
15		0,0	-2,-2	1,0	-2,-2
20		0,0	-2,-2	1,0	-2,-2
25		0,0	-2,-2	1,0	-2,-2
30		0,0	-2,-2	0,0	-2,-2
35		0,0	-2,-2	1,0	-2,-2
40		0,0	-2,-2	0,0	-2,-2
45		0,0	-2,-2	0,0	-2,-2
50		0,0	-2,-1	0,0	-1,-1

From this table, Location B and D are consistently moving away from Location A at an orientation of roughly 45° , indicating that they are both on one side of the dominant crack. Visual inspection produces a crack orientation of roughly -30° suggesting movement of the pieces might not always be normal to crack surface (60°). Locations A and C, then, would be on the opposite side of the crack, yet Location C has an x displacement component in the lower slices that A does not have, suggesting remaining strain in the concrete that has not manifested its self into a crack.

4.4.2 Results

This method is highly sensitive to the points chosen to evaluate the displacement field. Given the noise present, this sampling method cannot be used to extract meaningful bond information without further smoothing. Also, the code is written to produce only integer displacements, and thus the accuracy is extremely sensitive to resolution of images. This method does provide full 3D displacement fields, which are useful for visualization. Given these draw back, full 3D displacement fields were only generated for specimen P1, and can be found in Appendix D.

4.4.3 Conclusions

This method of motion extraction is one type of image registration. As this code was written by others for other purposes, a detailed evaluation cannot be carried out here except to say in its current state, it does not produce differentiable displacement fields. The displacement fields it does produce can be useful for visualizing 3D displacements during bond failure, but images with better resolution and further code development are needed.

4.5 Process 5: Bond Displacements from Elastic Registration

This section will discuss how elastic registration can be used to observe displacements due to bond failure. Using elastic registration and the classic FEM mesh, 2D displacement fields can be extracted from two sequential images, and radial displacements examined. This process is particularly appropriate for analyzing pairs of images collected before cracks develop, but can also be used to observe post-cracking behavior. These displacements can be detected on a sub-voxel level, and can show how the concrete is deforming radially before cracks develop or as pieces separate post-cracking. Two objectives of this process are to 1) Early crack detection and 2) strain orientation around the bar.

4.5.1 Method

Ideally 3D images would be registered. However it was found that the 3D problem was too computationally expensive for practical solution in the MATLAB environment. Thus, 2D images from the same “slice” of the specimen were registered. Results of the previous analysis, using motion segmentation described in Section 4.4, show that z direction displacements are negligible with this image resolution. Thus, registration of 2D images could be expected to produce meaningful results. The process used was:

- Run registration routine on select images (heights)
- Observe displacement field, take derivatives to calculate strain

Run registration routine on select images

The differences between the first two images during a bond test are often difficult to detect with the naked eye, as seen in Figure 4.13. The elastic image registration routine is then run as described in Section 3.3.2.

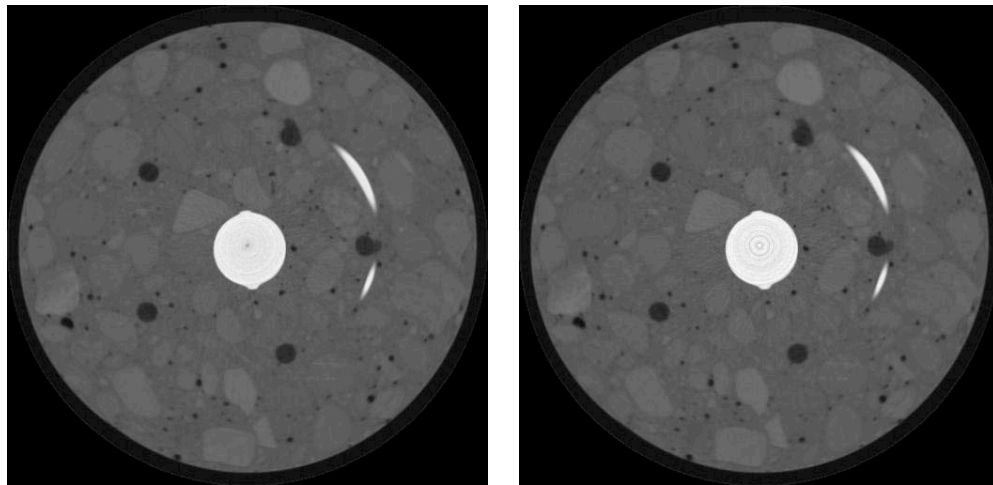


Figure 4.13 – Specimen P3W1A, Image 1 -> Image 2

Observe Displacement Field, Calculate Strains

Un-cracked Images:

The displacements generated are on the scale of $1/100^{\text{th}}$ of an inch, far below the resolution of the image. This means that the registration relies heavily on the interpolation schemes used to determine values between pixels. With a highly heterogeneous material like concrete, this can be the source of the unwanted discontinuities in the displacement fields, like those present in Figure 4.14.

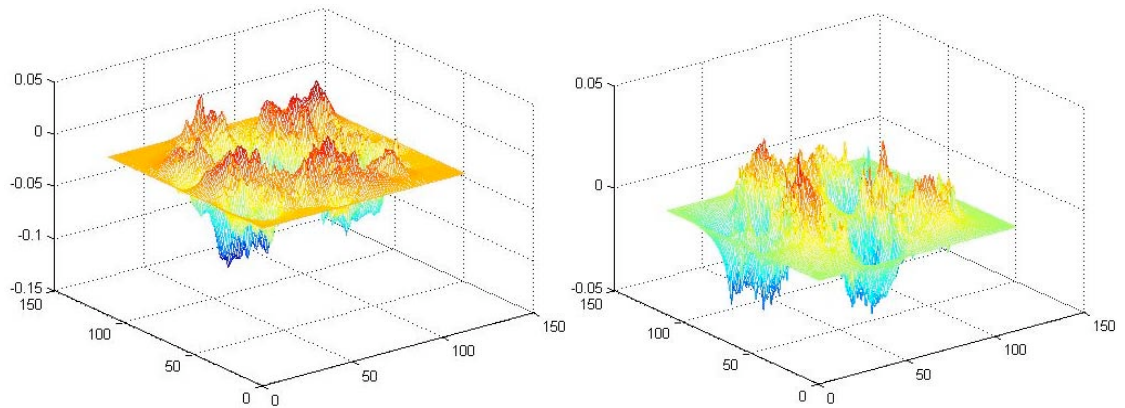


Figure 4.14 – x and y Displacement Fields for P3W1B-1->P3W1B-2

In an attempt observe these displacement fields differently, x and y displacements were converted into radial and tangential displacements; the rotation would show only in the tangential displacements (in units of length), leaving the radial displacements to show structural changes (Figure 4.15).

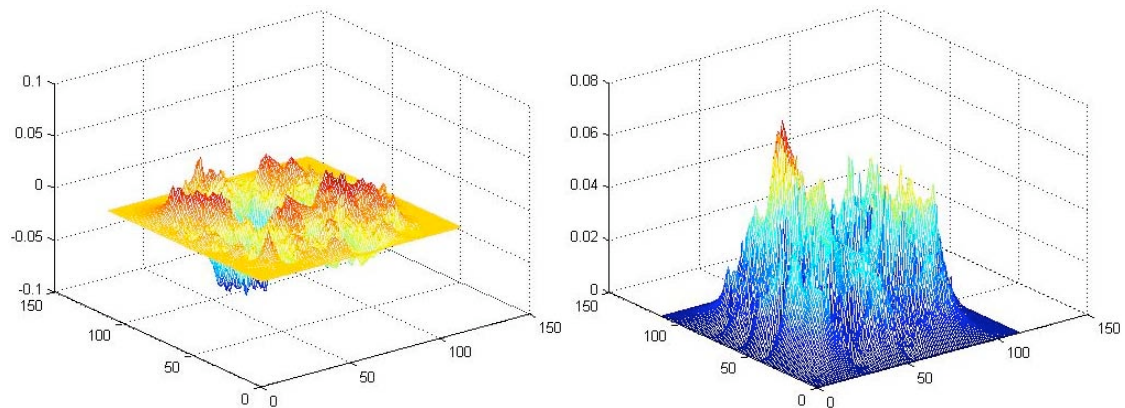


Figure 4.15 – Radial and Tangential Displacement Fields for P3W1B-1->P3W1B-2

All of these displacement plots are highly discontinuous, and show no clear trends. A quick calculation using the analogy of a thick-walled cylinder reveal that radial displacements necessary for the tensile failure of concrete should be an order of magnitude lower than what is currently detectable. This confirms the fact that the majority of displacements are due to noise, although some underlying trends may still be extracted. As a final check of relevance, principal strains are calculated from these displacement fields using traditional finite difference formulation:

$$\begin{aligned}
 \varepsilon_{xx} &= u_x(x+1, y) - u_x(x, y) \\
 \varepsilon_{yy} &= u_y(x, y+1) - u_y(x, y) \\
 \varepsilon_{xy} &= u_x(x, y+1) - u_x(x, y) \\
 \varepsilon_{yx} &= u_y(x+1, y) - u_y(x, y)
 \end{aligned} \tag{4.7}$$

$$\varepsilon_{p1,2} = \frac{\varepsilon_{xx} + \varepsilon_{yy}}{2} \pm \sqrt{\left(\frac{\varepsilon_{xx} - \varepsilon_{yy}}{2}\right)^2 + \varepsilon_{xy}^2}$$

The maximum principal strain field becomes Figure 4.16. While there appears to be some strain concentration around the bar, any other trends such as early strain localization (beginnings of crack), or appearance of grain boundaries are absent.

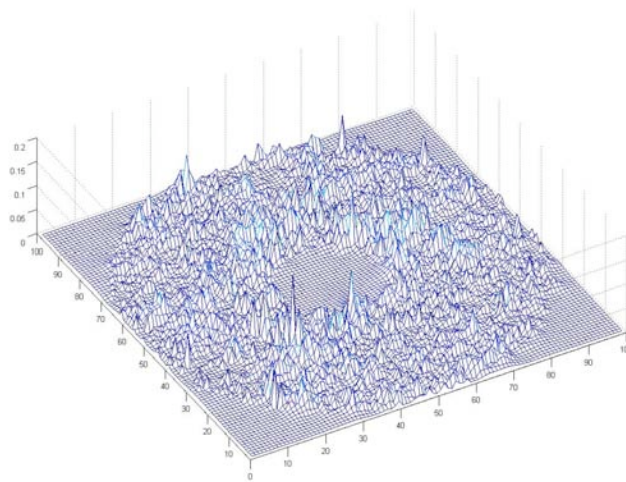


Figure 4.16 – Maximum Principal Strain Field

Cracked Images:

Cracked images, while presenting discontinuities, require a larger displacement field that is better detected by elastic registration. This information can also be useful in observing fracture behavior. For the two images in Figure 4.17, the X and Y displacement fields can be more accurately extracted in Figure 4.18, and closely resemble what the displacement fields should logically look like. The contour plots of these displacements, in Figure 4.19, make it possible to pick out the motion of each piece.

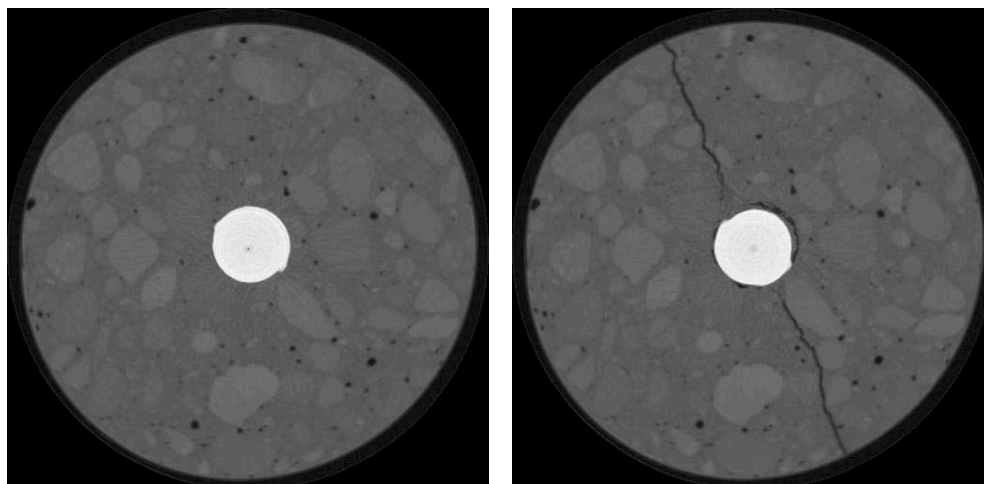


Figure 4.17– P1-2 -> P1-3 Image Sequence

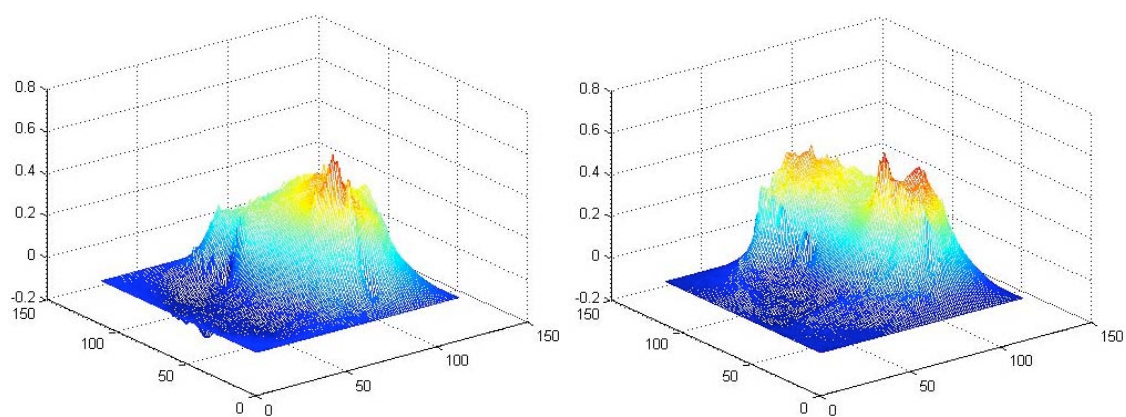


Figure 4.18 – x and y Displacement Fields for P1-2 -> P1-3

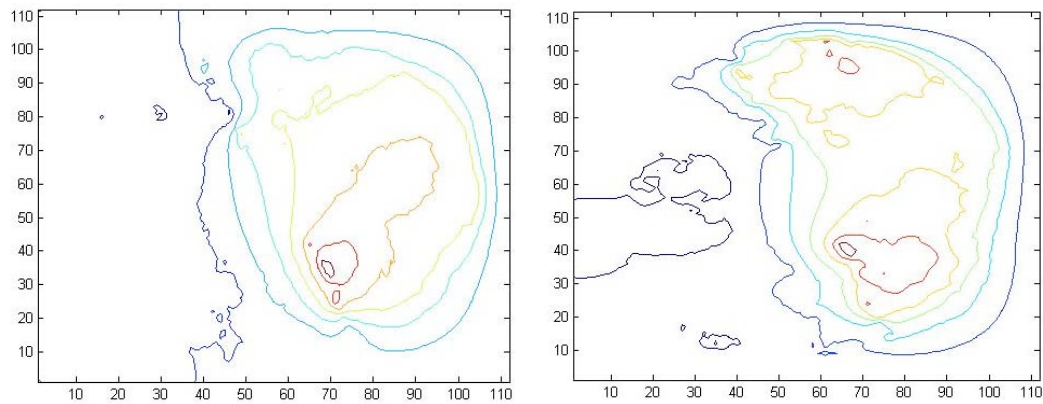


Figure 4.19 – Contour x and y Displacement Fields for P1-2 -> P1-3

A finite-difference, maximum principal strain calculation provides another level of analysis. As you can see in Figure 4.20, the large crack is easily detectable as a series of peaks bisecting the image. However there are also high principal strains around the edges of the image, reflecting the fixed, zero-displacement boundary requirement of this image registration routine.

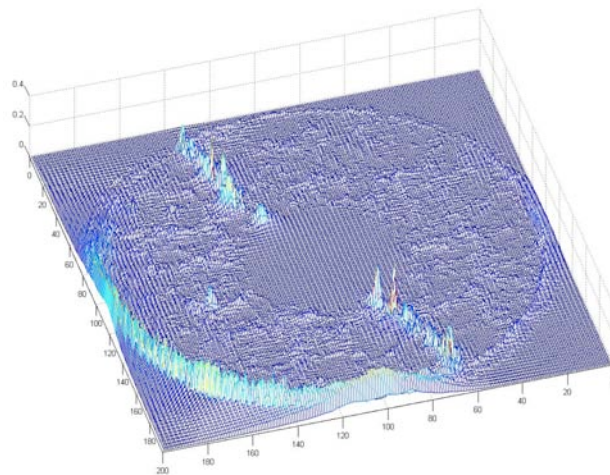


Figure 4.20 – Maximum Principal Strains from x and y Displacement Fields

4.5.2 Results

Early Crack Detection

One of the goals of elastic registration, and our progressive bond tests in general was early detection of cracks. By running image registration on an un-cracked image sequence (e.g. P3W1B-1 to P3W1B -2), then on an un-cracked to cracked image sequence (e.g. P3W1B -2 to P3W1B -3), a direct comparison of the principal strain fields can be made to see if early strains detected before cracking actually manifest to crack surfaces.

For images P3W1B -1 -> P3W1B -2, and P3W1B -2 -> P3W1B -3 the strain field contours are displayed in Figure 4.21.

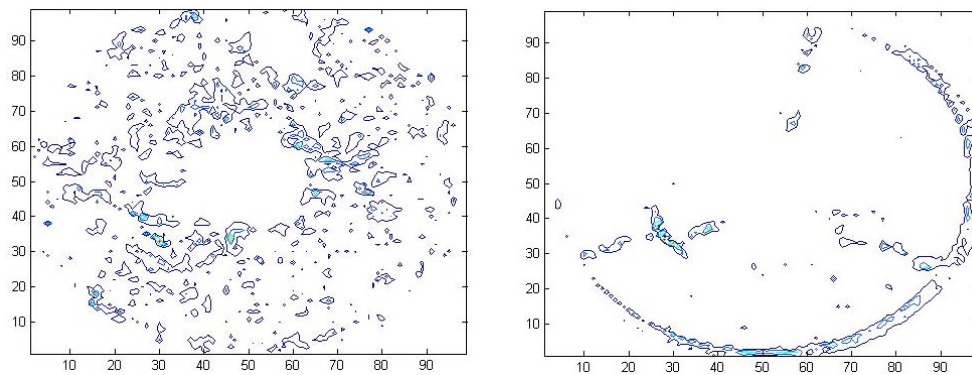


Figure 4.21 – Max. Principal Strain Field Contours (P3W1B-1->2, P3W1B-2->3)

A direct correlation is difficult to establish, and this was the case for all specimens. At the current resolution of the images, elastic registration of the un-cracked images is unfeasible due to the size of expected displacements relative to the size of “noise.” With higher resolutions, where the same magnitude displacements would span, say, 3-4 pixels this technique could be more useful for detecting elastic strain. Without

visible cracks though, it seems unlikely that elastic registration could detect early strain localization.

Strain Orientation around the Bar

The 2D analysis provides strains on a plane, yet bond failure is heavily dependent upon the changing strains in the Z (height) dimension, given the mechanical interaction of lugs with the concrete. Without an ideal 3D registration, multiple 2D registrations were performed with the intent of observing the variation in principal strains. For the uncracked deformations from P3W1B-1 to P3W1B-2, four principal strain fields separated by 1mm vertically are presented in Figure 4.22.

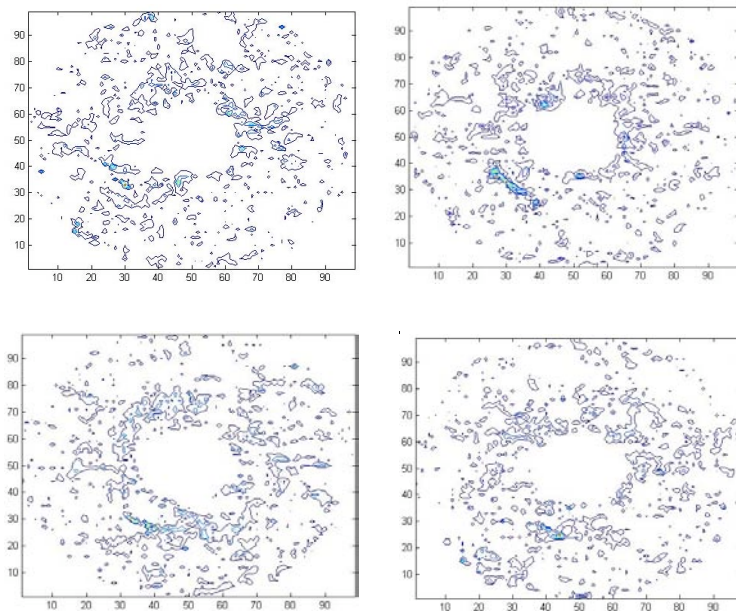


Figure 4.22 – Max. Principal Strain Contours (P3W1B) at 1mm Height Intervals

As mentioned before, these strains are highly discontinuous. While all contour plots reveal strain concentration around the bar, the data is too sparse to offer any new information about longitudinal strain. One might have hoped to see the “ring” of principal strains expand outward as strains are transferred from a lug out to the concrete

at 45-degrees. Elastic registration results for sample 2D slices for all specimens can be found in Appendix E.

4.5.3 Conclusions

A displacement field from bond failure is valuable information, especially if capturing pre-cracking deformations, and defined in 3D. This research provided a 2D displacement field, with difficulty in capturing elastic response. While these results are inadequate for further bond clarification, logical results were received. Refinement of elastic registration through different boundary conditions, higher resolution scans and faster computer routines could provide the accurate 3D displacement field needed to better quantify bond.

4.6 Process 6: Modified Elastic Registration

A modification of the elastic registration routine was used to capture the discontinuities before XFEM was implemented. Working on the premise that cracked surfaces carry very small to zero stiffness, this routine locally modifies the stiffness of individual elements where cracks may be opening up. By relaxing the stiffness, greater displacement gradients are allowed.

4.6.1 Method

In order to implement this modified elastic registration, the traditional registration must be run first. Then principal strains calculated, stiffness' reduced, and then the registration run again with the modified stiffness.

- Run traditional elastic registration, and calculate strains from displacement field
- Modify element stiffness
- Run elastic registration with modified stiffness

Run elastic registration, calculate strains

In a process identical to the previous section, elastic registration is run and principal strains at each point are calculated using central difference method.

Modify element stiffness

With the principal strains at each point, the element stiffness' can be modified. Using a simple equation, where a large principal strain correlates to a small stiffness, the elastic modulus is modified (Equation 4.8).

$$E_{new} = E_{old} \left(\frac{100}{\varepsilon_p + 1} \right) \quad (4.8)$$

Where E_{old} is the old element stiffness, E_{new} is the new element stiffness, and ε_p is the maximum principal strain in that element. After this is computed, the stiffness matrix must be re-assembled.

Run elastic registration with modified stiffness

With the modified stiffness matrix, elastic registration is run again in the same manner as before.

4.6.2 Results

This technique provided an improved displacement field. A comparison of a displacement field from elastic registration (Figure 4.23) and from the modified elastic registration (Figure 4.24) shows the improvement.

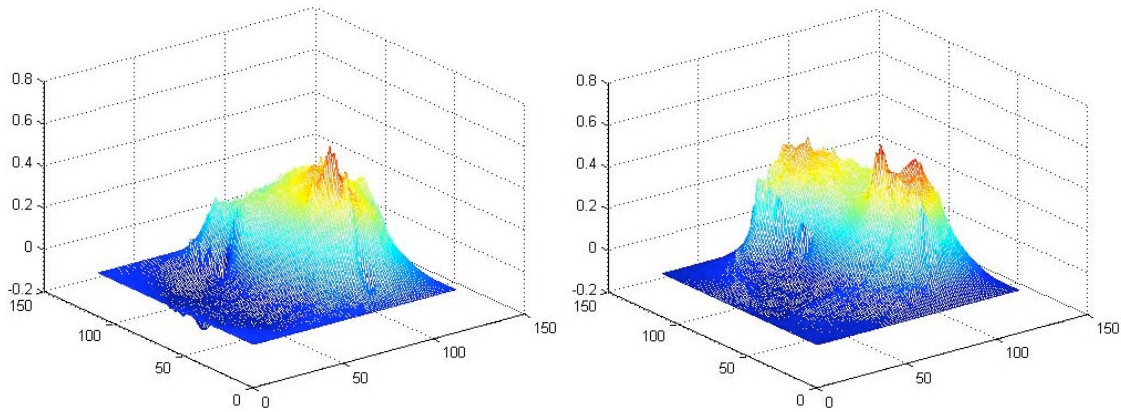


Figure 4.23 – Elastic Registration Displacement Fields for P1-2->P1-3

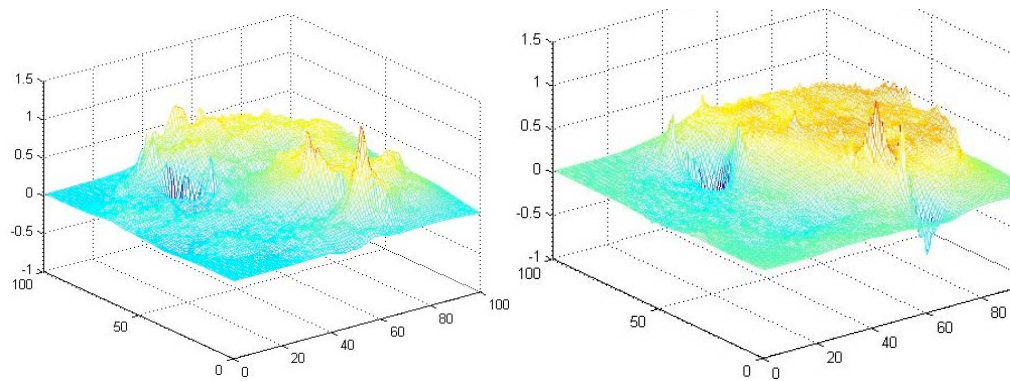


Figure 4.24 – Modified Elastic Registration Displacement Fields for P1-2->P1-3

The modified elastic registration displacement fields show a higher gradient at the crack boundary, and the half-circle displacement is more easily visible. The stiffness' were also relaxed around the specimen edges, allowing for more movement and less effect of the boundary conditions.

4.6.3 Conclusions

There are advantages and disadvantages to using the modified elastic registration routine. The major advantage of this routine is that it doesn't require any human intervention to determine where the cracks are; automatic calculation of principal strains

accomplishes this. Yet the disadvantages are it is computationally expensive, due to the need to re-mesh, and it doesn't truly model the zero-stiffness cracks that are present in the specimen, and thus is limited in its effectiveness.

4.7 Process 7: Displacements as Elastic + Inelastic Deformations

The XFEM image registration has the potential to more accurately model the un-cracked to cracked image sequence than elastic registration alone. This section will present XFEM image registration of bond images with pre-defined crack locations.

XFEM offers greater capability but also adds complexity to the image registration routine. Ideally, image registration would define where the cracks should be, and then solve the system in a way that minimizes the criteria. Given the multiple levels of complexity in this operation, this section will discuss XFEM image registration of bond images with manually defined cracks. This process will act as a precursor to future routines with automatic crack detection.

4.7.1 Method

Since this exercise is primarily intended to validate XFEM with image registration, the implementation only includes crack opening, and no crack tip effects. The procedure was:

- Visually identify crack locations, and define linear crack segments
- Run XFEM image registration and check convergence

Visually Identify Crack Locations

The first step in defining crack locations for XFEM is defining points in the image that when connected by a crack, adequately model the actual crack. For example, in Figure 4.25, the cracking of P1-3 can be reasonably estimated with a single longitudinal crack, ignoring local interaction around the bar.

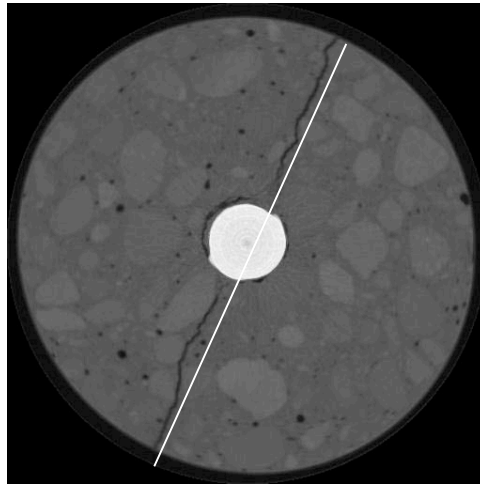


Figure 4.25 – Identify Crack Locations

Run XFEM Image Registration

XFEM analysis was run, and the displacements of the classical degrees of freedom are shown in Figure 4.26.

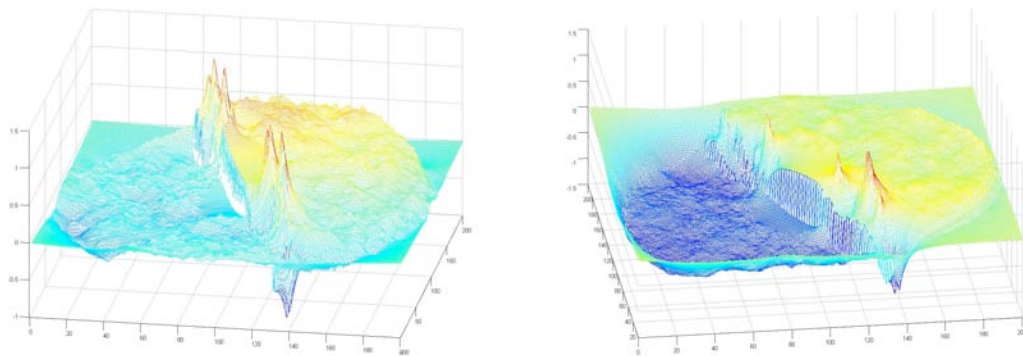


Figure 4.26 – x and y Displacements from XFEM with Linear Crack

This first, simplistic crack approximation does not yield fantastic results, but it is an improvement over elastic registration. The displacement fields capture the displacement trends, with the elastic potential requirement relaxed across the linearly

defined crack. Also, because of this relaxation, the actual crack locations begin to show up as displacement discontinuities. The displacement contour plots in Figure 4.27 show this phenomenon.

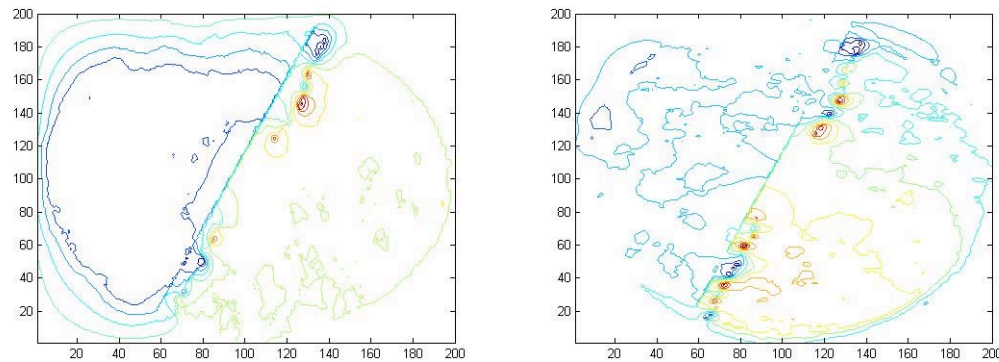


Figure 4.27 – x and y Displacement Field Contours

This first crack approximation reveals the true crack much better than elastic registration. This phenomenon could be used for future image registration routines, by first estimating an initial crack, then observing the displacement field and altering the geometry of the crack for a better fit.

4.7.2 Results

The displacement field received captures the cracking, but is also heavily affected by the boundary condition. The continuous zero-displacement boarder restrains the displacement, and is not an accurate representation of the actual movement of the specimen.

Also, while the movement due to cracking is visible, no other displacements (like material deformations) are reliably extractable. The ratio of noise to actual displacements is too high, and this is primarily due to the coarse resolution of the images. The magnitude of the displacements is calculated on a pixel-length scale and then converted

to units of length. Limitations in computing environment prevented inversion of sufficiently large matrices to produce large enough displacement fields. Along the same lines, to really extract meaningful bond information, 3D displacement data is needed but this wasn't possible due to the additional computational demand.

4.7.3 Conclusions

Elastic registration with an XFEM extension has demonstrated its ability to produce displacement fields with sharp discontinuities. Restrictions of resolution and boundary conditions kept this process from providing meaningful bond information, but this technique can be useful in the future. Greater resolutions, varying boundary conditions and 3D data still offer great potential for increasing in the understanding of bond.

CHAPTER 5 : CONCLUSIONS

5.0 Summary

X ray CT imaging of civil engineering materials is an emerging technique in the field of non-destructive evaluation, and the advantages have not yet fully been explored. With the right combination of imaging variables, X ray CT can provide clear, useful images for the evaluation of interior damage in reinforced concrete. The current energy sources are adequate for imaging up to 6 inches of concrete. Higher resolution scans, longer integration times, and number of views can only increase the accuracy and usefulness of each image.

3D images, as discrete representations of physical bodies can be processed in many different ways. This project discussed several image processing processes within three broad categories: visual inspection, single image processing, and multiple image processing.

5.1 Conclusions

In addition to providing visual pictures, these images contain incredible amounts of spatial and material information. Through image processing, bond has been evaluated using this information in several different ways with varying degrees of success.

5.1.1 *Visual Inspection*

Computers continue to improve, but visual inspection remains the most direct method of information collection and the same is true with X ray CT images. These images show the crushing of concrete around lugs, the split aggregates, and other bond failure characteristics that were previously invisible. These observations give rise to new questions about stress vs. crack width, crack branching, cracks traveling along grain boundaries vs. splitting aggregates, and the effect of low-density intrusions.

5.1.2 Image Threshold and Crack Extraction

By using threshold segmentation, crack surfaces are extracted and quantified by defining surface area and crack volume created. This process was effective for purposes of visualizing the nature of the fracture surface (flat vs. rough), identifying number and orientation of fracture planes, and generating approximate crack widths.

5.1.3 Fracture Analysis

Elements necessary for fracture energy calculations (like surface area created) can be extracted from the bond samples through single-image processing. For bond specimens, this technique showed that simple energy calculations can not adequately quantify failure.

5.1.4 Overall Structural Deformations

Using code written for small mortar samples, extraction of general trends in bond failure (how, where fracture occurred) was possible, but given the noise associated with each displacement field, calculated strains were inadequate.

5.1.5 Displacements as Elastic Deformations

Using elastic image registration, bond failure was modeled as an elastic body deforming. For the images received before fracture, this technique provided interesting displacement fields, but were heavily dominated by noise. For images showing fracture, this process generates a smooth displacement field, but reveals cracking as areas of high maximum principal strain. In general, greater resolutions and 3D analysis are necessary to produce meaningful results.

5.1.6 Modified Elastic Registration

This modification of the elastic registration routine locally altered the stiffness of individual elements according to principal strains. While this routine improved on elastic

registration for crack modeling and provided an automatic crack detection scheme, it is also computationally expensive and doesn't truly model the behavior of zero stiffness cracks.

5.1.7 Displacements as Elastic + Inelastic Deformations

The XFEM technique was used to capture both the elastic and inelastic deformations during bond failure. With a full functioning XFEM routine, the major difficulty is in the identification of cracks in the specimen, and in this project, one technique based on principal strains was unsuccessfully attempted. With manually defined cracks, XFEM image registration can produce improved discontinuous displacement fields over elastic registration, but greater development is needed to get truly useful data.

5.2 Recommendations for Future Research

X ray CT, at this resolution, proved quite effective for visual inspection and crack surface extraction. Further research with the intent of categorizing crack surfaces, imaged by X ray CT is highly recommended. Explicit fracture energy studies, investigation of crack width to stress, and crack path studies are all important areas of fracture mechanics that could be imaged using X ray CT. Further bond investigations must include 3D analysis to capture the necessary interaction. The usefulness of the image data generated in this project has not been exhausted, and it is quite possible that 3D analysis would expand the usefulness of this data.

BIBLIOGRAPHY

Alard, C. (2000) "Image subtraction with non-constant kernel solutions". *Astronomy and Astrophysics Supplement Series* Volume 144, pp.363-370.

Bookstein, F. L. (1989) "Principal Warps: Thin plate splines and the decomposition of deformations". *IEEE Trans. Pattern Analysis Machine Intelligence.*, Volume 11, Issue 6, pp. 567-585.

Broit, C (1981) "Optimal Registration of Deformed Images", Ph. D. thesis, Computer Information and Information Science, University of Pennsylvania.

Pla-Rucki, G. F., Eberhard, M. O. (1995) "Imaging of Reinforced Concrete: State of the Art Review", *Journal of Infrastructure Systems*, Volume 1, Issue 2, June, pp. 134-141.

Freeborough, P. A., Fox, N. C., (1998) "Modeling Brain Deformations in Alzheimer Disease by Fluid Registration of Serial 3D MR Images". *Journal of Computer Assisted Tomography*. Volume 22(5), September/October, pp 838-843.

Ketcham, R.A. and Carlson, W.D.,(2001). "Acquisition, optimization and interpretation of X-ray computed tomographic imagery: Applications to the geosciences". *Computers and Geosciences*, Volume 27, pp. 381-400.

Landis, E, Nagy, E, Keane, D (2003) "Microstructure and Fracture in three dimensions", *Engineering Fracture Mechanics*, Volume 70, pp 911-925.

Lawler, J. S., Keane, D. T., Shah, S. P., (2001) "Measuring Three-Dimensional Damage in Concrete under Compression", *Materials Journal of the American Concrete Institute*. Volume 98, Issue 6, pp. 465-475.

Maintz, J. B. A. and Viergever, M. A. (1998). "A survey of medical image registration", *Medical Image Analysis*, Volume 2, Issue 1, pp. 1-36.

Martin, J. (2006) “An Experimental Investigation of Bond in Reinforced Concrete”, Masters Thesis, Department of Civil and Environmental Engineering, University of Washington, Seattle

Martz, H. E., Scheberk, D. J., Roberson, G. P., Monteiro, P.J.M., (1993) “Computerized Tomography Analysis of Reinforced Concrete”, *Materials Journal of the American Concrete Institute*. Volume 90, Issue 3, pp. 259-264.

Maurer, C.R., Fitzpatrick, J.M., (1993), “A review of medical image registration, Interactive Image-Guided Neurosurgery”, American Association of Neurological Surgeons, pp. 17-44.

Modersitzki, Jan (2004) “Numerical Methods for Image Registration”, Oxford University Press.

Modersitzki, J , Haber, E. (2004) “Intensity gradient based registration and fusion of multi-modal images”. *Technical Report TR-2004-027-A*, Department of Mathematics and Computer Science, Emory University, Atlanta GA 30322, Jun 2004.

Monteiro, P.J.M., Pichot, C.Y., and Belkebir, K., (1998) “Computer Tomography of Reinforced Concrete”, Chapter 12, *Materials Science of Concrete, American Ceramics Society*.

Morgan, I.L., Ellinger, H., Klinksiek, R., Thompson, J. N.,(1980) “Examination of Concrete by Computerized Tomography”, *Journal of the American Concrete Institute*. Volume 77, Issue 1, pp. 23-27.

Sawhney, H and Kumar, R (1997) “True Multi-Image Alignment and its Application to Mosaicing and Lens Distortion Correction”, 1997 IEEE *Computer Society Conference on Computer Vision and Pattern Recognition*, vol. 00, pp. 450.

Szeliski, Richard (2005) “Image Alignment and Stitching : A Tutorial”, Microsoft Research, Microsoft Corporation, pp 1-77.

Thirion, J. P.(1998) “Image matching as a diffusion process: An analogy with Maxwell’s demons,” *Medical Image Analysis*, vol. 2, no. 3, pp. 243–260.

Vigneron, L. M., Verly, J. G., Warfield, S. K.,(2004) “Modelling Surgical Cuts, Retractions, and Resections via Extended Finite Element Method”, *Lecture Notes in Computer Science, Medical Image Computing and Computer-Assisted Intervention*, 7th International conference proceedings, September 26-29, 2004, Part II.

Viola, P.A., (1995) “Alignment by Maximum of Mutual Information”, Ph. D. thesis, Massachusetts Institute of Technology .

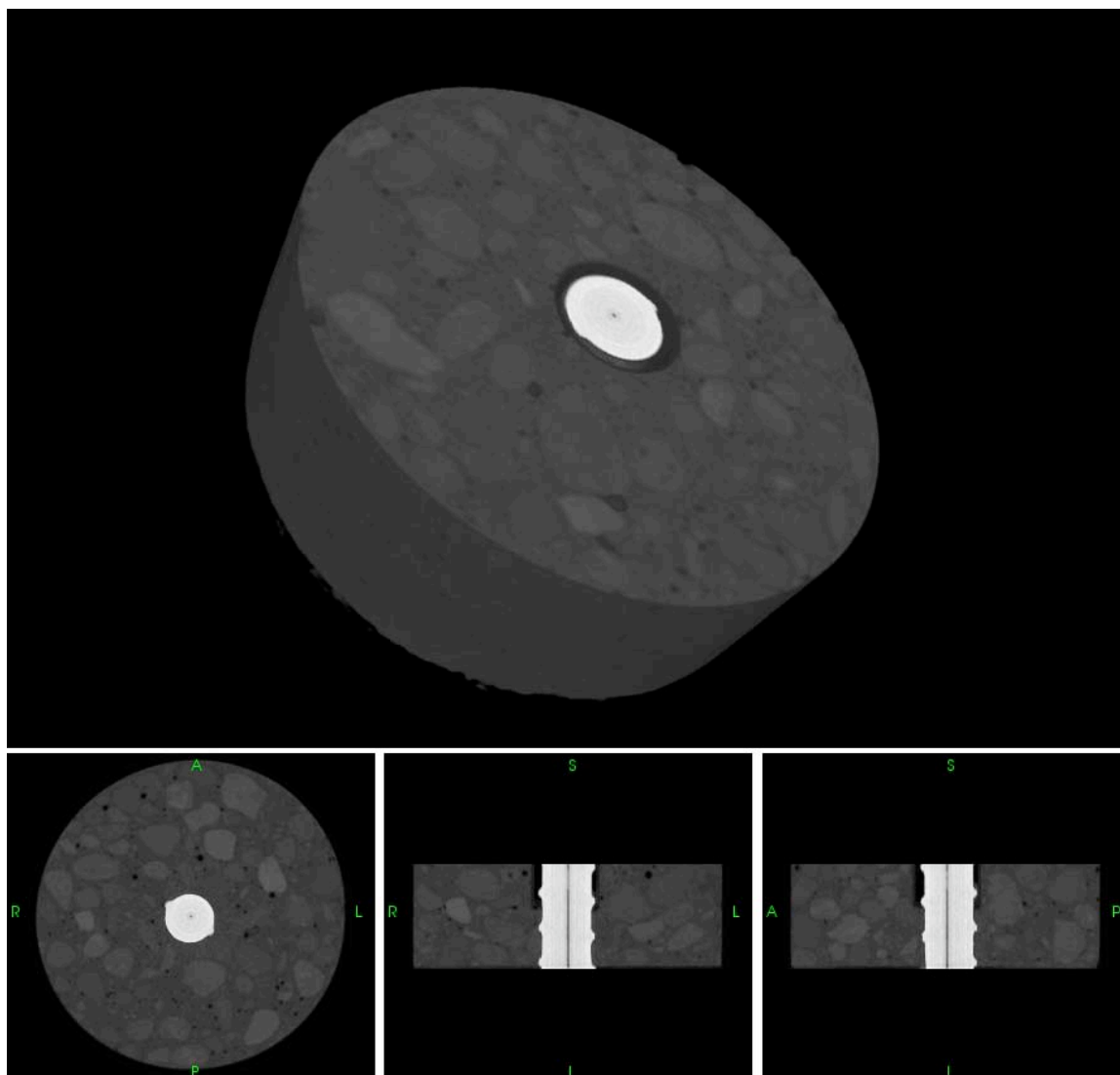
Zhang, Z, (1994) “Iterative point matching for registration of free-form curves and surfaces”, *International Journal of Computer Vision*, Volume 13, Issue 2 (October 1994), pp. 119 – 152.

Zhang, T, (2004) “Identification of Structural Changes from Volumetric Image Sequence”, Ph.D. thesis, Rensselaer Polytechnic Institute.

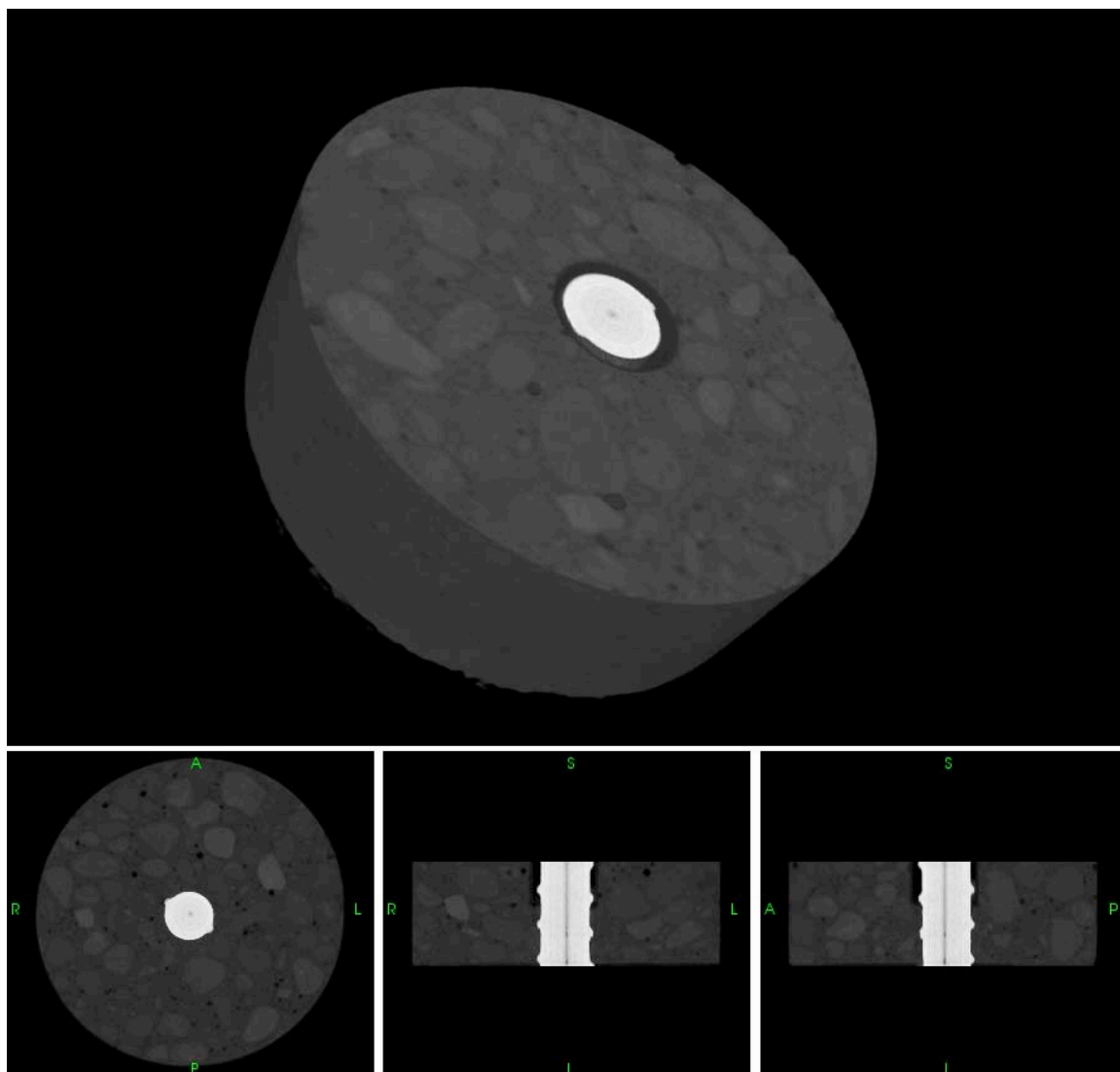
APPENDIX A: SPECIMEN 3D RECONSTRUCTIONS

Appendix A contains 3D reconstructions of all sequential data collected during this project. The images, as a collection of 2D, 16-bit TIFF files, were loaded in to the free software “Volview 2.0 – Volume Visualization” by Kitware. This software takes into account scaling factors and averages between the 2D images to render a 3D volume. For these images a linear averaging was used.

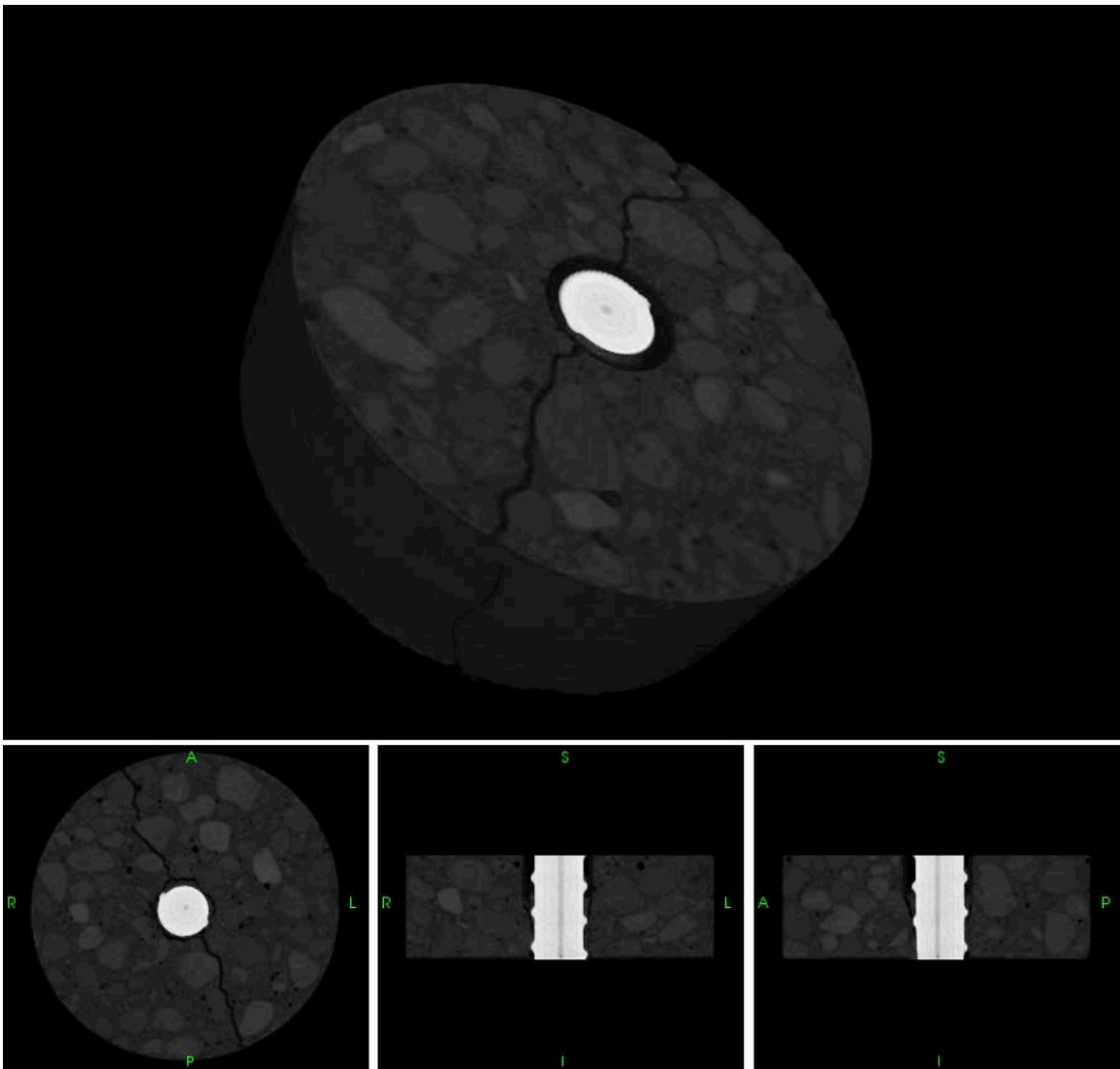
For the cracked specimens (images 3, 4 & 5), visual inspection data collected from each 2D slice is presented below the reconstruction.

P1 – 1

P1 – 2

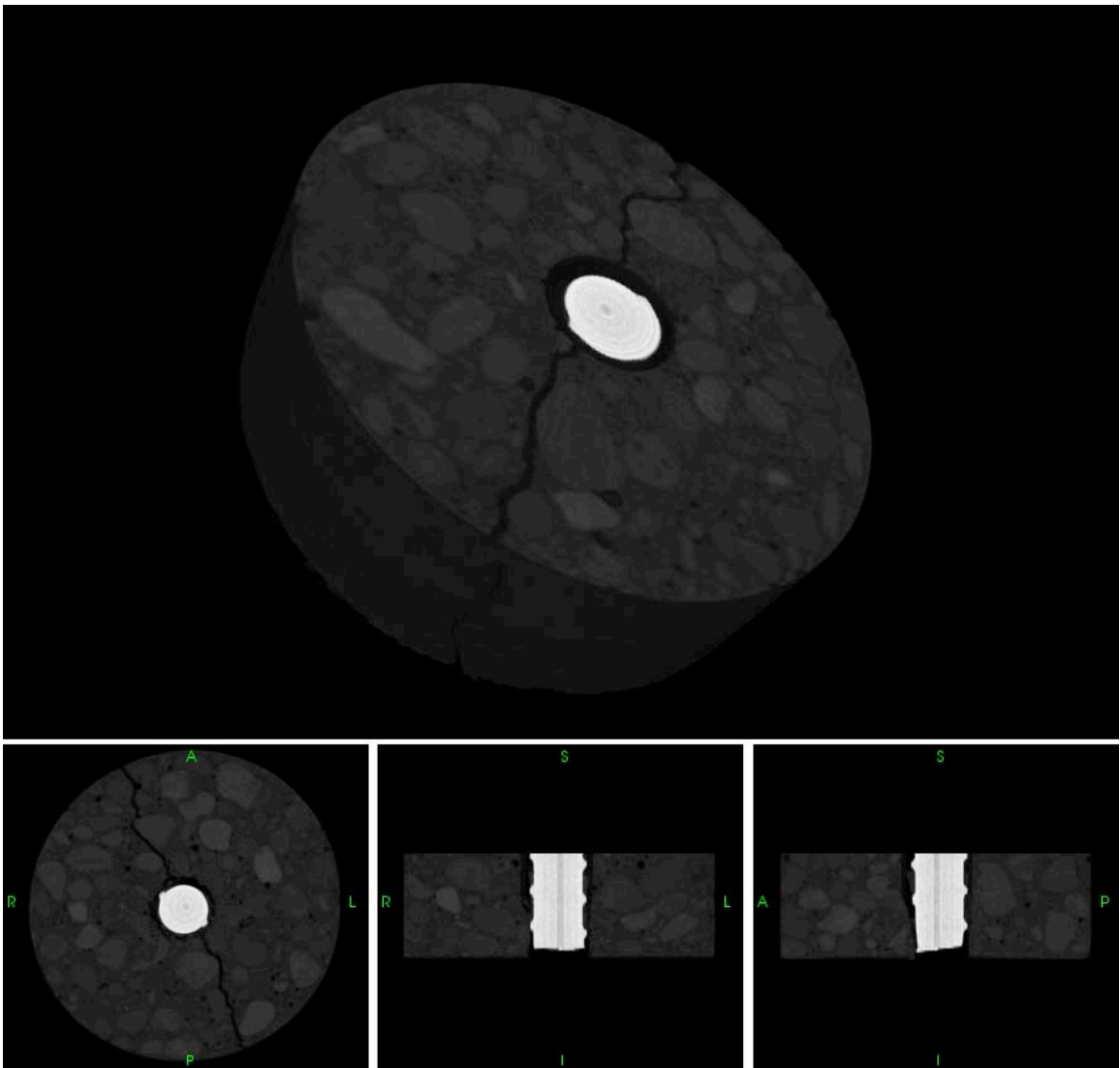


P1 – 3

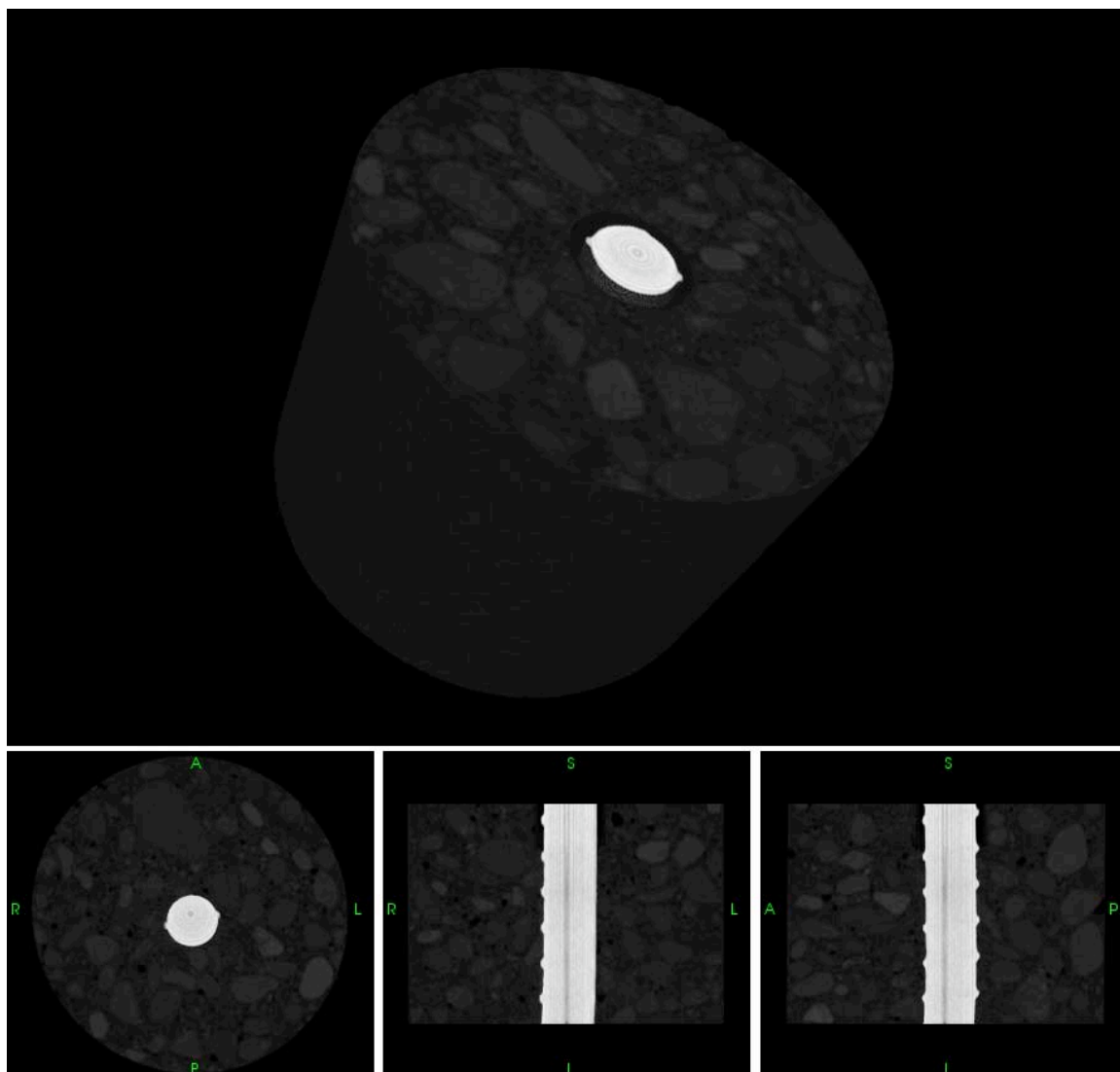


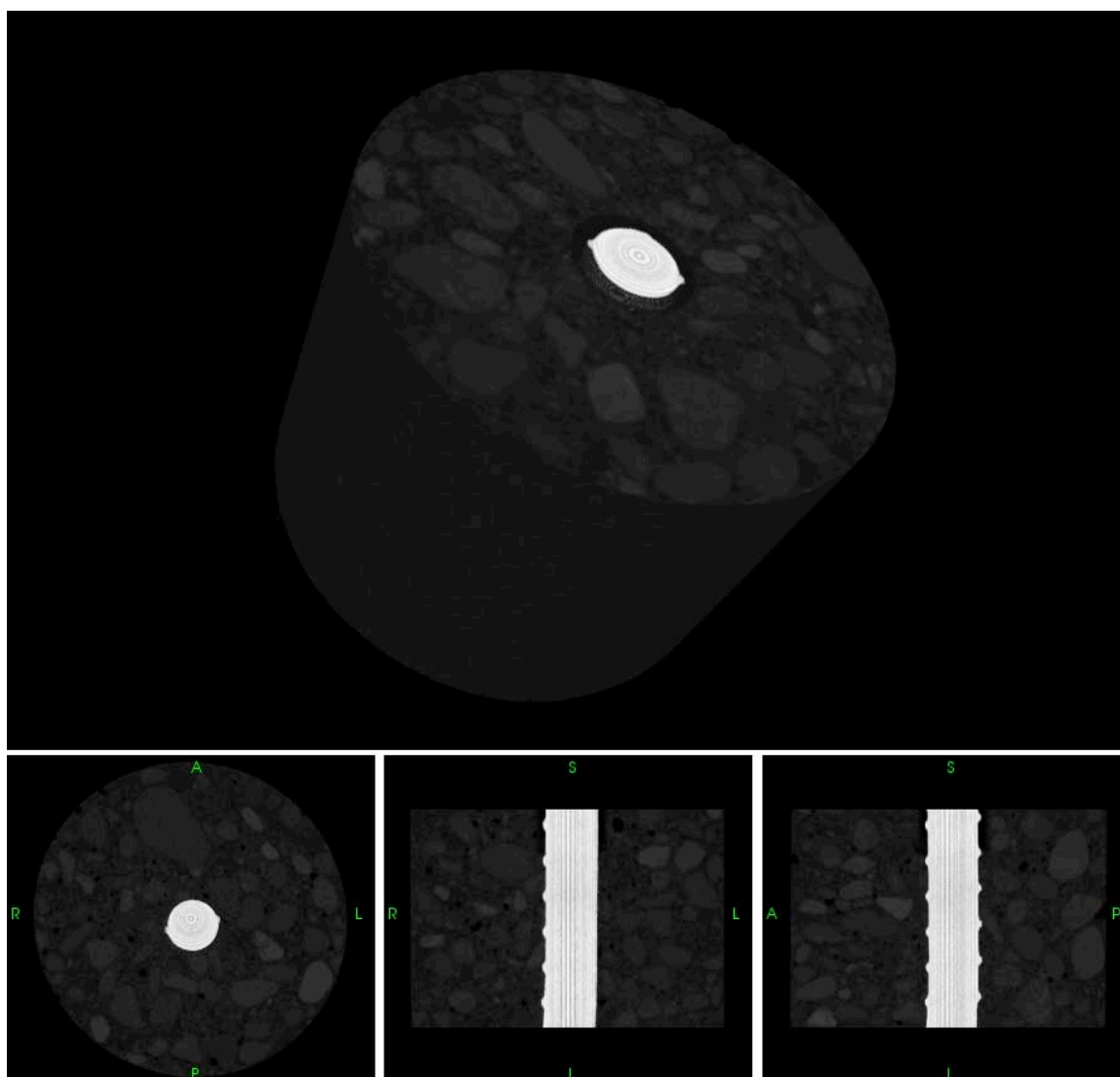
P1-3						
	Dominant Cracks	Orientation of Dominant Cracks	Number of Aggregates Split	Visual Crack Width	Significant Crack Branching	Significant Lug Crushing Around Bar
	1	0	0	Medium	No	Yes
	2	180	0	Medium	No	

P1 – 4

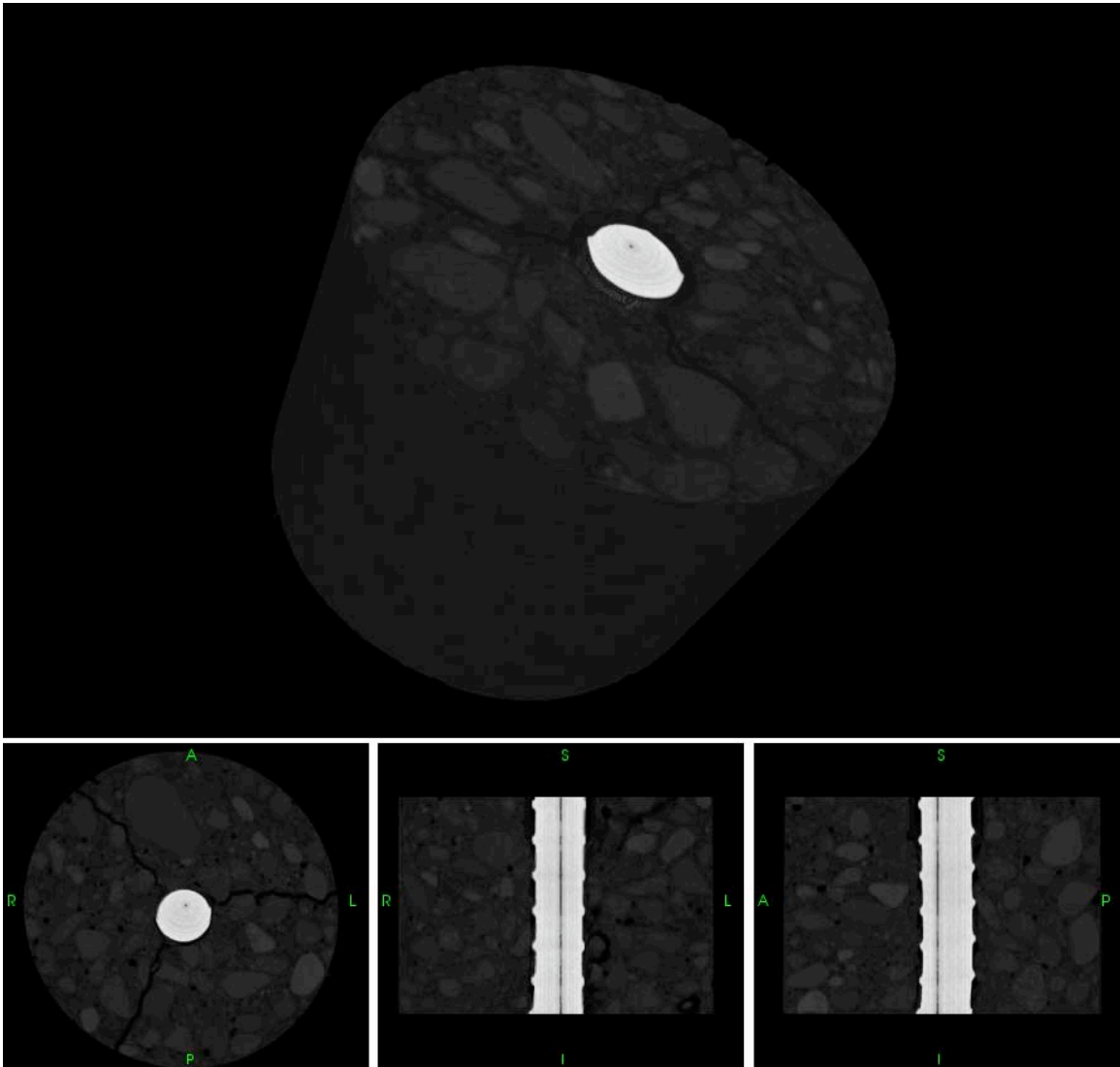


P1-4						
	Dominant Cracks	Orientation of Dominant Cracks	Number of Aggregates Split	Visual Crack Width	Significant Crack Branching	Significant Lug Crushing Around Bar
	1	0	0	Medium Wide	No	Yes
	2	180	0	Medium Wide	No	

P3F – 1

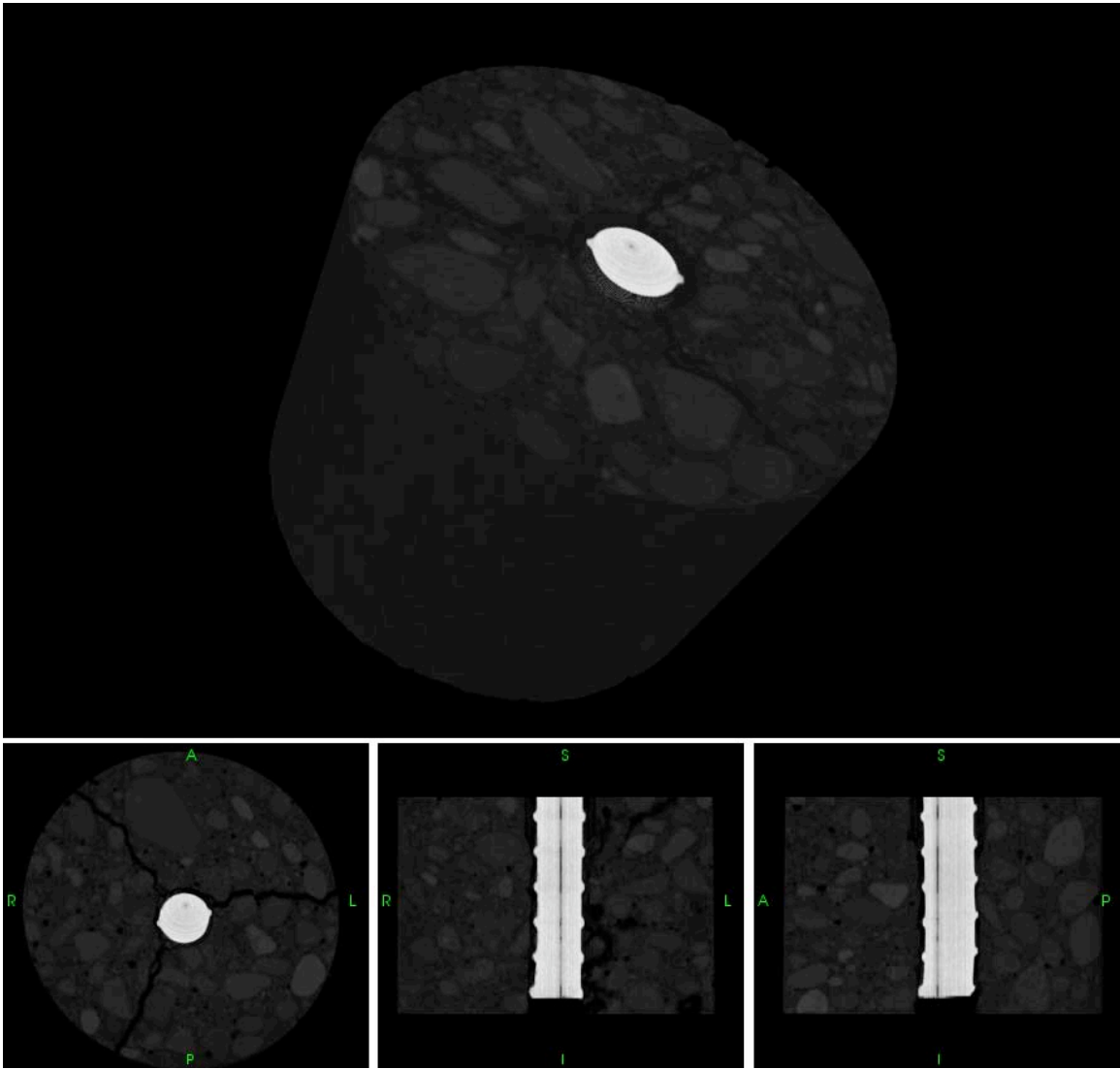
P3F – 2

P3F – 3



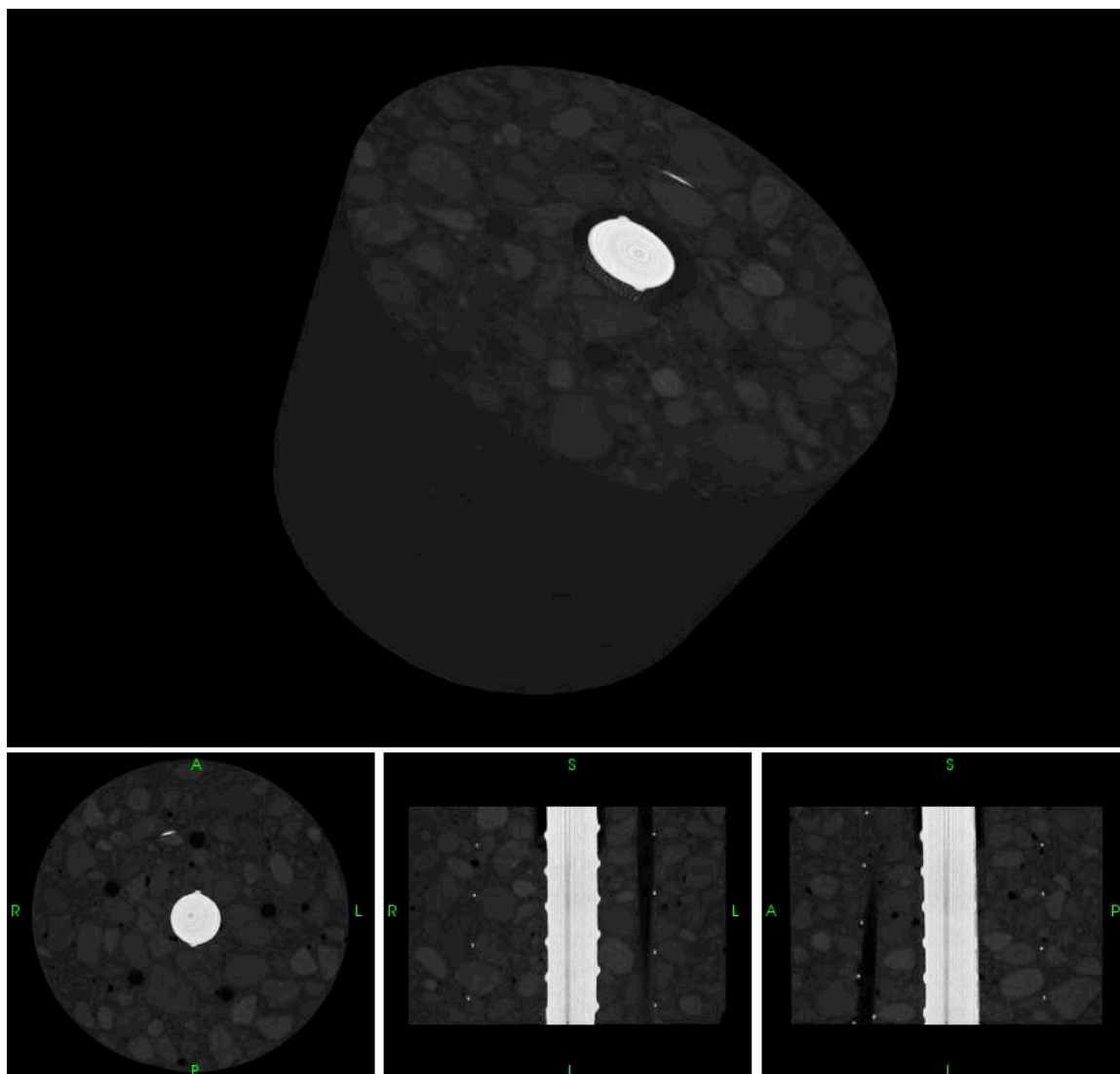
P3F-3						
	Dominant Cracks	Orientation of Dominant Cracks	Number of Aggregates Split	Visual Crack Width	Significant Crack Branching	Significant Lug Crushing Around Bar
	1	0	3	Wide	No	Yes
	2	130	2	Wide	No	
	3	230	1	Wide	No	

P3F-4

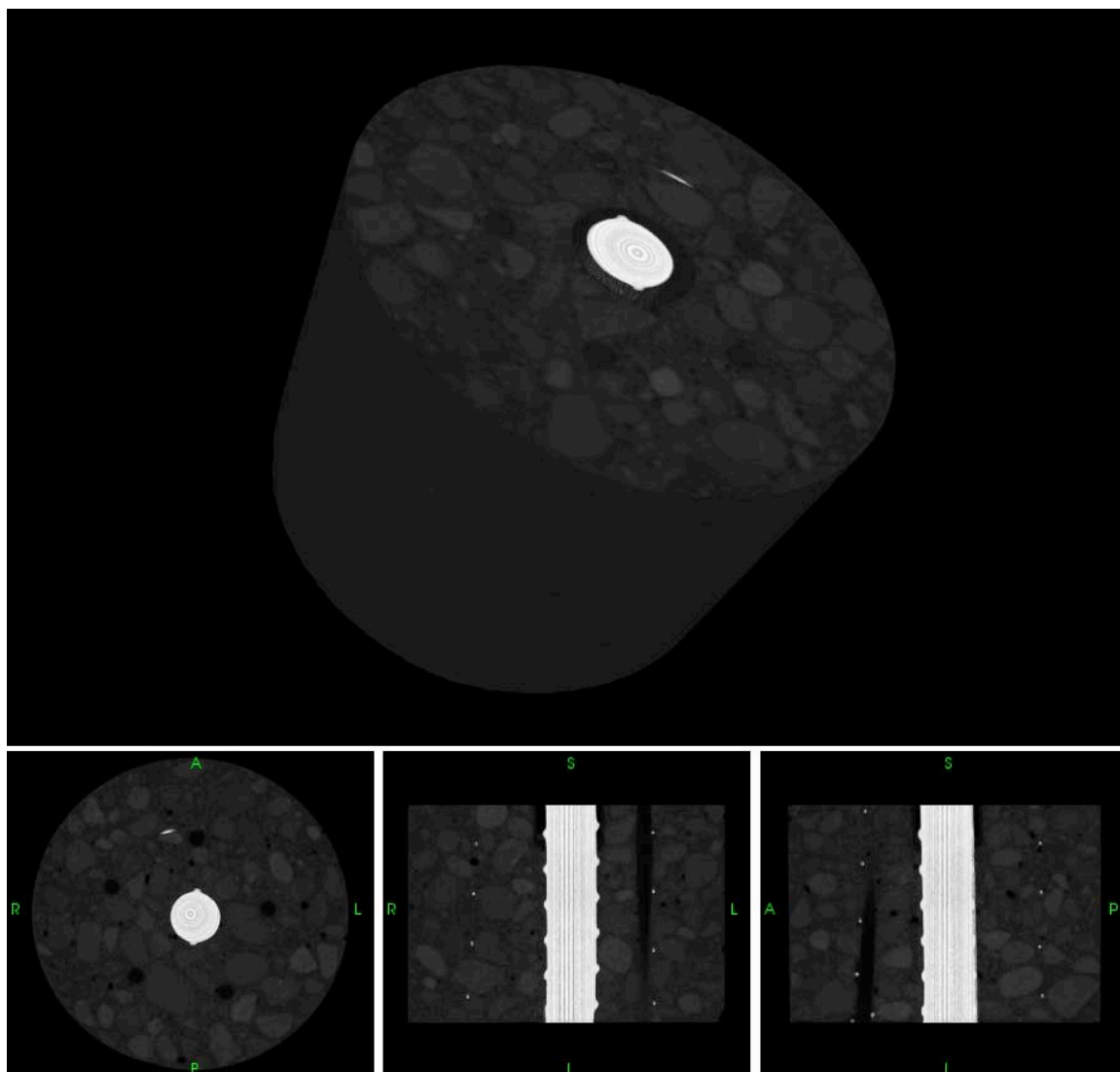


P3F-4						
	Dominant Cracks	Orientation of Dominant Cracks	Number of Aggregates Split	Visual Crack Width	Significant Crack Branching	Significant Lug Crushing Around Bar
	1	0	3	Very Wide	No	Yes
	2	130	2	Very Wide	No	
	3	230	1	Very Wide	No	

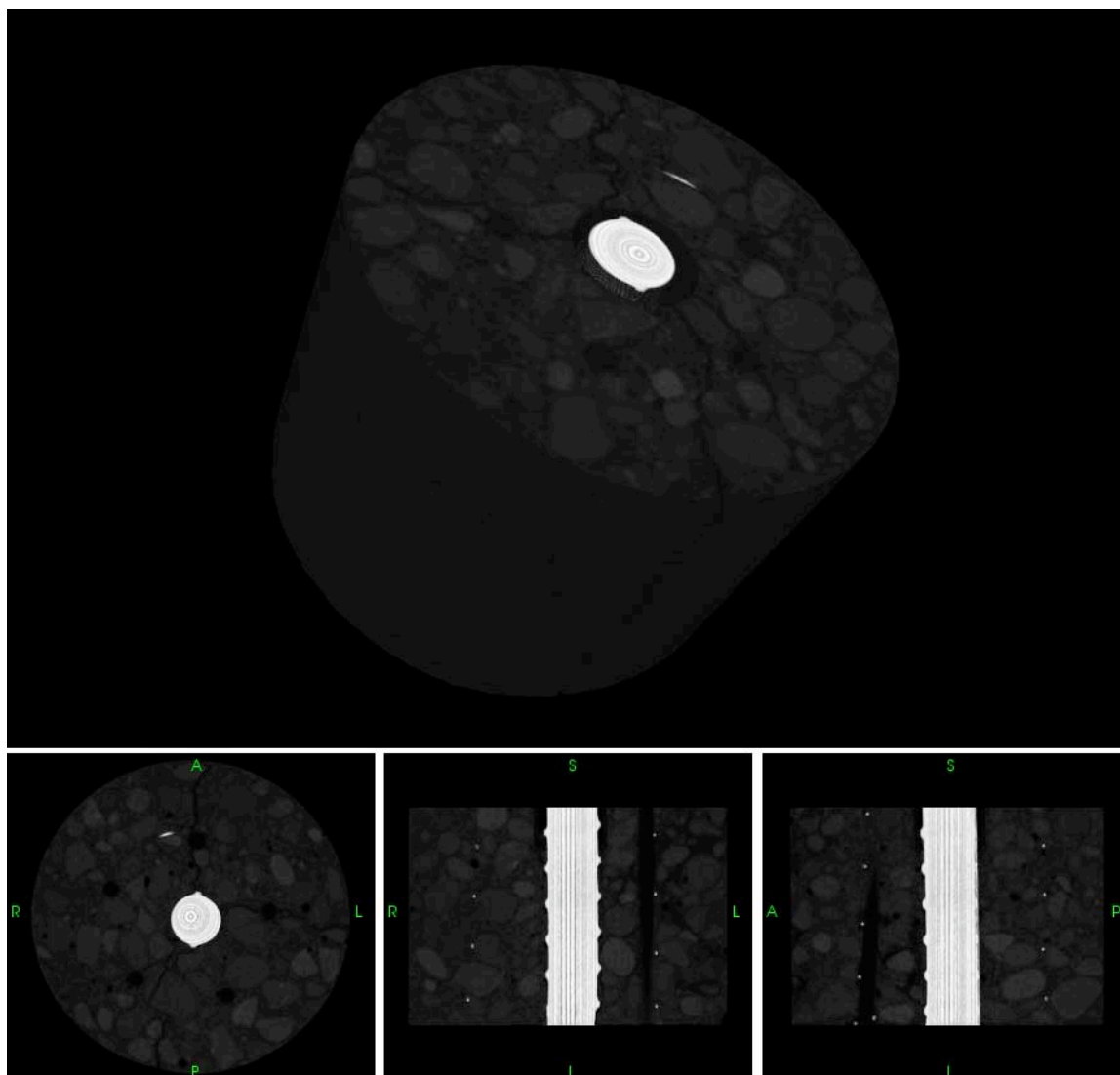
P3W1A-1



P3W1A-2

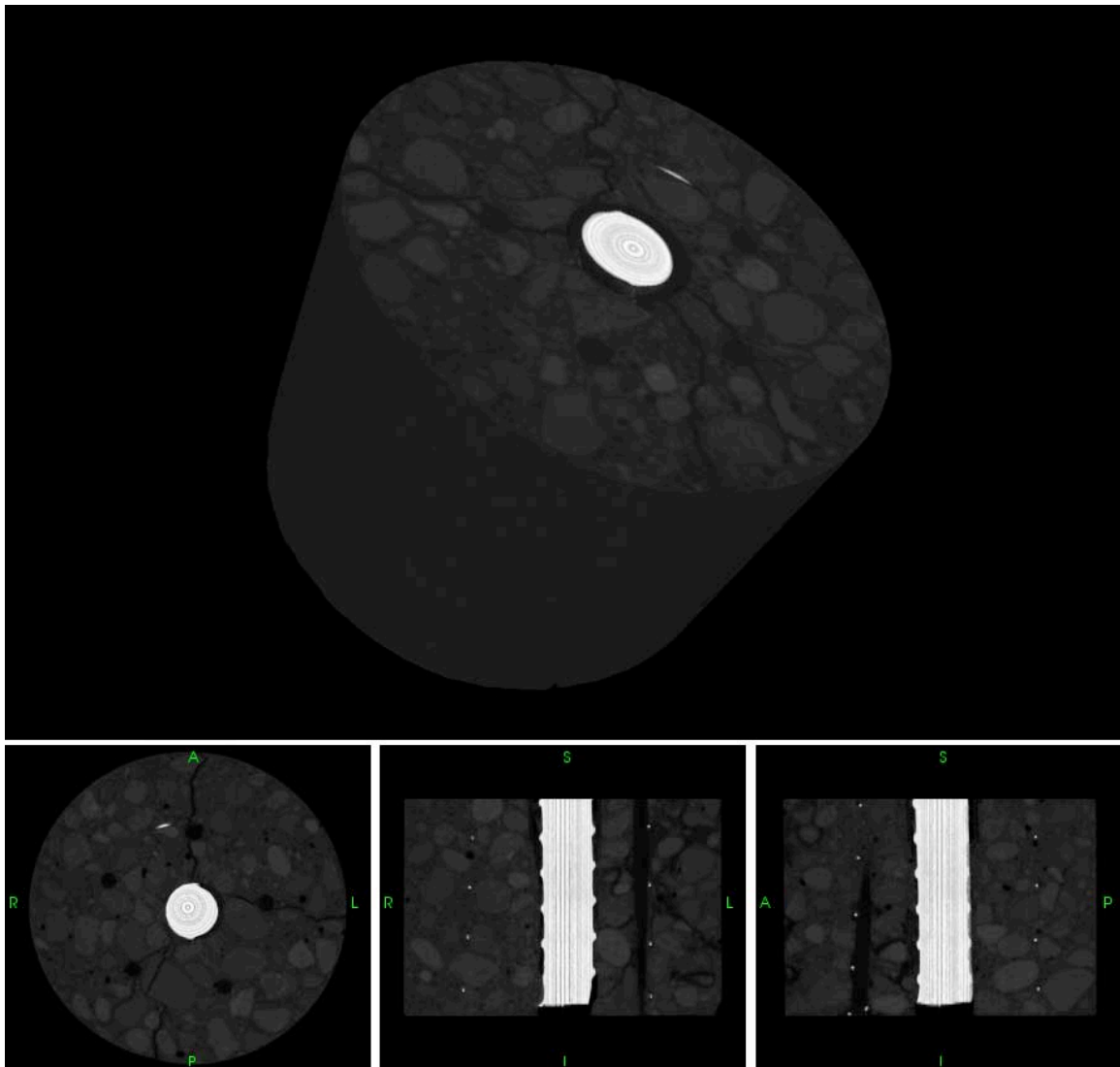


P3W1A-3



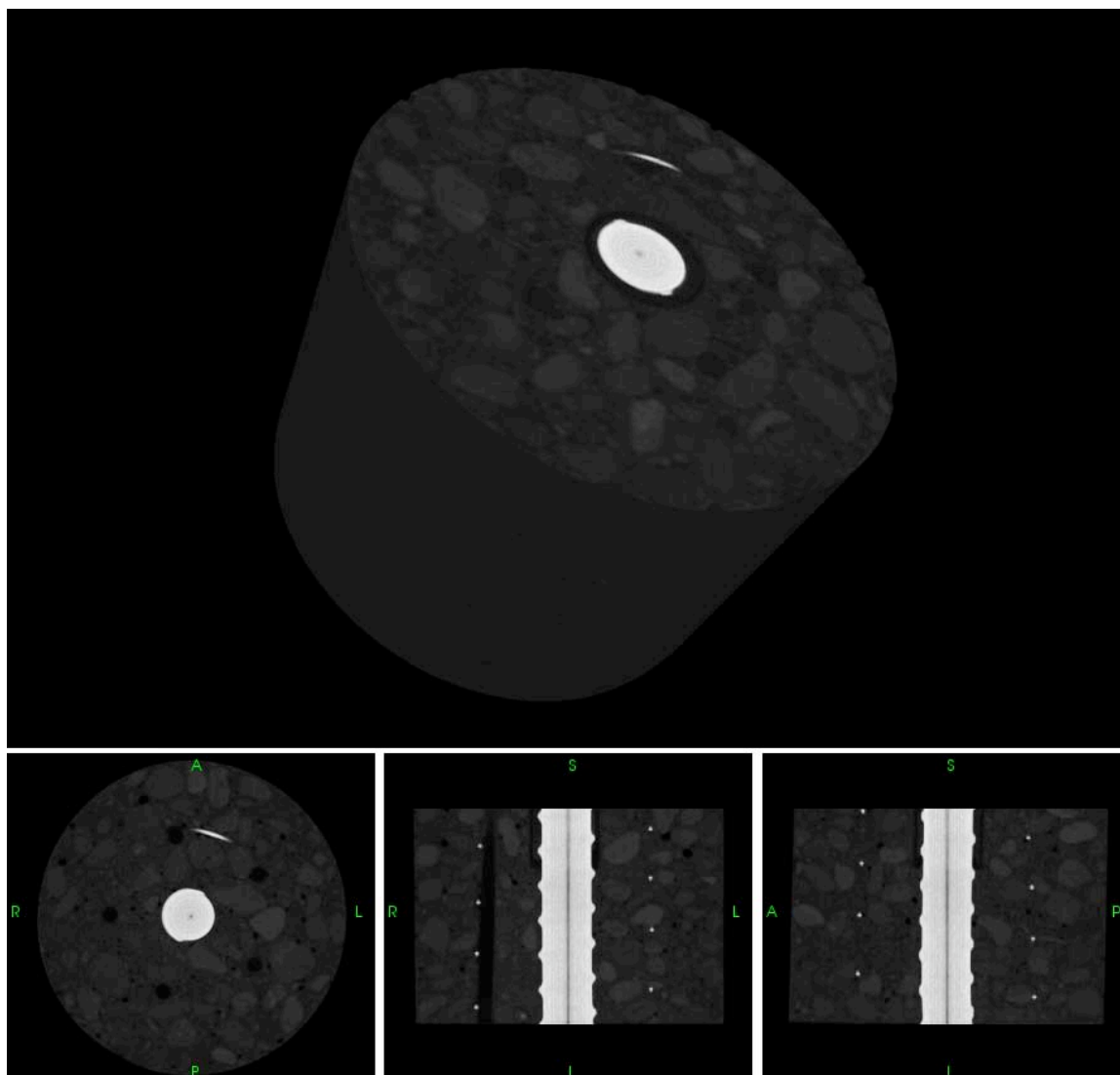
P3W1A-3							
	Dominant Cracks	Orientation of Dominant Cracks	Number of Aggregate Split	Visual Crack Width	Significant Crack Branching	Connect through Dowel ?	Significant Lug Crushing Around Bar
	1	0	0	Fine	Yes	Yes	None
	2	90	0	Med.	Some	Yes	
	3	180	1	Fine	Some	No	

P3W1A-4

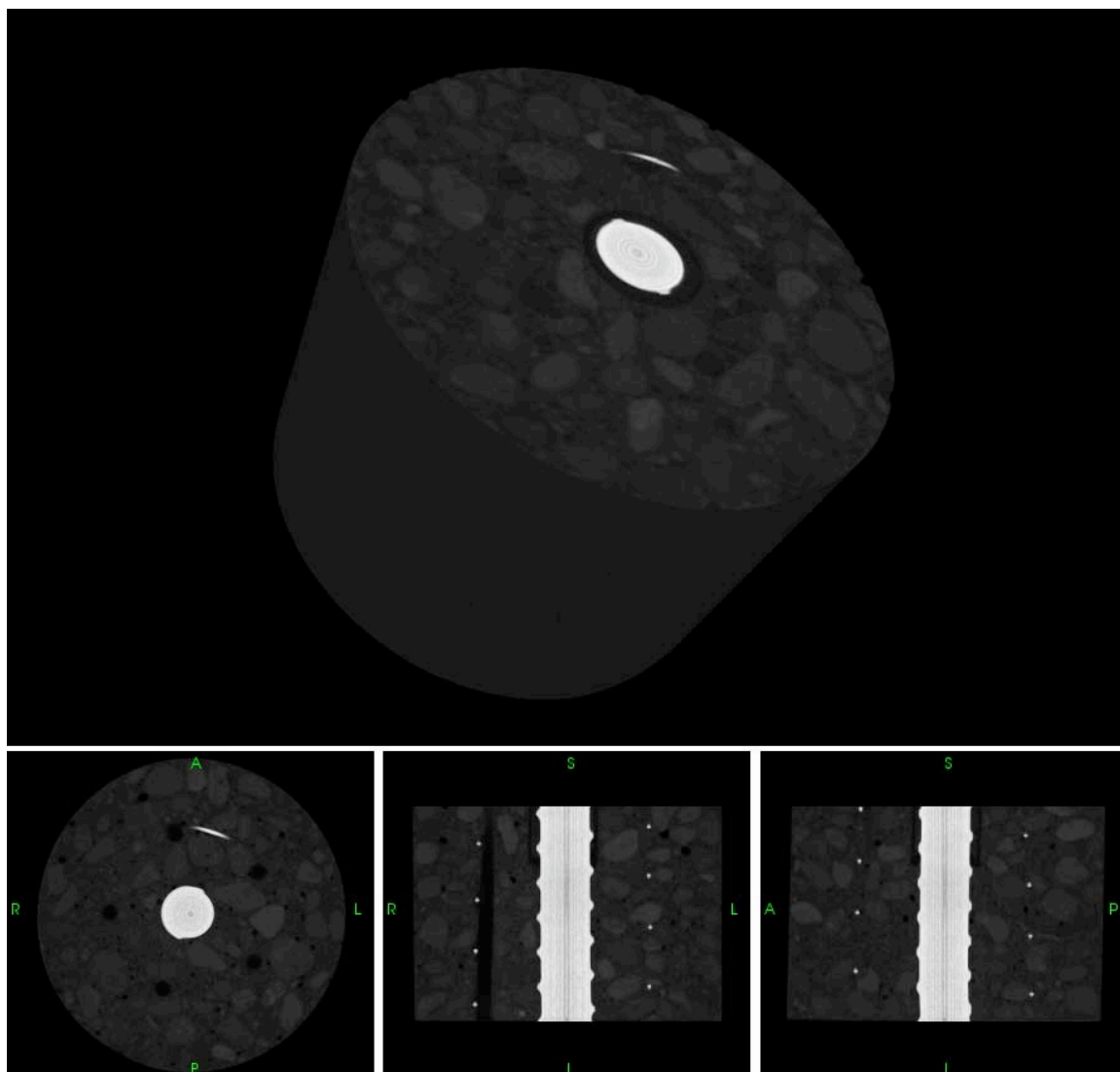


P3W1A-4							
	Dominant Cracks	Orientation of Dominant Cracks	Number of Aggregates Split	Visual Crack Width	Significant Crack Branching	Connect through Dowel ?	Significant Lug Crushing Around Bar
	1	0	0	Medium	Yes	Yes	None
	2	90	0	Medium	Some	Yes	
	3	180	1	Fine	Yes	No	

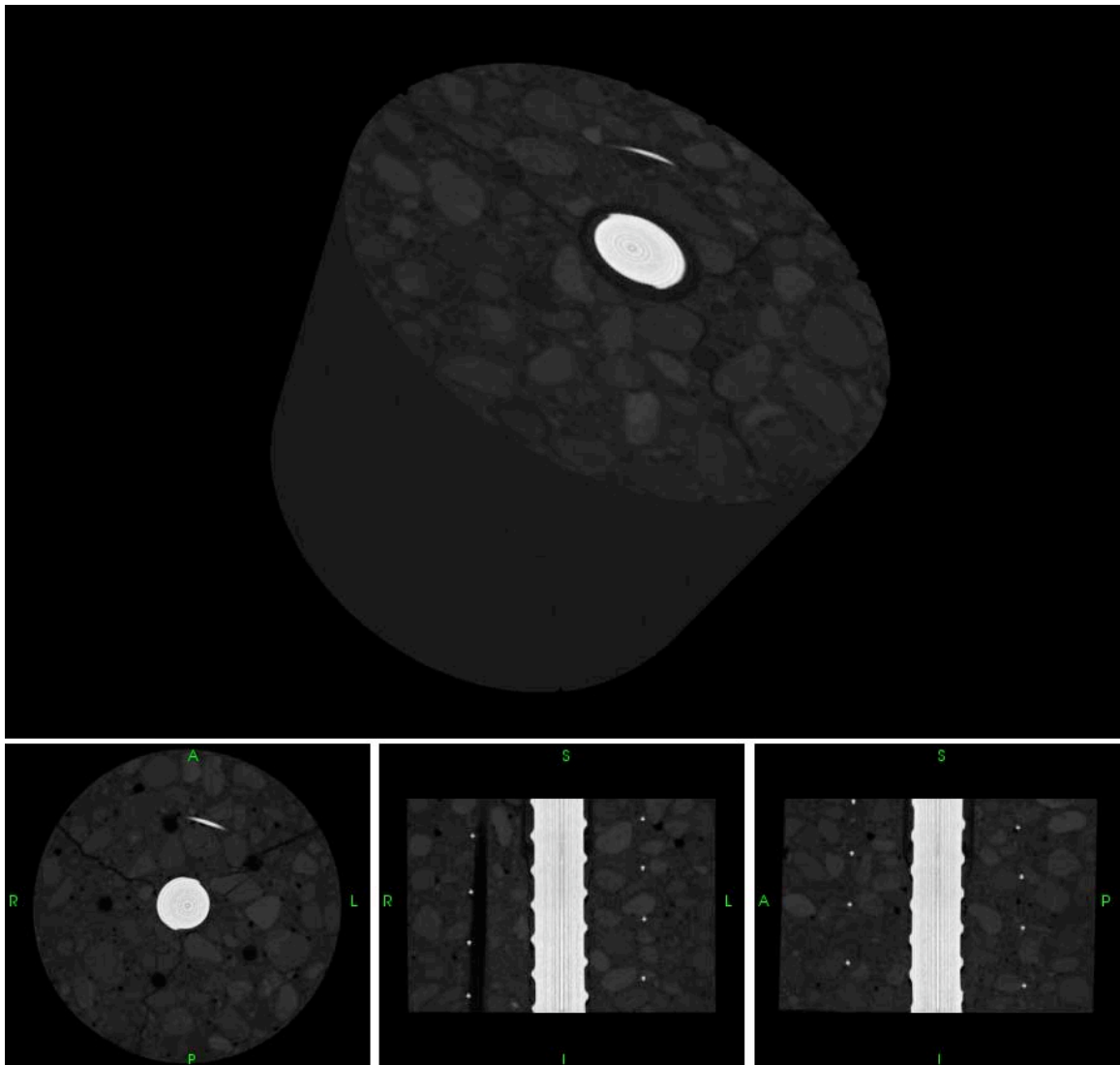
P3W1B-1



P3W1B-2

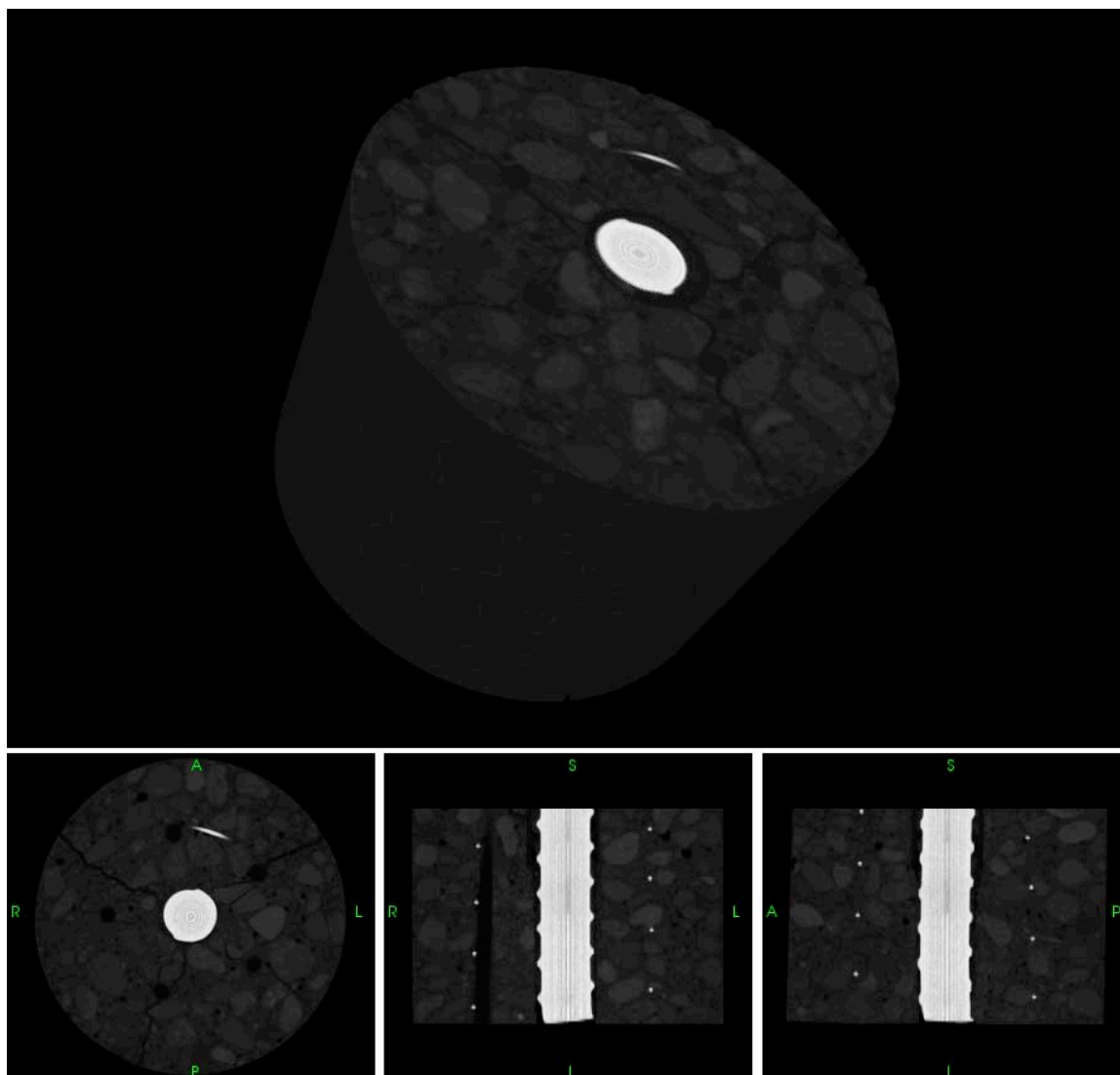


P3W1B-3



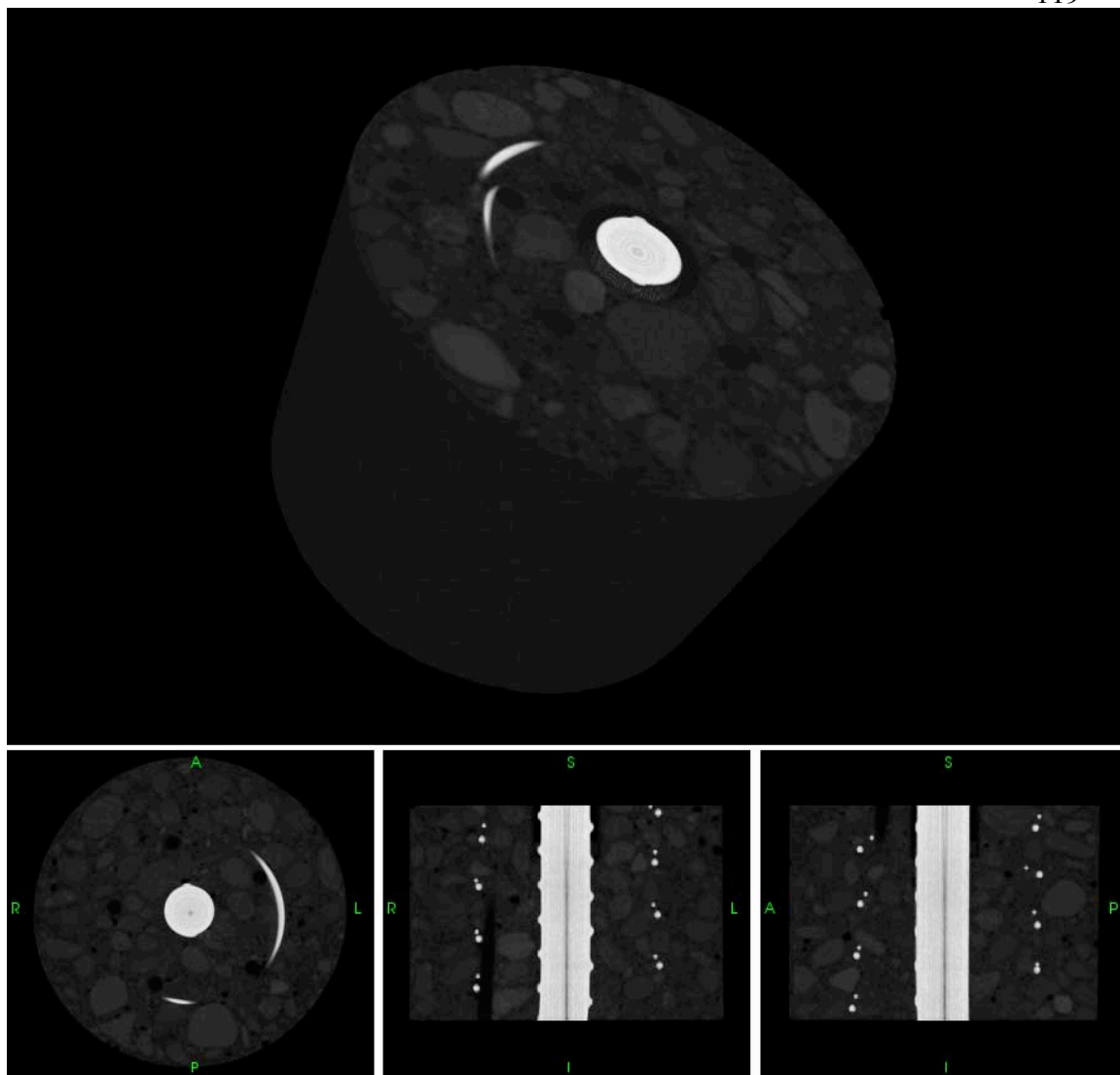
P3W1B-3							
	Dominant Cracks	Orientation of Dominant Cracks	Number of Aggregates Split	Visual Crack Width	Significant Crack Branching	Connect through Dowel ?	Significant Lug Crushing Around Bar
	1	0	1	Medium	No	Yes	Some
	2	100	1	Medium	Yes	No	
	3	200	1	Fine	No	Yes	

P3W1B-4

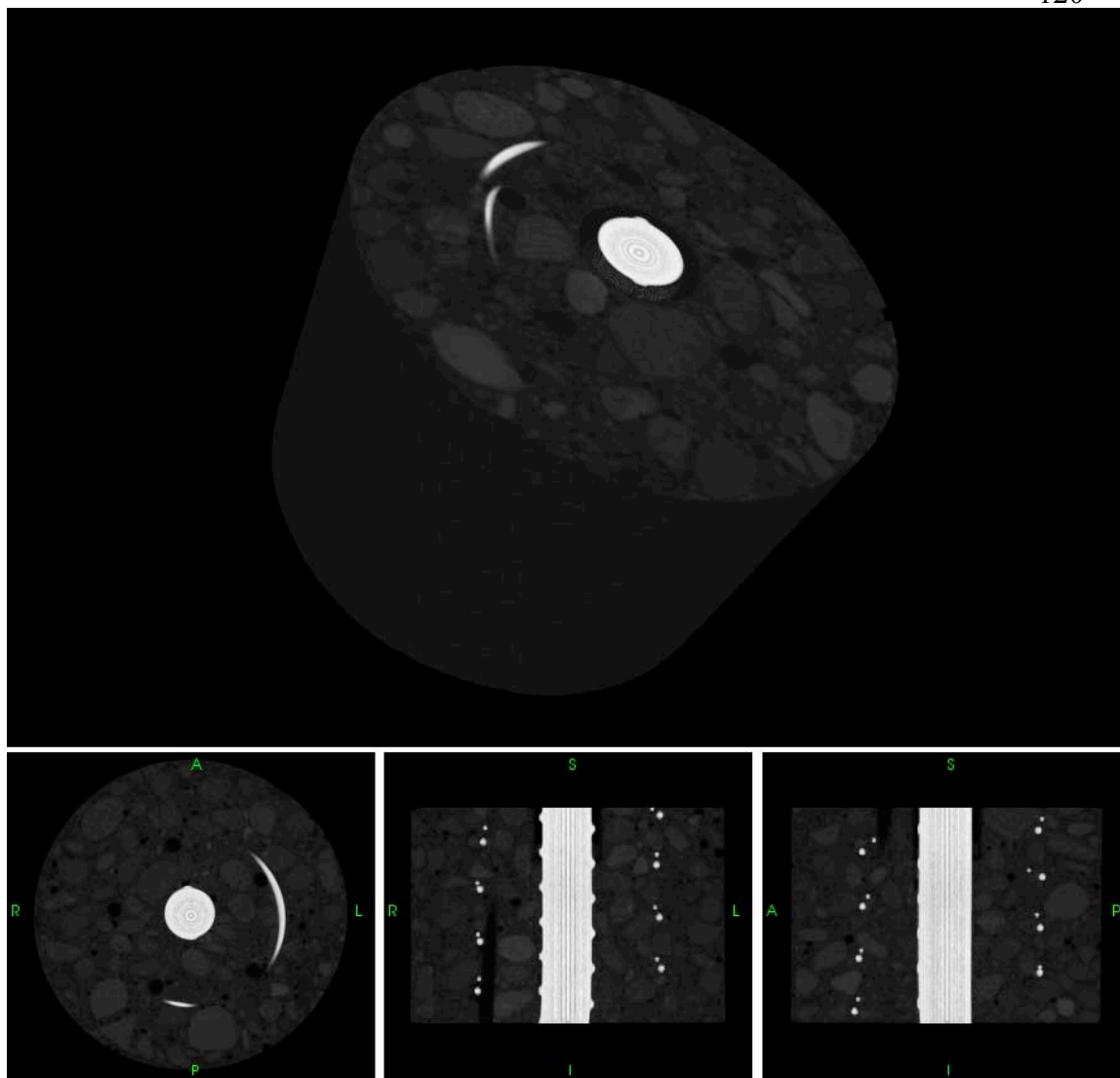


P3W1B-4							
	Dominant Cracks	Orientation of Dominant Cracks	Number of Aggregates Split	Visual Crack Width	Significant Crack Branching	Connect through Dowel ?	Significant Lug Crushing Around Bar
	1	0	1	Wide	No	Yes	Some
	2	100	1	Wide	Yes	No	
	3	200	1	Wide	No	Yes	
	4	260	0	Fine	No	Yes	

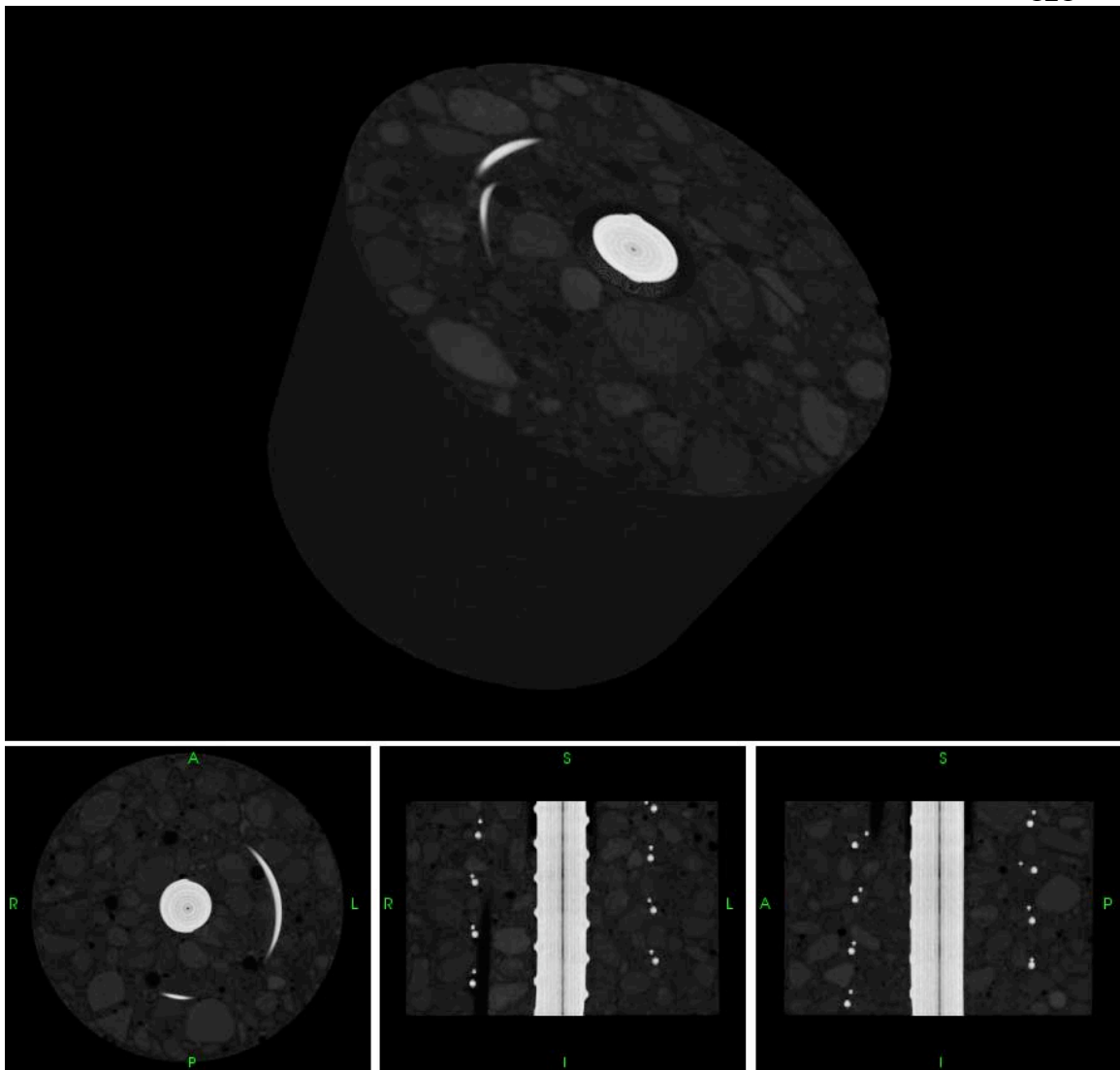
P3W2-1



P3W2-2

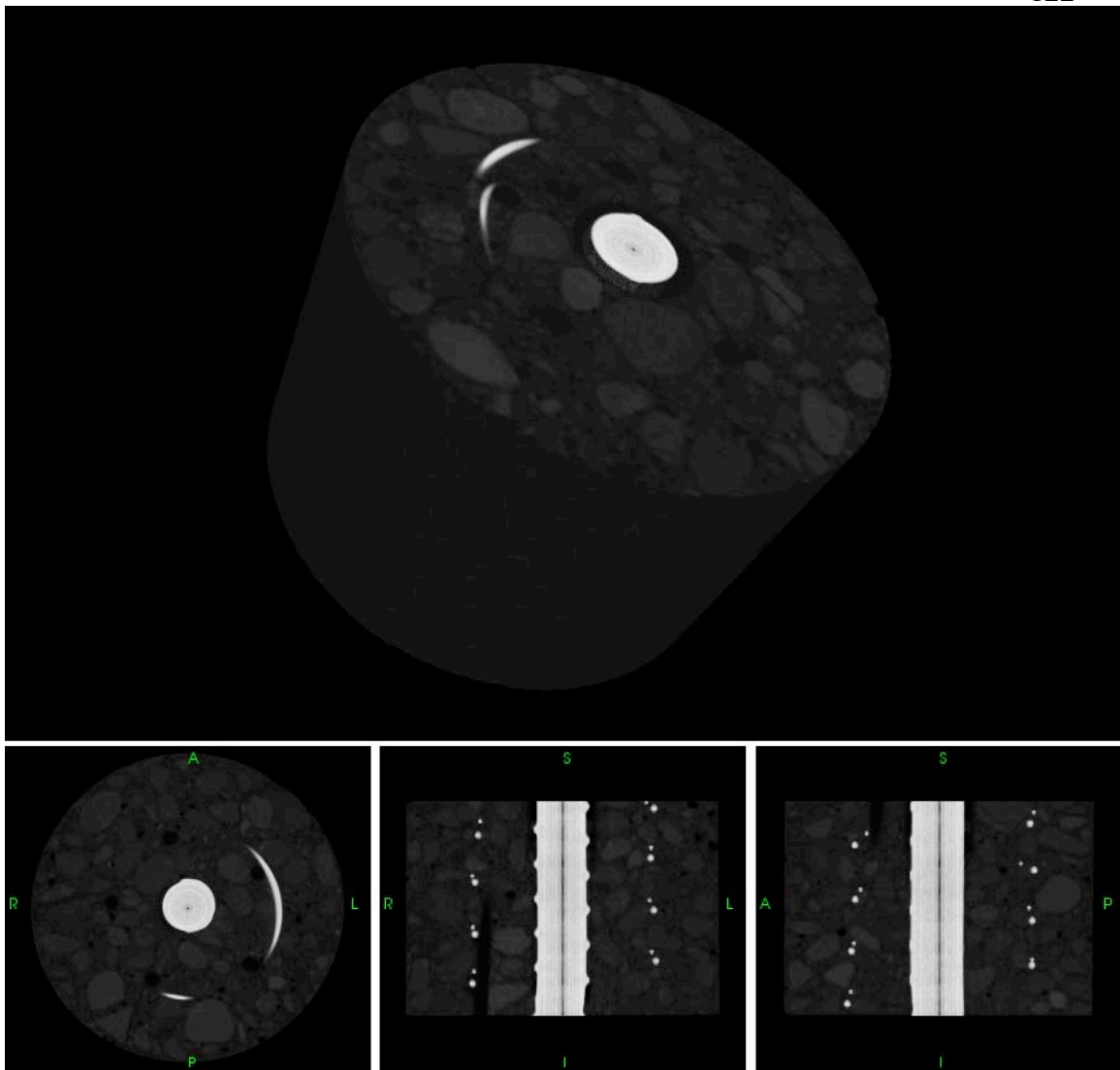


P3W2-3



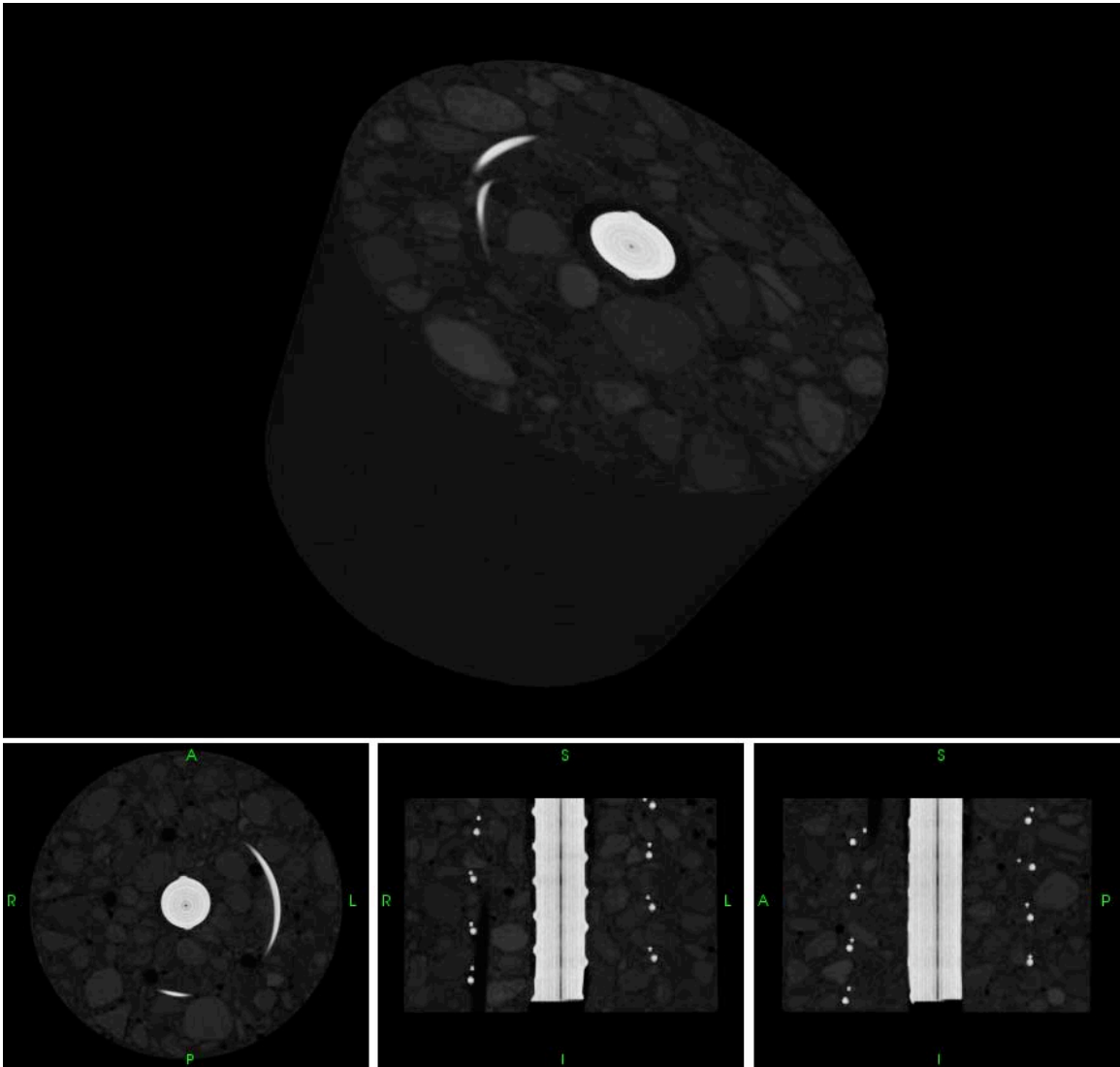
P3W2-3							
	Dominant Cracks	Orientation of Dominant Cracks	Number of Aggregates Split	Visual Crack Width	Significant Crack Branching	Connect through Dowel ?	Significant Lug Crushing Around Bar
	1	0	0	Very Fine	No	No	None
	2	180	0	Very Fine	No	Yes	

P3W2-4



P3W2-4							
	Dominant Cracks	Orientation of Dominant Cracks	Number of Aggregates Split	Visual Crack Width	Significant Crack Branching	Connect through Dowel ?	Significant Lug Crushing Around Bar
	1	0	0	V. Fine	No	No	None
	2	180	0	V. Fine	No	Yes	
	3	90	0	V. Fine	No	Yes	
	4	270	0	V. Fine	No	Yes	

P3W2-5



P3W2-5							
	Dominant Cracks	Orientation of Dominant Cracks	Number of Aggregates Split	Visual Crack Width	Significant Crack Branching	Connect through Dowel ?	Significant Lug Crushing Around Bar
	1	0	0	Fine	No	No	None
	2	180	0	Fine	No	Yes	
	3	90	0	Fine	No	Yes	
	4	270	0	Fine	No	Yes	

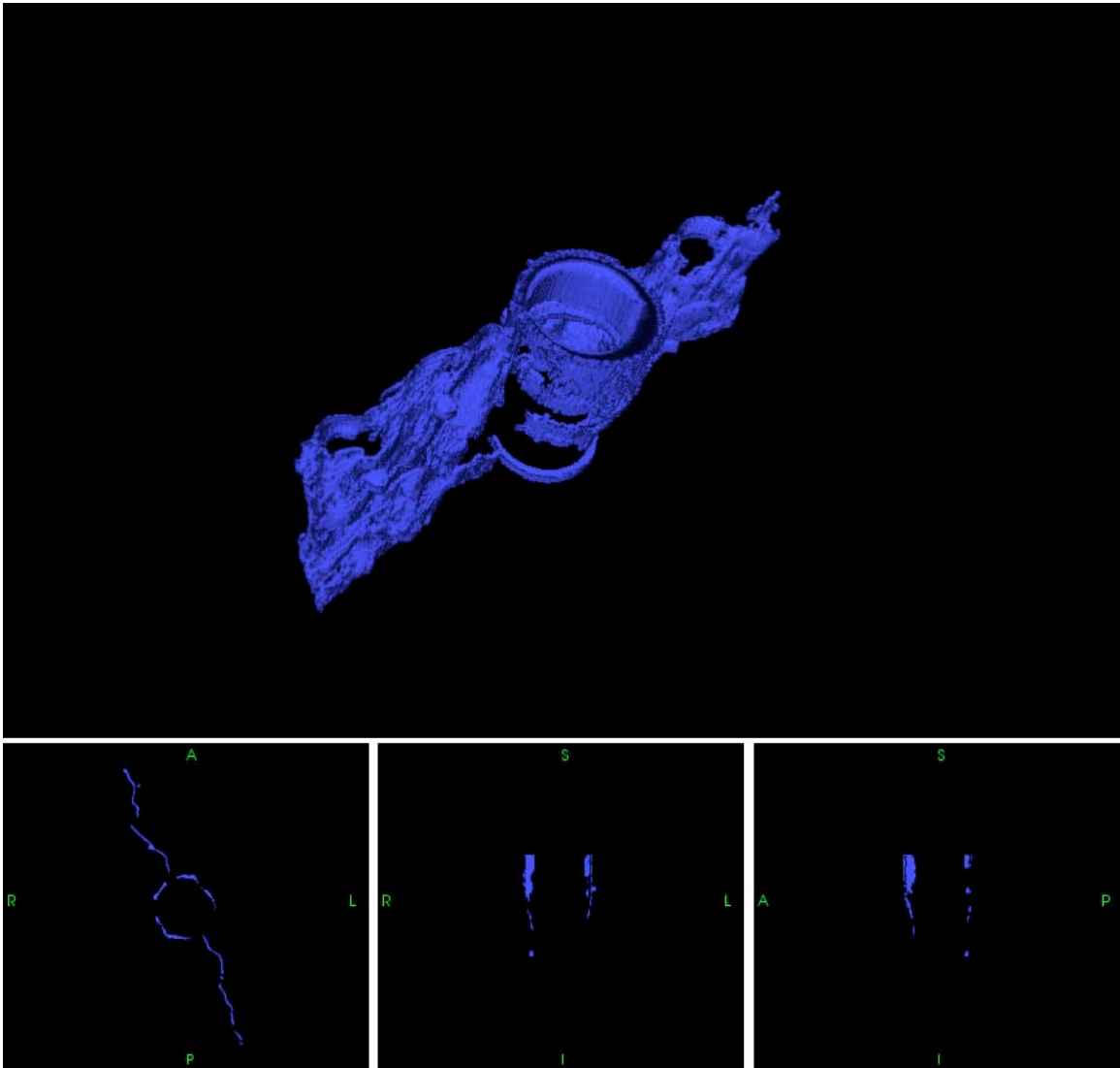
APPENDIX B: CRACK VOLUME RECONSTRUCTIONS

This Appendix contains information about crack surface area and volumes retrieved from the samples tested. A simple threshold routine was used to segment the data, with the threshold value selected to maximize the change in voids space within the load sequence. This allowed us to detect the most cracking (normalized). Using “Blob3D”, a IDL routine written by Richard Ketcham of the UTCT Lab at the University of Texas, we performed this thresholding, extracted the void space, separated the cracks from the voids, and calculated surface area and volume.

In some cases we were able to separate the crack volume in to cracks around the bar and dominant planar cracks, and their individual surface area and volume are presented. In other cases, due to the type of cracking, this was not possible. These values were useful in our fracture energy calculations.

P1-3

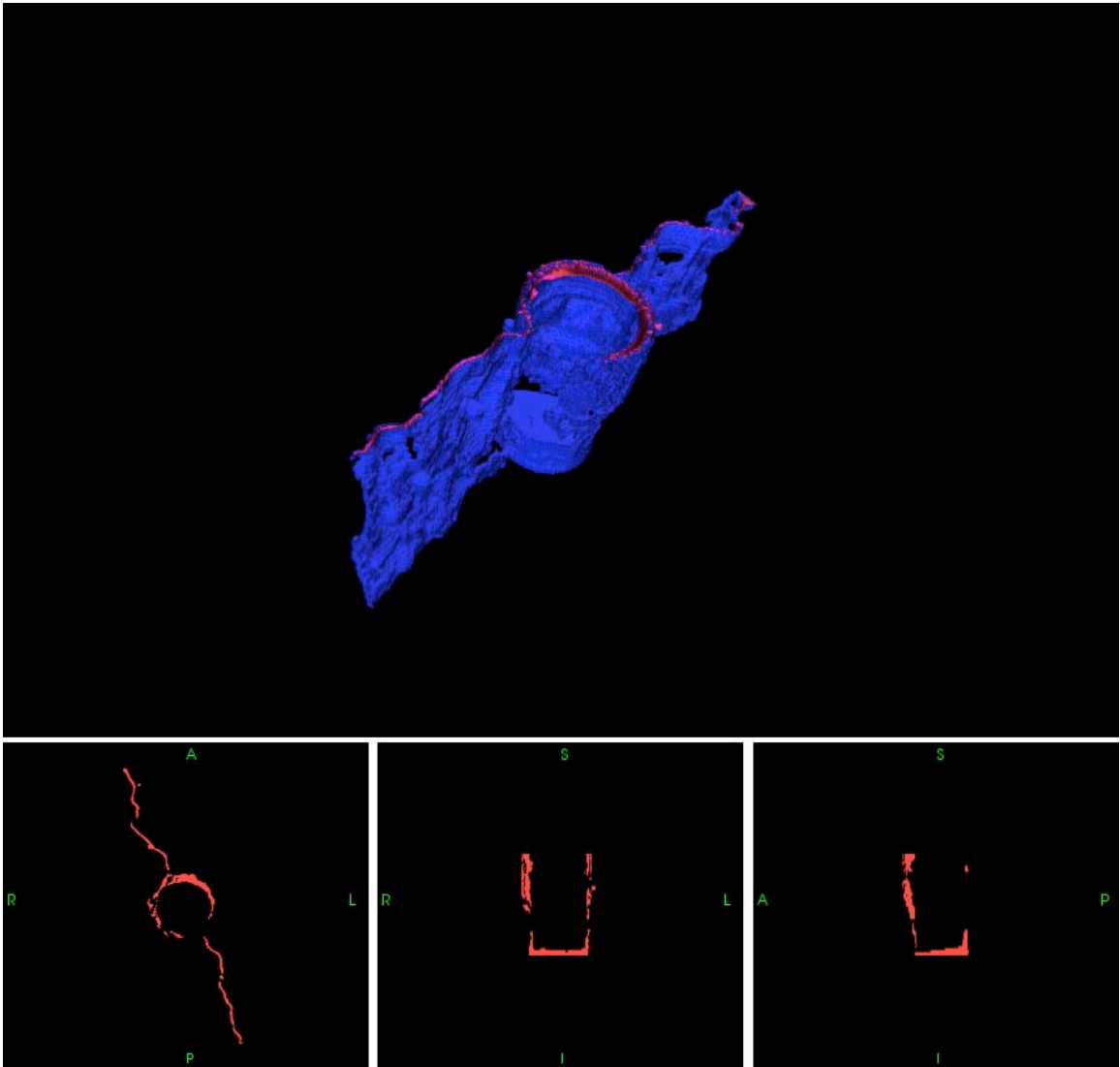
Threshold value = 13000



	Imaged "Crack" Surface Area (in^2)	Crack Surface Created (in^2)	Crack Volume (in^3)	Approximate "Width" (in)
P1-3				
Total	37.45	18.73	0.67	0.036
Crack 1	11.25	5.62	0.15	0.026
Crack 2	10.69	5.35	0.14	0.026
Bar	15.51	7.76	0.38	0.049

P1-4

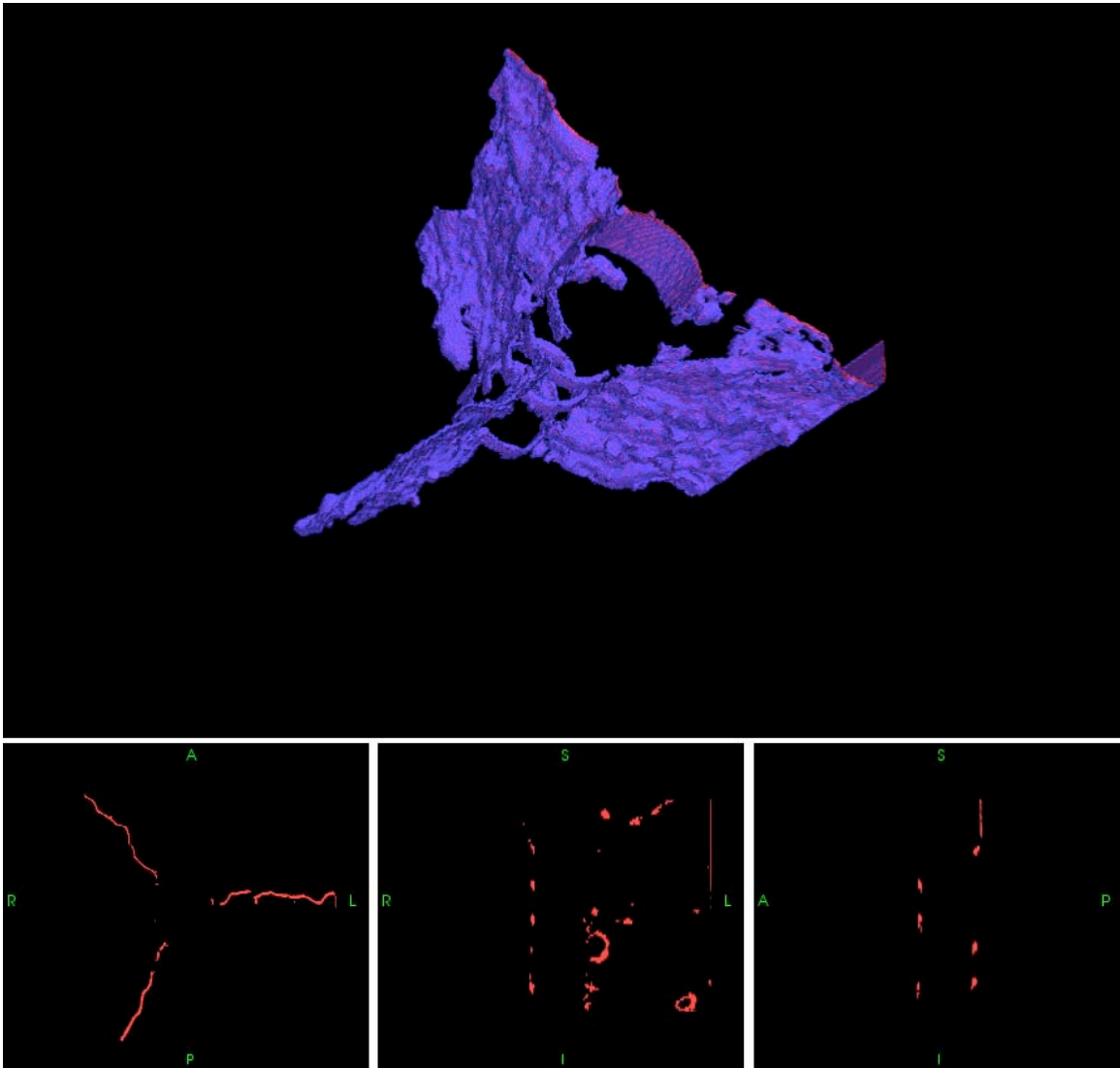
Threshold value = 13000



P1-4	Imaged "Crack" Surface Area (in^2)	Crack Surface Created (in^2)	Crack Volume (in^3)	Approximate "Width" (in)
Total	41.05	20.53	0.84	0.041
Crack 1	11.56	5.78	0.19	0.034
Crack 2	11.57	5.79	0.19	0.033
Bar	17.92	8.96	0.46	0.051

P3F-3

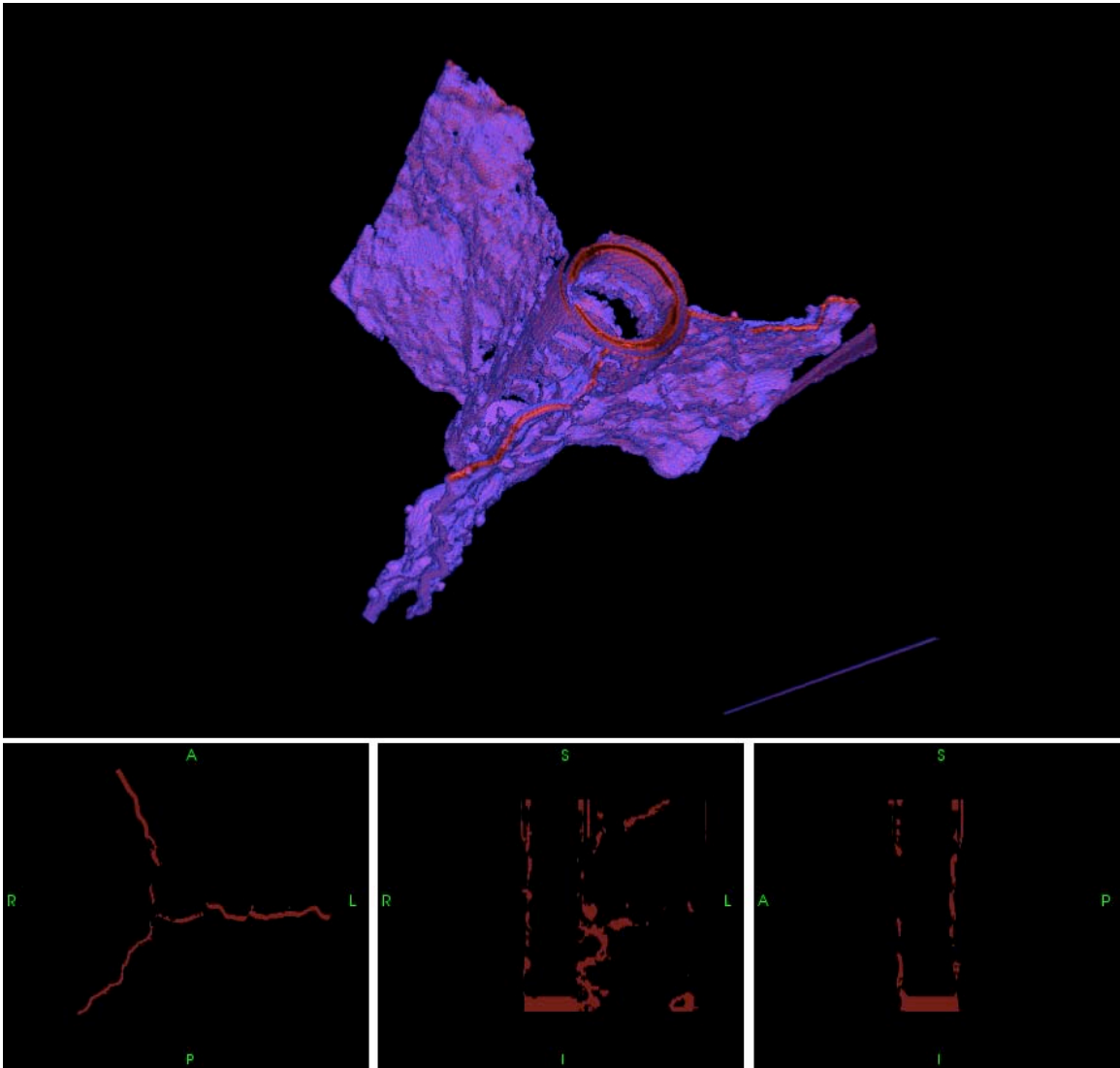
Threshold value = 10000



P3F-3	Imaged "Crack" Surface Area (in^2)	Crack Surface Created (in^2)	Crack Volume (in^3)	Approximate "Width" (in)
Total	106.29	53.15	2.25	0.042
Crack 1	24.20	12.10	0.57	0.047
Crack 2	25.67	12.83	0.64	0.050
Crack 3	23.23	11.61	0.41	0.036
Bar	16.63	8.31	0.36	0.044

P3F-4

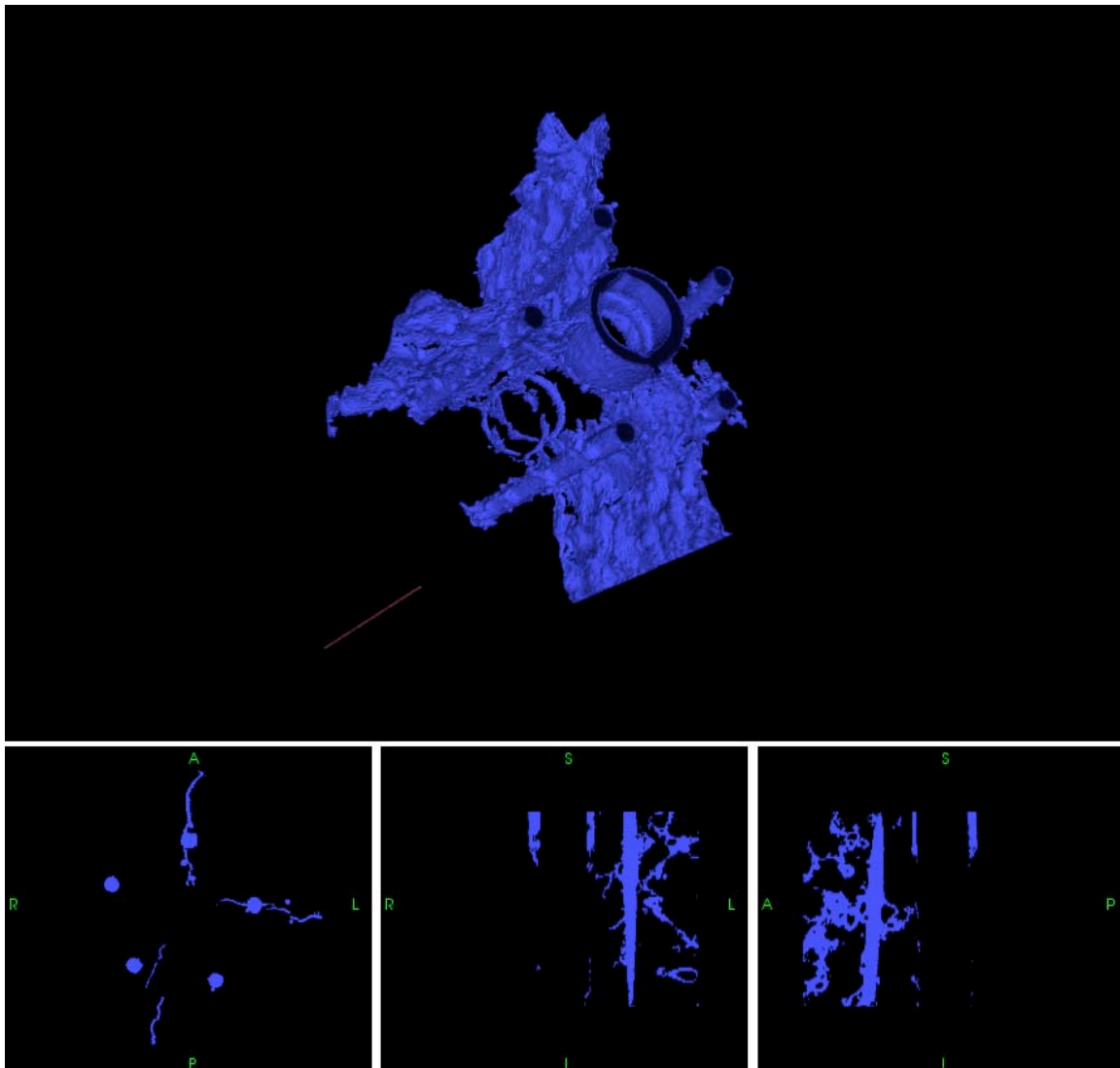
Threshold value = 10000



P3F-4	Imaged "Crack" Surface Area (in^2)	Crack Surface Created (in^2)	Crack Volume (in^3)	Approximate "Width" (in)
Total	108.07	54.04	2.98	0.055
Crack 1	23.74	11.87	0.71	0.059
Crack 2	28.99	14.49	0.80	0.056
Crack 3	26.73	13.36	0.85	0.064
Bar	28.62	14.31	0.61	0.043

P3W1A-3

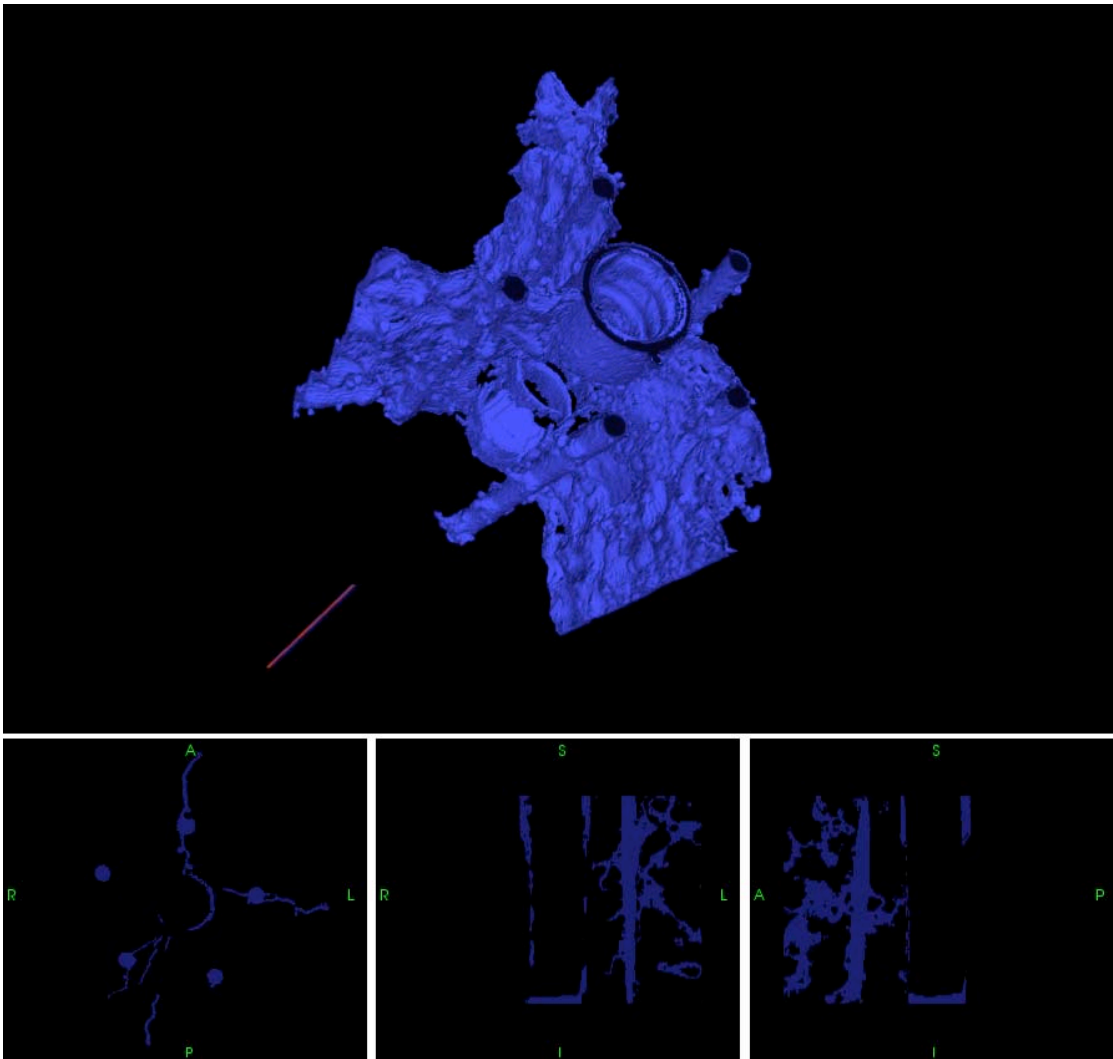
Threshold value = 17000



P3W1A-3	Imaged "Crack" Surface Area (in ²)	Crack Surface Created (in ²)	Crack Volume (in ³)	Approximate "Width" (in)
Total	97.48	48.74	2.14	0.044
Crack 1	25.84	12.92	0.46	0.036
Crack 2	22.17	11.08	0.39	0.035
Crack 3	25.93	12.96	0.62	0.048
Bar	21.51	10.76	0.65	0.060
Dowels (Each)	5.74		0.34	

P3W1A-4

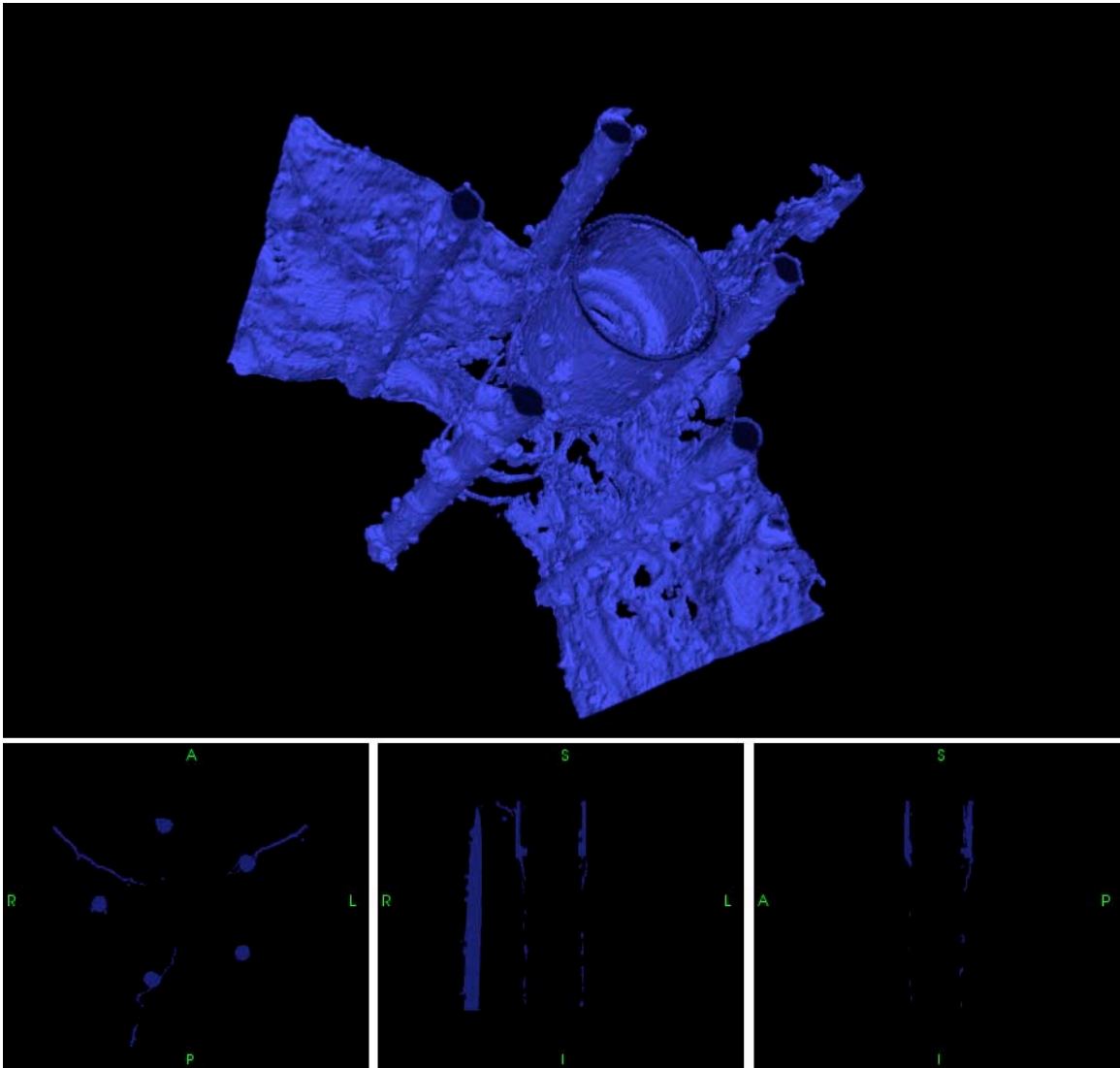
Threshold value = 17000



P3W1A-4	Imaged "Crack" Surface Area (in^2)	Crack Surface Created (in^2)	Crack Volume (in^3)	Approximate "Width" (in)
Total	135.54	67.77	2.45	0.036
Crack 1	32.89	16.44	0.79	0.048
Crack 2	30.43	15.21	0.71	0.047
Crack 3	28.16	14.08	0.76	0.054
Bar	44.07	22.03	1.21	0.055
Dowels (Each)	5.74		0.34	

P3W1B-3

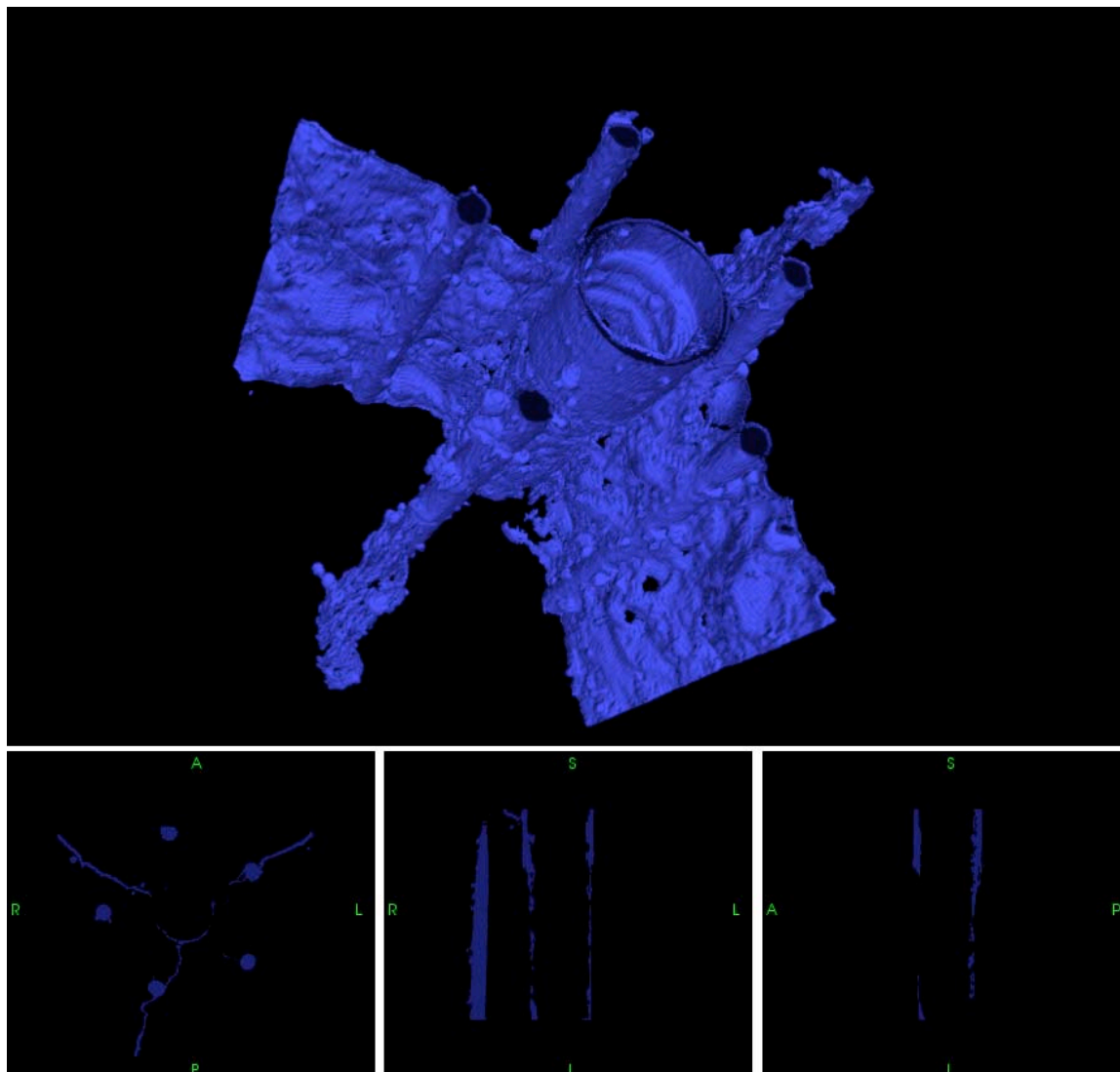
Threshold value = 16500



P3W1B-3	Imaged "Crack" Surface Area (in^2)	Crack Surface Created (in^2)	Crack Volume (in^3)	Approximate "Width" (in)
Total	95.80	47.90	1.94	0.041
Crack 1	25.37	12.69	0.46	0.036
Crack 2	21.77	10.88	0.47	0.043
Crack 3	24.68	12.34	0.66	0.053
Bar	24.12	12.06	0.65	0.054
Dowels	5.74		0.34	

P3W1B-4

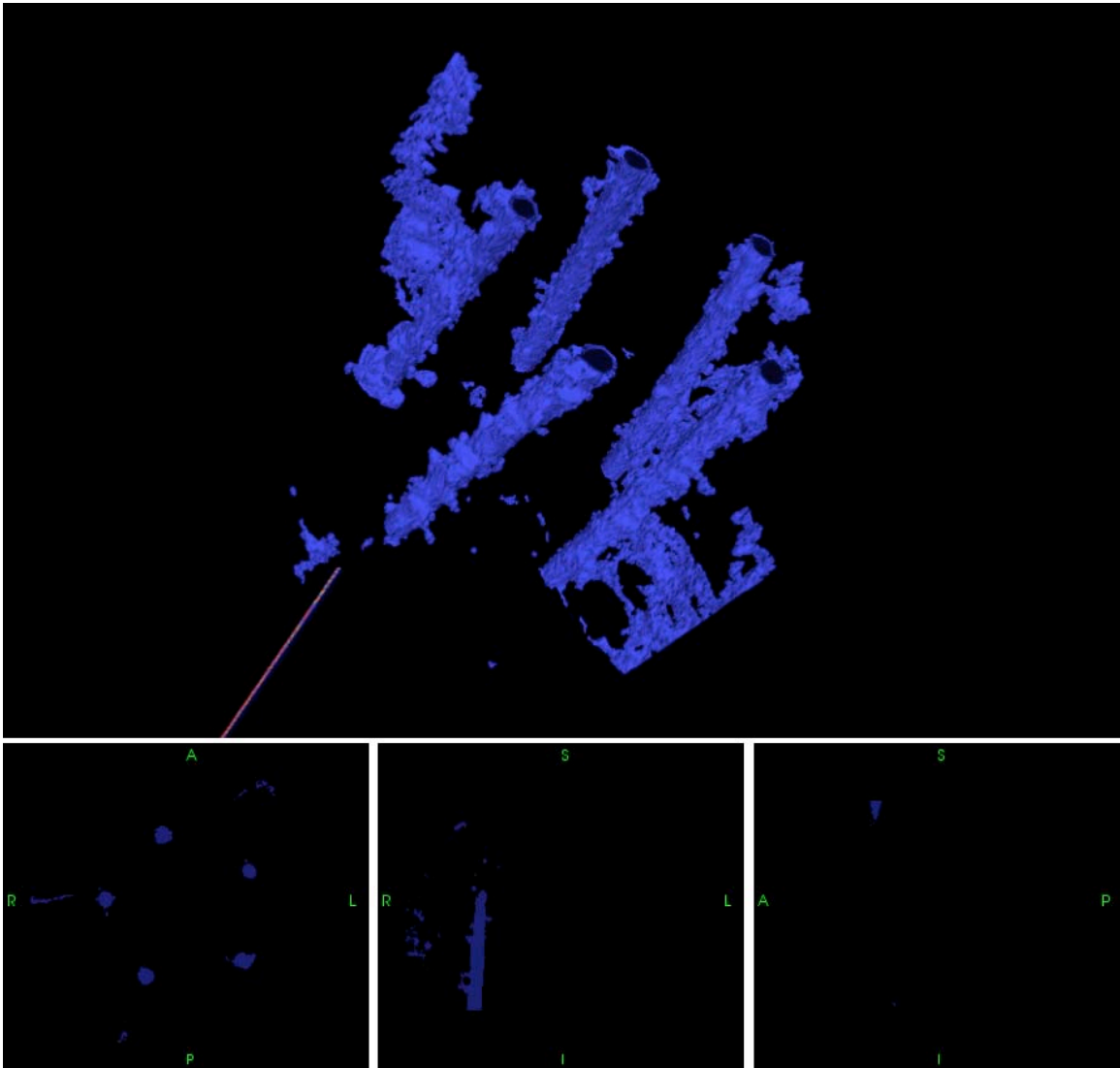
Threshold value = 16500



	Imaged "Crack" Surface Area (in ²)	Crack Surface Created (in ²)	Crack Volume (in ³)	Approximate "Width" (in)
P3W1B-4				
Total	121.89	60.95	2.70	0.044
Crack 1	31.24	15.62	0.67	0.043
Crack 2	27.51	13.75	0.58	0.042
Crack 3	25.38	12.69	0.83	0.065
Bar	37.76	7.43	0.63	0.084
Dowels	5.74		0.34	

P3W2-3

Threshold value = 17682

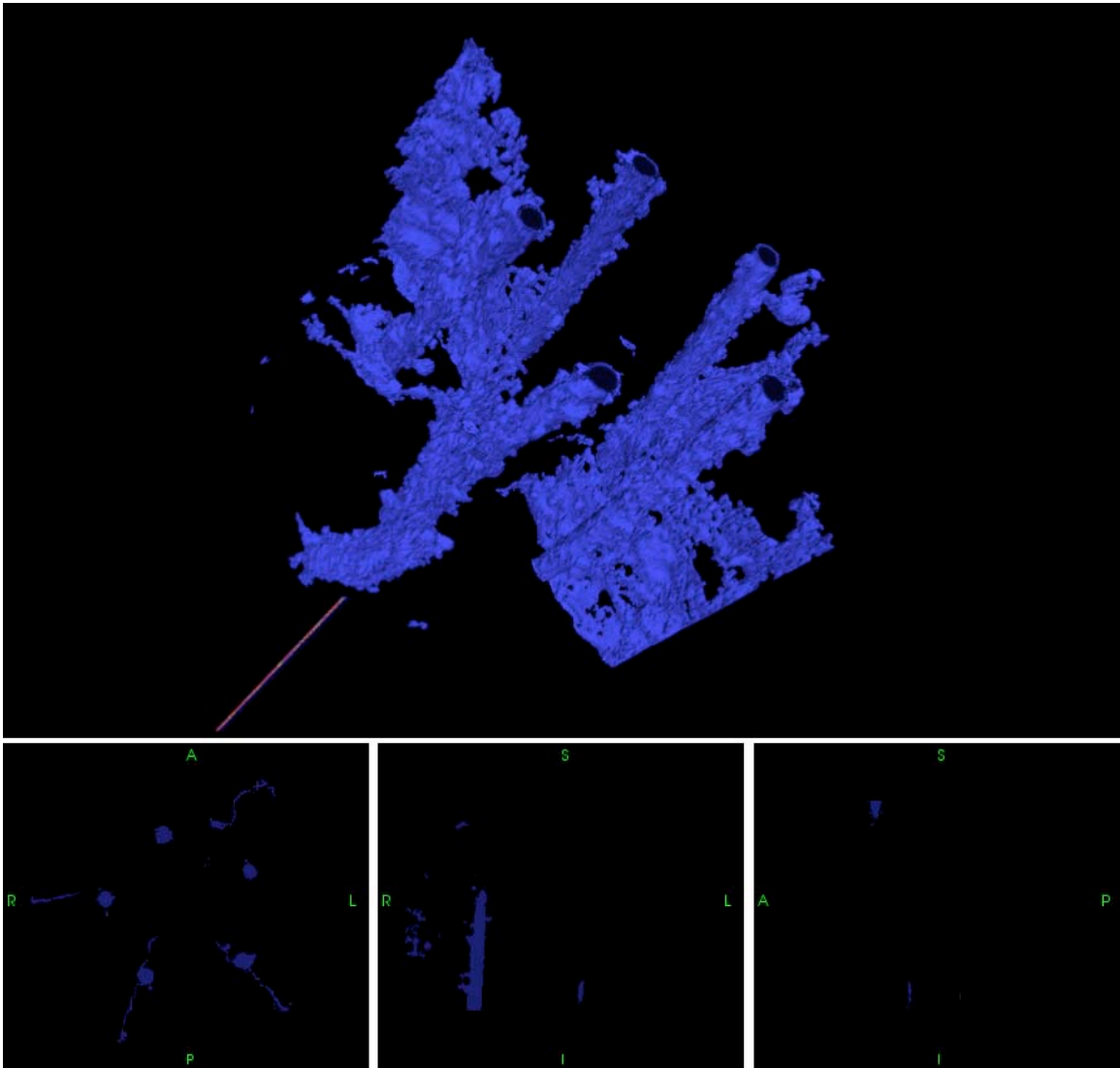


	Imaged "Crack" Surface Area (in^2)	Crack Surface Created (in^2)	Crack Volume (in^3)	Approximate "Width" (in)
P3W2-3				
Total	58.34	29.17	0.723	0.012
Dowels	5.74		0.34	

Note: Due to the small amount of cracking and the lack of dominant cracks, we will only include total surface area and volume created.

P3W2-4

Threshold value = 17682

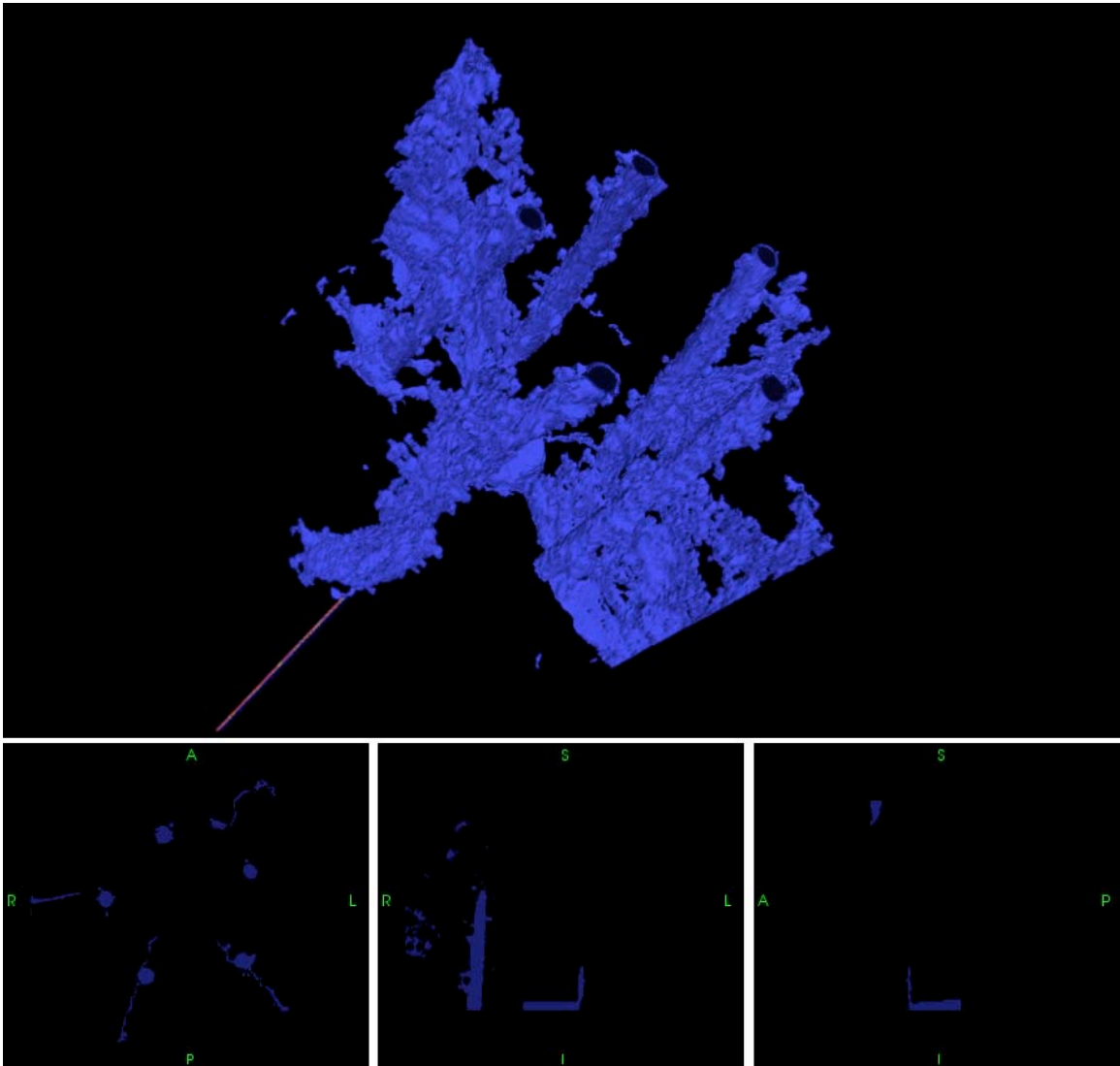


	Imaged "Crack" Surface Area (in^2)	Crack Surface Created (in^2)	Crack Volume (in^3)	Approximate "Width" (in)
P3W2-4				
Total	97.29	48.65	1.43	0.014
Dowels	5.74		0.34	

Note: Due to the small amount of cracking and the lack of dominant cracks, we will only include total surface area and volume created.

P3W2-5

Threshold value = 17682



	Imaged "Crack" Surface Area (in^2)	Crack Surface Created (in^2)	Crack Volume (in^3)	Approximate "Width" (in)
P3W2-5				
Total	103.3	51.67	1.72	0.017
Dowels	5.74		0.34	

Note: Due to the small amount of cracking and the lack of dominant cracks, we will only include total surface area and volume created.

APPENDIX C: FRACTURE ENERGY CALCULATIONS FOR EACH SAMPLE

Using the load displacement data, a calculated value of G_f , and the surface area created during fracture, we were able to perform simple energy calculations about the failure of bond. These calculations are listed for each incremental load step: strain energy in the concrete, strain energy in the steel, fracture energy released, work done by load applied, and resulting “Noise” – unaccountable energy release due to acoustic noise, crushing and kinetic motion.

P1-2 -> P1-3

P1	Energy Calculations	
	Scan 2	Scan 3
U in Bar (lb-in)	53.33	2.02
load (k)	15.586	3.032
stress (ksi)	19.84471154	3.8604623
strain	0.0006843	0.000133119
displacement (in)	0.006843004	0.001331194
U in Concrete (lb-in)	11.85	0.45
U (Bar+Conc) (lb-in)	65.18	2.47
_U (lb-in)	-62.71	
_F (lb-in)	449.50	
_A (in^2)	28.88	
Gf (lb/in)	0.65	
Gf * _A (lb-in)	18.77	
U_NOISE (lb-in)	494.87	
U_Noise/_F	1.10	

P3F-2 -> P3F-3

P3F	Energy Calculations	
	Scan 2	Scan 3
U in Bar (lb-in)	126.02	1.21
load (k)	23.96	2.35
stress (ksi)	30.50681949	2.99211293
strain	0.001051959	0.000103176
displacement (in)	0.010519593	0.001031763
U in Concrete (lb-in)	28.0	0.27
U (Bar+Conc) (lb-in)	154.02	1.48
_U (lb-in)	-152.54	
_F (lb-in)	1530.00	
_A (in^2)	95.50	
Gf (lb/in)	0.65	
Gf * _A (lb-in)	62.08	
U_NOISE (lb-in)	1620.46	
U_Noise/_F	1.06	

P3W1A-2 -> P3W1A-3

P3W1A	Energy Calculations	
	Scan 2	Scan 3
U in Bar (lb-in)	104.23	61.96
load (k)	21.79	16.8
stress (ksi)	27.74388968	21.39042435
strain	0.000956686	0.000737601
displacement (in)	0.009566859	0.007376008
U in Concrete (lb-in)	23.16	13.77
U (Bar+Conc) (lb-in)	127.39	75.73
_U (lb-in)	-51.66	
_F (lb-in)	979.00	
_A (in^2)	85.79	
Gf (lb/in)	0.65	
Gf * _A (lb-in)	55.77	
U_NOISE (lb-in)	974.89	
U_Noise/_F	1.00	

P3W1B-2 -> P3W1B-3

P3W1B	Energy Calculations	
	Scan 2	Scan 3
U in Bar (lb-in)	141.85	27.24
load (k)	25.42	11.14
stress (ksi)	32.36574923	14.18388853
strain	0.00111606	0.0004891
displacement (in)	0.011160603	0.004890996
U in Concrete (lb-in)	31.5	6.05
U (Bar+Conc) (lb-in)	173.35	33.29
_U (lb-in)	-140.06	
_F (lb-in)	1220.00	
_A (in^2)	73.42	
Gf (lb/in)	0.65	
Gf * _A (lb-in)	47.72	
U_NOISE (lb-in)	1312.34	
U_Noise/_F	1.08	

P3W1B-3 -> P3W1B-4

P3W1B	Energy Calculations	
	Scan 3	Scan 4
U in Bar (lb-in)	27.24	4.39
load (k)	11.14	4.47
stress (ksi)	14.18388853	5.691380765
strain	0.0004891	0.000196255
displacement (in)	0.004890996	0.001962545
U in Concrete (lb-in)	6.05	0.98
U (Bar+Conc) (lb-in)	33.29	5.37
_U (lb-in)	-27.92	
_F (lb-in)	2300.00	
_A (in^2)	22.18	
Gf (lb/in)	0.65	
Gf * _A (lb-in)	14.42	
U_NOISE (lb-in)	2313.5	
U_Noise/_F	1.01	

P3W2-2 -> P3W2-3

P3W2	Energy Calculations	
	Scan 2	Scan 3
U in Bar (lb-in)	253.77	147.49
load (k)	34	25.92
stress (ksi)	43.29	33.002369
strain	.00149265	0.001138013
displacement (in)	0.0149265	0.011380127
U in Concrete (lb-in)	56.39	32.7
U (Bar+Conc) (lb-in)	310.16	180.27
_U (lb-in)	129.89	
_F (lb-in)	913.00	
_A (in^2)	58.35	
Gf (lb/in)	0.65	
Gf * _A (lb-in)	37.93	
U_NOISE (lb-in)	841.85	
U_Noise/_F	0.92	

P3W2-3 -> P3W2-4

P3W2	Energy Calculations	
	Scan 3	Scan 4
U in Bar (lb-in)	147.49	50.75
load (k)	25.92	15.204
stress (ksi)	33.002369	19.35833404
strain	0.00113801	0.000667529
displacement (in)	0.01138013	0.006675288
U in Concrete (lb-in)	32.77	11.28
U (Bar+Conc) (lb-in)	180.26	62.02
_U (lb-in)	-118.24	
_F (lb-in)	5400.00	
_A (in^2)	38.95	
Gf (lb/in)	0.65	
Gf * _A (lb-in)	25.31	
U_NOISE (lb-in)	54.92.9	
U_Noise/_F	1.02	

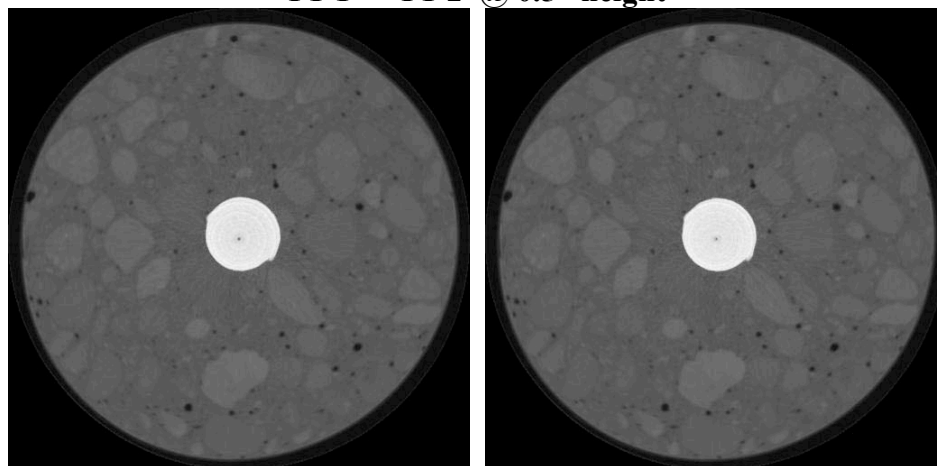
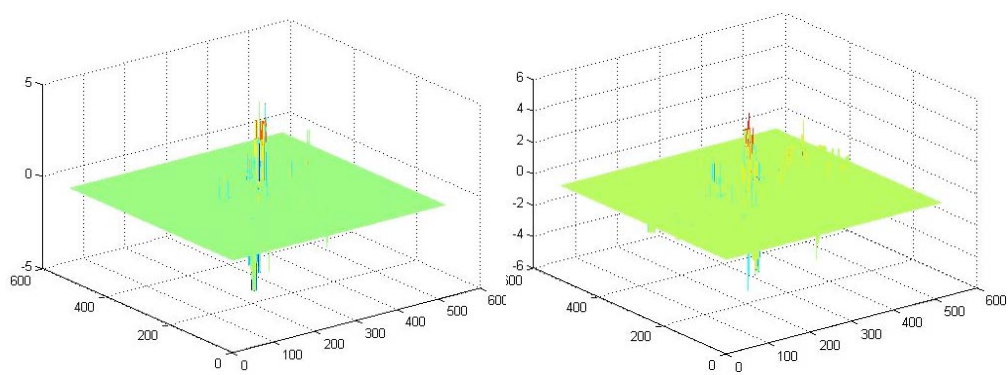
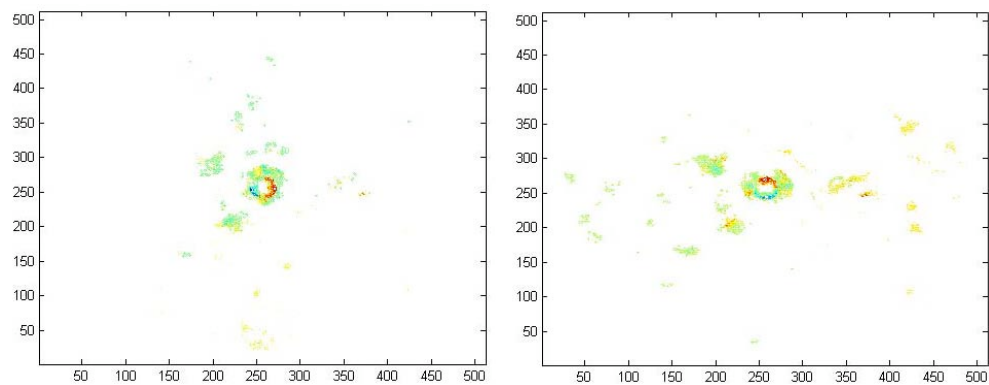
P3W2-4 -> P3W2-5

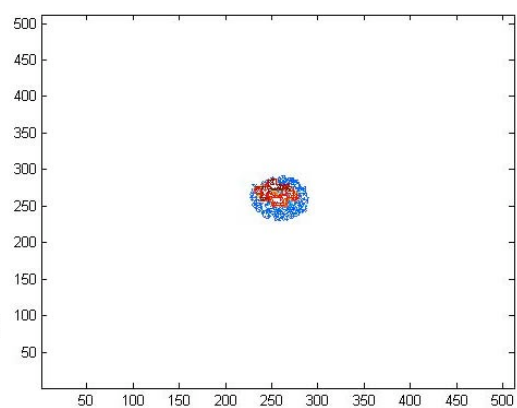
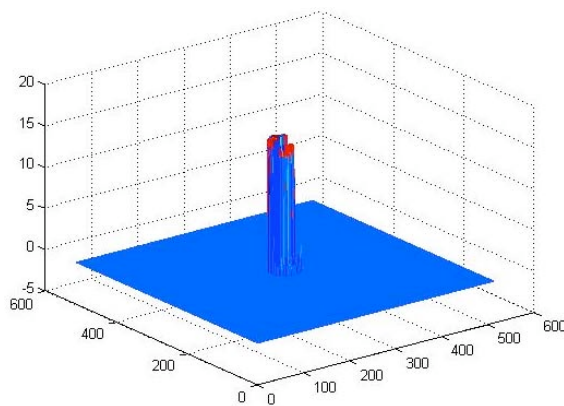
P3W2	Energy Calculations	
	Scan 4	Scan 5
U in Bar (lb-in)	50.75	32.94
load (k)	15.204	12.25
stress (ksi)	19.358334	15.59718442
strain	0.00066753	0.000537834
displacement (in)	0.00667529	0.005378339
U in Concrete (lb-in)	12.69	8.24
U (Bar+Conc) (lb-in)	63.43	41.18
_U (lb-in)	-22.25	
_F (lb-in)	5400.00	
_A (in^2)	6.04	
Gf (lb/in)	0.65	
Gf * _A (lb-in)	3.92	
U_NOISE (lb-in)	5418.33	
U_Noise/_F	1.00	

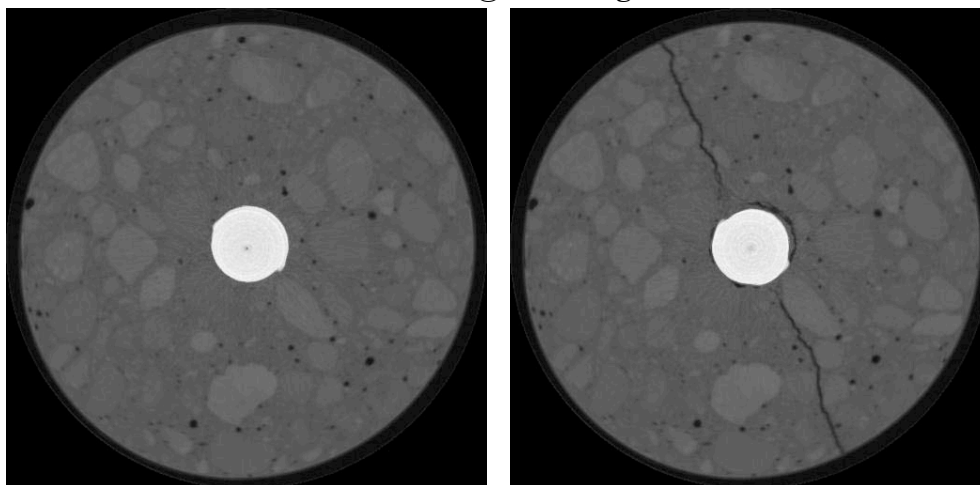
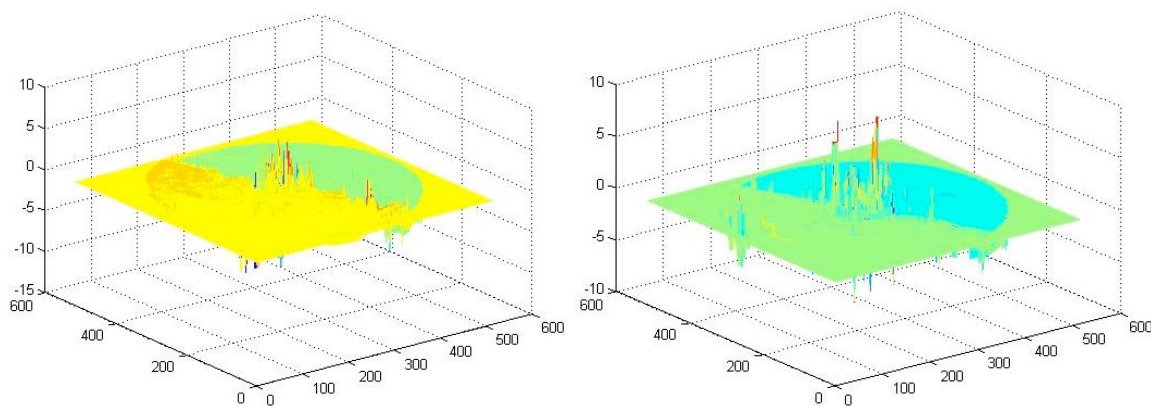
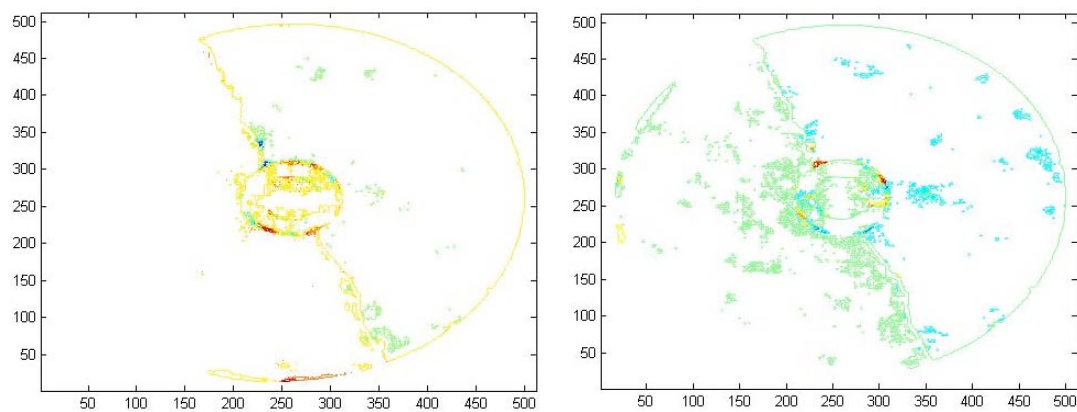
APPENDIX D: MOTION ESTIMATION

This Appendix will present processed data from the motion estimation routine. Due to the noise it produces, data was only processed for samples P1 and P3F.

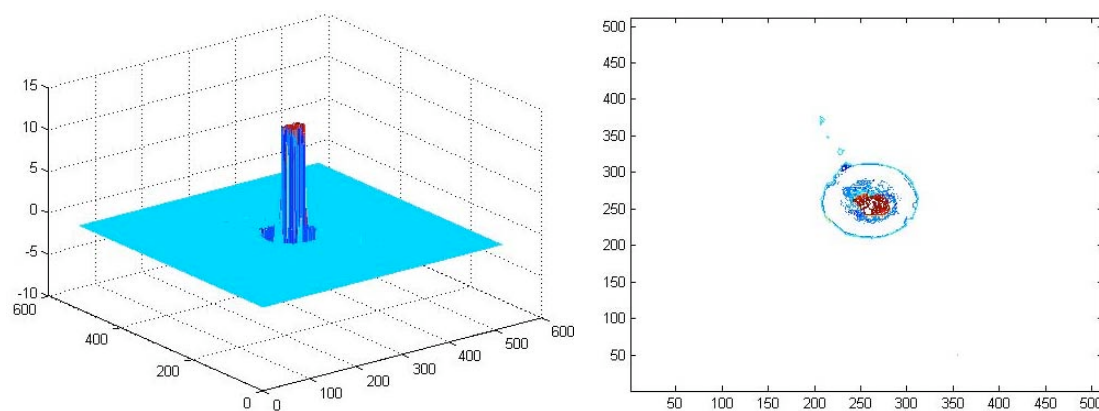
**Note: All X,Y Displacements are scaled to 1 pixel length = 0.012”
All Z Displacements are scaled to 1 pixel length = 0.039”**

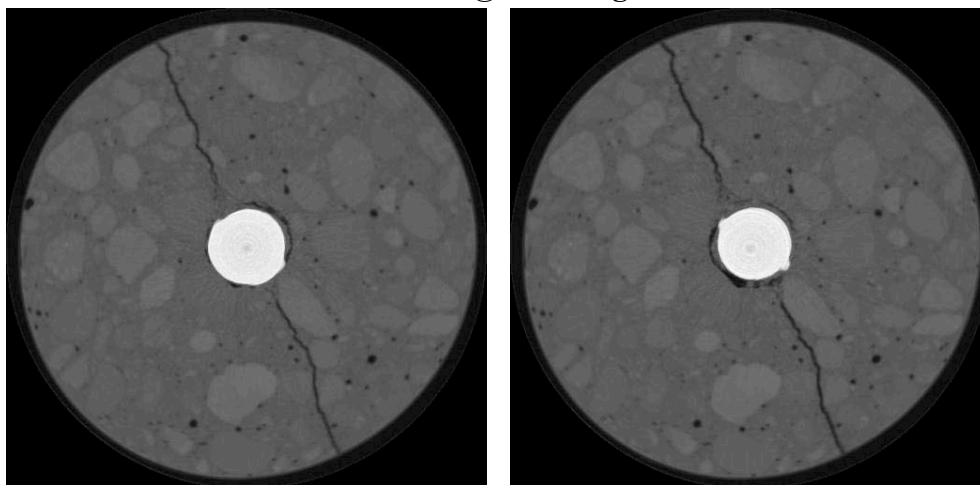
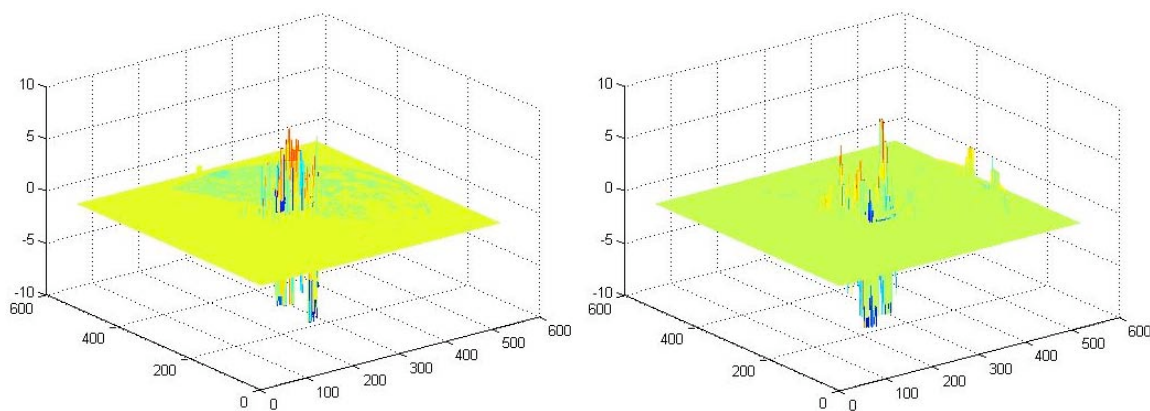
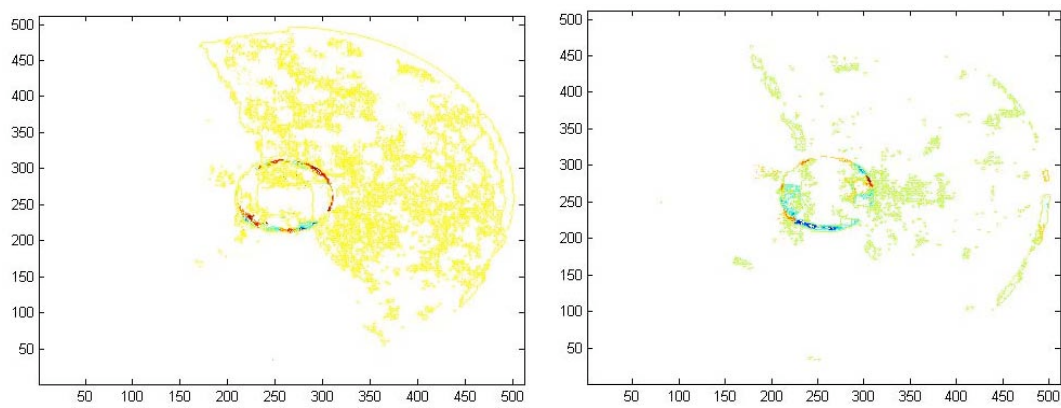
P1-1 → P1-2 @ 0.5" heightX and Y DisplacementX and Y Displacement ContoursZ Displacement

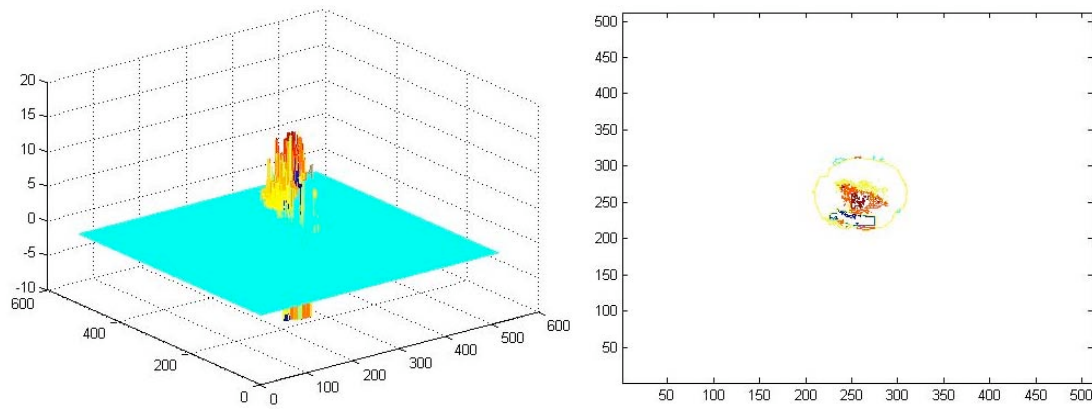


P1-2 -> P1-3 @ 0.5" heightX and Y DisplacementX and Y Displacement Contours

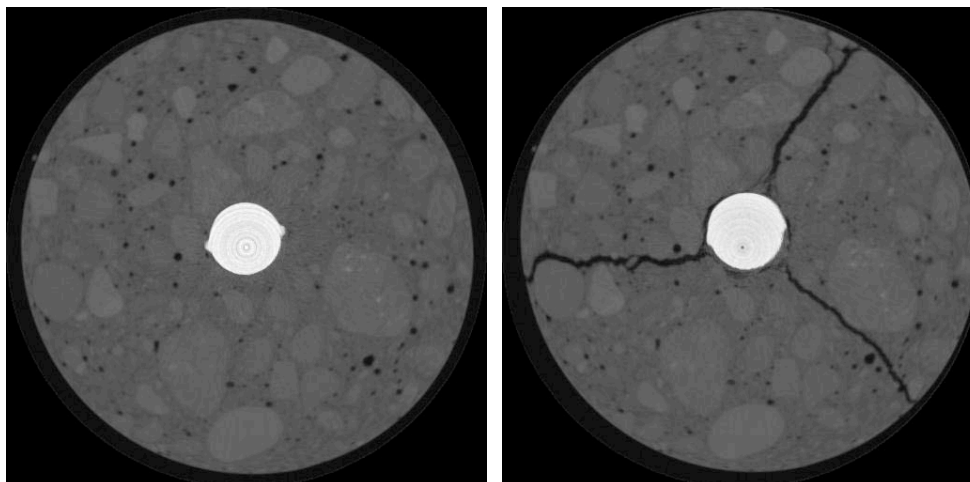
Z Displacement



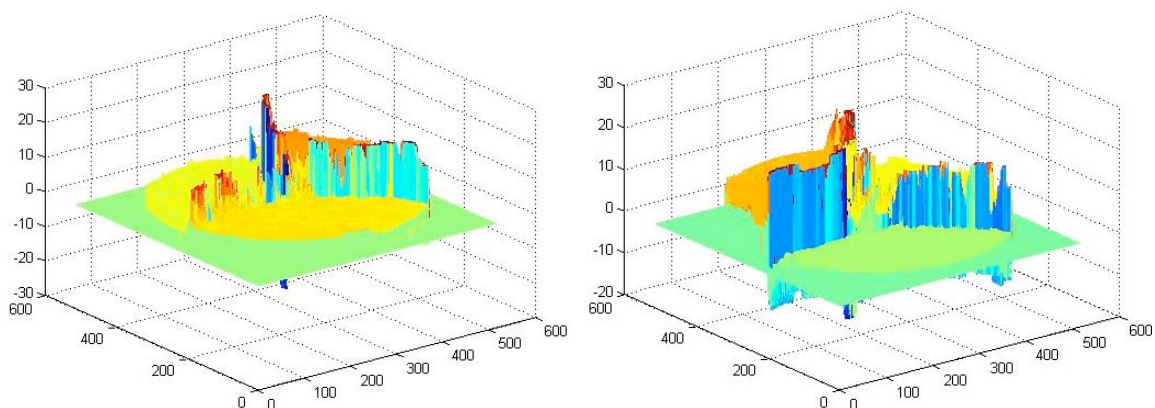
P1-3 -> P1-4 @ 0.5" heightX and Y DisplacementX and Y Displacement Contours

Z Displacement

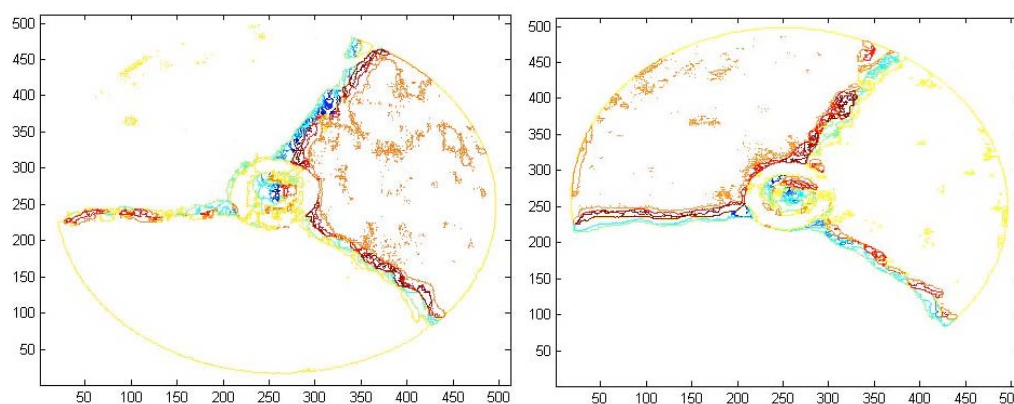
P3F-2 -> P3F-3 @ 0.5" height



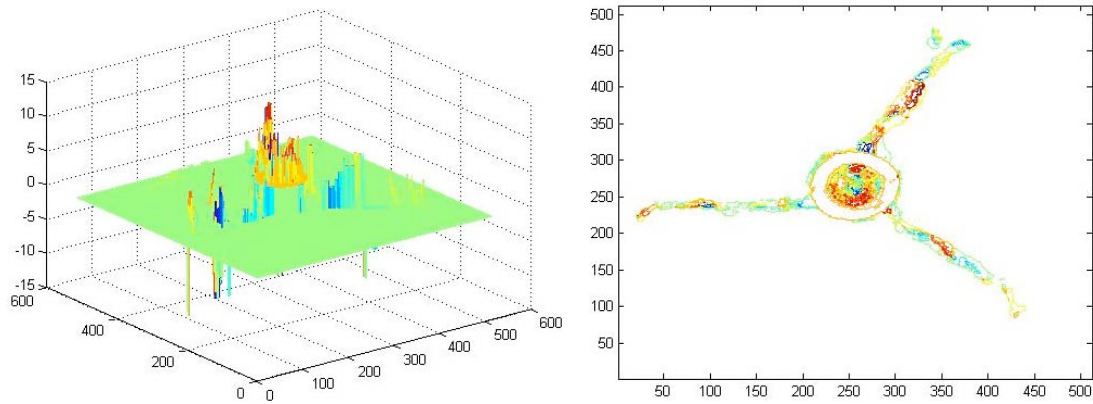
X and Y Displacement



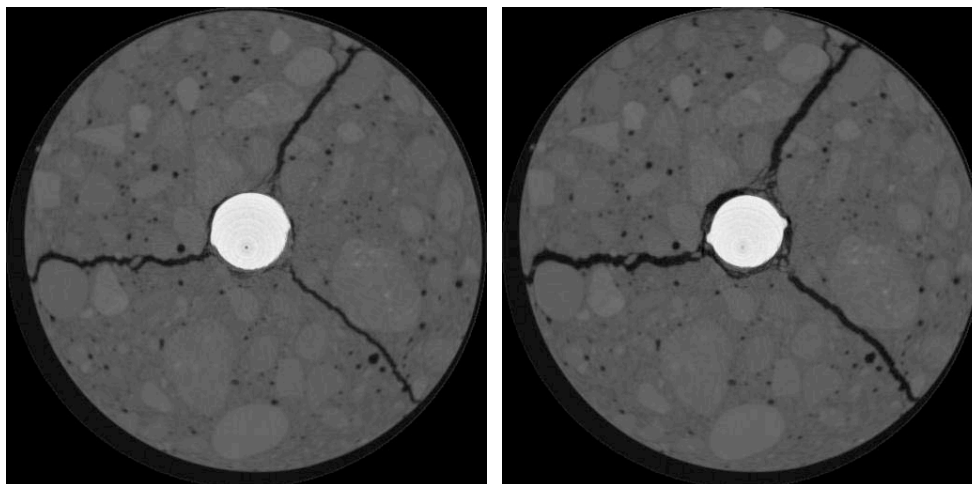
X and Y Displacement Contours



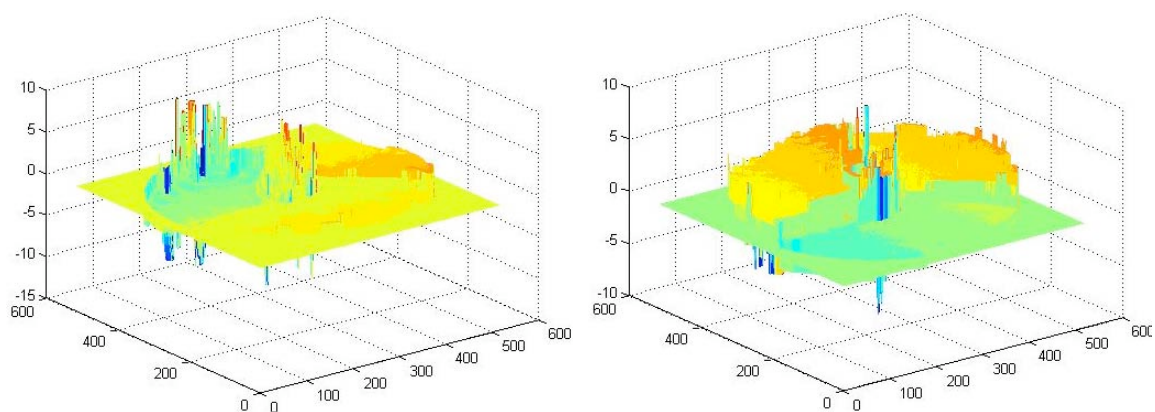
Z Displacement



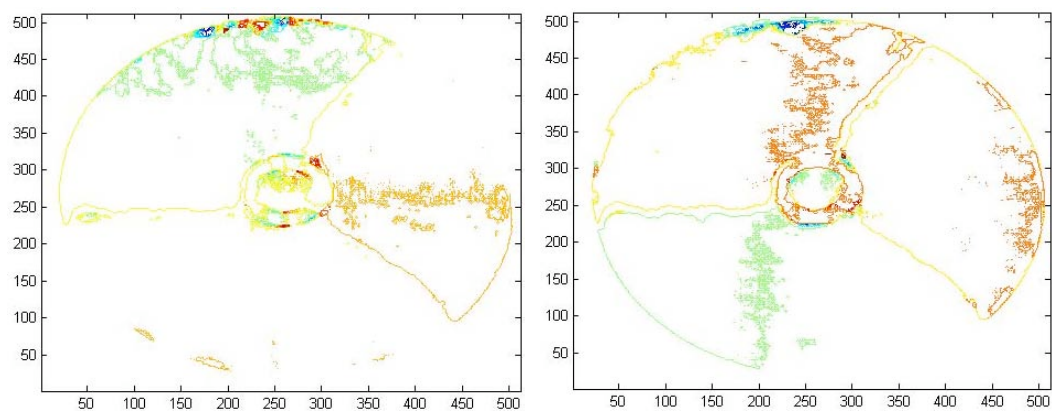
P3F-3 -> P3F-4 @ 0.5" height



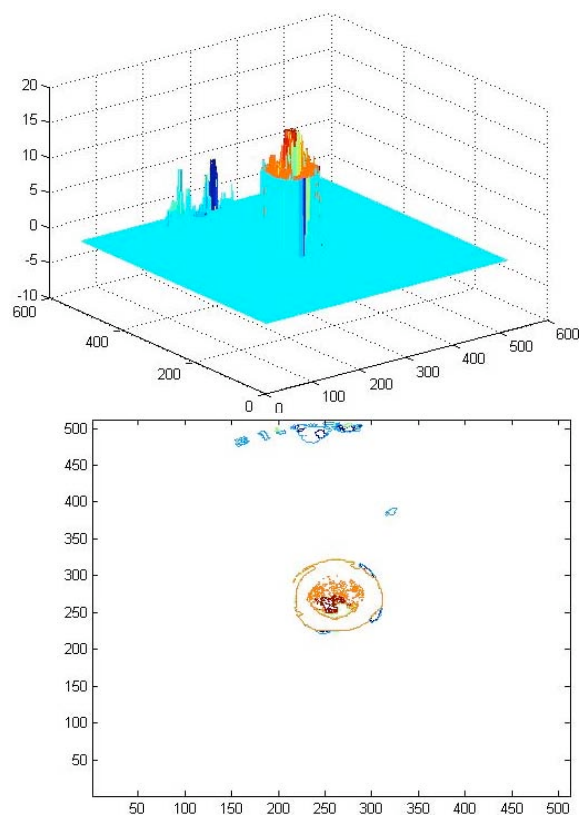
X and Y Displacement



X and Y Displacement Contours

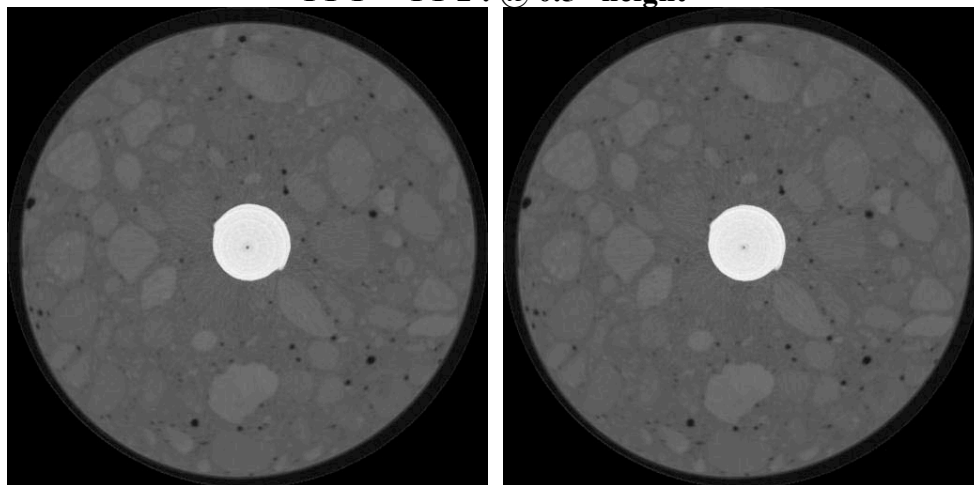


Z Displacement

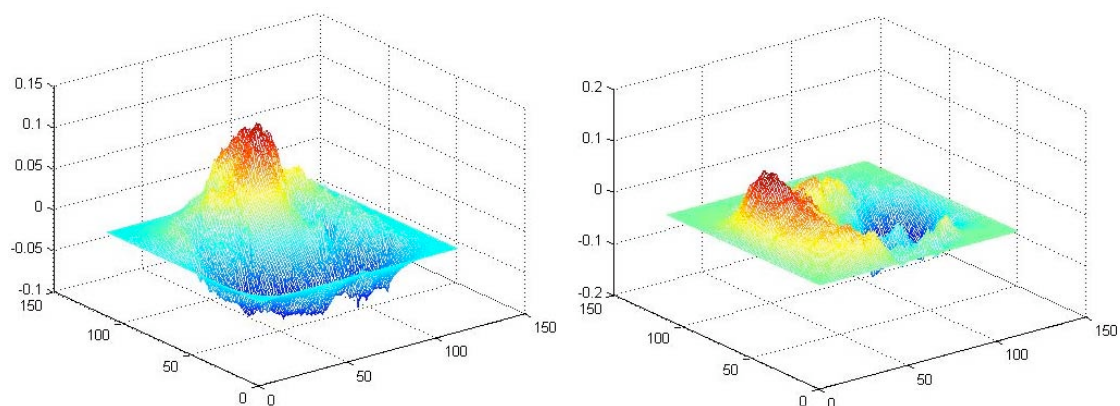


APPENDIX E : ELASTIC REGISTRATION

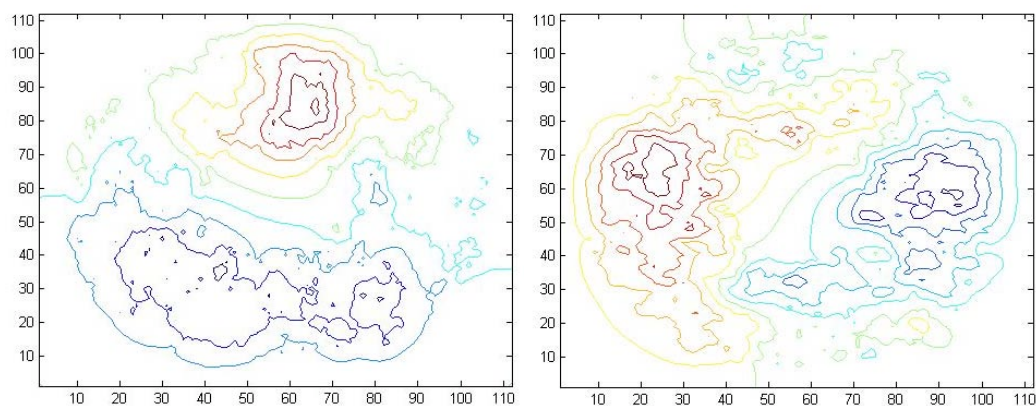
Note: All X,Y Displacements are scaled to 1 pixel length = 0.06"
P1-1 -> P1-2 : @ 0.5" height



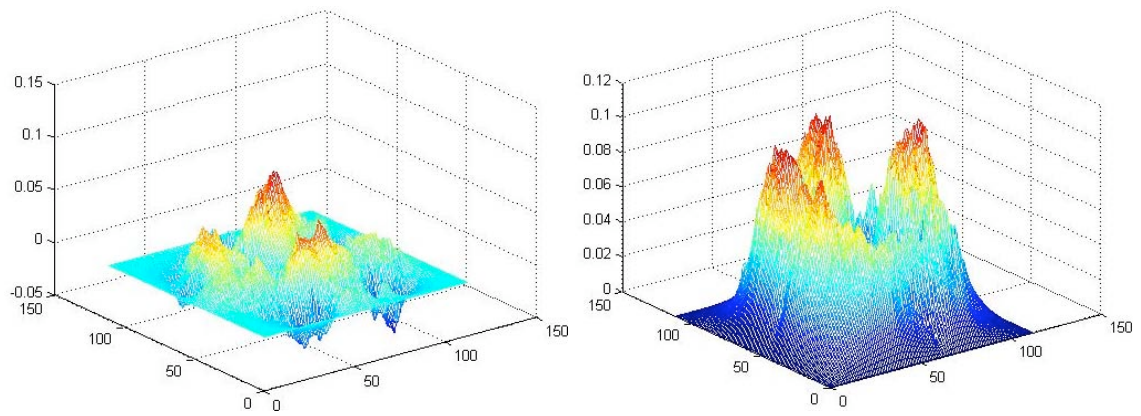
X and Y Displacement



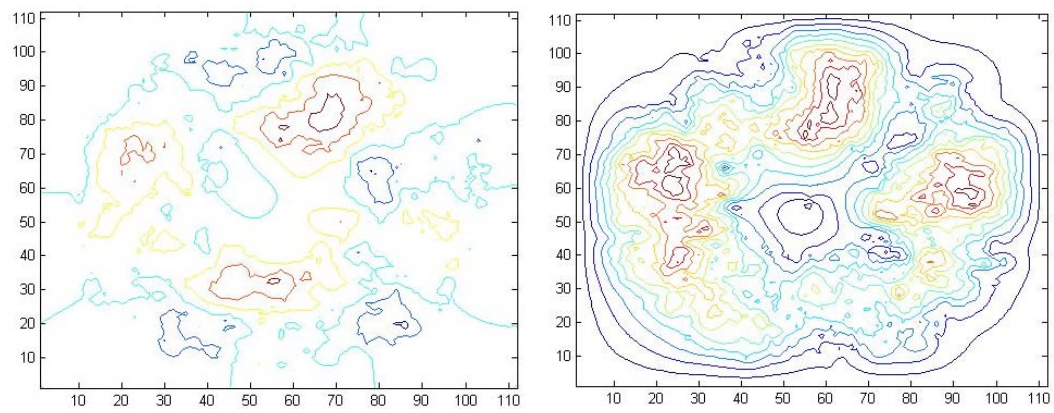
X and Y Displacement Contours



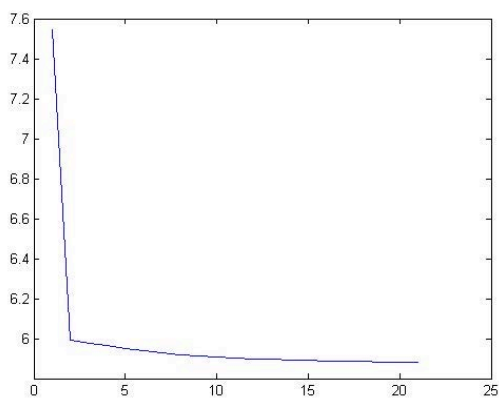
Radial and Tangential Displacement



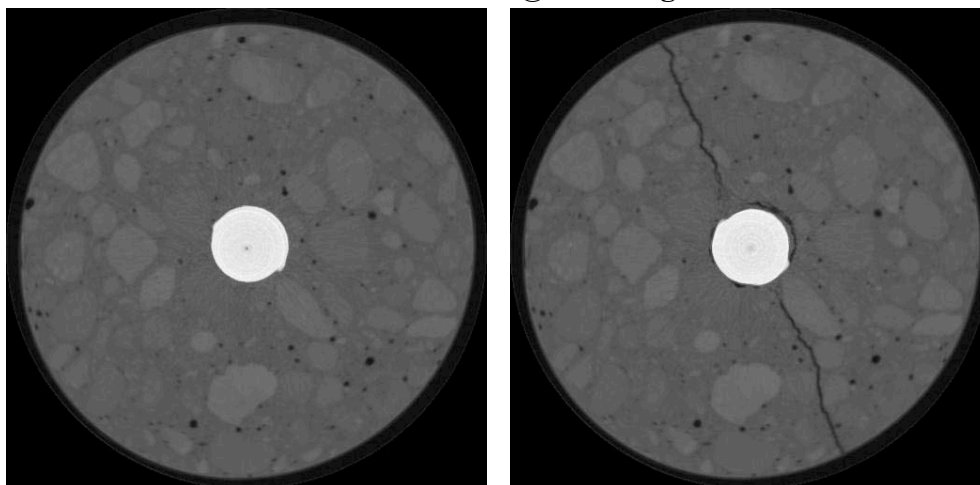
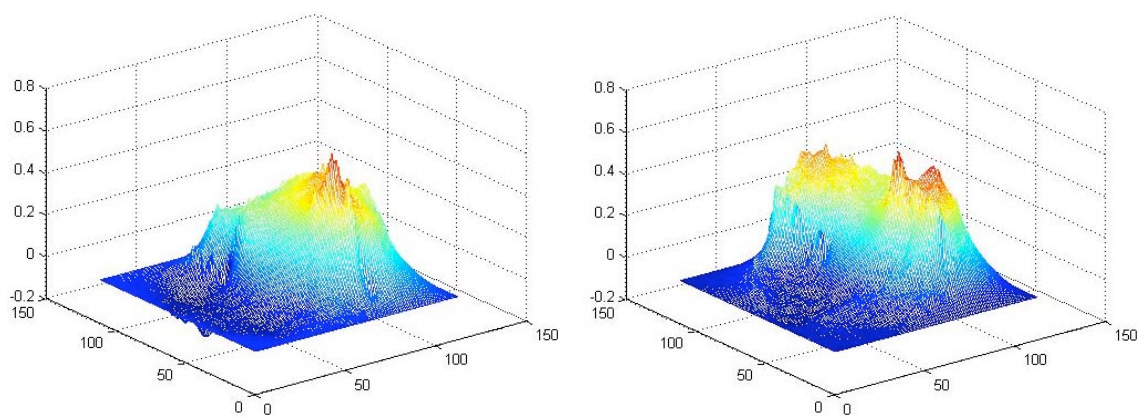
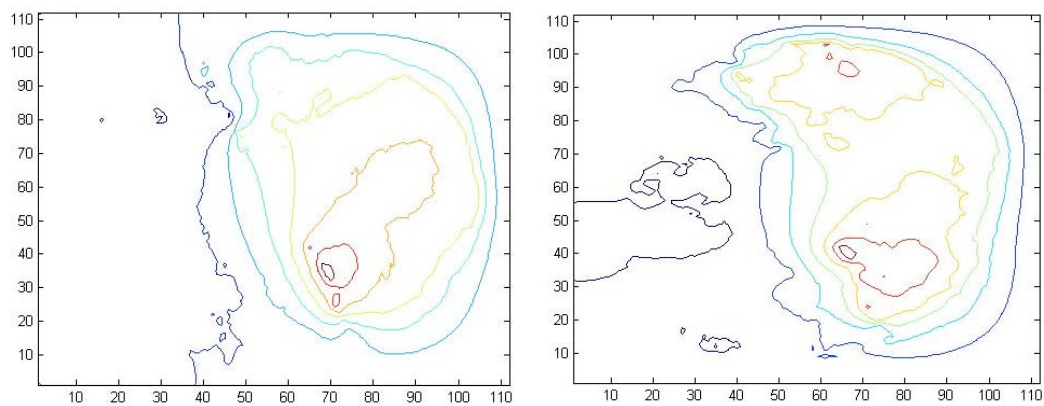
Radial and Tangential Displacement Contours



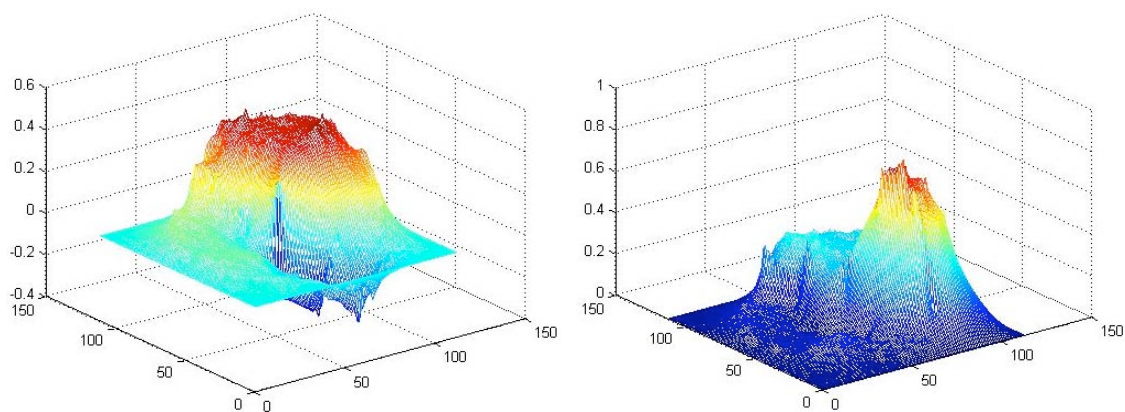
Objective Function



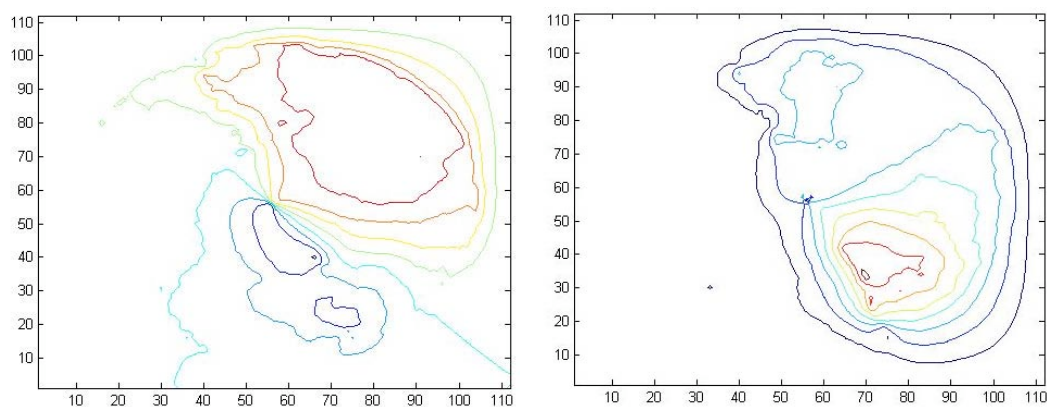
Iterations

P1-2 -> P1-3 @ 0.5" heightX and Y DisplacementX and Y Displacement Contours

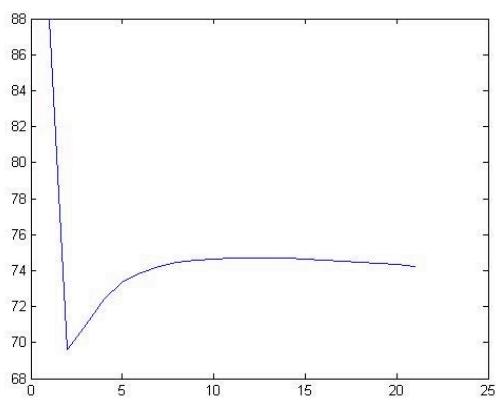
Radial and Tangential Displacement



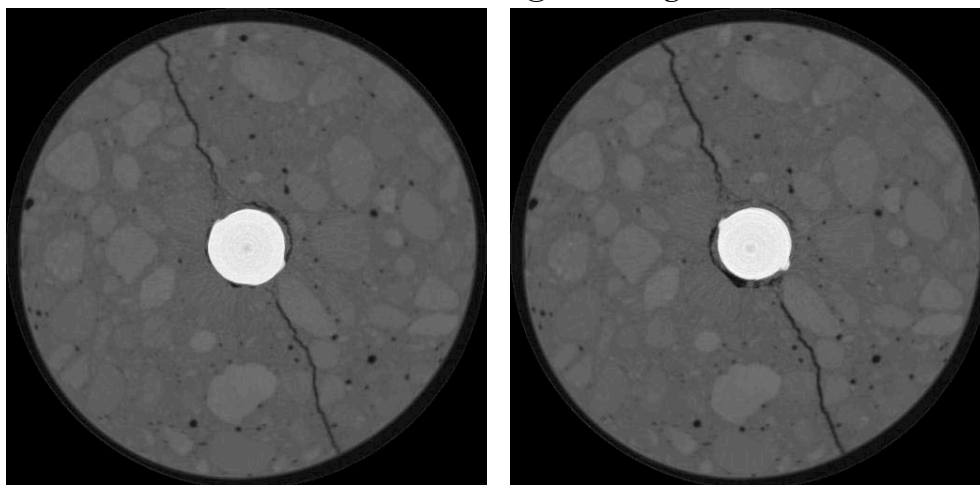
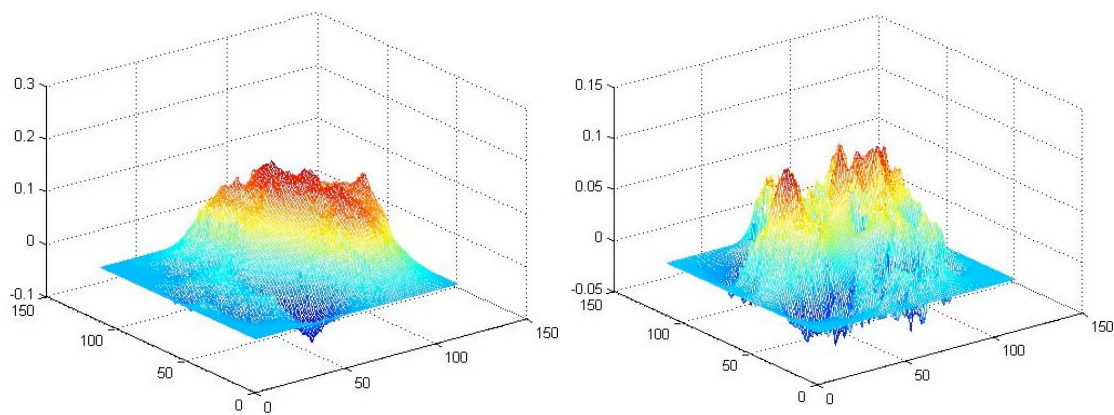
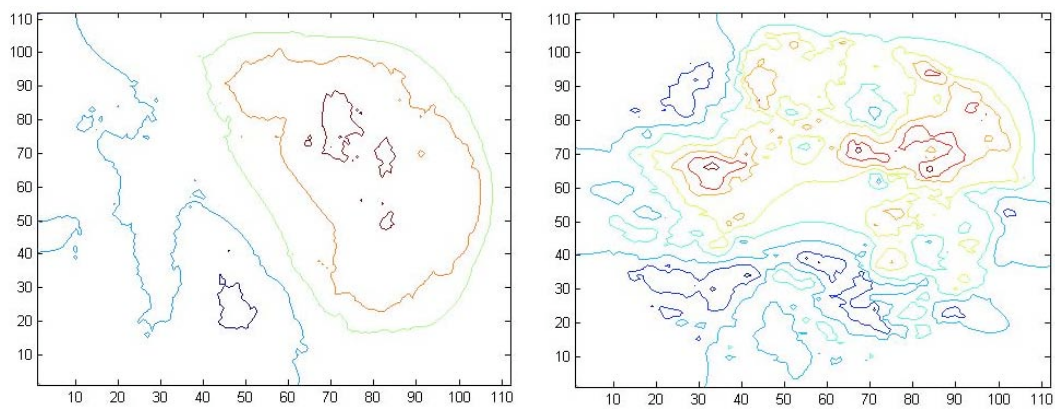
Radial and Tangential Displacement Contours



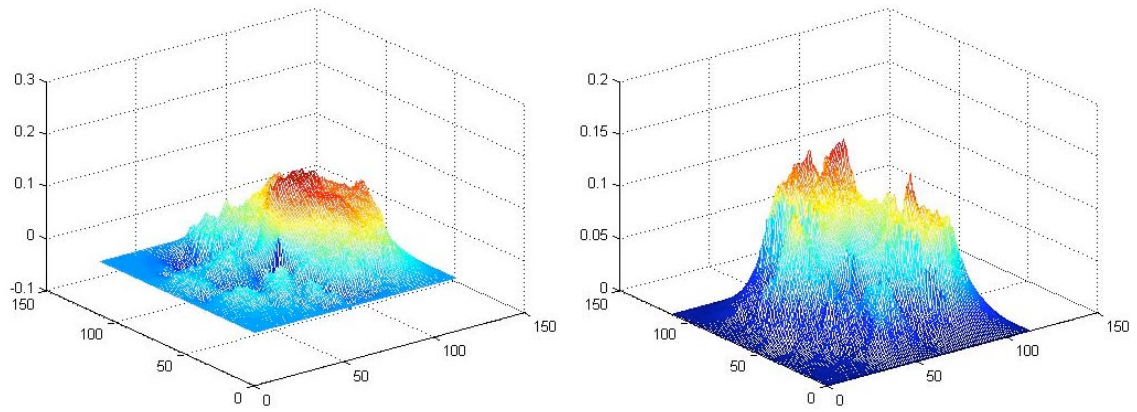
Objective Function



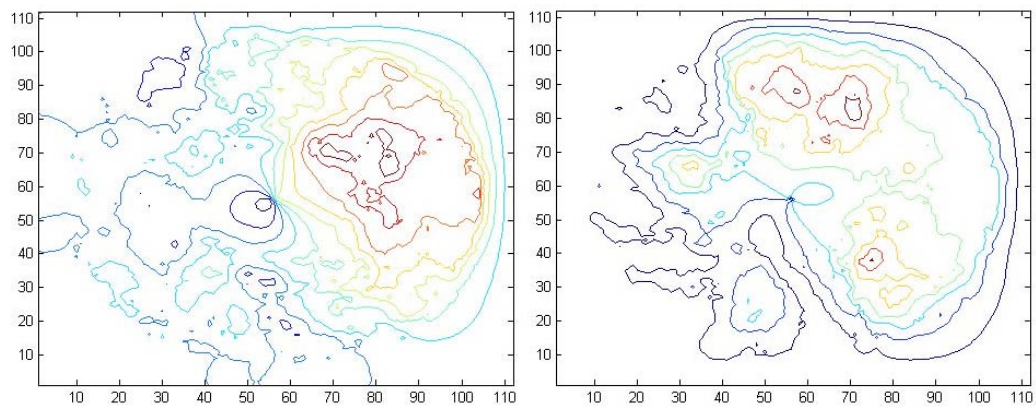
Iterations

P1-3 -> P1-4 @ 0.5" heightX and Y DisplacementX and Y Displacement Contours

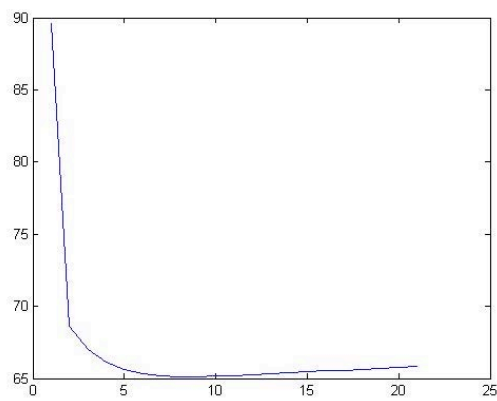
Radial and Tangential Displacement



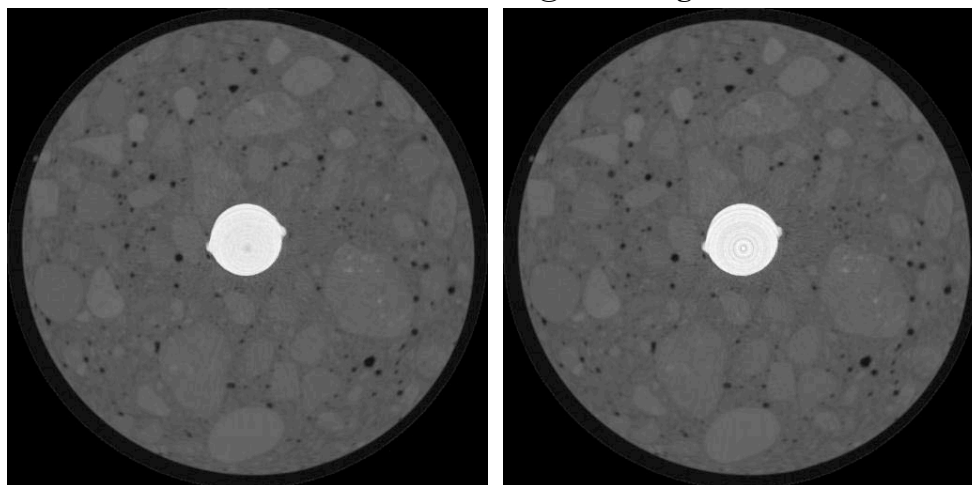
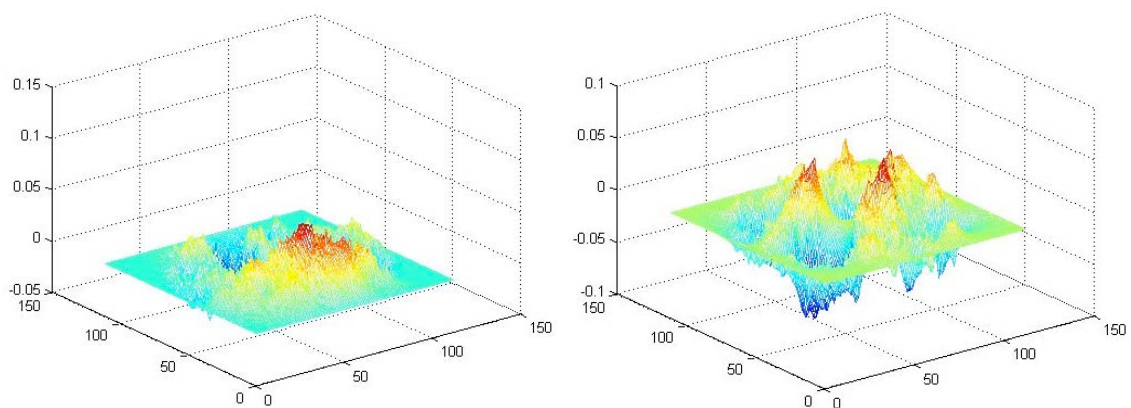
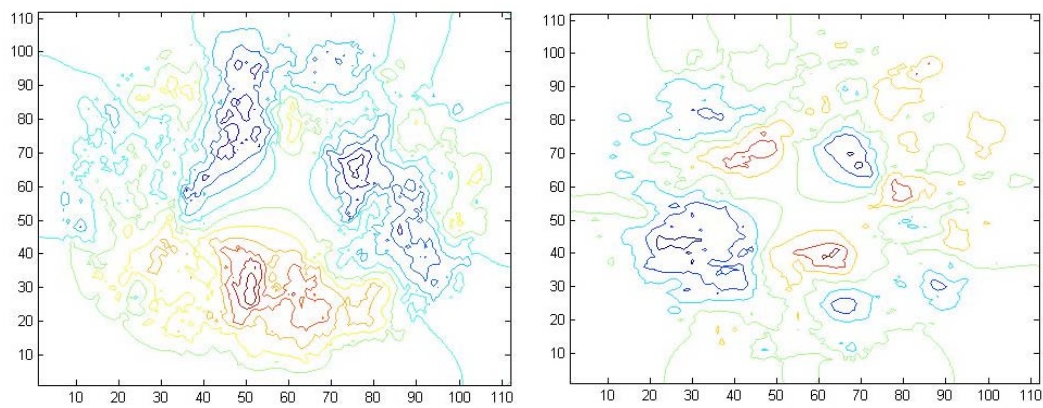
Radial and Tangential Displacement Contours



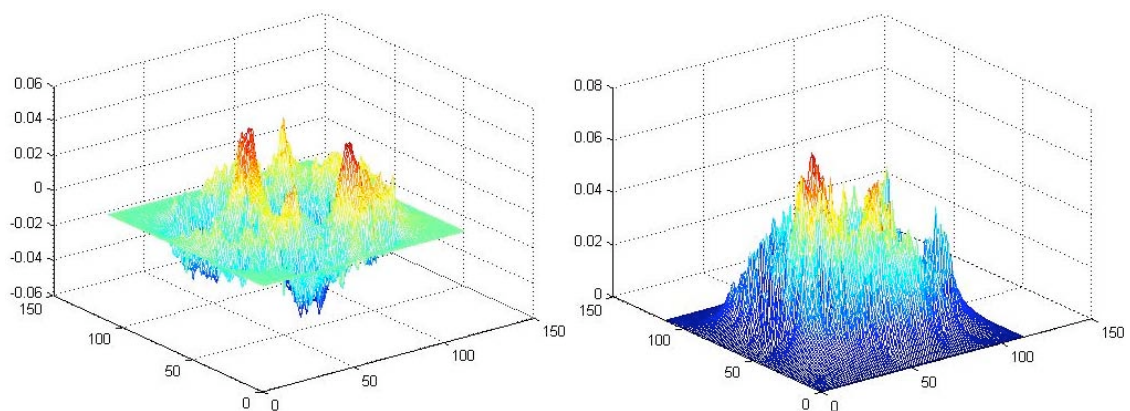
Objective Function



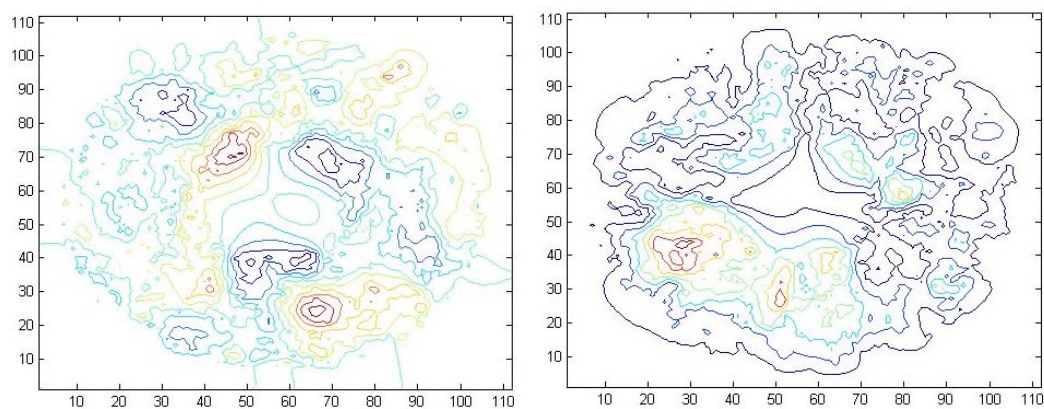
Iterations

P3F-1 -> P3F-2 @ 0.5" heightX and Y DisplacementX and Y Displacement Contours

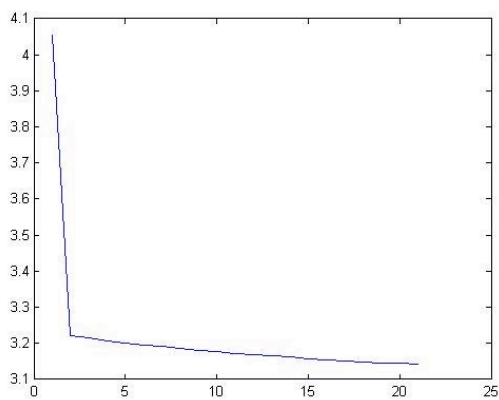
Radial and Tangential Displacement



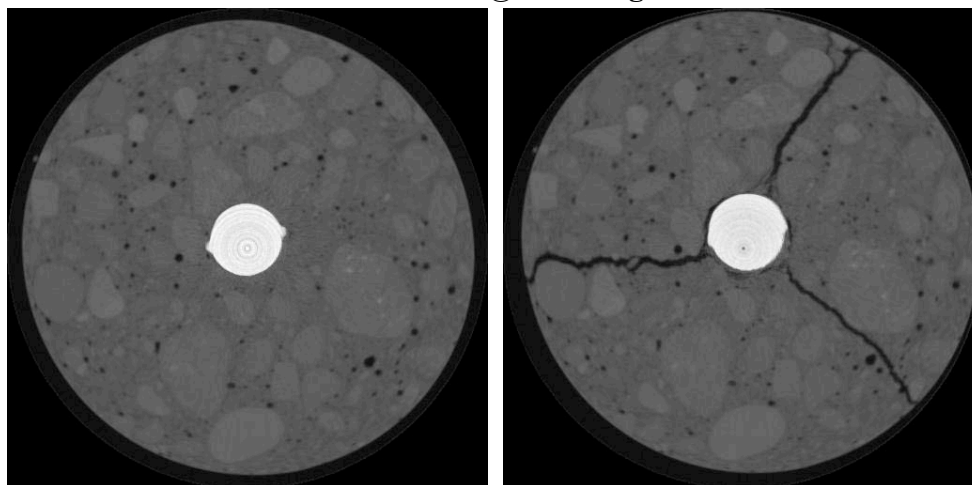
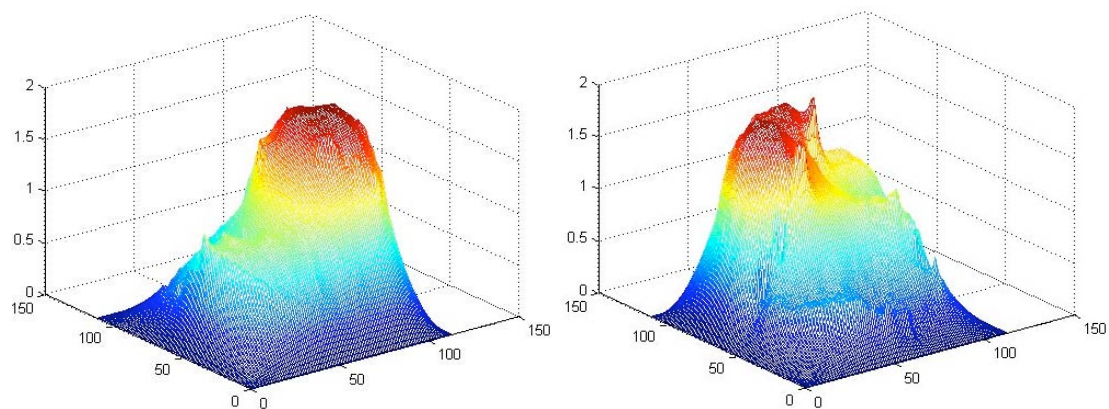
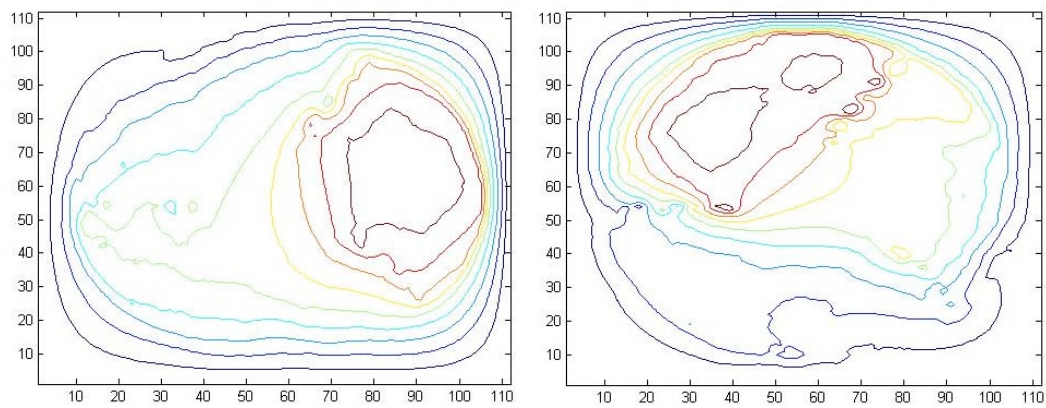
Radial and Tangential Displacement Contours



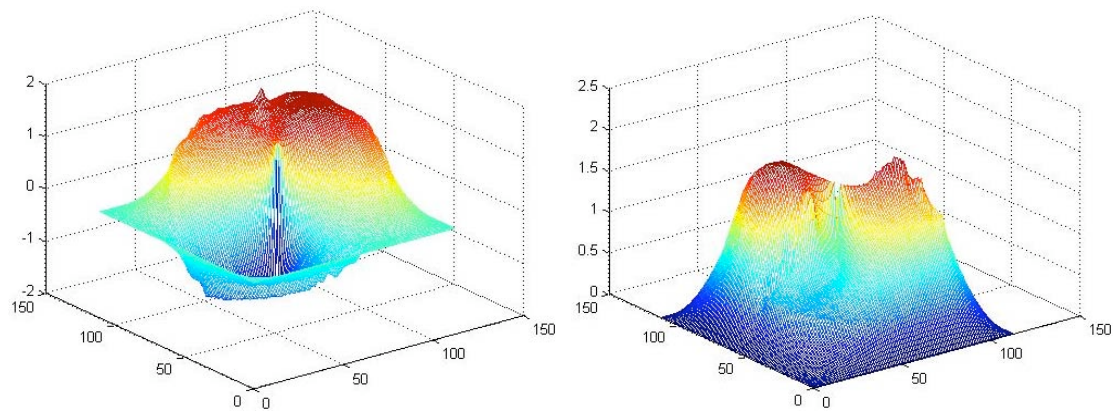
Objective Function



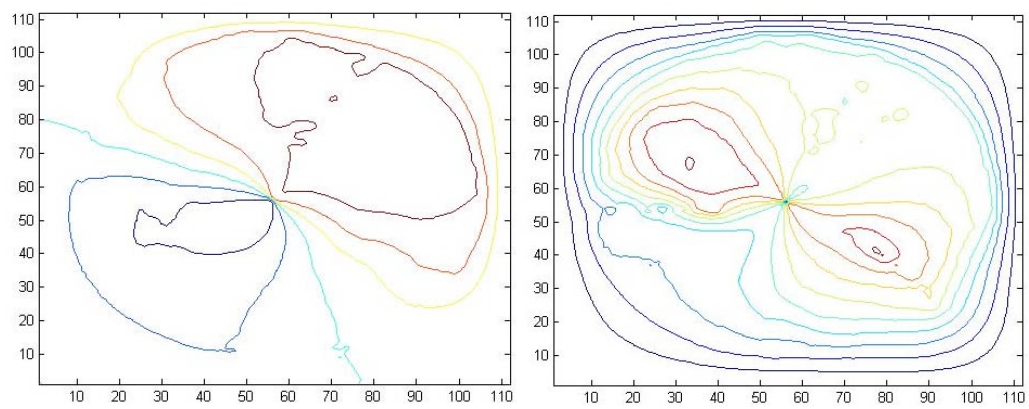
Iterations

P3F-2 -> P3F-3 @ 0.5" heightX and Y DisplacementX and Y Displacement Contours

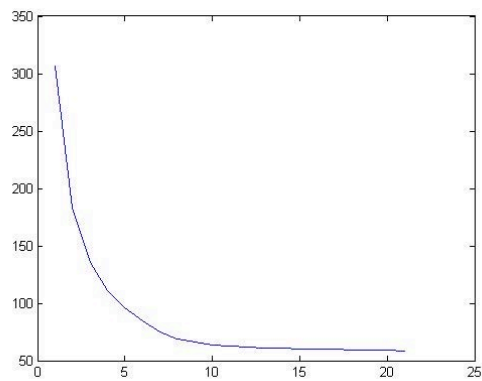
Radial and Tangential Displacement



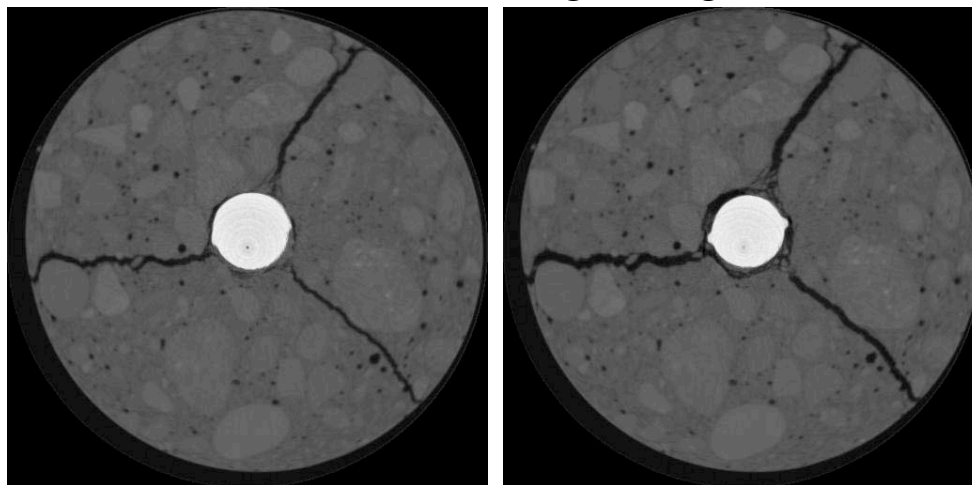
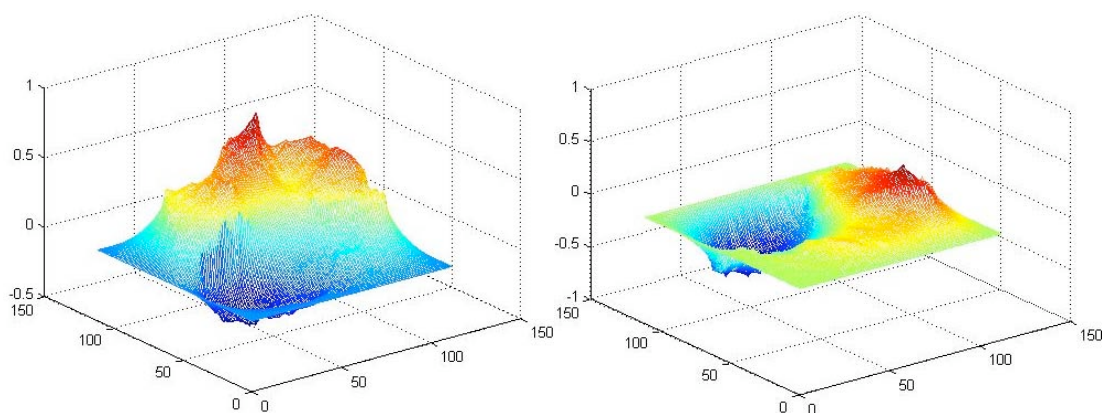
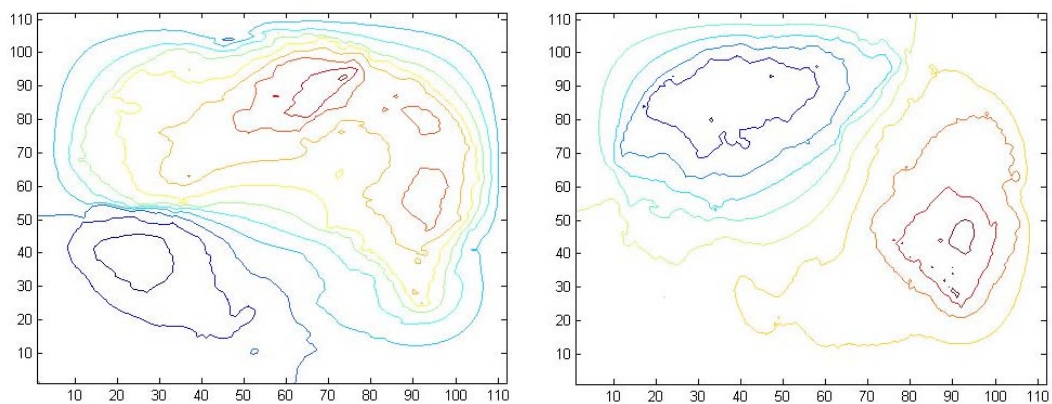
Radial and Tangential Displacement Contours



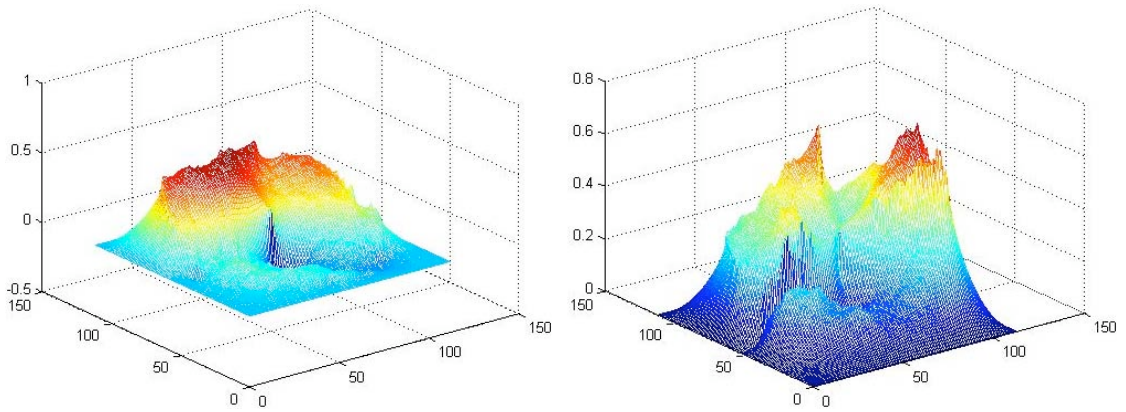
Objective Function



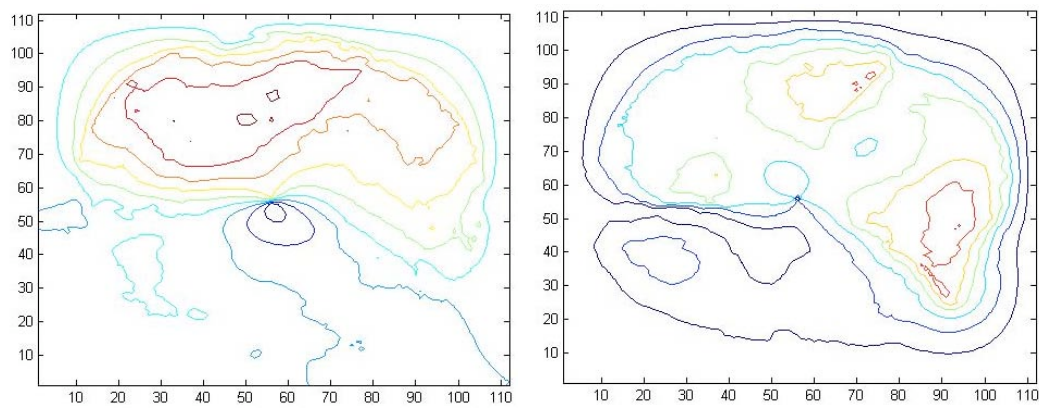
Iterations

P3F-3 -> P3F-4 @ 0.5" heightX and Y DisplacementX and Y Displacement Contours

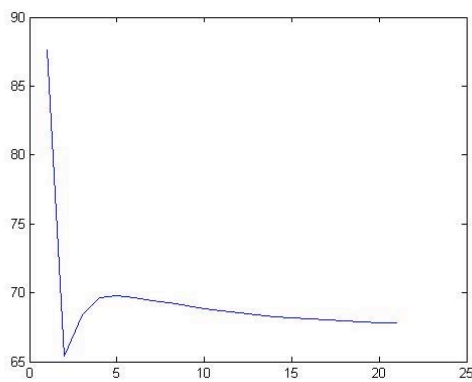
Radial and Tangential Displacement



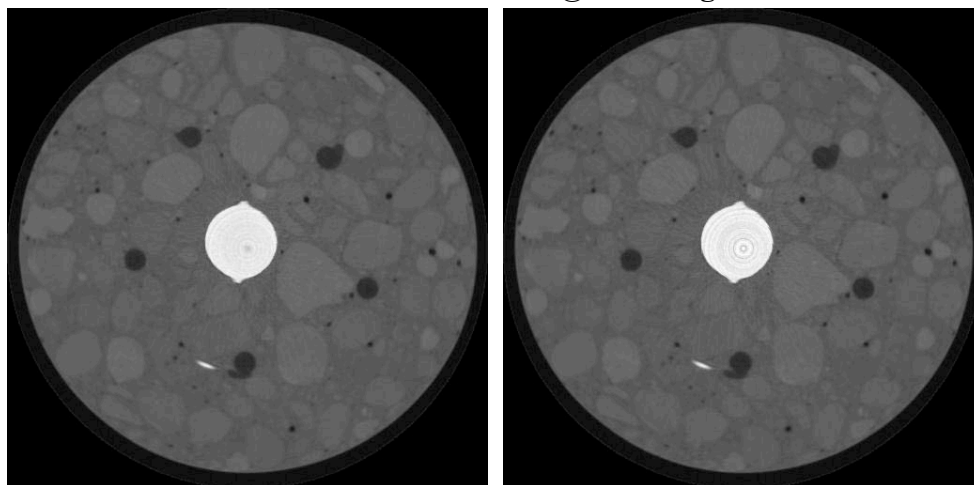
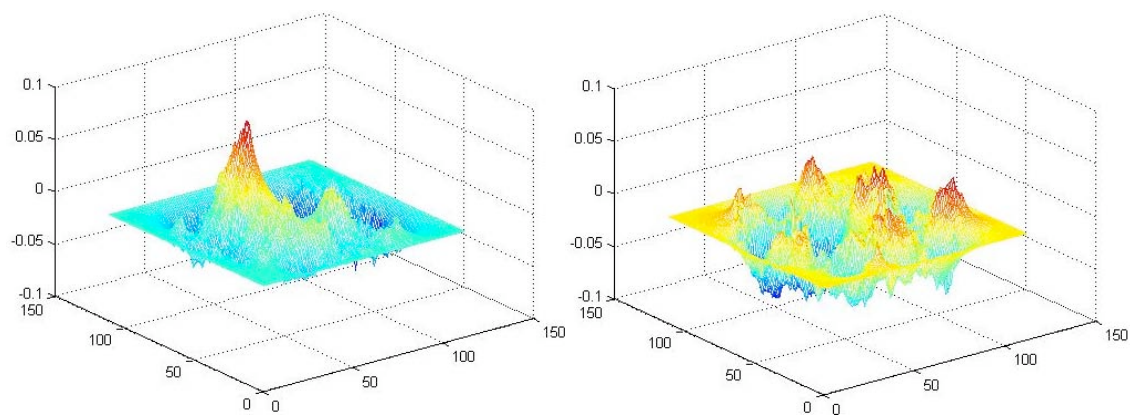
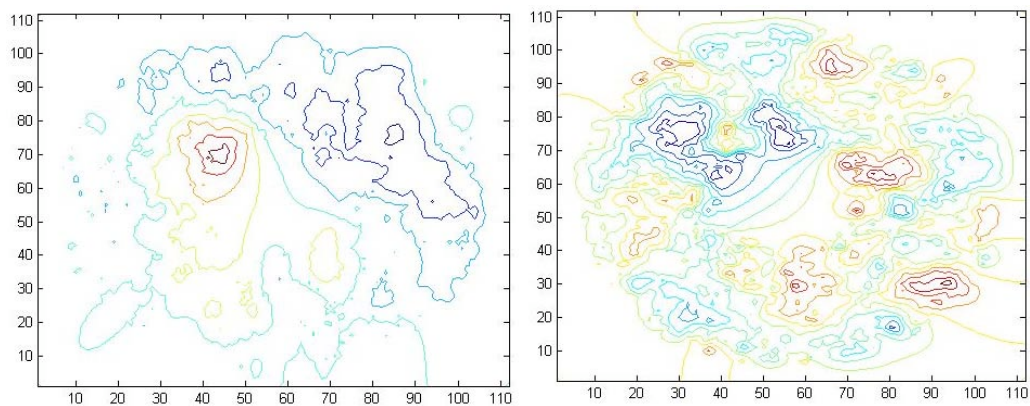
Radial and Tangential Displacement Contours



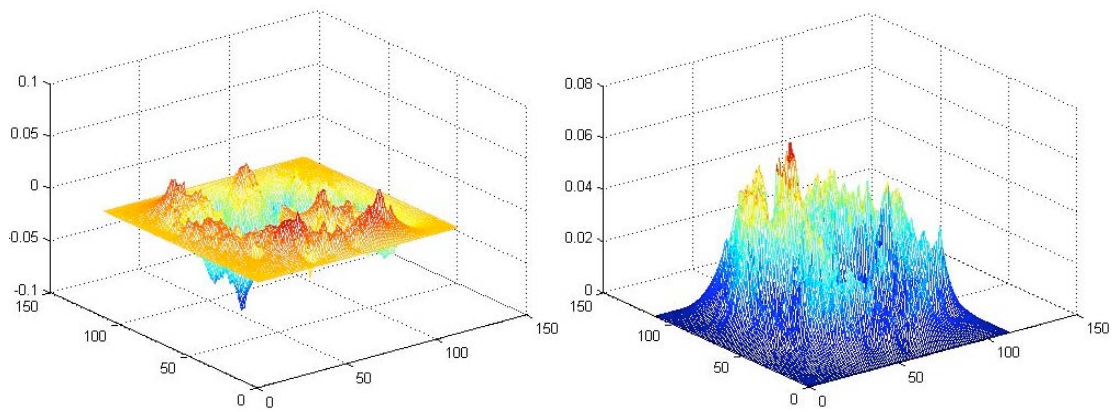
Objective Function



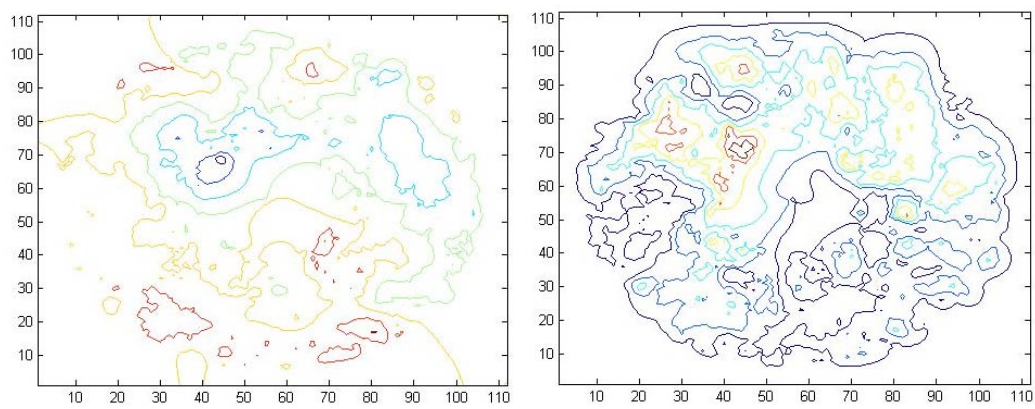
Iterations

P3W1A-1 -> P3W1A-2 @ 0.5" heightX and Y DisplacementX and Y Displacement Contours

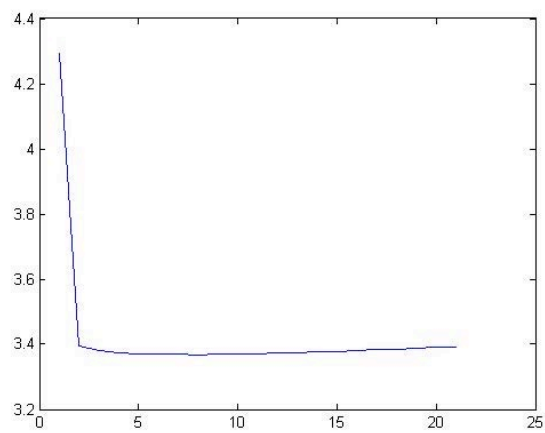
Radial and Tangential Displacement



Radial and Tangential Displacement Contours

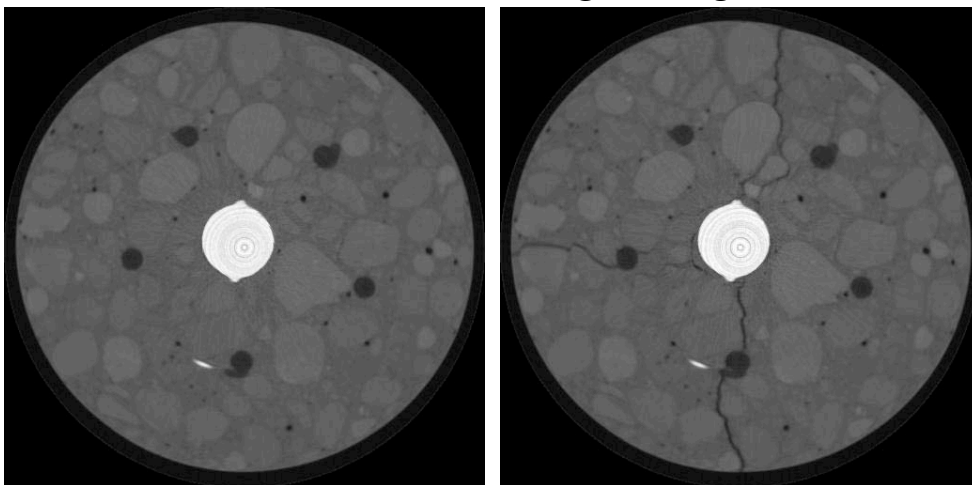


Objective Function

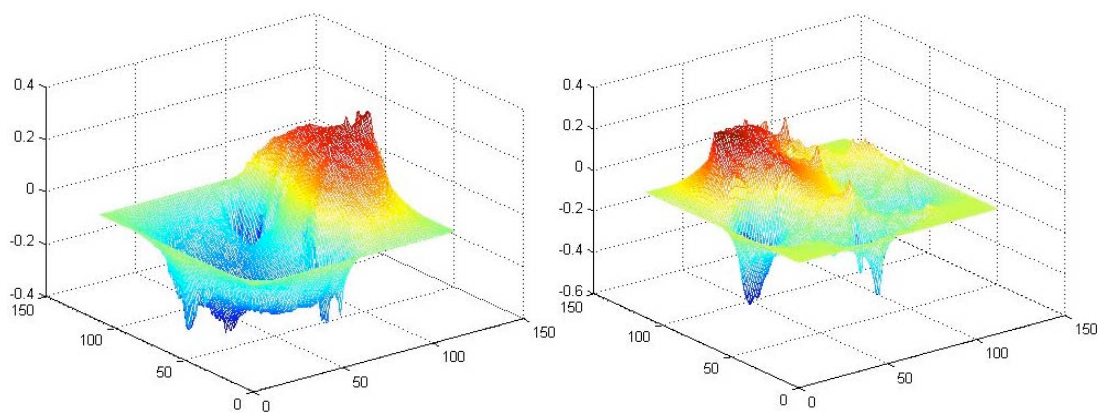


Iterations

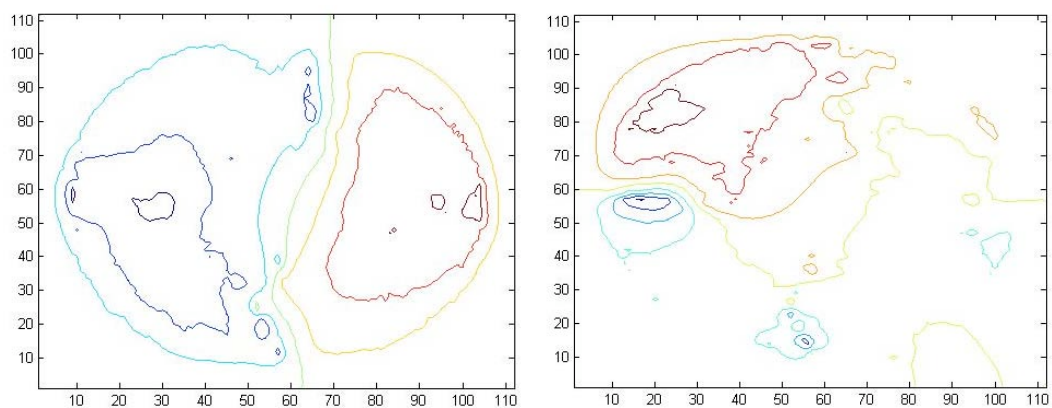
P3W1A-2 -> P3W1A-3 @ 0.5" height



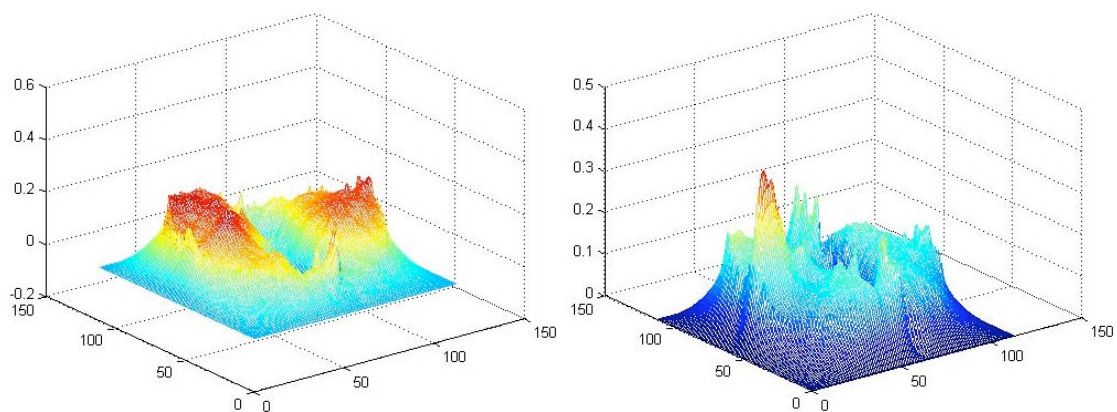
X and Y Displacement



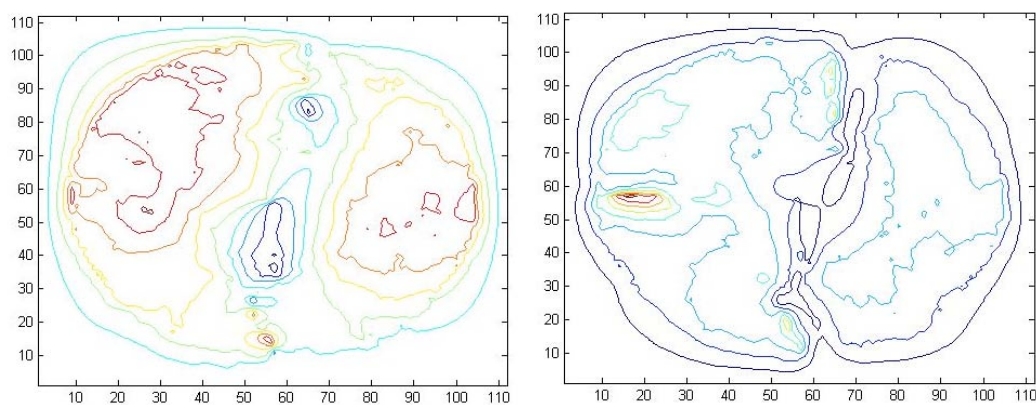
X and Y Displacement Contours



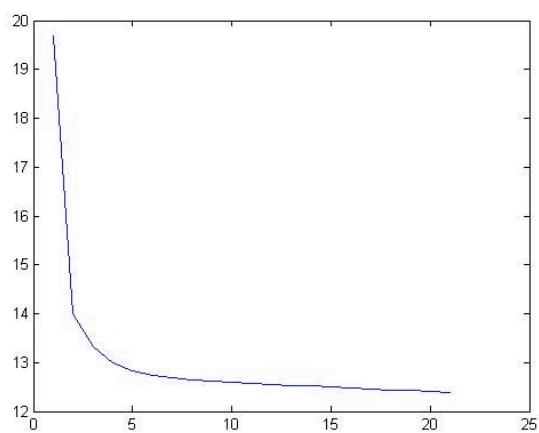
Radial and Tangential Displacement



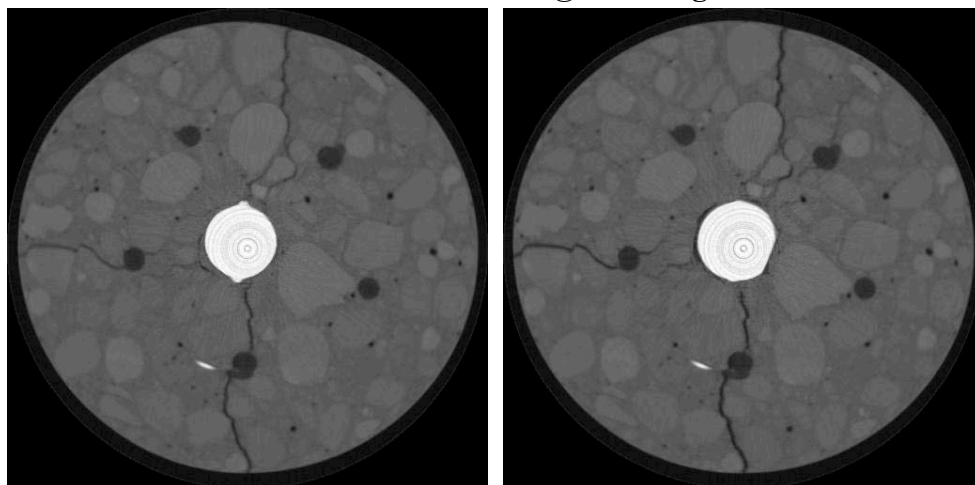
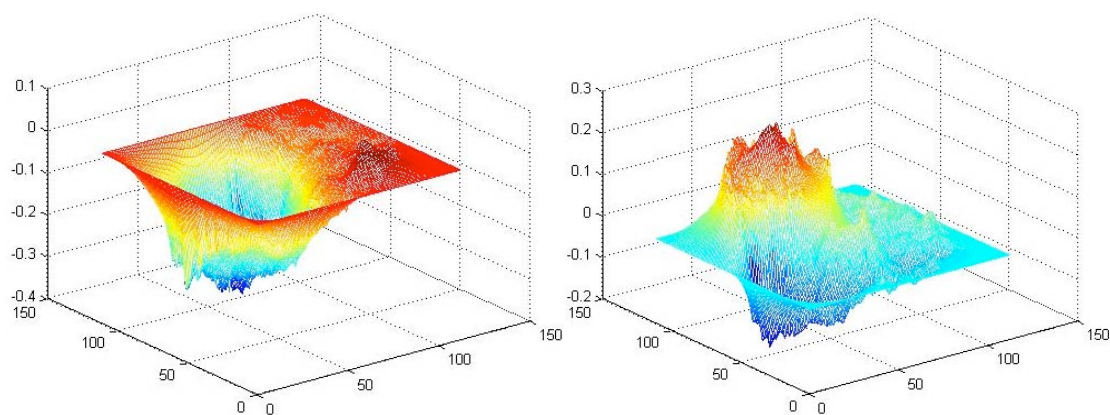
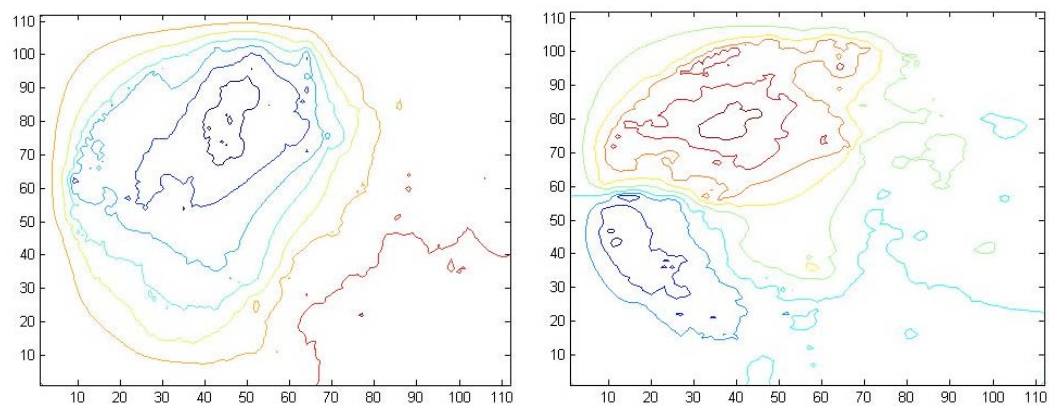
Radial and Tangential Displacement Contours



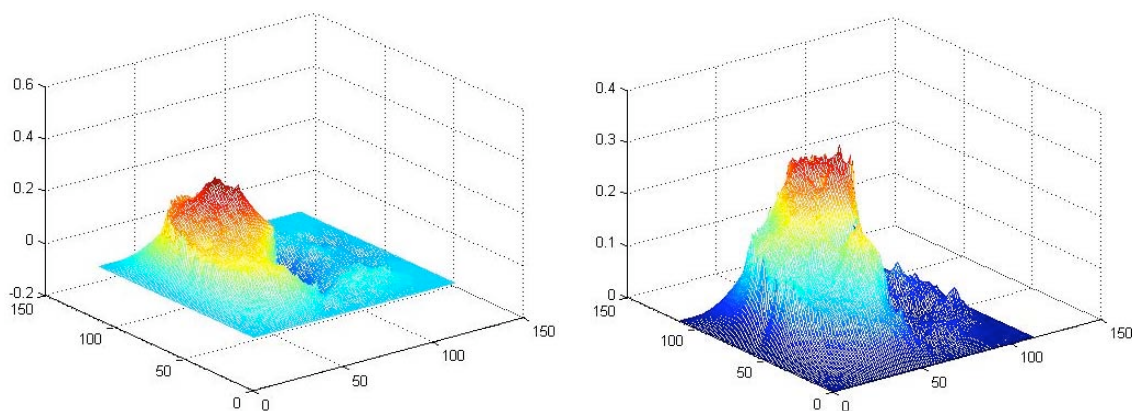
Objective Function



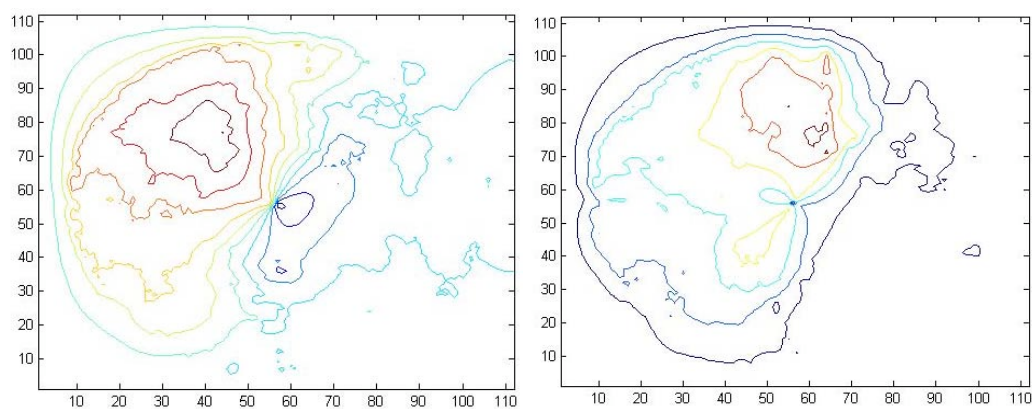
Iterations

P3W1A-3 -> P3W1A-4 @ 0.5" heightX and Y DisplacementX and Y Displacement Contours

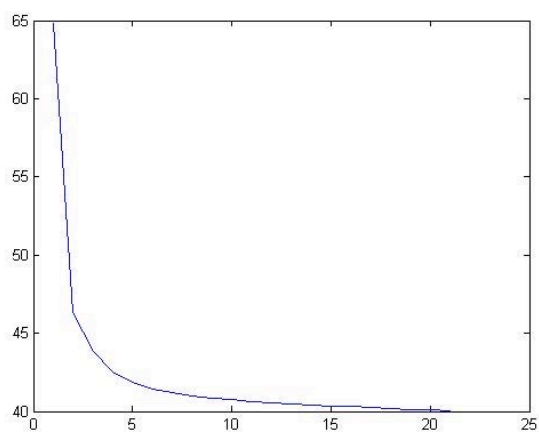
Radial and Tangential Displacement



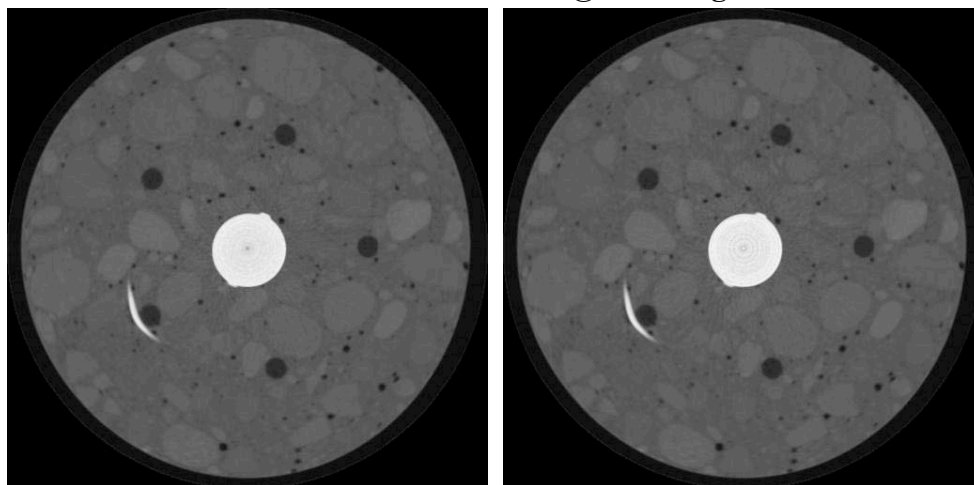
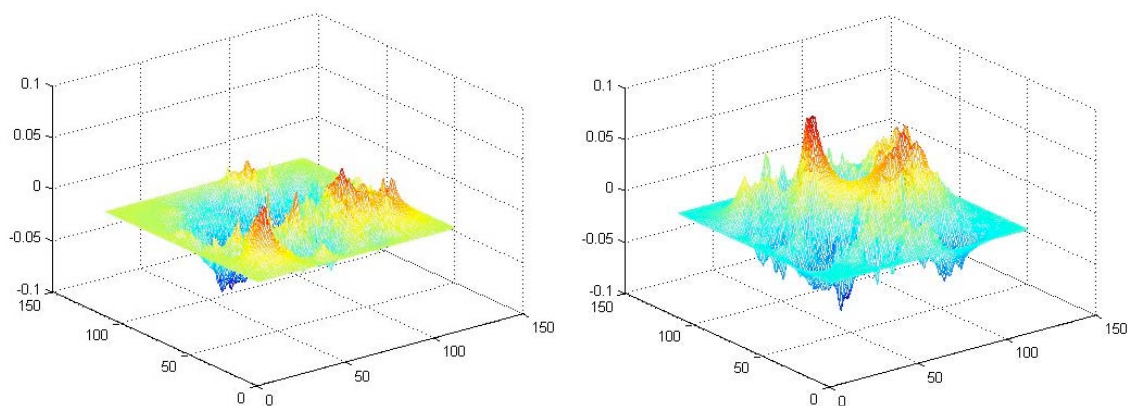
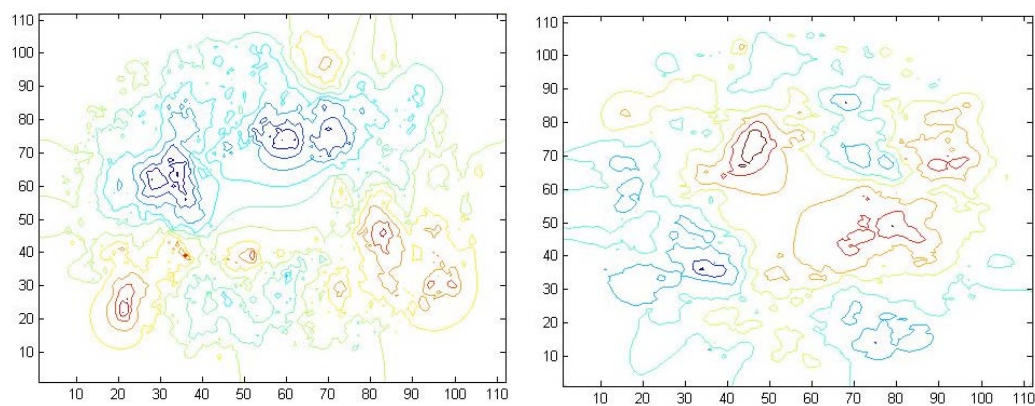
Radial and Tangential Displacement Contours



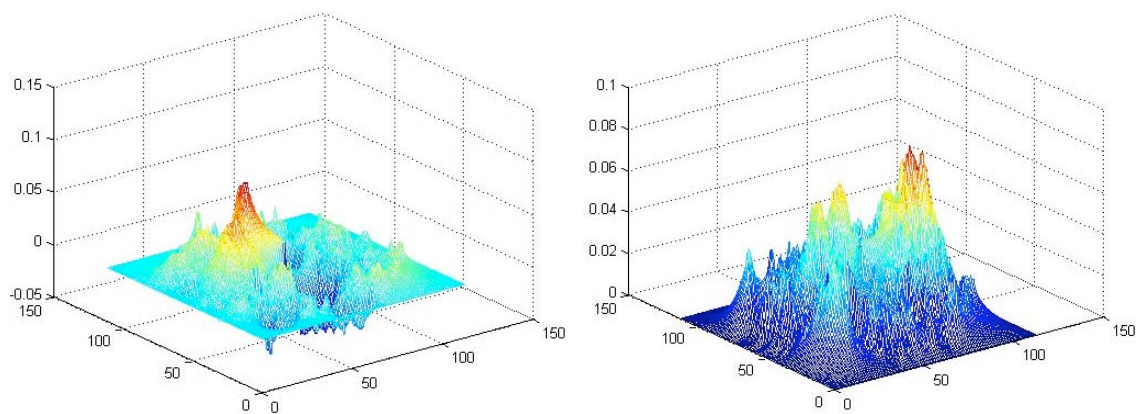
Objective Function



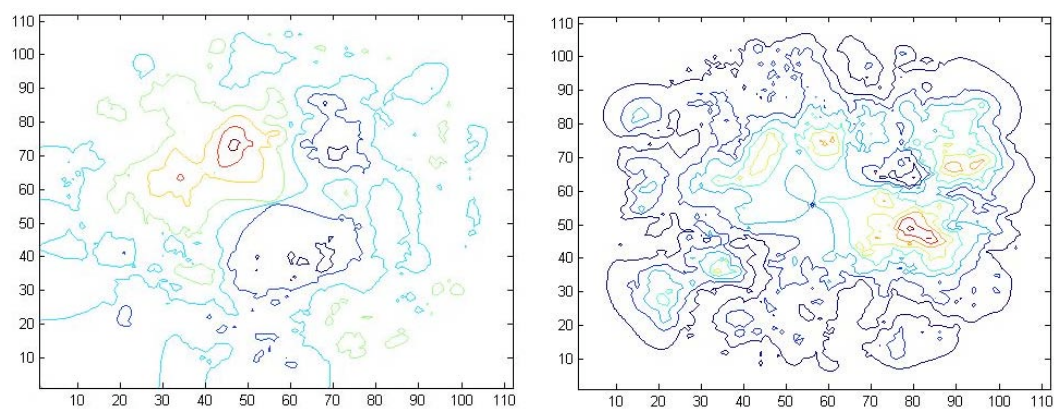
Iterations

P3W1B-1 -> P3W1A-2 @ 0.5" heightX and Y DisplacementX and Y Displacement Contours

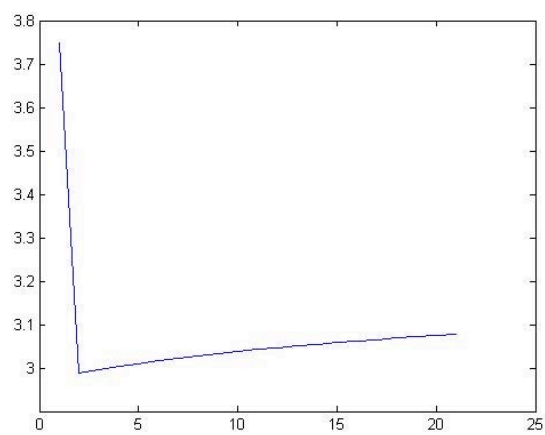
Radial and Tangential Displacement



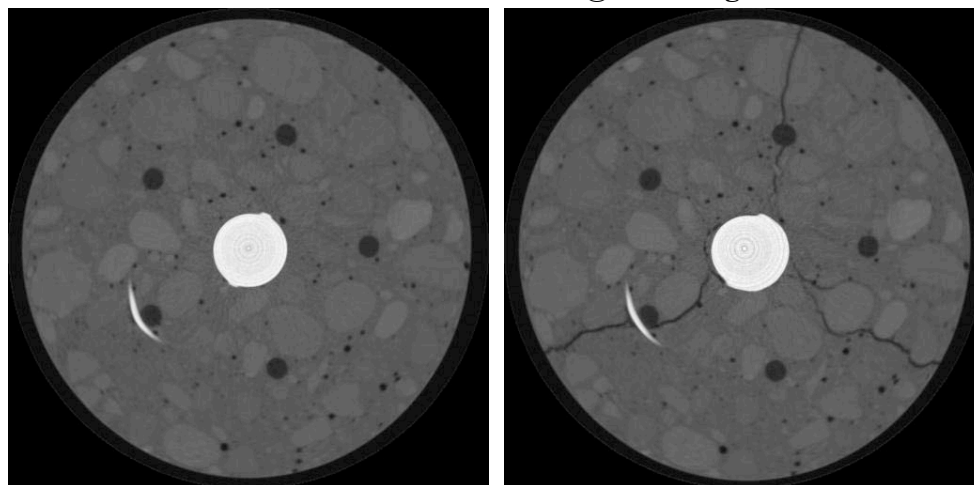
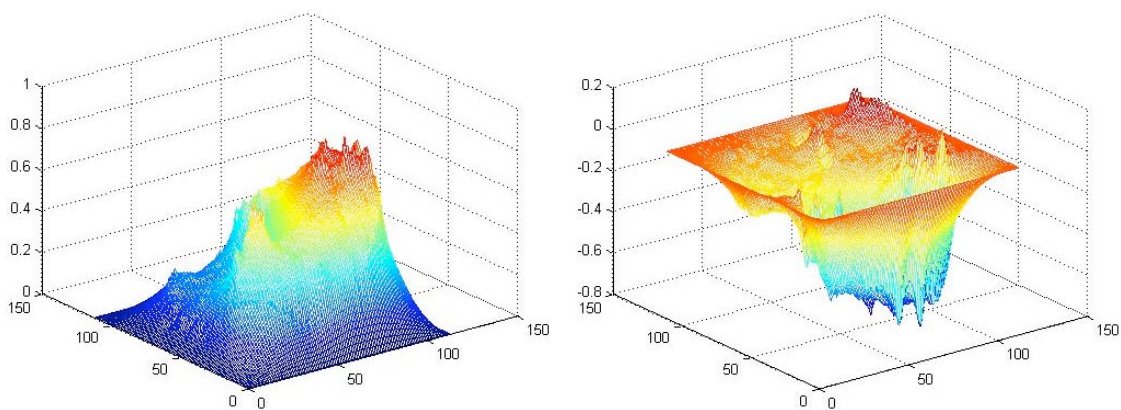
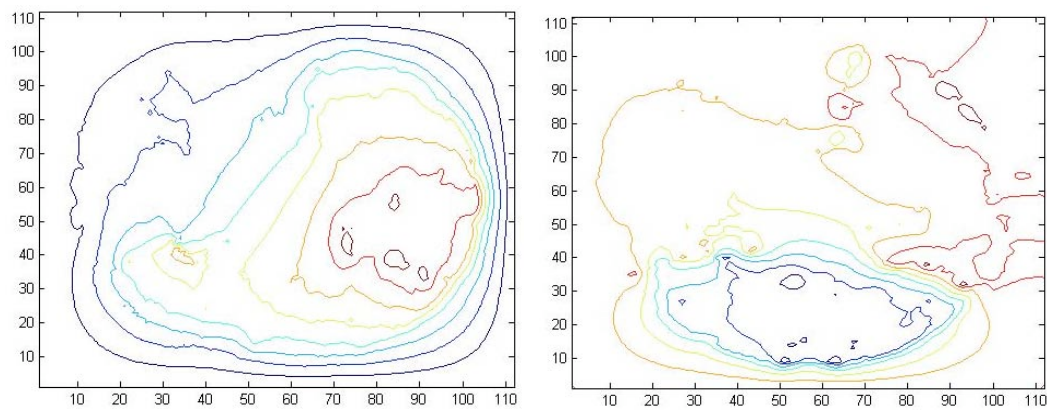
Radial and Tangential Displacement Contours



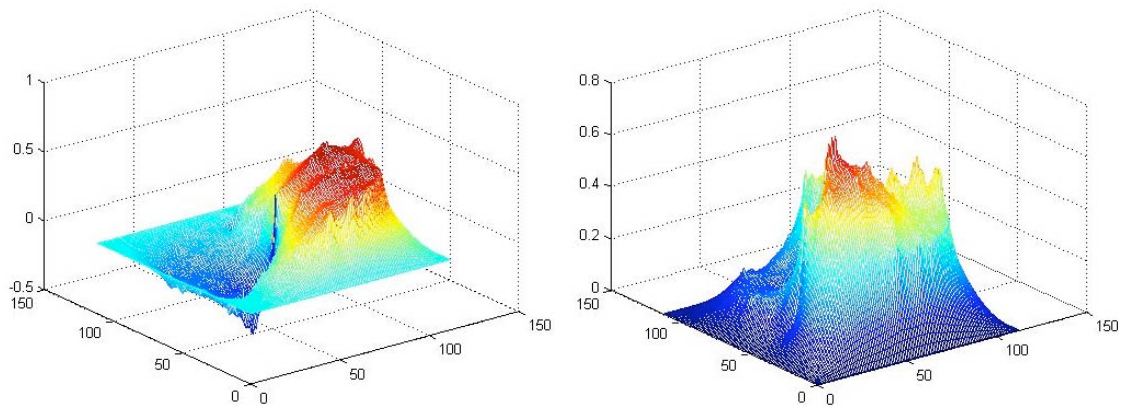
Objective Function



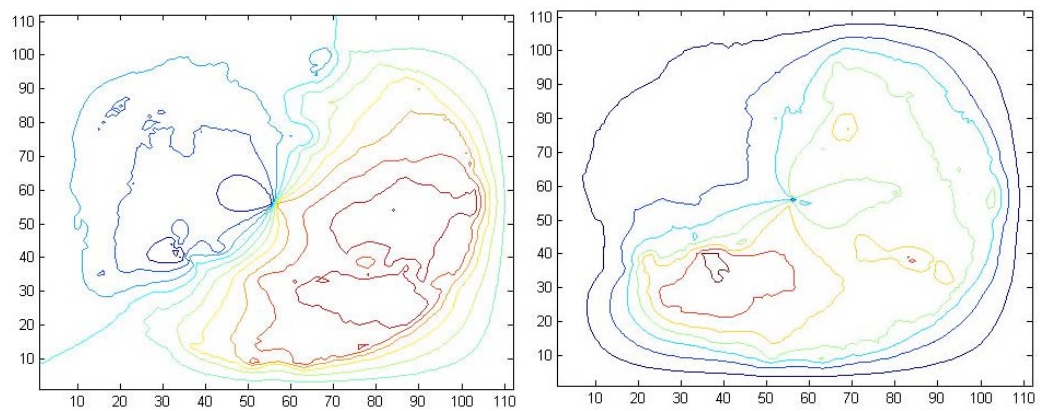
Iterations

P3W1B-2 -> P3W1A-3 @ 0.5" heightX and Y DisplacementX and Y Displacement Contours

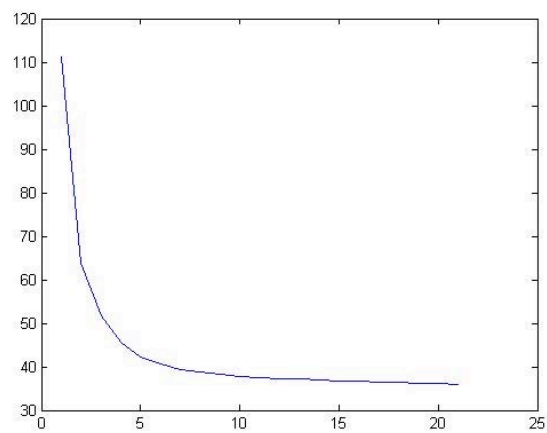
Radial and Tangential Displacement



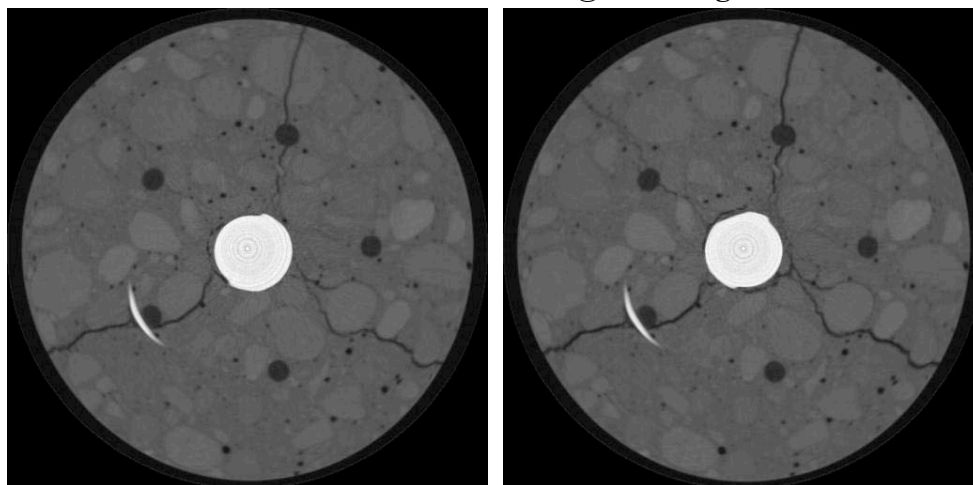
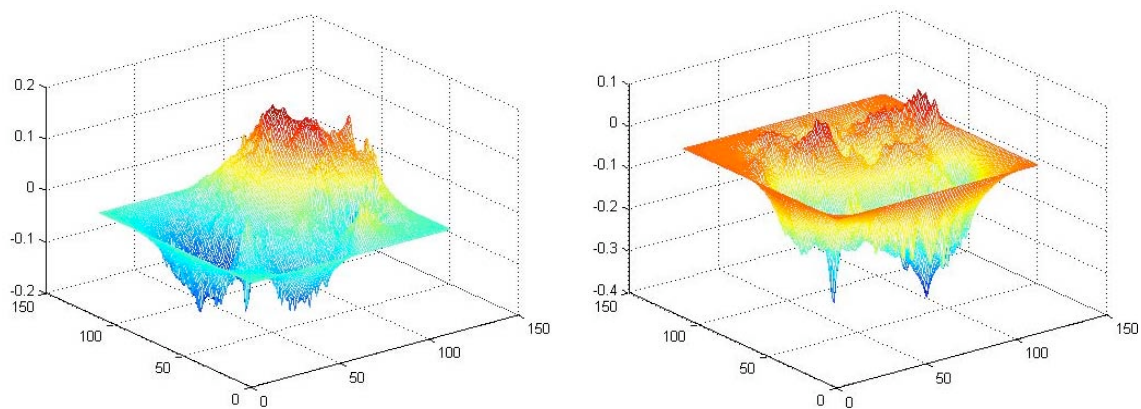
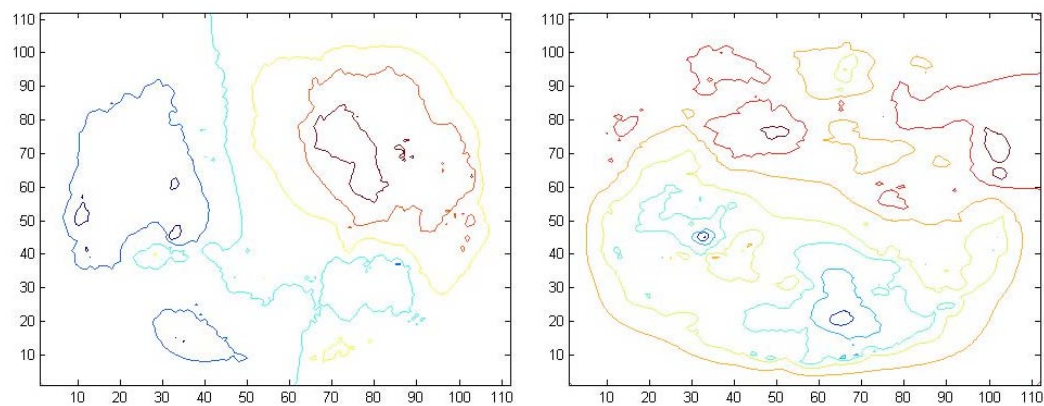
Radial and Tangential Displacement Contours



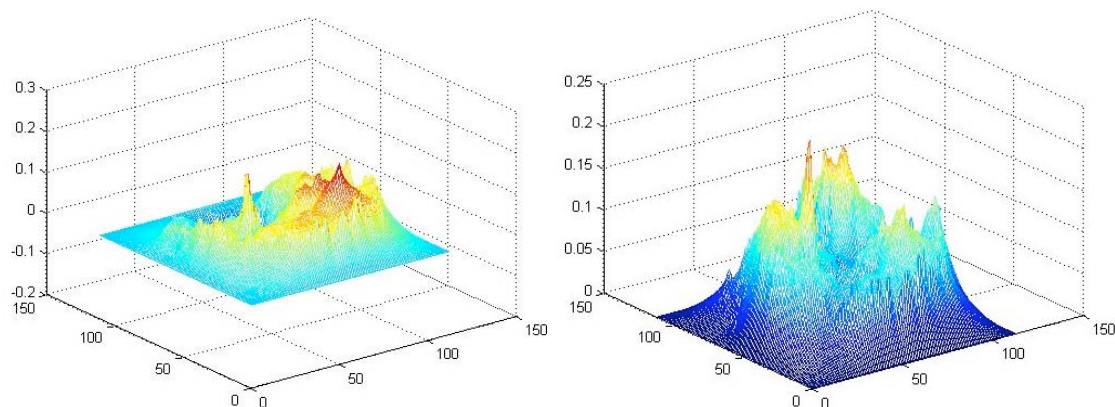
Objective Function



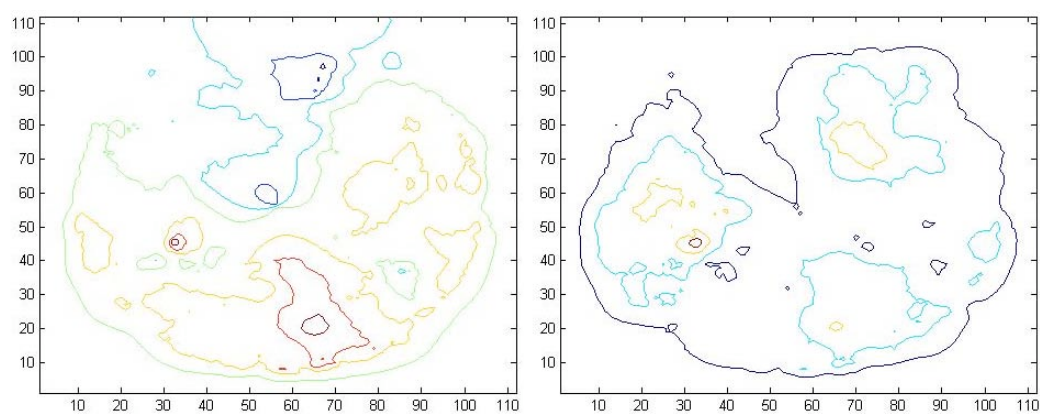
Iterations

P3W1B-3 -> P3W1A-4 @ 0.5" heightX and Y DisplacementX and Y Displacement Contours

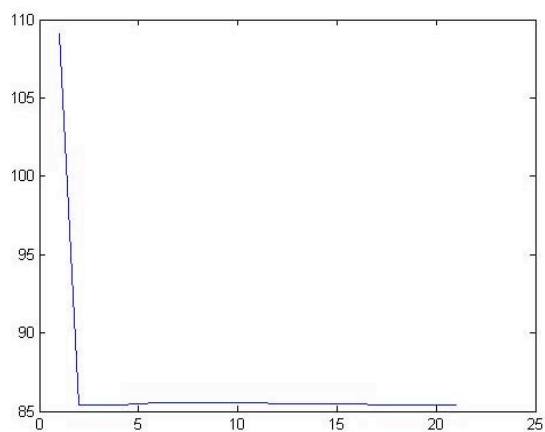
Radial and Tangential Displacement



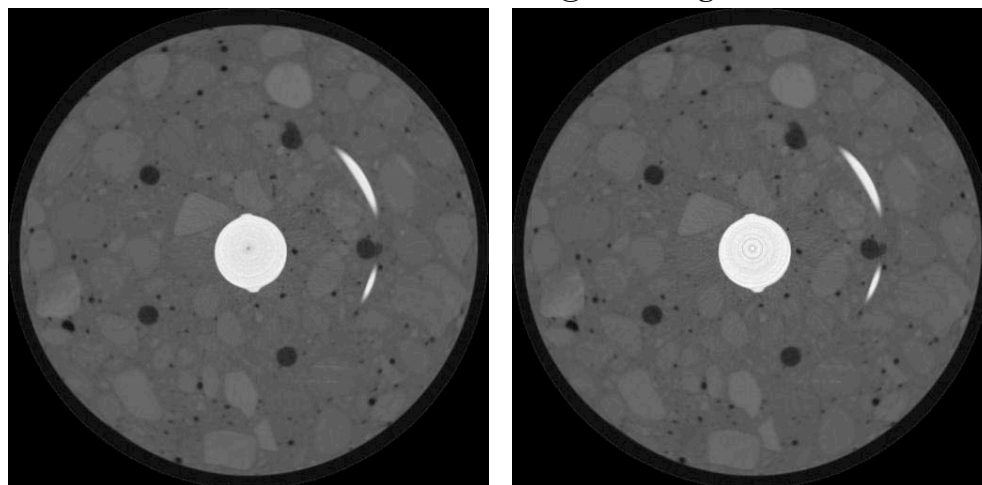
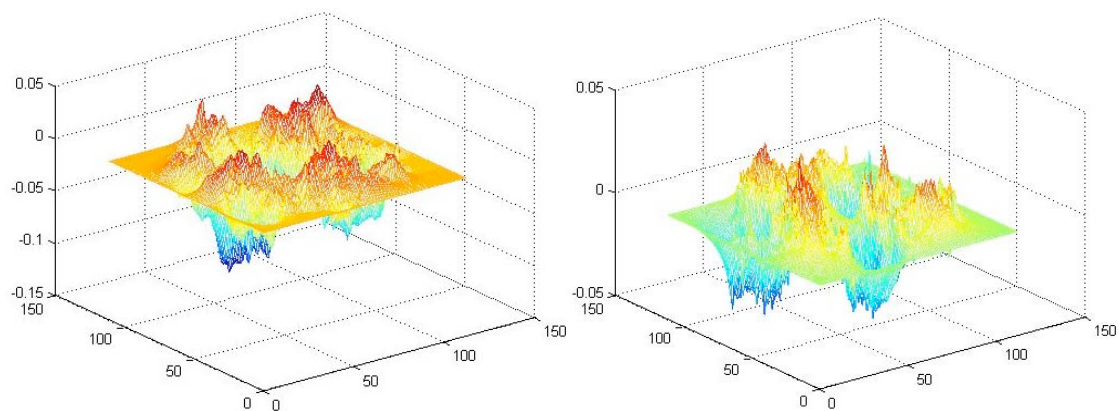
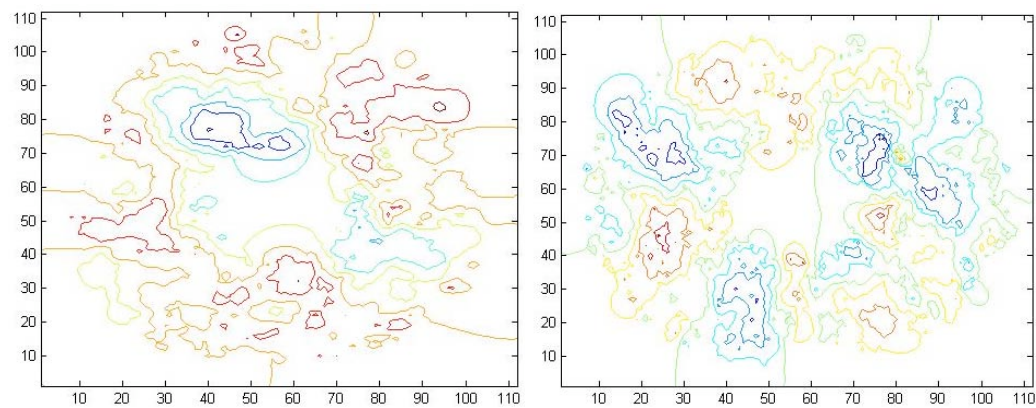
Radial and Tangential Displacement Contours



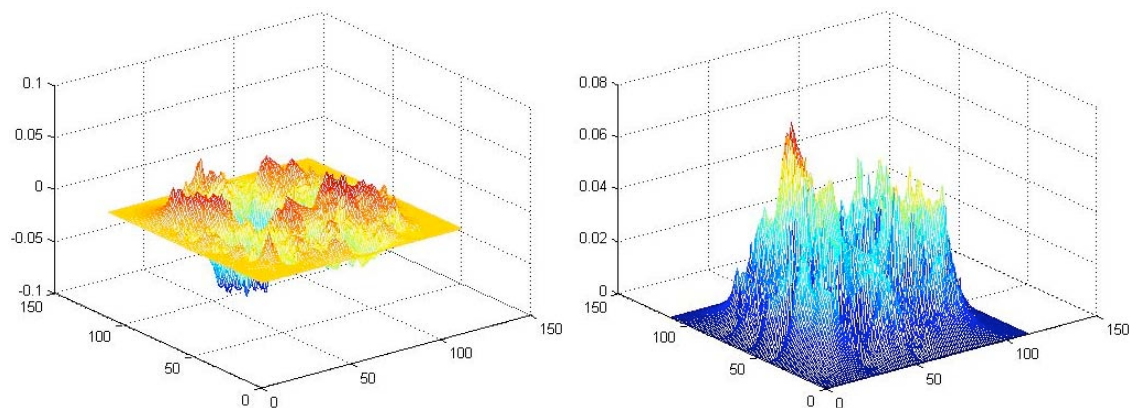
Objective Function



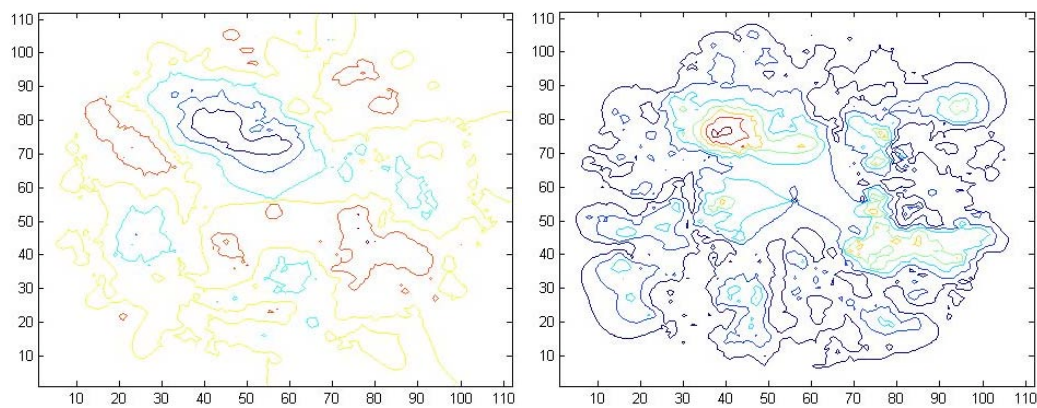
Iterations

P3W2-1 -> P3W2-2 @ 0.5" heightX and Y DisplacementX and Y Displacement Contours

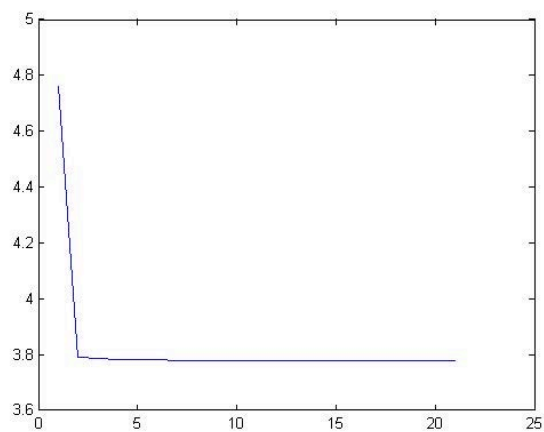
Radial and Tangential Displacement



Radial and Tangential Displacement Contours

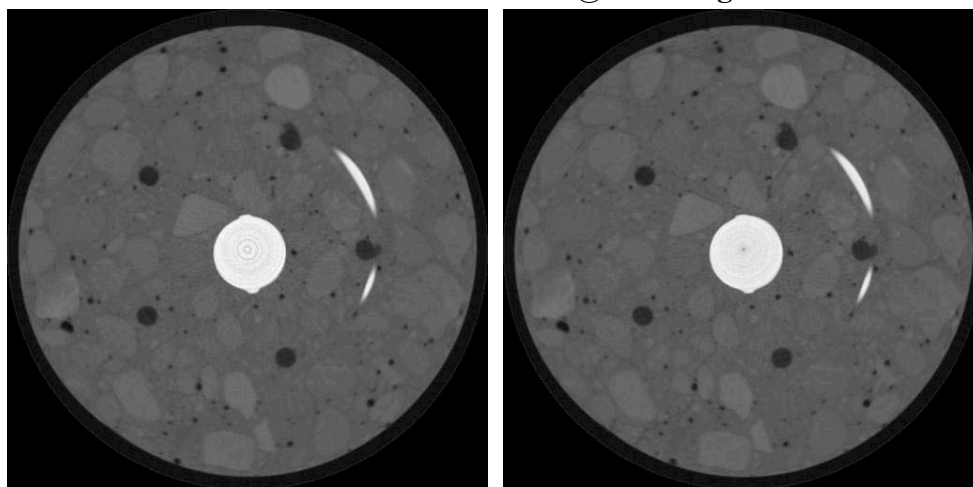


Objective Function

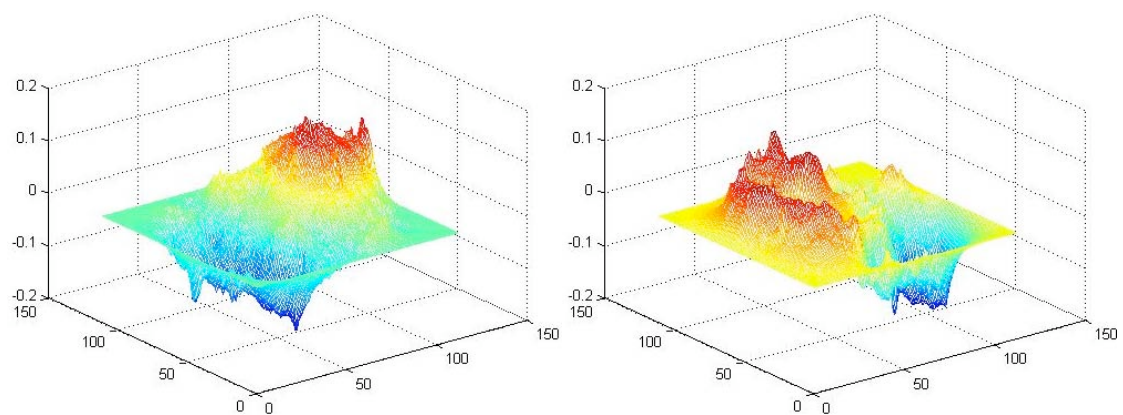


Iterations

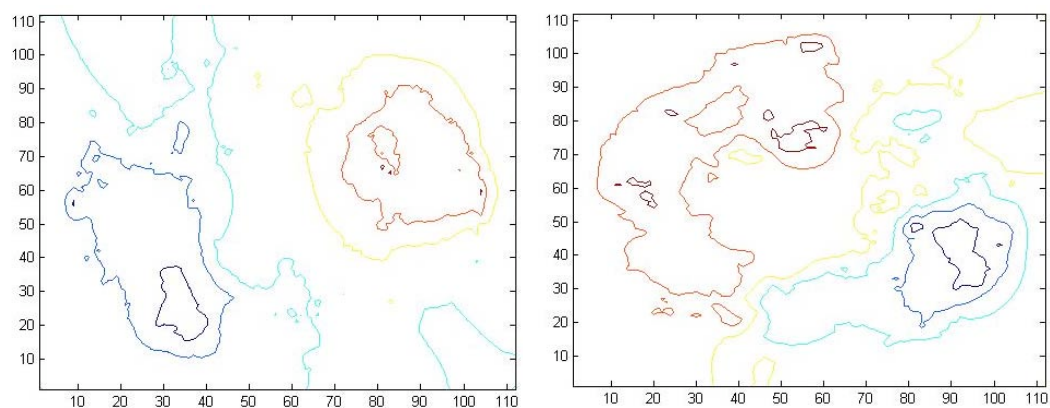
P3W2-2 -> P3W2-3 @ 0.5" height



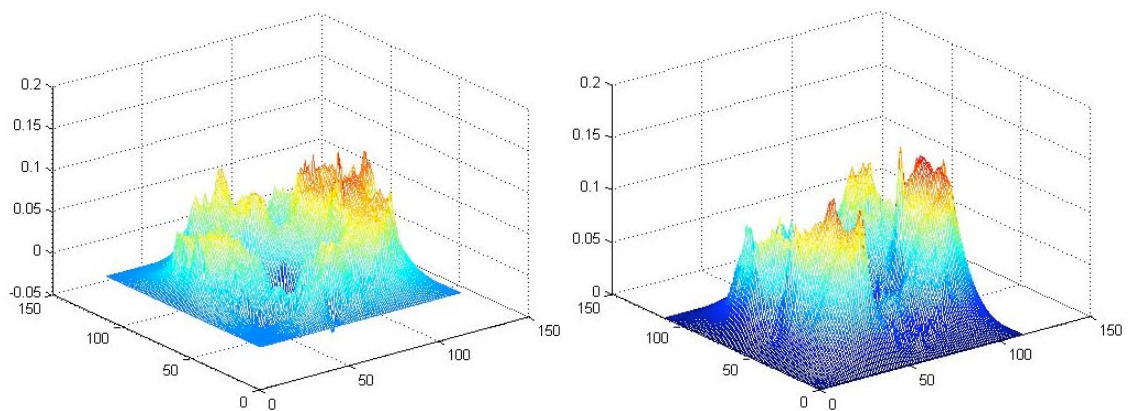
X and Y Displacement



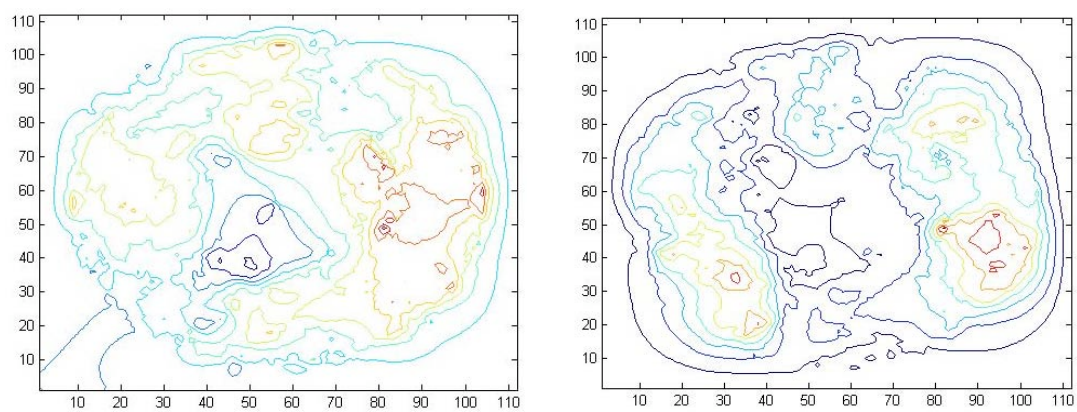
X and Y Displacement Contours



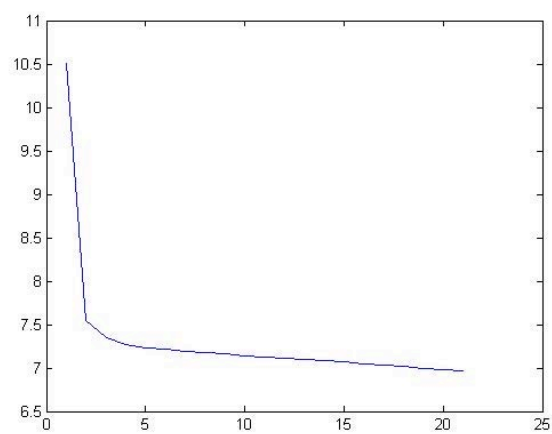
Radial and Tangential Displacement



Radial and Tangential Displacement Contours

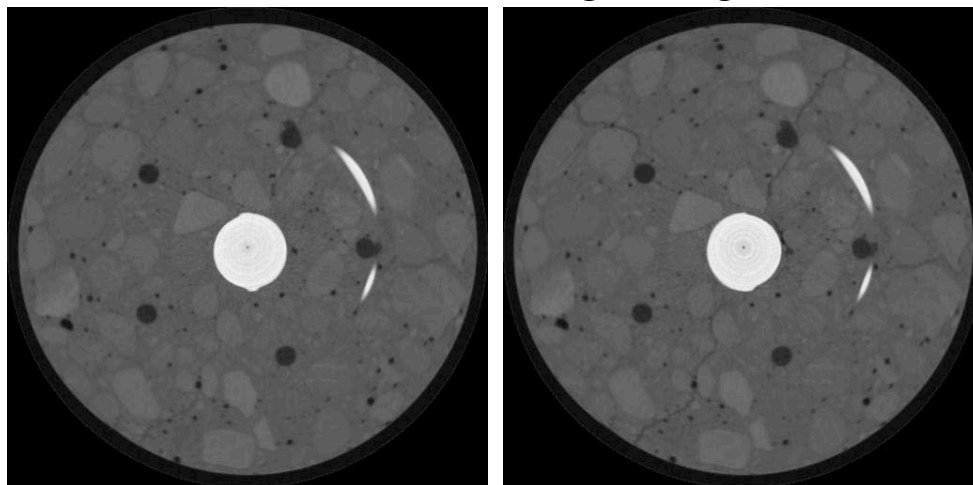


Objective Function

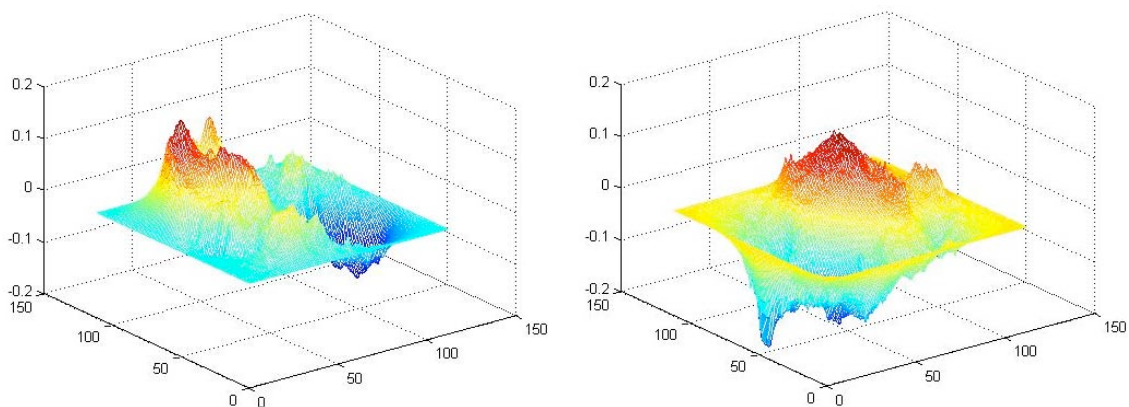


Iterations

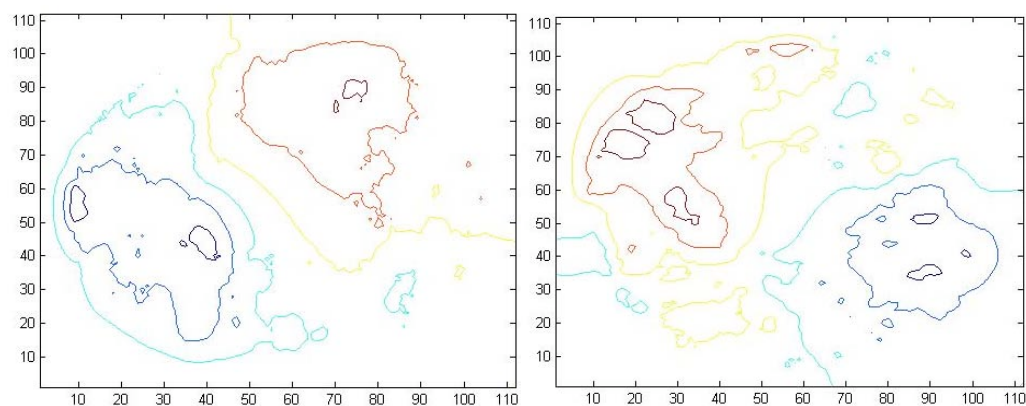
P3W2-3 -> P3W2-4 @ 0.5" height



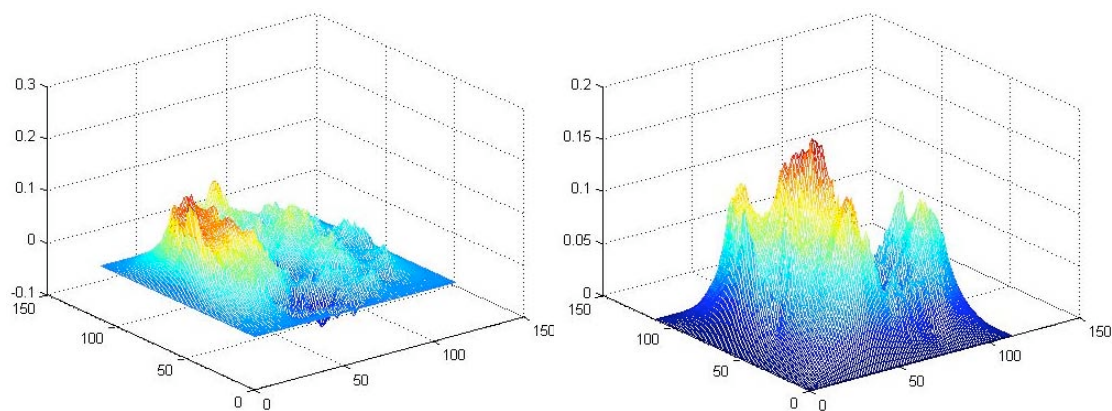
X and Y Displacement



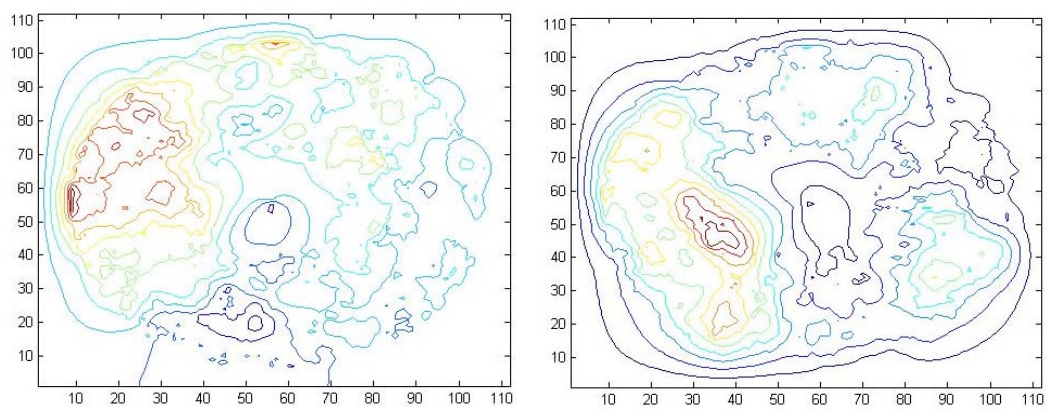
X and Y Displacement Contours



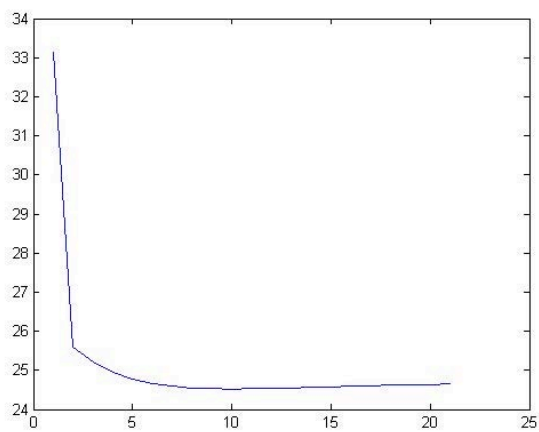
Radial and Tangential Displacement



Radial and Tangential Displacement Contours

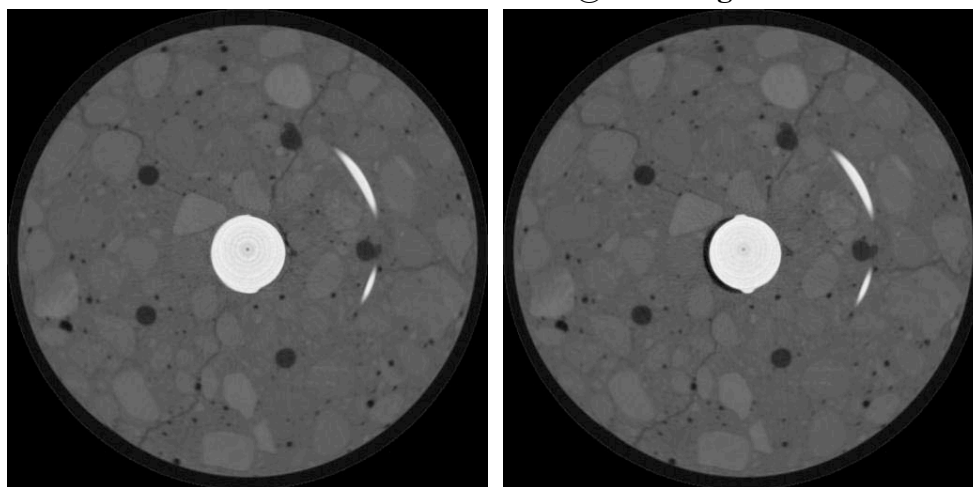


Objective Function

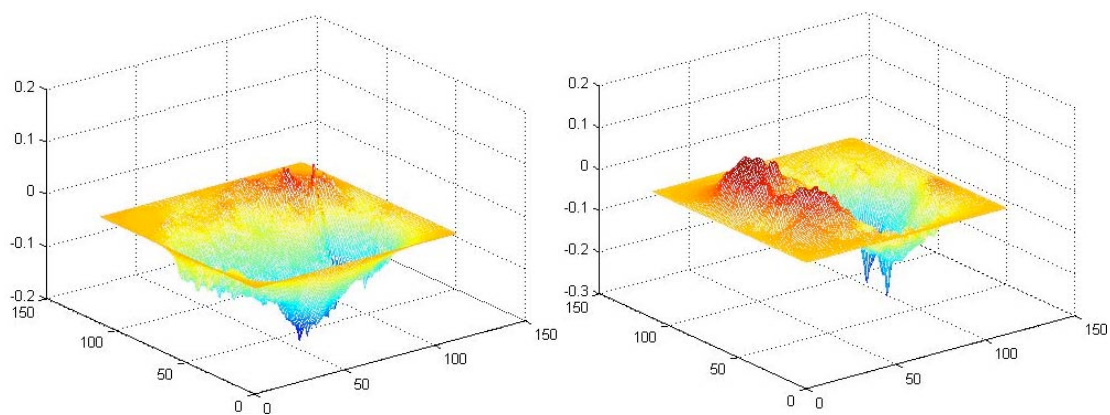


Iterations

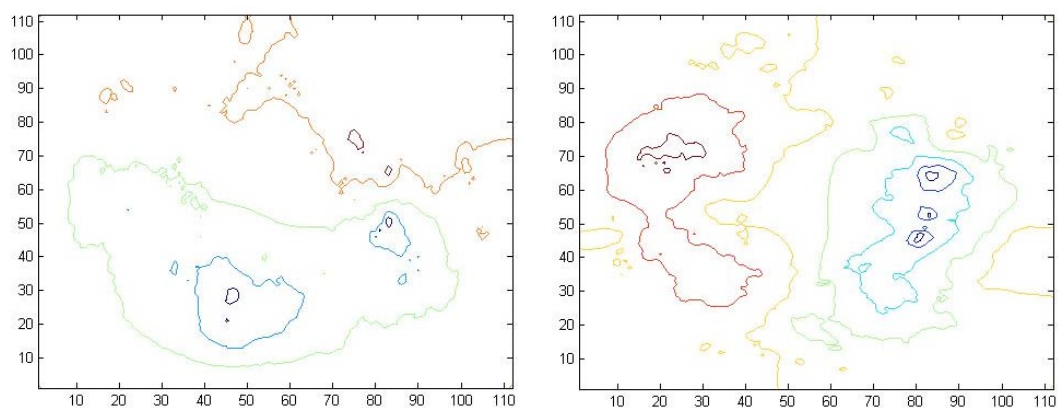
P3W2-4 -> P3W2-5 @ 0.5" height



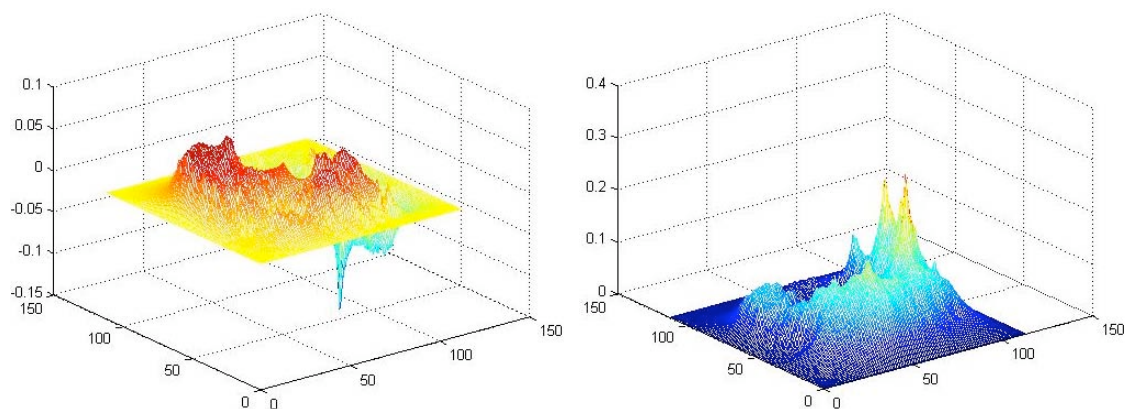
X and Y Displacement



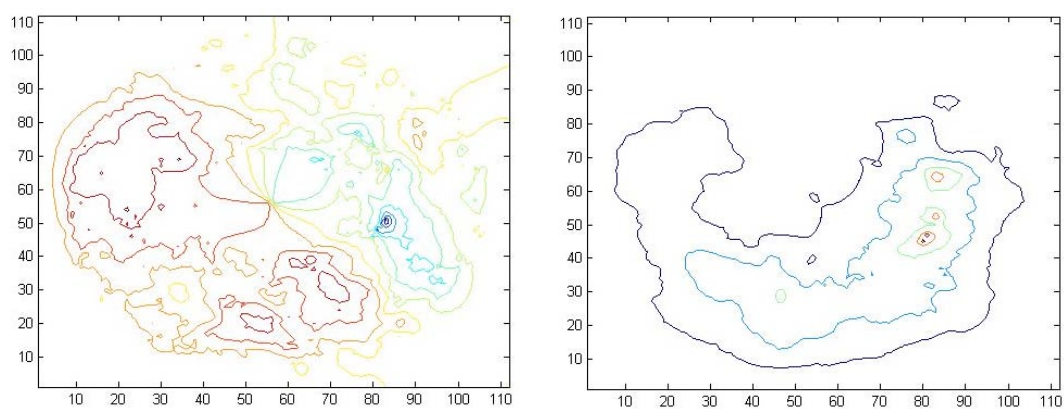
X and Y Displacement Contours



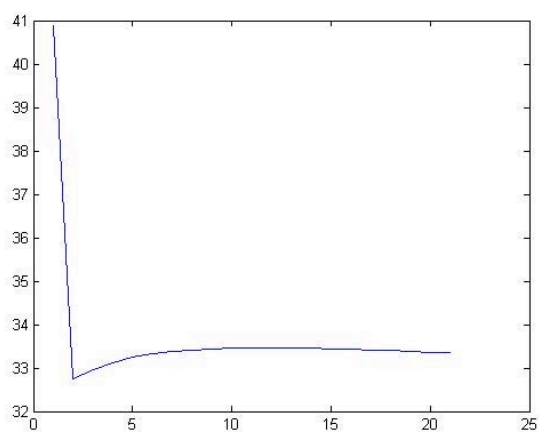
Radial and Tangential Displacement



Radial and Tangential Displacement Contours



Objective Function



Iterations

APPENDIX F : CODE IMPLEMENTATION

Motion Segmentation:

The routines listed below shrinkwrap, and vecfield are Unix routines provided by Zhang, 2004.

Step 1: Run **shrinkwrap** to generate map file to identify specimen in 3D space.

```
shrinkwrap inputfile header x y z outputfile
```

e.g. shrinkwrap Sample1 0 512 512 100 fb.map

Step 2: Run **vecfield** at increasing resolutions (or steps) to get vector field

```
vecfield file1 file2 header x y z resfile step options
```

e.g. vecfield Sample1 Sample2 0 512 512 100 Vectors 64 options

Options are outlined in the code, and can be seen by simply typing **vecfield** into Cygwin and pressing enter. Once **Vectors** is created at the 64 step, you must manually change the name to **Vectors64** in order for the code to find it for step 32. Look for it in the same directory as the code. Also, as it is a strictly binary file there is no extension. Then,

```
vecfield Sample1 Sample2 0 512 512 100 Vectors 32 options
```

```
vecfield Sample1 Sample2 0 512 512 100 Vectors 16 options ect.
```

Continue until Step 1, then you will have files **Vectors64**, **Vectors32**, **Vectors16**, **Vectors8**, **Vectors4**, **Vectors2**, and **Vectors1**, each a displacement field estimation of size $[X/step, Y/step, Z/step, 3]$.

Image Registration - Elastic Registration

The “ElasticRegistration.m” file is the main file for this routine. All top-level controls are changeable in this file.

$$[Tu, ur, uc, Obj, R, T] = \text{ElasticRegistration}(Ro, To, E, nu, i)$$

where Ro = Reference Image

To = Template Image

E = Elastic Modulus

nu = Poisson’s Ratio

i = number of iterations

This routine calls other files to perform other functions.

1. The first objective criterion is calculated and image is padded with zeros around the edges.
2. Then the Reference Image, E , and nu are sent to “**ElasticStiffness.m**” to assemble stiffness matrix (details can be found later in this appendix).
3. Free and Supported degrees of freedom are assigned through “**FixedBoundary.m**”, and then a stiffness matrix of free degrees of freedom **Kff** is defined.
4. The first displacement field is initialized, then applied to the template image to create the first deformed template image (**Tu**) through **ApplyElasticTransform.m**
5. Then a loop is initialized which contains calculation of forces and solutions. The more iterations, the better the convergence.
6. The two force fields are initialized, and the forces are calculated at each point looping over the image locations.

7. Using the function “**NormGrad.m**” a normalized gradient is calculated at each point. The forces in each direction are calculated and collected.
8. These forces in the x and y directions (or row and column), are assembled into a single force vector. Note: the function “**RemoveBarForces.m**” is an optional function that eliminates forces around the center bar, which, due to imaging artifacts, can disrupt convergence.
9. The free degrees of freedom are extracted from the force vector.
10. Using L U decomposition, the free displacements are solved for. $\mathbf{dU} = \mathbf{KffFf}$
11. The displacements from each iteration are added together, and separated into **ur** and **uc**(for row and column) displacement fields “**VectorToField.m**”
12. These displacements transform T to generate Tu
“**ApplyElasticTransform.m**”, and the objective function is calculated again.
13. This loop continues for the number of iterations pre-defined, and then the routine returns a final **ur, uc, Tu, Obj vector, R**

Image Registration - XFEM Registration

The “XFEMRegistration.m” file is the main file for this routine. All top-level controls are changeable in this file.

$[Tu, ur, uc, xur, xuc, Obj] = XFEMRegistration(Ro, To, E, nu, I, cracks)$

where Ro = Reference Image

To= Template Image

E = Elastic Modulus

nu = Poisson’s Ratio

i = number of iterations

cracks = beginning location and end location of crack (2x2 array)

This routine calls other files to perform other functions.

1. The first objective criterion is calculated and image is padded with zeros around the edges.
2. Then “**CrackExtension.m**”, defines a linear path between the two specified locations in **crack**– defining every point where the crack crosses an element boundary.
3. Then the Reference Image, E, nu and crack geometry are sent to “**XFEMStiffness.m**” to assemble stiffness matrix (details can be found later in this appendix).
4. Free and Supported classical degrees of freedom are assigned through “**FixedBoundary.m**”, enriched degrees of freedom are defined after, and then

a stiffness matrix of free degrees of freedom (classical and enriched) **Kff** is defined.

5. The first displacement field is initialized (**ur,uc,xur,xuc**), then applied to the template image to create the first deformed template image (**Tu**) through **ApplyInelasticTransform.m**
6. Then a loop is initialized which contains calculation of forces and solutions. The more iterations, the better the convergence.
7. The four force fields are initialized (**fr,fc,xfr,xfc**), and the forces are calculated at each point looping over the image locations. Note: No forces are applied to the enriched degrees of freedom.
8. Using the function “**NormGrad.m**” a normalized gradient is calculated at each point. The forces in each direction are calculated and collected.
9. These forces in the x and y directions (or row and column), are assembled into a single force vector. Note: the function “**RemoveBarForces.m**” is an optional function that eliminates forces around the center bar, which, due to imaging artifacts, can disrupt convergence.
10. The free degrees of freedom are extracted from the force vector.
11. Using L U decomposition, the free displacements are solved for. **dU = Kff\Ff**
12. The displacements from each iteration are added together, and separated into **ur, uc, xur, xuc** (for row and column) displacement fields
“**VectorToField.m**”
13. These displacements transform T to generate Tu
“**ApplyInelasticTransform.m**”, and the objective function is calculated again.
14. This loop continues for the number of iterations pre-defined, and then the routine returns a final **ur, uc, xuc, xur, Tu, Obj vector, R**

ApplyElasticTransform.m – Applies u_r and u_c to T to create T_u . Uses inverse transform – loops over T_u , determine where each pixel came from, uses averaging routine **Eval.m**

ApplyInelasticTransform - Applies u_r , u_c , x_u , x_c to T to create T_u . Uses direct transform, looping over T , finding destination of each pixel, then averaging locations to solve for areas not mapped

AreaCheck.m – Checks area of top and bottom of partitioned element, makes sure they add to four.

CalculateObjective.m – Returns objective criterion for two images, T_u and R . Uses sum of squared differences, but could be modified.

ClassicalB.m – Calculates B from parametric formulation and location of gauss point.

ConvertToRadial.m - Converts x and y (or u_r and u_c) displacements to radial and tangential displacements, for visualization.

ElasticStiffness.m – Generates elastic stiffness matrix. Initializes variables – freedom=nodes to dof, coord=nodes to location, degrees=elements to dof, location=element to location. Loop over elements, assign element stiffness matrix through “quad_el.m”

enrich_quad_el.m – Element stiffness for element cut by crack. Isoparametric formulation, first map crack to isoparametric space (**InvertLinearIsoparam.m**). Then

partition the element through “**PartitionElement.m**”. Then through “**TriangArea.m**” the area of the top and bottom of the element are calculated. “**AreaCheck.m**” makes sure top and bottom add to area of four. Then, numerical integration is carried out over the top and bottom areas, with locations and weights (Galerkin) from “**triquad.m**”. Then according to FEM rules, the B matrixes for the classical and enriched dof are calculated from “**ClassicalB.m**”. The stiffness matrix is calculated and assembled.

FieldToVector.m – Convert fields to vector for solution

Fixed Boundary.m – Defines fixed and supported degrees of freedom for a fixed boundary.

InvertLinearIsoparam.m – Inverts linear isoparametric formulation, for mapping cracks into isoparametric space.

NormGrad.m – Defines gradient at each point using least-squares approximation

PartitionElement – Cuts element in to “above” and “below” sections. Returns vertices of top and bottom.

quad_el.m - Element stiffness matrix. Isoparametric formulation, numerical integration is carried out over the element, four qauss points. Then according to FEM rules, the B matrixes are calculated from “**ClassicalB.m**”. The stiffness matrix is calculated and assembled.

SpringStiffness.m – Assembles stiffness matrix based on analogy of springs (longitudinal and shear), with k instead of E, nu. Not used in final implementation.

TriangArea.m – Calculates the area of triangles given verticies.

triquad.m – MATLAB script to define locations and weight for numerical integration of any triangle.

VectorToField.m – Converts solution from vector to field for visualization.

XFEMStiffness.m – Generates XFEM stiffness matrix. Initializes variables – freedom=nodes to dof, coord=nodes to location, degrees=elements to dof, location=element to location. Then using loop, define which elements are enriched by crack, and the location. Loop over elements, if element is enriched, sent to “**enrich_quad_el.m**”. Assign different portions of stiffness matrix to different names. If not enriched, assign element stiffness matrix through “**quad_el.m**”. If crack cuts element such that A_{top}/A_{bottom} is below tolerance, element is not enriched.